



UNIVERSITY COLLEGE LONDON

Faculty of Mathematics and Physical Sciences

Department of Physics & Astronomy

HERSCHEL STUDIES OF CORE
COLLAPSE SUPERNOVA REMNANTS
AT INFRARED WAVELENGTHS

Thesis submitted for the Degree of Doctor of
Philosophy of the University of London

by
Patrick James Owen

Supervisors:

Prof. Michael J. Barlow
Prof. Bruce M. Swinyard

Examiners:

Dr. David A. Green
Prof. Jonathan M. C. Rawlings

January 19, 2015

For Everyone

I, Patrick James Owen, confirm that the work presented in this thesis is my own. Where information has been derived from other sources, I confirm that this has been indicated in the thesis.

Abstract

Core collapse supernovae play a vital role in the evolution of the universe. They are major producers of metals and the only place where elements heavier than Iron can be made. These metals can then join to form molecules and dust, enriching the interstellar medium to provide cooling to form new stars. These molecules and dust, as well as metal cooling lines can all be observed in the infrared, making it a very interesting wavelength range in which to study supernovae and their remnants.

This investigation of supernova remnants in the infrared has been made possible by the European Space Agency's *Herschel* Space Observatory. *Herschel* studied the universe between 60 and 670 μm , covering the peak of dust emission, a large range of atomic fine structure cooling lines, a large portion of the Carbon Monoxide rotation ladder and other more exotic molecular line transitions.

This thesis presents spectroscopic observations of the Cassiopeia A and Crab supernova remnants using two of the *Herschel* instruments to investigate their structure, physics and chemistry. It also presents the results of radiative transfer models based on photometric *Herschel* data to investigate more physical measurements of the mass of dust in supernova remnants. These models, along with others are then used to investigate the nature of dust formation in supernovae and the composition of this dust.

Observations of the Crab Nebula with *Herschel* SPIRE made the first ever observation of a molecule containing a noble gas in space. Within the dense filaments of the nebula, two rotational lines of $^{36}\text{ArH}^+$ were observed. This discovery was followed up with the

VLT to try to find vibrational lines in the near infrared as well as an investigation of the potential presence of HeH^+ . Unfortunately these were unsuccessful. PACS and LWS observations were used to diagnose the conditions in the remnant, density, oxygen to nitrogen ratio and the ionic abundances of Nitrogen. Velocity information was also investigated and emitting regions compared to optical emission.

Observations of Cassiopeia A made with *Herschel* are compared with observations made using the NuSTAR $\gamma/\text{x-ray}$ telescope to investigate the effect of the presence of ^{44}Ti on formation and destruction of dust. The complex decay chain of ^{44}Ti leads to an abundance of high energy electrons which lead to the regions with strong ^{44}Ti emission being regions where there is little or no dust emission.

By using photoionisation models of the Crab Nebula we were about to determine the mass of dust in the remnant. This measurement takes in to account realistic heating of the dust, density distribution of the dust, the gas in the nebula and the size and species of the dust grains. We found that the dust mass is approximately twice the empirical dust mass estimate when these physical conditions are taken in to account.

Acknowledgements

Firstly massive thanks to Mike for giving me this opportunity and for putting up with me for the past few years. I couldn't have done it without his help and advice. Also really couldn't have done it without the help from Bruce, who also provided a massive amount of useful input. Antonia has to get thanks for sanity checks and science chats. Mikako also gets a science and sanity mention. Roger and Oskar for their better than mine knowledge of MOCASSIN and its *usability*.

I'd like to apologise to everyone who had the misfortune of sharing an office with me in my first few years here. I was a bit noisy at times (although I did actually work too!). I think an extra special mention has to go to Emma who really bore the brunt of the shenanigans of G18 and Beca who bore the brunt of the planes! (and was generally awesome). Barney and Bambam and Cris and Sree and Walter and Lucy and Antonia (again, you get thanked twice) and all the visitor who came to play Nicolas Cage. Thanks to everyone in the basement. Especially my OB22 peoples for all the popcorn.

Jen for putting up with me and generally being amazing.

For the chemical aids to sanity, those good people at the Euston Tap and the Algerian Coffee Company - without these I'd really not have made it through to the end. Swing Patrol Waterloo and Kings Cross (Swing and Balboa) peoples for general awesomeness and dancing and dancing and awesomeness.

Rich, Deej, Little Paul (who?) and GeorgeKelly. Thank you. Tea break?

Mum and Dad because apparently you'll actually read this bit.
Cheers.

*Something in the way he said it made Lyra imagine dust with a capital letter, as if
this wasn't ordinary dust.*

Philip Pullman in Northern Lights

Contents

Table of Contents	7
List of Figures	11
List of Tables	19
List of Acronyms	27
1 Dust in the Universe	31
1.1 Yeah, but what is dust?	33
1.2 How we observe dust	33
1.2.1 The <i>Herschel</i> Space Observatory	34
1.2.2 The <i>Spitzer</i> Space Telescope	37
1.2.3 Other Infrared and Sub Millimetre Observatories	37
2 Supernovae and their Remnants	39
2.1 Types of Supernovae	39
2.2 Supernova Remnants	41
2.3 Dust Formation in Supernovae and Supernova Remnants	41
2.3.1 Formation	41
2.3.2 Observed Dust Masses	42
2.3.3 Recent Observations with Herschel	42
2.4 Infrared atomic lines in Supernova Remnants	46
2.4.1 Fine Structure Lines	46
2.5 Molecules in Supernova Remnants	48

2.6 This Thesis	49
3 Herschel Spectroscopy of the Crab Nebula	51
3.1 The Crab Nebula with PACS	52
3.1.1 Nebula Diagnostics	53
3.1.2 Velocity Structure	57
3.2 The Crab Nebula with SPIRE-FTS	60
3.2.1 Unidentified Lines	60
3.2.2 Identifying the Line	61
3.2.3 Line Fluxes	62
3.2.4 Formation and Destruction Mechanisms for ArH ⁺	62
3.2.5 Argon Nucleosynthesis	65
3.2.6 ArH ⁺ with PACS	66
3.2.7 Temperature	66
3.3 Follow-up with the VLT	67
3.3.1 Observations	68
3.3.2 Data Reduction	71
3.3.3 Results	73
3.3.4 Upper Limits	76
3.4 HeH ⁺ with PACS	80
3.5 Conclusions	81
4 Herschel Spectroscopy of Cassiopeia A	83
4.1 Cassiopeia A with PACS	83
4.1.1 Oxygen	86
4.1.2 Upper Limits on the [O I] 145 μ m line	88
4.1.3 Carbon	99
4.2 Cas A with SPIRE	101
4.3 CO and Carbon	105
4.4 Dust in Cas A	105
4.4.1 NuSTAR	106
4.4.2 Comparisons of the NuSTAR and Herschel images of Cas A	107
4.5 Conclusions	107

5 Dust in the Crab Nebula	109
5.1 The Model	112
5.1.1 Geometry and Spectrum	112
5.1.2 Spectral Energy Distribution	113
5.1.3 Optical Lines	113
5.1.4 Grain species and optical properties	114
5.1.5 Density distributions	116
5.1.6 Nucleosynthesis	123
5.2 Results	125
5.2.1 Elemental Abundances	125
5.2.2 Dust Masses	125
5.2.3 Ionisation	145
5.3 Discussion	145
5.3.1 The importance of using both gas and dust	145
5.3.2 The importance of using a diffuse heating source	147
5.3.3 Clumping	147
5.3.4 Optical Properties	148
5.3.5 Grain Size Distribution	150
5.3.6 Continuous Distribution of Ellipsoids	154
5.3.7 Optical Depths of the Clumps	154
5.3.8 Total Nebula Mass	155
5.3.9 Predicting Photometric Fluxes	156
5.4 Alternative Dust Mass Estimates	156
5.4.1 The Temim and Dwek 2013 Estimate	156
5.4.2 Empirical Dust Masses	159
5.5 Conclusions	160
6 Conclusions and Future Work	163
6.1 The Crab Nebula	163
6.2 Cassiopeia A	165
6.3 Other future work	165
A Appendix A	167

B Appendix B	173
B.1 SP1	174
B.2 SP3	175
B.3 SP4	178
B.4 SP5	179
B.5 SP7	182
B.6 SP8	184
B.7 SP9	186
C Appendix C	189
Bibliography	191

List of Figures

1.1	SDSS J114816.64+525150.3, a quasar at $z = 6.42$ observed with IRAM 30 m telescope showing a rest frame IR excess corresponding to $10^8 M_\odot$ of dust taken from Bertoldi et al. (2003).	32
1.2	A Hubble Space Telescope optical image of the Andromeda Galaxy	34
1.3	An infrared image of the Andromeda galaxy taken with the Herschel Space Observatory	35
2.1	Multi wavelength observations of Cas A showing continuum at 6 cm (VLA) and 3.6 μm , warm dust at 24 μm (Spitzer) and 70 μm (Herschel), cool dust 100 μm (Herschel) and 70 μm (Herschel) and 160, 350 and 500 μm foreground dust taken from Barlow et al. (2010).	43
2.2	<i>Herschel</i> Observation of 1987A at 100, 160, 250 and 350 μm taken from Matsuura et al. (2011).	45
2.3	ALMA (mm and sub-mm), ATCA (mm), Hubble (visible) and Chandra (x-ray) observations of SN1987a showing the structure of the supernova remnant and location of the dust. Taken from Indebetouw et al. (2014).	46
2.4	The fine structure splitting in the ground state of doubly ionised oxygen.	47
3.1	The position of the PACS-IFU observations of the Crab Nebula plotted on a PACS 70 μm image.	52
3.2	The position of the ISO-LWS observations of the Crab Nebula plotted on a PACS 70 μm image.	53
3.3	The 25 individual PACS spaxels plotted in velocity space. The 88 μm [O III] line is in black, the 63 μm [O I] line is in red and the 158 μm [C II] line is in green.	58

3.4	A map of the 88 μm [O III] for each PACS-IFU spaxel, plotted over the PACS 70 μm map plotted as a contour plot.	58
3.5	A map of the 63 μm [O I] for each PACS-IFU spaxel, plotted over the PACS 70 μm map plotted as a contour plot.	59
3.6	A map of the 158 μm [C II] for each PACS-IFU spaxel, plotted over the PACS 70 μm map plotted as a contour plot. Note the scale is an order of magnitude less than the plots for the [O I] and [O III] maps.	59
3.7	The SPIRE-FTS observations of the Crab Nebula shown on a 70 μm PACS broadband image. Green circles are the SSW detectors, white circles are the SLW detectors. Circles with a cross denote the detectors in which the unidentified line was observed.	60
3.8	SLW D4 spectrum to showing the one of the unidentified line at 618 GHz. .	61
3.9	SSW B1 spectrum to showing the one of the unidentified line at 1235 GHz. .	62
3.10	A <i>Herschel</i> PACS 70 μm image with the size and location of the Loh et al. (2011) H ₂ knots shown as green circles.	64
3.11	PACS-IFU observations of the region of the J=3-2 161.98 μm $^{36}\text{ArH}^+$ line. .	66
3.12	The rotation diagram used to determine the temperature of $^{36}\text{ArH}^+$ in the SLW-C3 SSW D4 and PACS-IFU observations	67
3.13	The location of the Loh et al. (2011) knot 1 (magenta circle) and nearby <i>Herschel</i> SPIRE-FTS detectors that detected $^{36}\text{ArH}^+$ (green circle for SSW, blue circle for SLW).	68
3.14	Finding chart for the VLT observations showing the slit position of the CRIRES spectrometer in blue on the 2MASS catalogue image of the crab nebula. The Loh et al. (2011) knot 1 position is shown as a green circle. .	69
3.15	The Targeting of the VLT showing the spectrograph slit over the central knots.	70
3.16	The raw spectral data from CRIRES observations of the Crab Nebula before any processing has taken place	71
3.17	The spectral data from CRIRES observations of the Crab Nebula after they have been processed using a median filtering technique to remove cosmic rays from the data.	72
3.18	The spectrum of the observation of HeH ⁺ R(1) (blue) and model sky from the ETC (green).	73

3.19	The modelled blackbody spectrum of ι Tau used for flux calibration.	74
3.20	The spectrum of the region of the HeH^+ R(0) 3364.09 nm line taken with VLT-CRIRES.	74
3.21	The spectrum of the region of the HeH^+ R(1) 3302.10 nm line taken with VLT-CRIRES.	75
3.22	The spectrum of the region of the ArH^+ ($v=1-0, J=2-1$) 3799.99 nm line taken with VLT-CRIRES.	75
3.23	The spectrum of the region of the $r\text{H}^+$ ($v=1-0, J=1-0$) 3827.75 nm line taken with VLT-CRIRES.	76
3.24	The 8 coadded spectra of the whole slit of the spectrograph in the region of the HeH^+ R(1) 3302.10 nm line taken with VLT-CRIRES.	76
3.25	The 8 coadded spectra of the whole slit of the spectrograph in the region of the HeH^+ R(0) 3364.09 nm line taken with VLT-CRIRES.	77
3.26	The 8 coadded spectra of the whole slit of the spectrograph in the region of the $r\text{H}^+$ ($v=1-0, J=1-0$) 3827.75 nm line taken with VLT-CRIRES.	77
3.27	The 8 coadded spectra of the whole slit of the spectrograph in the region of the ArH^+ ($v=1-0, J=2-1$) 3799.99 nm line taken with VLT-CRIRES.	78
3.28	The spectrum of the region of the HeH^+ R(1) 3302.10 nm line taken with VLT-CRIRES.	78
3.29	The spectrum of the region of the HeH^+ R(0) 3364.09 nm line taken with VLT-CRIRES.	79
3.30	The spectrum of the region of the $r\text{H}^+$ ($v=1-0, J=1-0$) 3827.75 nm line taken with VLT-CRIRES.	79
3.31	The spectrum of the region of the ArH^+ ($v=1-0, J=2-1$) 3799.99 nm line taken with VLT-CRIRES.	80
3.32	PACS-IFU observations of the region of the $J=1-0$ $149.25 \mu\text{m}$ HeH^+ line.	81
3.33	PACS-IFU observations of the region of the $J=2-1$ $74.83 \mu\text{m}$ HeH^+ line.	82
4.1	The observations of Cas A with <i>Herschel</i> PACS-IFU plotted on a PACS 70 μm image.	84
4.2	The 5x5 PACS-IFU observation SP1 of Cas A in velocity space. The black line shows the $88 \mu\text{m}$ [O III] line, the red line shows the $63 \mu\text{m}$ [O I] line and the green shows the $157 \mu\text{m}$ [C II] line.	86

4.3	The 5x5 PACS-IFU observation SP2 of Cas A in velocity space. The black line shows the 88 μm [O III] line, the red line shows the 63 μm [O I] line and the green shows the 157 μm [C II] line.	87
4.4	The 5x5 PACS-IFU observation SP3 of Cas A in velocity space. The black line shows the 88 μm [O III] line, the red line shows the 63 μm [O I] line and the green shows the 157 μm [C II] line.	88
4.5	The 5x5 PACS-IFU observation SP4 of Cas A in velocity space. The black line shows the 88 μm [O III] line, the red line shows the 63 μm [O I] line and the green shows the 157 μm [C II] line.	89
4.6	The 5x5 PACS-IFU observation SP5 of Cas A in velocity space. The black line shows the 88 μm [O III] line, the red line shows the 63 μm [O I] line and the green shows the 157 μm [C II] line.	90
4.7	The 5x5 PACS-IFU observation SP6 of Cas A in velocity space. The black line shows the 88 μm [O III] line, the red line shows the 63 μm [O I] line and the green shows the 157 μm [C II] line.	91
4.8	The 5x5 PACS-IFU observation SP7 of Cas A in velocity space. The black line shows the 88 μm [O III] line, the red line shows the 63 μm [O I] line and the green shows the 157 μm [C II] line.	92
4.9	The 5x5 PACS-IFU observation SP8 of Cas A in velocity space. The black line shows the 88 μm [O III] line, the red line shows the 63 μm [O I] line and the green shows the 157 μm [C II] line.	93
4.10	The 5x5 PACS-IFU observation SP9 of Cas A in velocity space. The black line shows the 88 μm [O III] line, the red line shows the 63 μm [O I] line and the green shows the 157 μm [C II] line.	94
4.11	The relative flux of the red shifted emission of the [O III] 88 μm in Cas A plotted over a contour map of the PACS 70 μm image.	95
4.12	The relative flux of the blue shifted emission of the [O III] 88 μm in Cas A plotted over a contour map of the PACS 70 μm image.	96
4.13	The relative flux of the red shifted emission of the [O I] 63 μm in Cas A plotted over a contour map of the PACS 70 μm image.	97
4.14	The relative flux of the blue shifted emission of the [O I] 63 μm in Cas A plotted over a contour map of the PACS 70 μm image.	98
4.15	[O I] Fine-structure energy levels	98

4.16	The relative flux of the red shifted emission of the [C II] 157 μm in Cas A plotted over a contour map of the PACS 70 μm image.	100
4.17	The relative flux of the blue shifted emission of the [C II] 157 μm in Cas A plotted over a contour map of the PACS 70 μm image.	101
4.18	Positions of the SSW detectors of the three <i>Herschel</i> SPIRE-IFU on Cas A plotted on a 70 μm image. The "Central" observation is shown in top left, top right is the "North West" and bottom left is the "North" observation. . .	102
4.19	Positions on Cas A of the regions where CO is detected by SPIRE. Also included the PACS CO detections of Wallström et al. (2013) plotted on a 70 μm image.	103
4.20	A CO population to determine temperature and column density using <i>Herschel</i> SPIRE-FTS observations of Cas A-NW with detector SSW C4.	103
4.21	A CO population to determine temperature and column density using <i>Herschel</i> SPIRE-FTS observations of Cas A-NW with detector SSW C5.	104
4.22	A CO population to determine temperature and column density using <i>Herschel</i> SPIRE-FTS observations of Cas A-NW with detector SSW C5 and the <i>Herschel</i> PACS observations from Wallström et al. (2013).	104
4.23	<i>Herschel</i> PACS 70 μm map of Cas A with the regions with where CO has been detected shown in green and the regions where the [C II] lines have been observed shown in red.	105
4.24	^{44}Ti map of Cas A made with the NuSTAR telescope taken from (Grefenstette et al. 2014).	106
4.25	The top left is the <i>Herschel</i> PACS 70 μm map, the bottom left is ^{44}Ti map of Cas A made with the NuSTAR telescope taken from (Grefenstette et al. 2014). The top right is the ^{44}Ti in blue over the PACS 70 μm dust emission in red and the bottom right is the PACS 70 μm dust emission with the ^{44}Ti shown as contours in green.	107
5.1	A composite HST and <i>Herschel</i> 70 μm image showing the dust emission closely tied to the optical knots and filaments.	111
5.2	The input Spectrum used to heat the dust and ionise the gas, taken from Hester (2008) and adjusted for Planck Collaboration (2011) in the sub-mm. .	113
5.3	A cartoon schematic of the geometry I	116

5.4	A cartoon schematic of the geometry II	117
5.5	A cartoon schematic of the geometry III	118
5.6	A cartoon schematic of the geometry IV	118
5.7	A cartoon schematic of the geometry V	119
5.8	A cartoon schematic of the geometry VI	120
5.9	A cartoon schematic of the geometry VII	120
5.10	A cartoon schematic of the geometry VIII	121
5.11	A cartoon schematic of the geometry IX	122
5.12	A cartoon schematic of the geometry X	122
5.13	A cartoon schematic of the geometry XI	123
5.14	A cartoon schematic of the geometry XII	124
5.15	A cartoon schematic of the geometry XIII	124
5.16	Best fit models plotted with observed SEDs for the six different sets of optical constants using a smooth isotropic density distribution with an electron density of 775 cm^{-3}	135
5.17	Best fit models plotted with observed SEDs for the six different sets of optical constants using a smooth isotropic density distribution in a shell in the outer third of the nebula with a density of 850 cm^{-3} outside the diffuse radiation source	136
5.18	Best fit models plotted with observed SEDs for the six different sets of optical constants using a smooth isotropic density distribution in a shell 0.5 pc thick and a inner axes of 2.1×1.4 pc entirely inside the diffuse radiation source.	137
5.19	Best fit models plotted with observed SEDs for the six different sets of optical constants using a smooth isotropic density distribution in a shell all the way to the edge of the nebula and a inner axes of 2.1×1.4 pc entirely inside the diffuse radiation source.	138
5.20	Best fit models plotted with observed SEDs for the six different sets of optical constants using a smooth isotropic density distribution in a shell all the way to the edge of the nebula and a inner axes of 2.3×1.7 pc entirely inside the diffuse radiation source.	139

5.21 Best fit models plotted with observed SEDs for the six different sets of optical constants using a smooth isotropic density distribution in a shell 0.1 pc thick and a inner axes of 1.1×1.1 pc entirely inside the diffuse radiation source.	140
5.22 Best fit models plotted with observed SEDs for the six different sets of optical constants using a density distribution when all of the matter is in clumps with radius 0.111 pc and a density of 1400 cm^{-3}	141
5.23 Best fit models plotted with observed SEDs for the six different sets of optical constants using a density distribution when all of the matter is in clumps of radius 0.037 pc with a density of 1900 cm^{-3}	142
5.24 Best fit models plotted with observed SEDs for the six different sets of optical constants using a density distribution when all of the matter is in clumps of radius 0.037 pc with a density of 1900 cm^{-3}	143
5.25 Best fit models plotted with observed SEDs for the six different sets of optical constants using a density distribution when all of the matter is in clumps of radius 0.037 pc with a density of 1900 cm^{-3}	144
5.26 Synchrotron subtracted infrared SEDs of the best fit dust mass for the gas and dust model and a model with the same parameters with no gas, just dust.	146
5.27 The ultraviolet SED for models with gas and dust, gas only and dust only .	146
5.28 Best fit model SED for model x (black line) along with a model run with identical geometry, dust mass and elemental abundance but with a central point source as the heating source (blue line)	147
5.29 $Q_{\text{abs}}(\lambda)$ against Wavelength for amorphous carbon grain optical constants used and a grain size of $0.1 \mu\text{m}$	148
5.30 the effect of varying the power law slope α on the fitted SED..	152
5.31 the effect of varying the maximum grain size, a_{max} on the fitted SED.	152
5.32 the effect of varying the minimum grain size, a_{min} on the fitted SED..	153

This page was intentionally left blank

List of Tables

2.1	The different types of core collapse supernovae.	40
3.1	Information on the position and integration time of spectroscopic measurements of the Crab Nebula using <i>Herschel</i> PACS-IFU and ISO-LWS.	54
3.2	Crab Nebula far-infrared line fluxes, electron densities and relative ion abundances. Line intensities relative to [O III] F _(88 μm) =100. PACS relative flux calibration uncertain at 52 μm	56
3.3	Details of the <i>Herschel</i> SPIRE-FTS observation of the Crab Nebula.	60
3.4	SPIRE-FTS radial velocity and line surface brightness measurements for the J = 1-0 and 2-1 rotational lines of ³⁶ ArH ⁺ from the Crab Nebula	63
3.5	Information about the VLT-CRIRES observations of the Crab Nebula ArH ⁺ and HeH ⁺	70
3.6	The factors used in calculating the upper limits of detection in the CRIRES spectra. Heliocentric correction for motion of the earth taken from ESO Sky Calendar Tool http://www.eso.org/sci/observing/tools/calendar/airmass.html	79
3.7	The upper limits of detection of the HeH ⁺ R(0), R(1) and ArH ⁺ (v=1-0, J=1-0) and (v=1-0, J=2-1) lines with VLT-CRIRES	80
4.1	The positions of the PACS Spectroscopic observations of Cas A	85
4.2	The upper limits on the red shifted component of the [O I] 145 μm emission in the SP1 observations of Cas A measured by PACS-IFU	89
4.3	The upper limits on the blue shifted component of the [O I] 145 μm emission in the SP1 observations of Cas A measured by PACS-IFU	90

4.4	The upper limits on the red shifted component of the [O I] 145 μm emission in the SP4 observations of Cas A measured by PACS-IFU	90
4.5	The upper limits on the blue shifted component of the [O I] 145 μm emission in the SP4 observations of Cas A measured by PACS-IFU	91
4.6	The upper limits on the red shifted component of the [O I] 145 μm emission in the SP5 observations of Cas A measured by PACS-IFU	91
4.7	The upper limits on the blue shifted component of the [O I] 145 μm emission in the SP5 observations of Cas A measured by PACS-IFU	92
4.8	The upper limits on the red shifted component of the [O I] 145 μm emission in the SP7 observations of Cas A measured by PACS-IFU	99
4.9	The upper limits on the blue shifted component of the [O I] 145 μm emission in the SP7 observations of Cas A measured by PACS-IFU	99
4.10	The upper limits on the red shifted component of the [O I] 145 μm emission in the SP8 observations of Cas A measured by PACS-IFU	99
4.11	The upper limits on the blue shifted component of the [O I] 145 μm emission in the SP8 observations of Cas A measured by PACS-IFU	100
4.12	The upper limits on the red shifted component of the [O I] 145 μm emission in the SP9 observations of Cas A measured by PACS-IFU	100
5.1	Integrated Fluxes for the Crab Nebula. <i>Spitzer</i> data are taken from Temim et al. (2006), <i>Herschel</i> data are taken from Gomez et al. (2012) and <i>Planck</i> data are taken from Planck Collaboration (2011).	114
5.2	Elemental abundances of emitting gas in the Crab Nebula relative to hydrogen	126
5.3	Elemental abundances of emitting gas in the Crab Nebula relative to hydrogen	127
5.4	Observed and modelled absolute H $_{\beta}$ flux. Observed and modelled line strengths relative to H $_{\beta}$ and their ratio. All observed lines are taken from Smith (2003), except for [C I] 9824+9850 from Rudy et al. (1994), [Ar III] 7136+7751 from Davidson & Fesen (1985) and [Ar III] 89911 from Temim et al. (2012).	128

5.5 Observed and modelled absolute H_{β} flux. Observed and modelled line strengths relative to H_{β} and their ratio. All observed lines are taken from Smith (2003), except for [C I] 9824+9850 from Rudy et al. (1994), [Ar III] 7136+7751 from Davidson & Fesen (1985) and [Ar III] 89911 from Temim et al. (2012).	129
5.6 Observed and modelled absolute H_{β} flux. Observed and modelled line strengths relative to H_{β} and their ratio. All observed lines are taken from Smith (2003), except for [C I] 9824+9850 from Rudy et al. (1994), [Ar III] 7136+7751 from Davidson & Fesen (1985) and [Ar III] 89911 from Temim et al. (2012).	130
5.7 Observed and modelled absolute H_{β} flux. Observed and modelled line strengths relative to H_{β} and their ratio. All observed lines are taken from Smith (2003), except for [C I] 9824+9850 from Rudy et al. (1994), [Ar III] 7136+7751 from Davidson & Fesen (1985) and [Ar III] 89911 from Temim et al. (2012).	131
5.8 Observed and modelled absolute H_{β} flux. Observed and modelled line strengths relative to H_{β} and their ratio. All observed lines are taken from Smith (2003), except for [C I] 9824+9850 from Rudy et al. (1994), [Ar III] 7136+7751 from Davidson & Fesen (1985) and [Ar III] 89911 from Temim et al. (2012).	132
5.9 Observed and modelled absolute H_{β} flux. Observed and modelled line strengths relative to H_{β} and their ratio. All observed lines are taken from Smith (2003), except for [C I] 9824+9850 from Rudy et al. (1994), [Ar III] 7136+7751 from Davidson & Fesen (1985) and [Ar III] 89911 from Temim et al. (2012).	133
5.10 Observed and modelled absolute H_{β} flux. Observed and modelled line strengths relative to H_{β} and their ratio. All observed lines are taken from Smith (2003), except for [C I] 9824+9850 from Rudy et al. (1994), [Ar III] 7136+7751 from Davidson & Fesen (1985) and [Ar III] 89911 from Temim et al. (2012).	134
5.11 The results for model . the smooth isotropic density distribution.	135

5.12 The results for model II. the smooth isotropic density distribution with outer axes of 4.0×2.9 pc and inner axes of 3.0×2.0 pc outside the radiation source.	136
5.13 The results for model IV. the smooth isotropic density distribution in a shell 0.5 pc thick and a inner axes of 2.1×1.4 pc entirely inside the diffuse radiation source.	137
5.14 The results for model IV. the smooth isotropic density distribution with outer axes of 4.0×2.9 pc and inner axes of 2.1×1.4 pc entirely inside the diffuse radiation source.	138
5.15 The results for model V. the smooth isotropic density distribution with outer axes of 4.0×2.9 pc and inner axes of 2.13×1.7 pc entirely inside the diffuse radiation source.	139
5.16 The results for model VI. the smooth isotropic density distribution in a shell 0.1 pc thick and a inner axes of 1.1×1.1 pc entirely inside the diffuse radiation source..	140
5.17 The results for model VII. A clumpy geometry with clumps starting at axes of 3.0×2.0 pc decreasing with r^{-2} entirely outside the radiation source. The clumps have a of radius 0.111 pc with a density of 1400 cm^{-3}	141
5.18 The results for model VIII. A clumpy geometry with clumps starting at axes of 3.0×2.0 pc decreasing with r^{-2} entirely outside the radiation source. The clumps have a of radius 0.037 pc with a density of 1900 cm^{-3}	142
5.19 The results for model IX. A clumpy geometry with clumps starting at axes of 2.1×1.4 pc decreasing with r^{-2} entirely inside the radiation source.	143
5.20 The results for model X. A clumpy geometry with clumps starting at axes of 2.3×1.7 pc decreasing with r^{-2} entirely inside the radiation source.	144
5.21 Global ionisation fractions of elements in the clumpy models	145
5.22 The results for model X. A clumpy geometry with clumps starting at axes of 2.3×1.7 pc decreasing with r^{-2} entirely inside the radiation source using a CDE scattering routine rather than a Mie scattering routine.	154
5.23 The mass of dust, gas and the optical depth of each clump from centre to surface for the model with the clumps outside the radiation field.	155
5.24 The mass of dust, gas and the optical depth of each clump from centre to surface for the model with the clumps embedded in the radiation field.	155

5.25	The masses of emitting gas phase elements in the Crab Nebula determined by the MOCASSIN models	157
5.26	The masses of emitting gas phase elements in the Crab Nebula determined by the MOCASSIN models	158
5.27	Observed and predicted photometric fluxes for the <i>Herschel</i> wave bands and their colour correction factors.	159
5.28	Dust masses in the crab nebula calculated empirically using equation 5.1. . .	159
A.1	The red shifted component of the [O I] 63 μm emission in the Crab Nebula measured by PACS-IFU	168
A.2	The blue shifted component of the [O I] 63 μm emission in the Crab Nebula measured by PACS-IFU	169
A.3	The red shifted component of the [O III] 88 μm emission in the Crab Nebula measured by PACS-IFU	170
A.4	The blue shifted component of the [O III] 88 μm emission in the Crab Nebula measured by PACS-IFU	171
A.5	The red shifted component of the [C II] 158 μm emission in the Crab Nebula measured by PACS-IFU	171
A.6	The red shifted component of the [C II] 158 μm emission in the Crab Nebula measured by PACS-IFU	172
B.1	The blue shifted component of the [O I] 63 μm emission in the SP1 observations of Cas A measured by PACS-IFU	174
B.2	The red shifted component of the [O I] 63 μm emission in the SP1 observations of Cas A measured by PACS-IFU	174
B.3	The blue shifted component of the [O III] 88 μm emission in the SP1 observations of Cas A measured by PACS-IFU	175
B.4	The red shifted component of the [O III] 88 μm emission in the SP1 observations of Cas A measured by PACS-IFU	176
B.5	The red shifted component of the [O III] 88 μm emission in the SP3 observations of Cas A measured by PACS-IFU	177
B.6	The blue shifted component of the [O III] 88 μm emission in the SP3 observations of Cas A measured by PACS-IFU	177

B.7 The red shifted component of the [C II] 157 μm emission in the SP3 obser-	
vations of Cas A measured by PACS-IFU	178
B.8 The blue shifted component of the [C II] 157 μm emission in the SP3 ob-	
servations of Cas A measured by PACS-IFU	178
B.9 The red shifted component of the [O III] 88 μm emission in the SP4 obser-	
vations of Cas A measured by PACS-IFU	179
B.10 The blue shifted component of the [O III] 88 μm emission in the SP4 obser-	
vations of Cas A measured by PACS-IFU	180
B.11 The blue shifted component of the [O I] 63 μm emission in the SP4 obser-	
vations of Cas A measured by PACS-IFU	180
B.12 The blue shifted component of the [O I] 63 μm emission in the SP4 obser-	
vations of Cas A measured by PACS-IFU	180
B.13 The red shifted component of the [C II] 157 μm emission in the SP4 obser-	
vations of Cas A measured by PACS-IFU	181
B.14 The blue shifted component of the [C II] 157 μm emission in the SP4 ob-	
servations of Cas A measured by PACS-IFU	181
B.15 The red shifted component of the [O III] 88 μm emission in the SP5 obser-	
vations of Cas A measured by PACS-IFU	182
B.16 The blue shifted component of the [O III] 88 μm emission in the SP5 obser-	
vations of Cas A measured by PACS-IFU	182
B.17 The blue shifted component of the [O I] 63 μm emission in the SP5 obser-	
vations of Cas A measured by PACS-IFU	182
B.18 The blue shifted component of the [O I] 63 μm emission in the SP5 obser-	
vations of Cas A measured by PACS-IFU	183
B.19 The red shifted component of the [C II] 157 μm emission in the SP5 obser-	
vations of Cas A measured by PACS-IFU	183
B.20 The blue shifted component of the [C II] 157 μm emission in the SP5 ob-	
servations of Cas A measured by PACS-IFU	183
B.21 The red shifted component of the [O III] 88 μm emission in the SP7 obser-	
vations of Cas A measured by PACS-IFU	184
B.22 The blue shifted component of the [O III] 88 μm emission in the SP7 obser-	
vations of Cas A measured by PACS-IFU	184

B.23 The red shifted component of the [O I] 63 μ m emission in the SP7 observations of Cas A measured by PACS-IFU	185
B.24 The blue shifted component of the [O I] 63 μ m emission in the SP7 observations of Cas A measured by PACS-IFU	185
B.25 The red shifted component of the [O III] 88 μ m emission in the SP8 observations of Cas A measured by PACS-IFU	186
B.26 The blue shifted component of the [O III] 88 μ m emission in the SP8 observations of Cas A measured by PACS-IFU	186
B.27 The red shifted component of the [O I] 63 μ m emission in the SP8 observations of Cas A measured by PACS-IFU	187
B.28 The blue shifted component of the [O I] 63 μ m emission in the SP8 observations of Cas A measured by PACS-IFU	187
B.29 The red shifted component of the [O III] 88 μ m emission in the SP9 observations of Cas A measured by PACS-IFU	188
B.30 The blue shifted component of the [O III] 88 μ m emission in the SP9 observations of Cas A measured by PACS-IFU	188
B.31 The red shifted component of the [O I] 63 μ m emission in the SP9 observations of Cas A measured by PACS-IFU	188
C.1 Values of n and k measured by Uspenskii et al. (2006) between 2.8 nm and 30 nm for an amorphous carbon sample and extrapolated n and k for Zubko et al. (1996) ACAR and BE amorphous carbon samples	190

This page was intentionally left blank

List of Acronyms

ACAR - An interstellar amorphous carbon dust analogue

ADU - Analogue to Digital Converter

AGB - Assymtotic Giant Branch

ALMA - Atacama Large Millimetre/Sub-Millimetre Array

BE - An interstellar amorphous carbon dust analogue

Cas A - Cassiopeia A

CDE - Continuous Distribution of Ellipsoids

CRIRES - Cryogenic Infrared Echelle Spectrograph - A VLT instrument

ESA - European Space Agency

ESO - European Southern Observatory

ETC - Exposure Time Calculator

FIR - Far Infrared

FTS - Fourier Transform Spectrometer

IFU - Ingrated Field Unit

IR - Infrared

IRAC - Infrared Array Camera - A *Spitzer* instrument

IRS - Infrared Spectrometer - A *Spitzer* instrument

ISM - Interstellar Medium

ISO - Infrared Space Observatory

LTE - Local Thermodynamic Equilibrium

LWS - Long Wavelength Spectrograph - An ISO Instrument

MIPS - Multiband Imaging Photometer for Spitzer - A *Spitzer* Instrument

MRN - Mathis, Rumpl, & Nordsieck (1977) - a widely used garnishee distribution

NASA - National Aeronautics and Space Administration

NIR - Near Infrared

NuSTAR - Nuclear Spectroscopic Telescope Array

PACS - Photodetecting Array Camera and Spectrometer - A *Herschel* Instrument

PAH - Poly Aromatic Hydrocarbon

PWN - Pulsar Wind Nebula

QSO - Quasi Stellar Object or Quasar

SED - Spectral Energy Distribution

SLW - SPIRE Long Wavelength - A Spire Detector Array

SN - Supernova

SN1987A - Supernova 1987A

SNe - Supernovae

SNR - Supernova Remnant

SPIRE - Spectral and Photometric Imaging Receiver - A *Herschel* Instrument

SSW - SPIRE Short Wavelength - A Spire Detector Array

SWS - Short Wavelength Spectrograph - An ISO Instrument

UV - Ultraviolet

VLT - Very Large Telescope

WISE - Wide-field Infrared Survey Explorer

This page was intentionally left blank

Chapter 1

Dust in the Universe

For dust thou art, and unto dust shalt thou return

Genesis 3:19

Cosmic dust plays a vital role in the evolution of the universe. It plays an essential role in the formation of molecules (Hirashita & Ferrara 2002). It is needed to cool down star forming clouds to allow second generation stars to be born (Schneider et al. 2004). It is vital in the formation of planets (Boehler et al. 2013) and is one of the biggest causes of uncertainty in cosmological observations (Wood-Vasey et al. 2007).

The origin of dust in the universe is currently a topic of great debate in astrophysics. Recent sub-millimetre and millimetre observations of galaxies and quasars (QSO's) out to redshifts of around 6 have found these objects to be very dusty. These observations have found around $10^8 M_\odot$ of dust assuming a 50 K dust temperature (Bertoldi & Cox 2002; Omont et al. 2001; Carilli et al. 2001) as illustrated in Figure 1.1 which shows the rest frame sub millimetre observation of SDSS J114816.64+525150.3, a quasar at $z = 6.42$. The first stars formed somewhere between $z = 10 - 50$ (Greif & Bromm 2006) and the oldest galaxies observed at around $z = 10$ (Bouwens et al. 2011) giving a time of around 500 megayears for the dust observed at $z = 6$ to have formed.

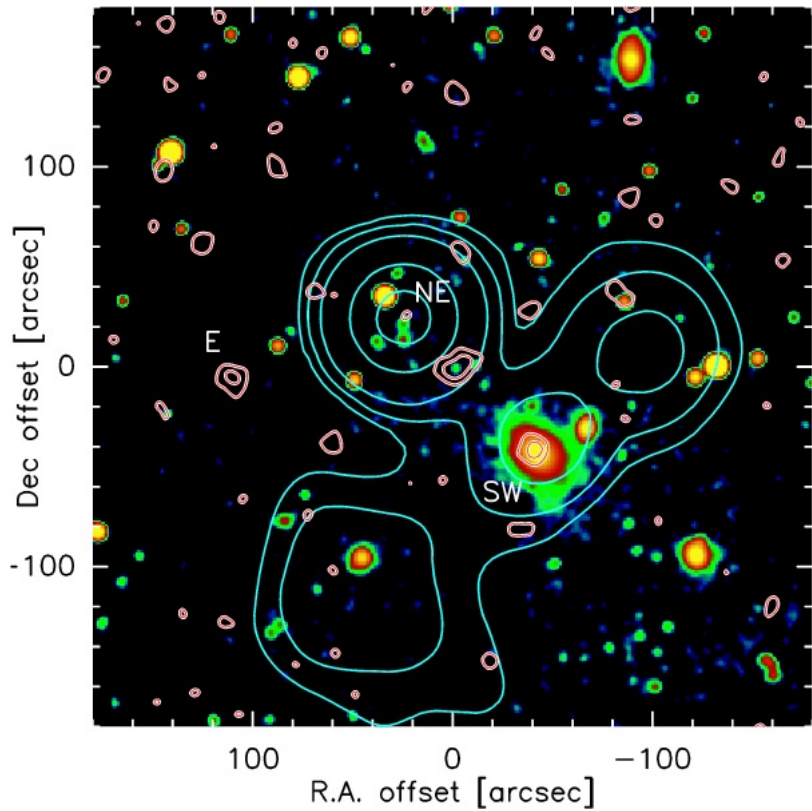


Figure 1.1. SDSS J114816.64+525150.3, a quasar at $z = 6.42$ observed with IRAM 30 m telescope showing a rest frame IR excess corresponding to $10^8 M_\odot$ of dust taken from Bertoldi et al. (2003).

In the local universe Assymtotic Giant Branch (AGB) stars are considered to be the significant source of dust. AGB stars are stars those which had a mass of $0.85\text{--}8 M_\odot$ after they have left the main sequence and finished hydrogen and helium core burning. AGB stars have a low surface temperature (usually around 3500 K) but high luminosity ($10^3 L_\odot$) caused by a degenerate oxygen or carbon core surrounded by hydrogen and helium burning layers. As AGB stars evolve they develop strong winds which lead to losing up to 80% of their mass which forms an envelop of gas and dust. AGB stars cannot be the source of the dust observed at high redshift, as the universe is too young for stars small enough to become AGB stars to have been formed and evolved far enough to become dust producing. Additionally, dust budgets of local metal poor galaxies find a discrepancy between the total amount of dust observed and that which has been produced by AGB stars(Matsuura et al. 2009, 2013).

1.1 Yeah, but what is dust?

When we discuss dust, we are talking about small particles ranging in size from a few molecules to a radius of $\sim 1 \mu\text{m}$. Dust can be divided into two major different species, silicates and carbonaceous materials. Broadly speaking these can be considered analogous to sand and soot particles, although the astronomical samples are much smaller than either of these.

Silicates are made up of stable condensates of Silicon and Oxygen along with other elements such as Iron and Magnesium into complex molecules such as Olivine (MgFeSiO_3) and Pyroxene (MgFeSiO_4). These molecules then clump together to form dust grains. In the interstellar medium (ISM) it is nearly all amorphous (Li & Draine 2002) although in the regions where it forms it appears to be more crystalline.

Carbonaceous dust is made up of many different kinds of carbon containing material. It includes everything from small poly aromatic hydrocarbons (PAHs) and fullerenes to large chunks of glassy, amorphous carbon and also includes graphite and diamonds.

Which species of dust dominates is determined by the ratio of carbon to oxygen. Carbon Monoxide (CO) is formed with the available oxygen and carbon, and whichever is left over from this formation of CO then forms dust. If the $\frac{\text{C}}{\text{O}} > 1$ then carbon chemistry dominates and the majority of dust formed will be carbonaceous. Conversely if $\frac{\text{C}}{\text{O}} < 1$ then the chemistry is dominated by oxygen and silicate dusts will form.

1.2 How we observe dust

Dust absorbs light in ultraviolet and optical wavelengths and re-emits in the infrared. This thermal emission can be observed allowing direct observation of dust. This emission peaks at around $100 \mu\text{m}$ for cold dust so to measure masses and characterise dust properties a range of observations to build up a spectral energy distribution (SED) at these wavelengths is needed. In addition to this dust does not absorb light in the infrared allowing us to observe emission lines from atoms and molecules where optical emission lines would not be visible due to their absorption by the dust. Figure 1.2 shows a Hubble Space Telescope optical image of the Andromeda galaxy. Dust in its spiral arms can clearly be



Figure 1.2. A Hubble Space Telescope optical image of the Andromeda Galaxy

seen silhouetted against the emitted light from the galaxy. Figure 1.3 shows the same galaxy in the far infrared. The orangey colour is the same dust seen in silhouette emitting the optical/uv energy it has absorbed in the infrared.

Although astronomy in the infrared is very good at seeing through clouds of dust, infrared light can not pass through the water vapour in the earths atmosphere, as a result the most effective way of doing infrared astronomy is to use space based observatories. The most powerful of these observatories have been the European Space Agency (ESA) *Herschel* space observatory in the far infrared and sub millimetre ($60\text{-}670\ \mu\text{m}$) and NASA's *Spitzer* space telescope in the near and mid infrared ($3\text{-}180\ \mu\text{m}$).

1.2.1 The *Herschel* Space Observatory

The Herschel Space Observatory (Pilbratt et al. 2010) was a space observatory run by the European Space Agency (ESA) with involvement from the National Aeronautics and Space Agency (NASA) to explore the universe in the far infrared and sub millimetre regions of the spectrum. The satellite was launched on the 14th of May 2009 along with ESA's *Planck*



Figure 1.3. An infrared image of the Andromeda galaxy taken with the Herschel Space Observatory

mission. It operated until the 29th of April 2013, when it ran out of the liquid helium, used to cool the detectors to cryogenic temperatures. It was in an orbit around the L2 Lagrange point meaning that the earth is always between it and the sun. Its mirror was 3.5 m, which is currently the largest to have been put in to space, despite this, because of the relationship between resolving power and wavelength *Herschel* has a similar resolving power to early telescopes developed by Galileo. *Herschel* had three instruments on board, PACS - a camera and spectrometer operating from 55 to 210 μm , SPIRE a camera and spectrometer for wavelengths of 194 to 672 μm and HIFI, A heterodyne detector giving a very high spectral resolution between 157-212 μm and 240-625 μm .

PACS (Photodetecting Array Camera and Spectrometer)

The Photodetector Array Camera and Spectrometer (PACS) (Poglitsch et al. 2010) instrument is an imaging camera and low-resolution spectrometer covering wavelengths from 55 to 210 μm . Its spectrometer has a resolving power of between $R = 1000$ and $R = 5000$ and works simultaneously in two bands as it can use two of its three gratings at a time. The PACS spectrometer is an Integrated Field Unit (IFU). An IFU is an instrument that combines spectrographic and imaging capabilities to obtain spectra that are specially resolved. The PACS-IFU is made up of 5×5 square spaxels 9.4 arcsec sides, giving a 47×47 arcsec field of view. There are a number of important atomic and ionic fine structure transition lines within this wavelength range which can be used to diagnose temperature, density and composition of gaseous regions including supernova remnants. The spectrometer also has a high enough resolution to be able to obtain velocity information about these components allowing us to look at the 3D structure of objects. The camera has three imaging bands at 70, 100 and 160 μm .

SPIRE (Spectral and Photometric Imaging Receiver)

The Spectral and Photometric Imaging Receiver (SPIRE) (Griffin et al. 2010) instrument is also a photometer (camera) and spectrometer operating between 200 and 670 μm . The spectrometer is an imaging Fourier Transform Spectrometer consisting of two arrays of bolometer detectors; one array of 35 (originally 37, but 2 of the bolometers are dead) detectors covering the 194-313 μm wavelength range (SSW - SPIRE Short Wavelength) and the other an array of 19 detectors covering the 303-671 μm wavelength range (SLW - SPIRE Long Wavelength). This wavelength range contains a large number of molecular rotational

lines including many Carbon Monoxide lines as well as OH⁺ and other more exotic species. The camera images simultaneously at 250, 350 and 500 μm , when combined with the PACS camera can provide a full spectral energy distribution at far infrared wavelengths, covering the peak of dust emission which allows measurement of dust masses.

1.2.2 The *Spitzer* Space Telescope

The Spitzer Space Telescope is an infrared space observatory launched by NASA in 2003. Originally it covered a wavelength range of 3-100 μm , but ran out of its cryogenic coolant in May 2009 meaning that it currently only operates a warm mission with two photometric bands at 3.6 μm and 4.5 μm .

In its full mission Spitzer had three instruments: IRAC, IRS and MIPS. IRAC (Infrared Array Camera) is a camera which operates at 3.6, 4.5, 5.8 and 8 μm . It is this instrument that is still partially operational. IRS (Infrared Spectrograph) was a spectrometer which operated in four wavelength ranges at different resolutions. It covered 4.3-14 and 14 to 40 μm at low resolution and 10-19.5 and 19-37 μm at high resolution. MIPS (Multiband Imaging Photometer for Spitzer) was a three detector photometer array which operated at 24, 70 and 160 μm . This wavelength range gave information about the peak of dust emission but did not constrain the SED as well as *Herschel*, nor was it as sensitive.

1.2.3 Other Infrared and Sub Millimetre Observatories

Planck

The *Planck* space craft was operated by ESA and designed to observe anisotropies in the Cosmic Microwave Background. Although primarily a cosmology mission, *Planck* made all sky maps in 9 sub-millimetre and millimetre wavelengths. These maps can be used to investigate the interstellar medium of our galaxy as well as observations of point sources within the map which can be used to constrain their spectral energy distributions in this wavelength (e.g. Crab Nebula (Gomez et al. 2012), see chapter 5). These maps can also be used to investigate effects such as the polarisation of dust (Planck Collaboration 2014) on very large scales which in turn can give information about large scale magnetic field structures .

ISO

The Infrared Space Observatory (ISO) was a space telescope for infrared astronomy that operated between 1995 and 1998. It was designed and operated by ESA and covered a wavelength range from 2.5-240 μm . ISO had four scientific instruments

- ISOCAM - a camera imaging between 2.5 and 17 μm
- ISOPHOT - a photo-polarimeter to measure the amount of radiation emitted in wavelength range 2.5-240 μm
- SWS - a short wavelength spectrometer operating between 2.5 and 45 μm
- LWS - a long wavelength spectrometer operating between 45 and 196 μm

ALMA

The Atacama Large Millimetre/Sub-Millimetre Array (ALMA) is an interferometer array of 54 12 metre radio antennae and 12 7 metre antennae, 5000 meters above sea level in the Atacama desert of northern Chile. It operates in between 350 μm and 10mm (although coverage is not complete due to absorption and emission in the Earths atmosphere). The array has much higher sensitivity than both single dish sub-millimeter observatories such as the James Clerk Maxwell Telescope and other arrays SMA and IRAM Plateau de Bure. The distance between the antennae can be varied between 150 m and 14 km to allow it to zoom in and out. Because of this long baseline it has almost unparalleled spatial and velocity resolution. ALMAs observation bands include one at 450 μm (band 9) and one at 870 μm (band 7) which can be used for the observation of cold dust as well as other bands useful for constraining background emission and synchrotron spectra in SEDs.

Chapter 2

Supernovae and their Remnants

Star go poof, star go boom

Antonia Bevan

Core collapse supernovae are the violent deaths of massive stars. They produce explosions incredibly luminous explosions which often brighter than their host galaxies. Once the core of a star reaches a point where it requires more energy per nucleon to fuse than it gives releases, fusion stops. This destroys the mechanism of hydrostatic support in the star which then collapses in on itself and then explodes.

There is another type of supernova (Type Ia) which are caused by thermonuclear runaway of carbon/oxygen white dwarves and do not create dust (Gomez et al. 2012), and are thus beyond the scope of this thesis.

2.1 Types of Supernovae

Supernovae are typically characterised by their properties in the visible part of the electromagnetic spectrum. Type I supernovae do not have hydrogen present in their spectra, whereas Type II. Each of these classes contains multiple subclasses depending on features in their spectra and the shape of their light curves (the light intensity over time) which are summarised in table 2.1.

Supernova Type	Defining Characteristics	Progenitor Mass	Progenitor Type	Examples
Type I	Hydrogen deficient			
Ib	helium rich	25	Wolf-Rayet Stars	
Ic	Helium Poor, no Si II	25	Wolf-Rayet Stars, Binaries	
Type II	Hydrogen Present			
IIb	similar to Type Ib SN	25-30	Wolf-Rayet Stars	
II-L	Light curve decreases linearly in magnitude	15-25		
IIIn (narrow)	narrow emission lines on a broad base can be split in to two subclasses		SAGB stars	
IIIn Low Luminosity		8-10		
IIIn Super luminous		25-30	LBV stars	
II-P (plateau)	blue, almost featureless spectrum	8-25	RSG	

Table 2.1. The different types of core collapse supernovae.

2.2 Supernova Remnants

Supernovae evolve through several stages between explosion and merging entirely with the surrounding interstellar medium. Initially the remnant expands freely sweeping up interstellar and circumstellar material. This phase lasts until the supernova has swept up its own mass in external material. At this point the remnant enters what it known as the Sedov phase. During this phase a strong reverse shock also propagates back through the ejecta heating it. This phase ends when the shocks are slow enough that significant radiative cooling can take place. This can take hundreds to thousands of years. The a remnant becomes a cool dense shell around a hot interior which continues pressure driven expansion know as the snowplough phase. Finally as the interior cools, the shell expands from its own momentum, eventually merging with the ISM. This whole process takes approximately 30,000 years from the initial explosion.

2.3 Dust Formation in Supernovae and Supernova Remnants

Fast and efficient dust formation is required to explain observations of large reservoirs of dust in early galaxies. Due to their short life times and the large amounts of metals they produce, core collapse supernovae have been suggested as this source (Morgan & Edmunds 2003). For supernovae to be able to produce enough dust to fit observations, they must be incredibly efficient producers of dust, requiring as much as $1 M_{\odot}$ to be produced per supernova event for the required amounts to be injected in to the interstellar medium after destruction rates are taken in to account (Dwek et al. 2007).

2.3.1 Formation

There are two main theories of dust formation in supernovae. Those based on classical nucleation theory and those which use a chemical kinetic approach.

Nucleation theory assumes that when a gas is supersaturated; particles form seeds which then accrete more particles. This method has been used to model dust formation in supernovae by Todini & Ferrara (2001) and Bianchi & Schneider (2007). Using these models in conditions found in supernovae of different sizes they find that supernovae of

progenitor size 12-40 M_{\odot} are capable of forming 0.1-0.6 M_{\odot} of dust, which is enough to account for the dust masses observed in the early universe.

The chemical kinetic description of the ejecta is based on the initial chemical composition of the gas and a set of chemical reactions describing the chemical processes in the ejecta. Cherchneff & Dwek (2009, 2010) used these techniques to investigate the masses of dust formed in primordial pair instability supernovae and a 20 M_{\odot} core collapse supernova. These was then extended by Sarangi & Cherchneff (2013) to investigate Type II core collapse supernovae in the local universe. Chemical kinetic models tend to predict far less dust than models using classical nucleation theory, predicting to the order $10^{-2} M_{\odot}$ of dust.

2.3.2 Observed Dust Masses

Previously, observations of dust formed in supernova ejecta have only found 10^{-4} - $10^{-2} M_{\odot}$ of hot (200-900 K) dust (Wooden et al. 1993; Sugerman et al. 2006; Kotak et al. 2009). These observation were mostly taken in the near infrared and of dust formed very close to the supernova event. This view of supernova dust formation is being challenged by recent observations of older supernovae and remnants in the far infrared and submillimetre wavelengths leading to the discovery of much larger masses of cold dust.

2.3.3 Recent Observations with Herschel

Cassiopeia A

Cassiopeia A (Cas A) is a young oxygen rich supernova remnant (SNR). It is approximately 3.4 kpc away (Reed et al. 1995) and around 330 years old (Fesen et al. 2006). Cas A is one of the most-studied objects in the sky, having been observed in all wavelengths from radio waves through to γ -rays. Recent observations in the near infrared of light echoes due to absorption, re-emission and scattering by interstellar dust show that it is the remnant of a Type IIb supernova of initial mass of around 15 M_{\odot} (Krause et al. 2008).

The mass of dust in Cas A has been much studied and has been a controversial topic. Dunne et al. (2003) reported as much as 4 M_{\odot} of dust in the remnant. This was later refuted by Krause et al. (2004) who showed that most of this emission was not actually

in the remnant, but in foreground molecular clouds by associating the dust emission with emission from OH molecules. Using the *Spitzer* space telescope Rho et al. (2008) measured between 0.02 and 0.05 M_{\odot} of warm dust (between 65–265 K). Although the strong foreground emission prevents direct observation of cold dust, observations with *Herschel* were able to identify a cool dust component of 0.08 M_{\odot} (Barlow et al. 2010).

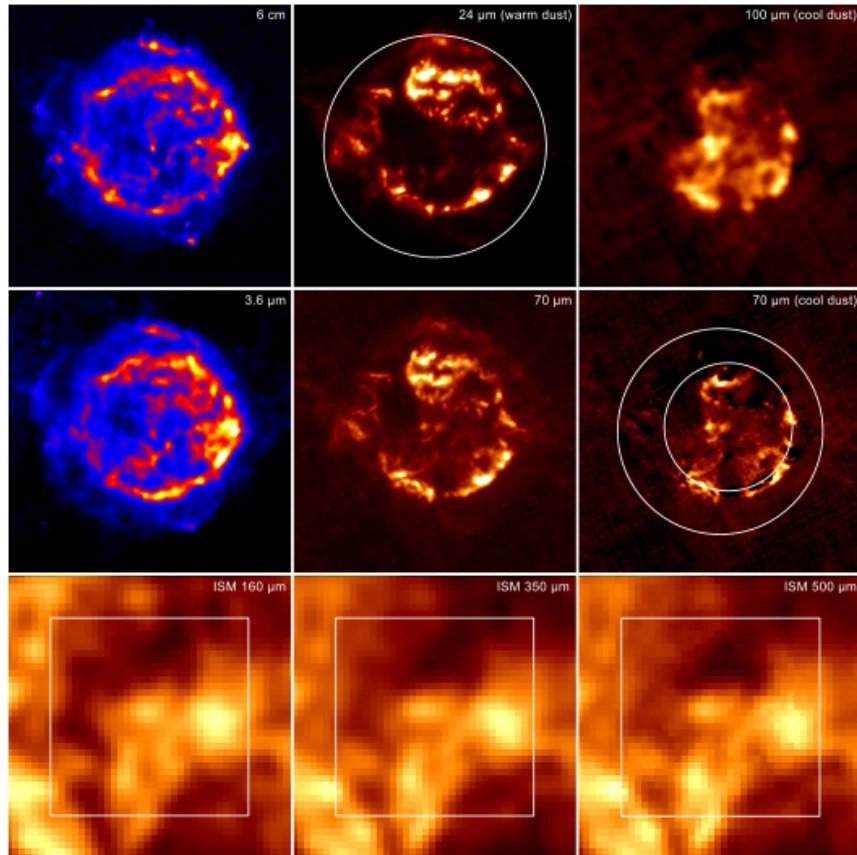


Figure 2.1. Multi wavelength observations of Cas A showing continuum at 6 cm (VLA) and 3.6 μm , warm dust at 24 μm (*Spitzer*) and 70 μm (*Herschel*), cool dust 100 μm (*Herschel*) and 70 μm (*Herschel*) and 160, 350 and 500 μm foreground dust taken from Barlow et al. (2010).

Figure 2.1 shows multi wavelength observations of Cas A to constrain its dust. The top left and middle left show the 6 cm and 3.6 μm observations used to constrain the background spectrum. The top central and central image show the contributions to from the warm dust component at 24 μm (top central) and 70 μm (central). The top right and central right show the emissions from the cool dust component at 100 μm (top right) and 70 μm (centre right). The bottom row shows the ISM foreground at 160, 250 and 500 μm , the features across these wavelengths are very consistent and completely obscure

any emission from within the remnant. It may be possible, using other techniques such as examining the red/blue asymmetry caused to optical emission lines by dust in the remnant to investigate whether there is any cold dust formed with in it but there is no way of identifying it using the infrared/sub-millimetre excess. The warm and cool dust components combined give a dust mass of approximately $0.1 M_{\odot}$ of dust in the Cassiopeia A supernova remnant.

Supernova 1987A

First observed on the 23rd of February 1987, SN1987A is the nearest core collapse supernova in modern times. It is approximately 51 kpc away in the Large Magellanic Cloud (LMC), a dwarf galaxy orbiting our own. Given previous assumptions that supernovae only produced $10^{-3} M_{\odot}$ of dust it was not chosen as a target for the *Herschel* Space Observatory as it was predicted to not be detectable in the far infrared and sub-millimetre. During the HERITAGE survey (Meixner et al. 2013), a *Herschel* survey of the LMC, an unexpected signal was detected coincident with the location of SN1987A, at 100, 160, 250 and 350 μm wavelengths, shown in Figure 2.2. This turned out to be a large reservoir of previously unobserved cold dust. Analysis of this data showed between 0.4 and 0.7 M_{\odot} of dust, depending on the dust species used (Matsuura et al. 2011). Observations at earlier epochs had found 10^{-4} solar masses of dust (Wooden et al. 1993; Ercolano et al. 2007). This result was considered controversial with many people questioning whether the dust was formed in the ejecta or if it was pre-existing dust that had been formed by the progenitor star. Supernova progenitors such as η Carina have been shown to produce similar amounts of dust (Gomez et al. 2010). Follow up 450 μm observations of SN1987A with ALMA (Indebetouw et al. 2014) were able to resolve the location of the dust in the remnant showing that the cold dust was located entirely in the central ejecta region rather than in the circumstellar ring of pre-supernova material as shown in Figure 2.3. As well as the 450 μm image, Figure 2.3 shows observations of SN1987A at other wavelengths to demonstrate its structure, which a bright ring of material that was ejected by the progenitor before going supernova and a central ejecta region. The ejecta region is expanding and will begin to interact with the outer ring. This will form shockwaves travelling back inward towards the central ejecta region. This may have an impact on the amount of dust in the remnant. It will be observed over the coming decades with interest to see how much

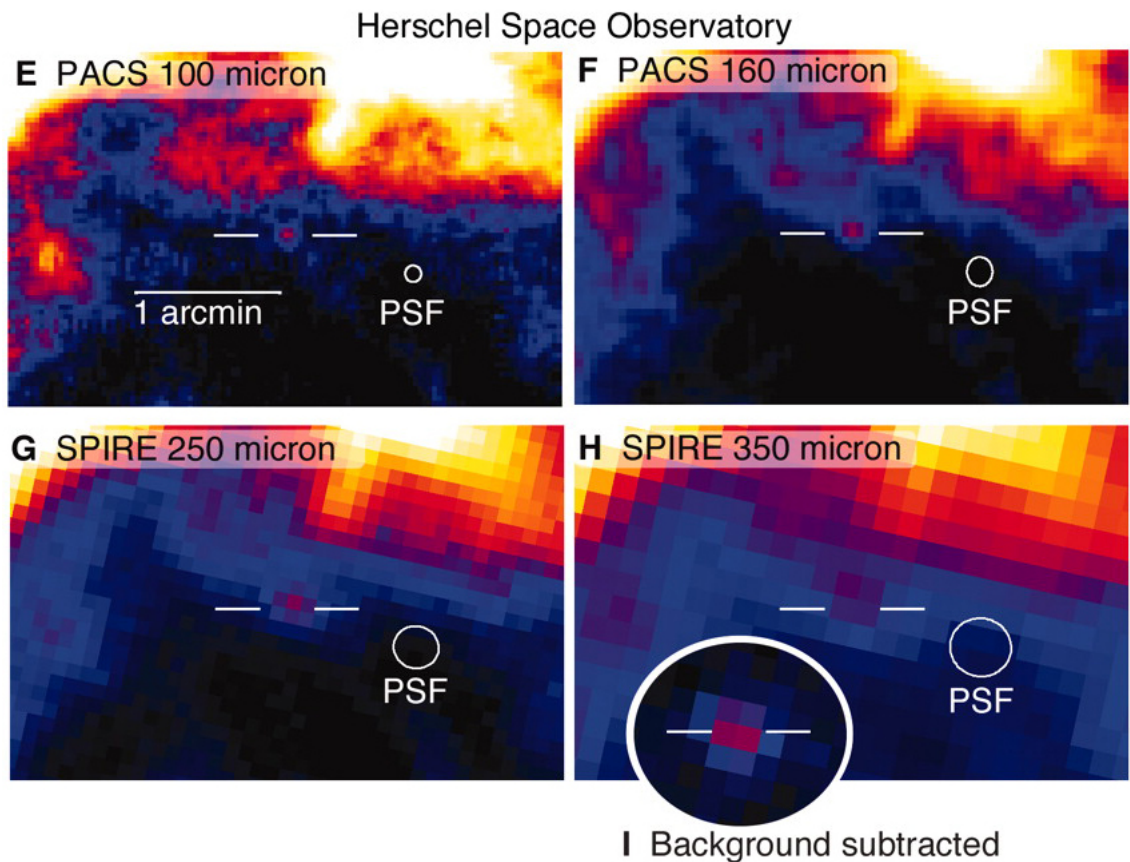


Figure 2.2. *Herschel* Observation of 1987A at 100, 160, 250 and 350 μm taken from Matsuura et al. (2011).

of the dust survives, and if any more forms in the shocked regions and in the cold regions formed in between shocks.

With these results for SN1987A and Cas A along with the Crab Nebula, which will be discussed in more detail in Chapter 5. We are starting to build up a body of evidence for highly efficient condensation of dust by supernovae and their remnants. The masses of dust formed are potentially enough to account for the large masses of dust observed in high redshift galaxies.

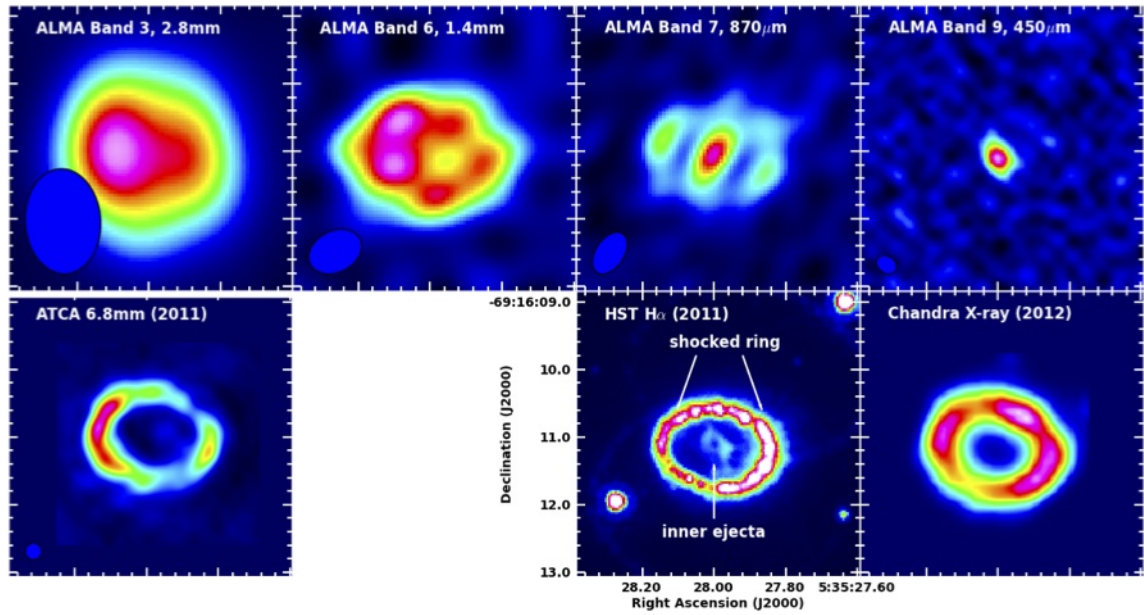


Figure 2.3. ALMA (mm and sub-mm), ATCA (mm), Hubble (visible) and Chandra (x-ray) observations of SN1987a showing the structure of the supernova remnant and location of the dust. Taken from Indebetouw et al. (2014).

2.4 Infrared atomic lines in Supernova Remnants

2.4.1 Fine Structure Lines

When some spectral lines are examined at a very high resolution they display a splitting and are found to be closely spaced doublets and triplets rather than a single line. This small splitting of the spectral lines is caused by an interaction between an electron's spin, S, and its orbital angular momentum, L. This is called the spin-orbit interaction.

In the frame of reference where the electron is stationary with the nucleus orbiting it, the motion of the nucleus generates a magnetic field. The electron also has an intrinsic magnetic field caused by its spin. These two magnetic fields couple giving a difference in energy depending on their orientation.

These fine structure lines can be excited by collisions with electrons and other atoms. When these lines de-excite they emit a photon which carries away energy, cooling the region. These fine structure lines of ground state atoms and ions are often in the far infrared. Figure 2.4 shows a schematic energy level diagram of the O²⁺ ion including this

line ground state splitting. This is the same structure as N⁺ and C species. The energies of the transitions is different for the different species. The neutral Oxygen ground state

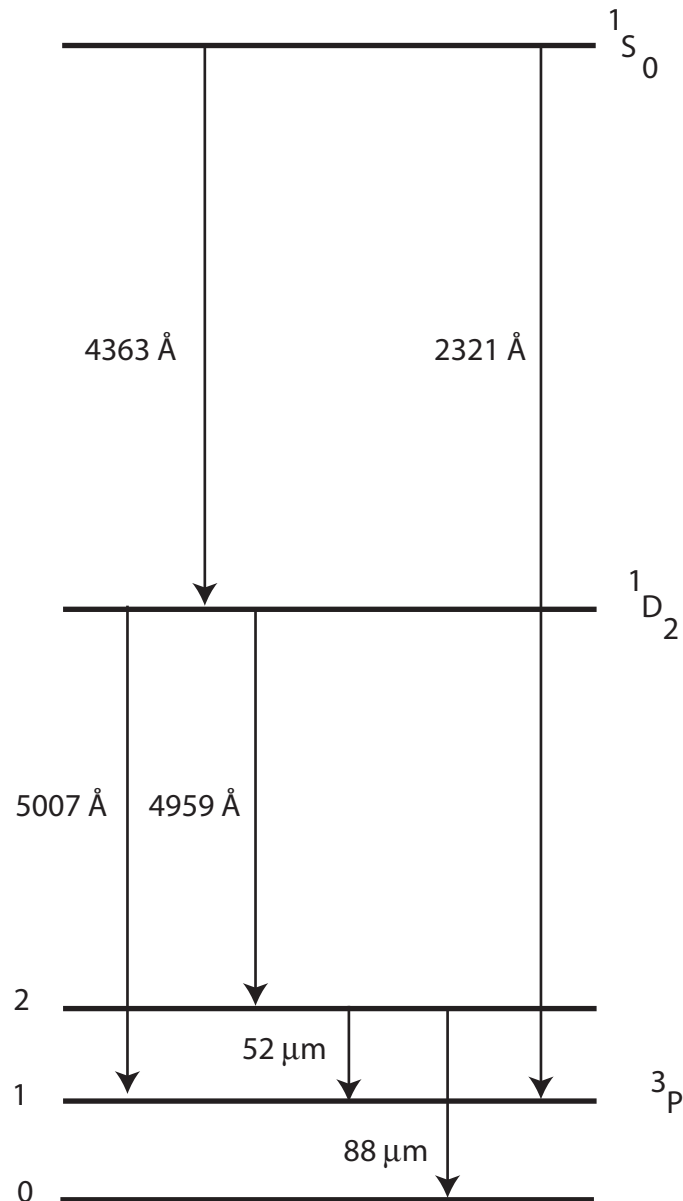


Figure 2.4. The fine structure splitting in the ground state of doubly ionised oxygen.

the energy levels are reversed.

2.5 Molecules in Supernova Remnants

Studies of local supernova remnants have shown that they can form both dust and molecules. Herschel observations of Cassiopeia A (Cas A) show that it has formed CO (Rho et al. 2009; Wallström et al. 2013) (see Chapter 4) while the Crab Nebula has been observed to have formed OH⁺ and ³⁶ArH⁺ (Barlow et al. 2013) (see Chapter 3). Supernova 1987A has also been observed to have formed SiO and CO molecules (Kamenetzky et al. 2013).

Carbon Monoxide (CO) is an important coolant. As a fast forming molecule it also plays a vital role in controlling the chemistry and dust formation of a region by looking up all of which ever species is less abundant. If more carbon is left after CO has formed then the chemistry will be carbon based and amorphous carbon dust species will form where as if there is more oxygen is left over then that will drive the chemistry and silicate dusts will be more likely to form.

As well as being an important coolant, and of interest in its own right, CO, and other molecules, can be used to help diagnose conditions in regions where it is observed by looking at its rotational temperature.

Observations of molecular the strengths of different rotational transitions can be tied to physical conditions within an object. A temperature can be determined from the column densities of several rotational energy states and their upper energy level of that state and the statistical weight of that energy level using Equation .

$$\frac{N_u}{g_u} = \frac{N_{\text{tot}}}{Q(T_{\text{rot}})} e^{\frac{-E_u}{T_{\text{rot}}}} \quad (2.1)$$

where N_u is the population at a given energy level g_u is the statistical weight of the N_{tot} is the total column density of the molecule, $Q(T_{\text{rot}})$ is the rotational partition function. For diatomic molecules, which all molecules observed in supernova remnants so far have been, the rotational partition function is $Q(T) = kT/hB$ when kT is the boltzmann temperature, B is the rotational constant, $\frac{h}{8\pi^2 I}$ where I is the moment of inertia, and h is the Planck constant. By plotting this logarithmically a straight line slope fitted to this gives $\frac{-1}{T_{\text{rot}}}$, which can then give us the rotationally temperature within the system. The column density, the number of absorbers/molecules per unit area, can be determined from

the intercept of this slope. To do this correctly, the solid angle of the telescope beam filled by the source of the emission needs to be taken in to account.

2.6 This Thesis

This thesis presents infrared spectroscopic observations of galactic supernova remnants the Crab Nebula in Chapter 3 and Cassiopeia A in Chapter 4 using *Herschel* PACS-IFU and SPIRE-FTS. These observations are used to investigate structure and conditions within these supernova remnants. In addition to the *Herschel* observations, Chapter 3 contains follow up observations of the Crab Nebula made with ESO's Very Large Telescope. Chapter 4 also contains investigations in to the dust in Cas A and correlations between far infrared dust maps and ^{44}Ti maps from γ -ray observations. Chapter 5 contains a full 3D radiative transport model treating gas and dust in the Crab Nebula. This model is fitted to photometric data from *Herschel* taken from Gomez et al. (2012) to investigate the dust content of the nebula as well as optical emission lines taken from Smith (2003) to investigate the gas properties and atomic abundances.

This page was intentionally left blank

Chapter 3

Herschel Spectroscopy of the Crab Nebula

OOOOOOG! THE CLAW

Those aliens in Toy Story

The Crab Nebula is the remnant of a supernova that was observed by the Chinese in 1054. It is thought to be around 2 kpc away(Trimble 1968). The is one of the most-studied objects in the sky, having been observed in all wavelengths from radio waves through to γ rays. It is thought that it was an Type IIn-P core-collapse supernova of a progenitor with an initial mass of around $10 M_{\odot}$ (Smith 2013). It consists of a central pulsar that drives a pulsar wind nebula (PWN). The synchrotron radiation from this PWN in turn ionises the dense filaments of ejecta.. It is a good choice for investigating the formation of dust in supernovae and supernova remnants as it is close enough to be resolved so the supernova and interstellar/circumstellar components can be separated. It is also young enough that the thermal emission from the remnant is dominated by its ejecta rather material that has been swept up.

3.1 The Crab Nebula with PACS

A spectrum was taken of the central region of the Crab Nebula on the 4th of April 2011 PACS instrument at RA 5h 34m 29.44s DEC 22° 0' 32.52". This position is shown in Figure ?? plotted over a 70 μ m image of the Crab Nebula along with the off target positions used in the chopping to remove background. Two observations have been made at this position; one for the wavelength ranges 51-72 μ m and 102-146 μ m (Range Mode SED B2A + Short R1) and one for the 70-105 μ m and 140-220 μ m (Range Mode SED B2B + Long R1). Data was reduced to level 2 using the standard PACS ranged SED pipeline in HIPE version 8.0.1 (Ott 2010a). Additional data were taken from the ISO-LWS archive covering a similar wavelength range (shown in Figure ??). Information on these observations can be found in Table 3.1.

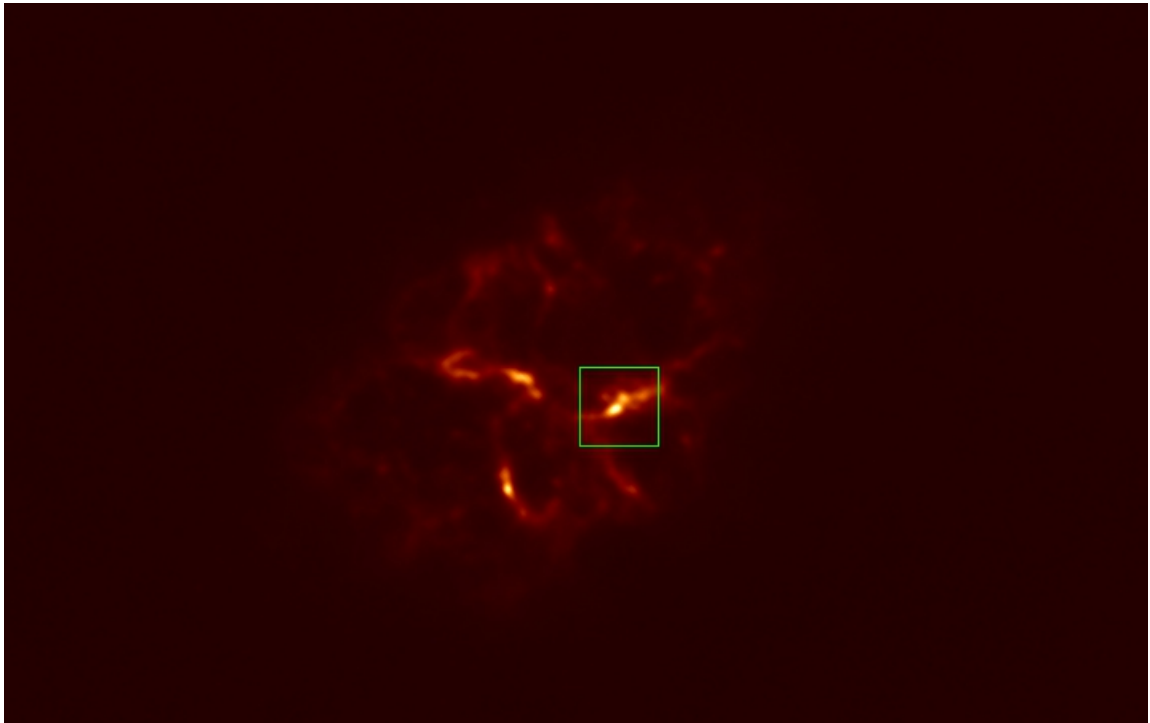


Figure 3.1. The position of the PACS-IFU observations of the Crab Nebula plotted on a PACS 70 μ m image.

HIPE (Herschel Interactive Processing Environment) is a data retrieval and processing package for the *Herschel* Space Observatory. It provides access to the Herschel Science Archive and allows for processing and reduction and calibration of data for export as well

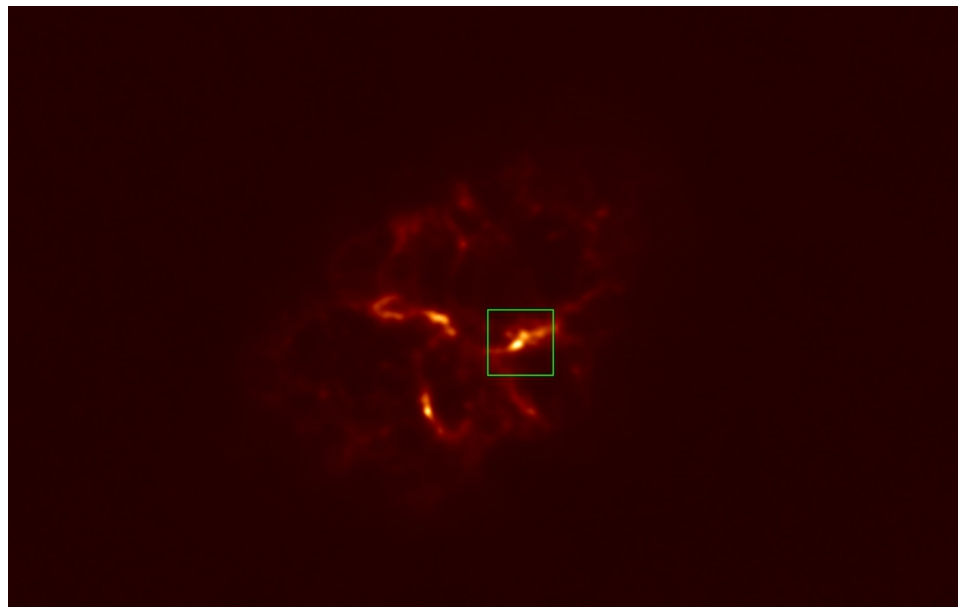


Figure 3.2. The position of the ISO-LWS observations of the Crab Nebula plotted on a PACS 70 μm image.

as some analysis tools.

3.1.1 Nebula Diagnostics

Determining conditions such as temperature and density in nebulae, including supernova remnants can be done by comparing line ratios of atomic transitions. This can be done by taking the intensity ratio of two lines of the same ion. If the different levels have similar excitation energies then the relative excitation rates of these two levels depend on the collision strengths and electron densities. If the two levels have different critical densities, the relative population between these two levels will be dependent on the density, therefore the ratio of the line intensities they emit will also be density dependent.

The critical density of a level i is given by

$$n_{cr}(i) = \frac{\sum_{i>j} A_{ij}}{\sum_{i \neq j} c_{ij}} \quad (3.1)$$

A_{ij} is the Einstein A coefficient, the probability of the transition occurring spontaneously, and c_{ij} is the collisional excitation or de-excitation rate. When the density is much larger

Instrument	Date	Time	RA	DEC	TDT/ObsID	Time
ISO-LWS	1997-10-09	01:18:54	05h 34m 34.27s	22° 01' 02.4"	69501241	1124s
ISO-LWS	1997-10-09	01:29:10	05h 34m 32.02s	22° 02' 04.6"	69501242	1126s
ISO-LWS	1997-10-09	01:48:46	05h 34m 29.31s	22° 00' 37.0"	69501243	1124s
ISO-LWS	1997-10-09	02:08:20	05h 34m 34.19s	21° 59' 54.7"	69501244	1630s
PACS	2011-04-04	12:40:19	05h 34m 29.44s	22° 00' 32.52"	1342217847	2267s
PACS	2011-04-04	13:20:18	05h 34m 29.42s	22° 00' 47.17"	1342217847	1139s

Table 3.1. Information on the position and integration time of spectroscopic measurements of the Crab Nebula using *Herschel* PACS-IFU and ISO-LWS.

than the critical density, collisions dominate and the system can be represented by a Boltzmann population of energy levels.

The 52 and 88 μm fine structure lines of [O III] provide good diagnostic lines for determining electron density, as they have low excitation energies (both much lower than typical nebula temperatures) but different critical densities. This means that there is only a very small temperature dependence but strong density dependence for the ratio of their intensities so that $I_{88 \mu\text{m}}/I_{52 \mu\text{m}}$ ratio is a good diagnostic for the electron density. The energy difference between the fine structure lines and the [O III] optical 5007 Å line means that there is a strong temperature dependence on the ratio of line intensities, so $I_{88 \mu\text{m}}/I_{5007\text{\AA}}$ can be used as a diagnostic for temperature. By measuring the 52 and 88 μm and the 5007 Å [O III] lines the density and temperature of a nebula can be diagnosed.

Using the *Herschel* PACS spectral observations along with archive data from the Infrared Space Observatory Long Wavelength Spectrometer (ISO-LWS) some of the conditions in the nebula have been determined as shown in Table 3.2. The PACS fluxes are the coadding of all 25 spaxels. All of the line fluxes are relative to the 88 μm [O III] line flux. Although there is an obvious line with the same profile as the other oxygen lines at 52 μm in the PACS spectra, as it is at the extreme shortwave end of the PACS wavelength coverage (and below its official limit) the responsivity is very low and calibration poor, so we rely on the ISO-LWS measurements.

Using the 88/52 μm [O III] line ratio, we determined the electron densities to be 135-485 cm^{-3} . These are systematically lower than the electron densities measured using optical [S II] lines by MacAlpine et al. (1996) and 18.7 and 33.5 μm [S III] from Temim et al. (2006) who found values ranging from 830-1230 cm^{-3} . Sankrit et al. (1998) observations with the Hubble space telescope found that while the sulphur is in the dense filaments, a lot of the [O III] emission comes from sheaths around the filaments, which is consistent with the lower electron densities determined by using the ionised oxygen emission.

By looking at the ratio of [O III] to [N III] lines we can also determine the ratio of oxygen to nitrogen. This ratio ranges between 10 and 35, showing the Crab Nebula to

	Coadded LWS	LWS #1	LWS #2	LWS #3	LWS #4	Coadded PACS
[O III] 52 μm^*	116 ± 9	168 ± 12	109 ± 2	140 ± 9	91 ± 4	(75 ± 4)
[N III] 57 μm	11 ± 2	14 ± 2	5 ± 1	18 ± 4		
[O I] 63 μm	46 ± 2	69 ± 3	39 ± 1	58 ± 2	36 ± 2	46 ± 2
[O III] 88 μm	100	100	100	100	100	100
[N II] 122 μm	3.4 ± 0.2	8 ± 1	2.5 ± 0.3	2.9 ± 0.3	2.6 ± 0.3	2.0 ± 0.2
[O I] 146 μm	2.2 ± 0.1	4.0 ± 0.2	1.9 ± 0.1	1.5 ± 0.3	1.9 ± 0.3	2.8 ± 0.2
[C II] 158 μm	7.8 ± 0.3	12.4 ± 0.8	6.9 ± 0.4	12 ± 1	5.9 ± 0.3	9.3 ± 0.5
$F_{(88 \mu\text{m})} (\times 10^{-14} \text{ W m}^{-2})$	14.9 ± 0.4	1.94 ± 0.08	5.9 ± 0.1	2.19 ± 0.05	4.64 ± 0.09	3.6 ± 0.1
$F(52)/F(88)$	1.16 ± 0.07	1.68 ± 0.07	1.1 ± 0.03	1.4 ± 0.07	0.91 ± 0.05	
$N_e(\text{O III}) (\text{cm}^{-3})$	240 ± 30	485 ± 30	220 ± 20	350 ± 30	135 ± 20	
$F(52+88)/F(57)$	18.5 ± 1	18.9 ± 0.7	42.8 ± 3	12.8 ± 1		
O^{2+}/N^{2+}	15.0 ± 0.9	14.4 ± 0.5	35 ± 3	17 ± 1		
$F(122)/F(57)$	0.29 ± 0.05	0.54 ± 0.1	0.51 ± 0.1	0.16 ± 0.04		
N^+/N^{2+}	2.3 ± 0.4	5.3 ± 1	3.9 ± 1	1.4 ± 0.4		

Table 3.2. Crab Nebula far-infrared line fluxes, electron densities and relative ion abundances. Line intensities relative to [O III] $F_{(88 \mu\text{m})}=100$. PACS relative flux calibration uncertain at 52 μm

be very nitrogen poor. MacAlpine & Satterfield (2008) split the Crab Nebula in to three domains, all of which were nitrogen poor having ratios of 7.2, 21 and 260 for each of the domains. All of our measurements are in agreement with domain 2. The $122/57\text{ }\mu\text{m}$ ratio is used to determine the ratio of ionisation states in Nitrogen. Singly ionised Nitrogen is the dominant species with an N^+/N^{2+} ratio of between 2.3 and 5.3.

3.1.2 Velocity Structure

The velocity structure and expansion of supernova remnants can be investigated using the doppler red and blue shift of atomic line emissions to determine velocities

$$v = \frac{\Delta\lambda}{\lambda} c \quad (3.2)$$

where v is the velocity, λ is the rest wavelength of the observed line and $\Delta\lambda$ is the difference between the observed and rest wavelengths of this line and c is the speed of light. As supernova remnants are expanding both towards and away from us, the line profile is double peaked around the rest wavelength. As infrared lines are not obscured by dust in the supernova remnant we are able to use the far infrared fine structure lines to observe both blue (towards us) and red (away from us) components of these lines. As they are obscured by the dust in the remnant only the blue shifted lines are observable, which does not give us a complete picture.

Figure 3.3 show the 25 spaxels PACS-IFU of the Crab Nebula (see Table 3.1) plotted in velocity space. The $88\text{ }\mu\text{m} [\text{O III}]$ line is in black, the $63\text{ }\mu\text{m} [\text{O I}]$ line is in red and the $158\text{ }\mu\text{m} [\text{C II}]$ line is in green. A table of fluxes and velocities for each of these lines can be found in Appendix A.

Figures 3.4, 3.5 and 3.6 show the fluxes of the individual spaxels of the PACS-IFU observations of the central knot of the crab nebula plotted on a $70\text{ }\mu\text{m}$ PACS contour plots. Whilst stronger in the regions when the $70\text{ }\mu\text{m}$ emission is brightest (and thus the dustiest region), the $88\text{ }\mu\text{m} [\text{O III}]$ comes from all over the observed region. The $63\text{ }\mu\text{m} [\text{O I}]$ and $158\text{ }\mu\text{m} [\text{C II}]$ emissions are coincident only with the brightest dustiest regions of the observation. This is because of the dust cooling and shielding allowing the lower ionisation stages to exist.

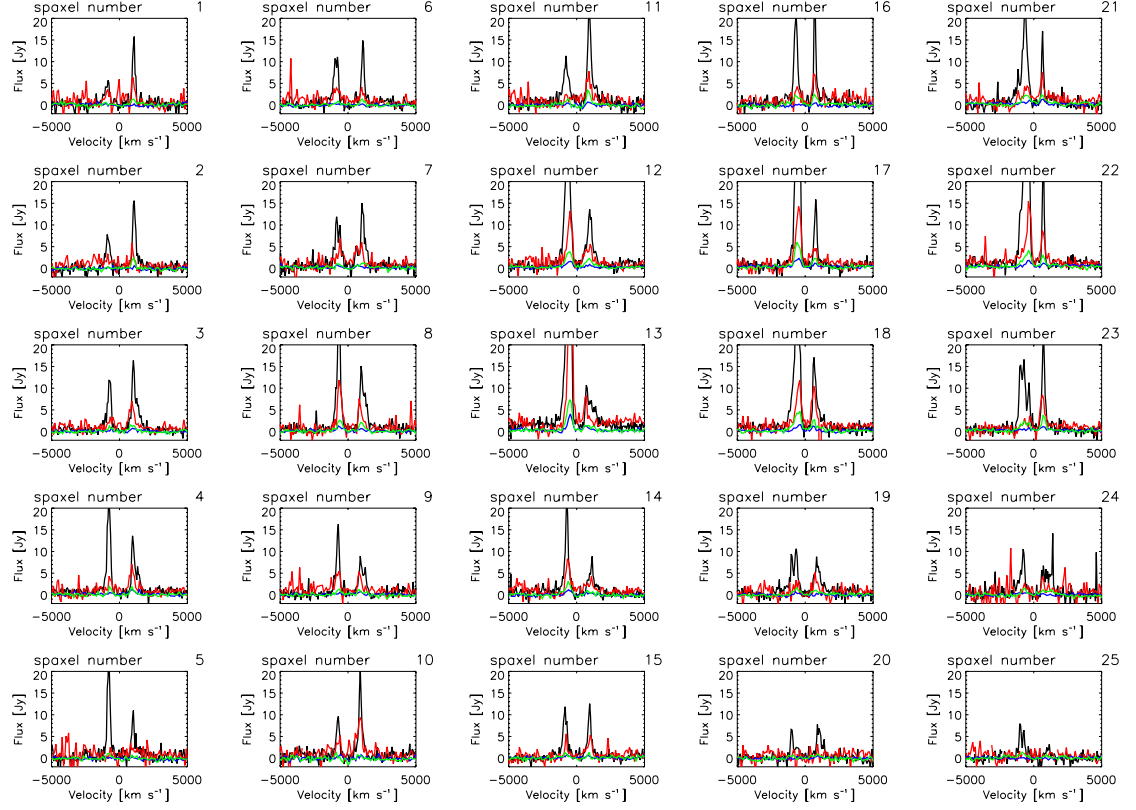


Figure 3.3. The 25 individual PACS spaxels plotted in velocity space. The 88 μm [O III] line is in black, the 63 μm [O I] line is in red and the 158 μm [C II] line is in green.

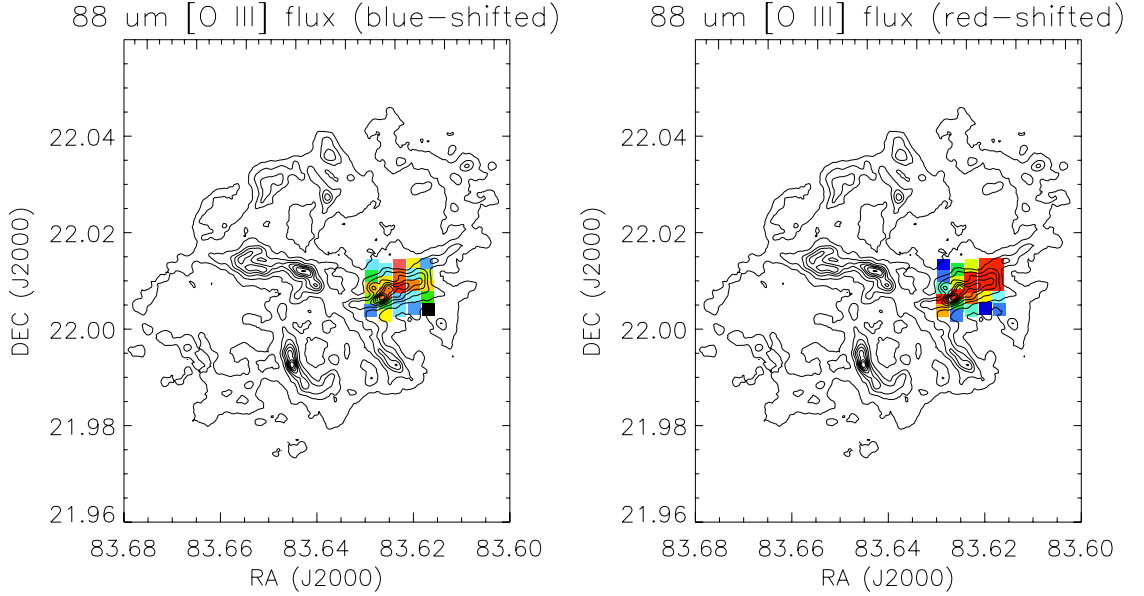


Figure 3.4. A map of the 88 μm [O III] for each PACS-IFU spaxel, plotted over the PACS 70 μm map plotted as a contour plot.

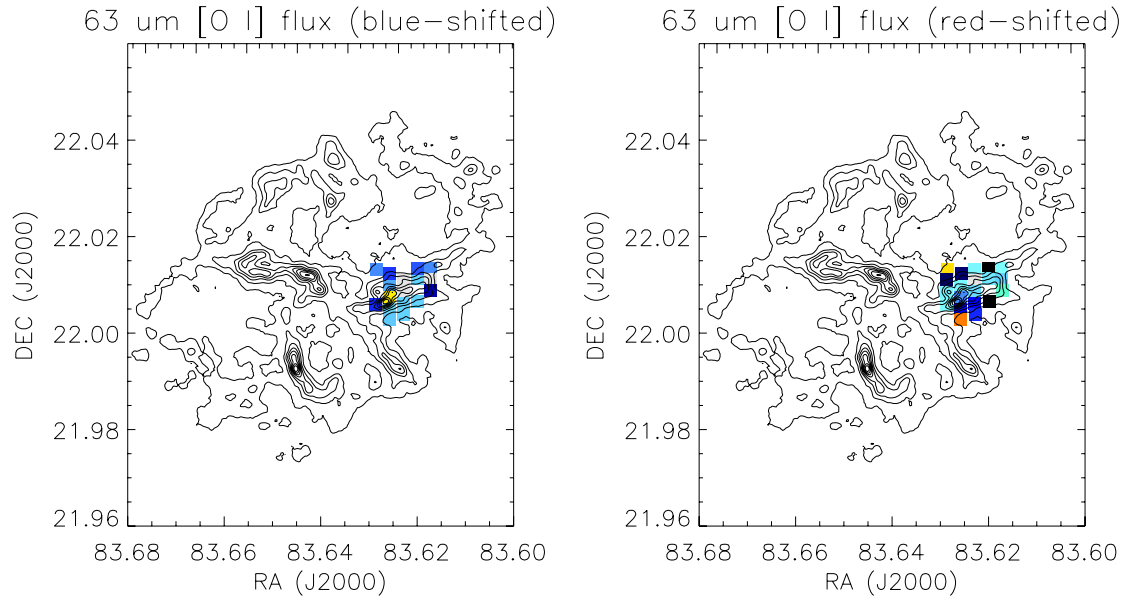


Figure 3.5. A map of the 63 μm $[\text{O I}]$ for each PACS-IFU spaxel, plotted over the PACS 70 μm map plotted as a contour plot.

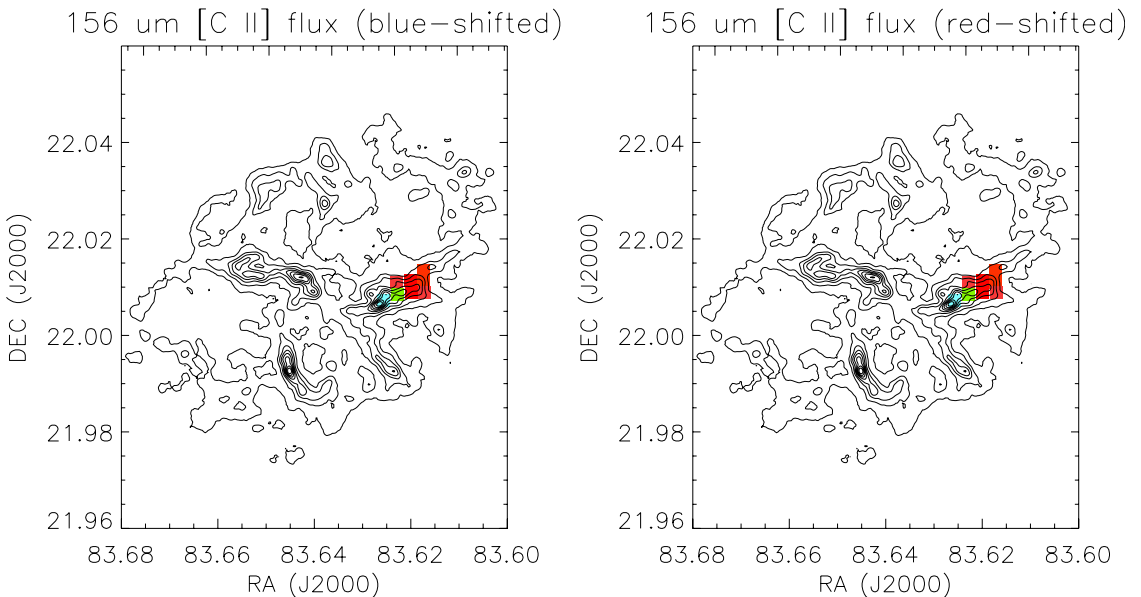


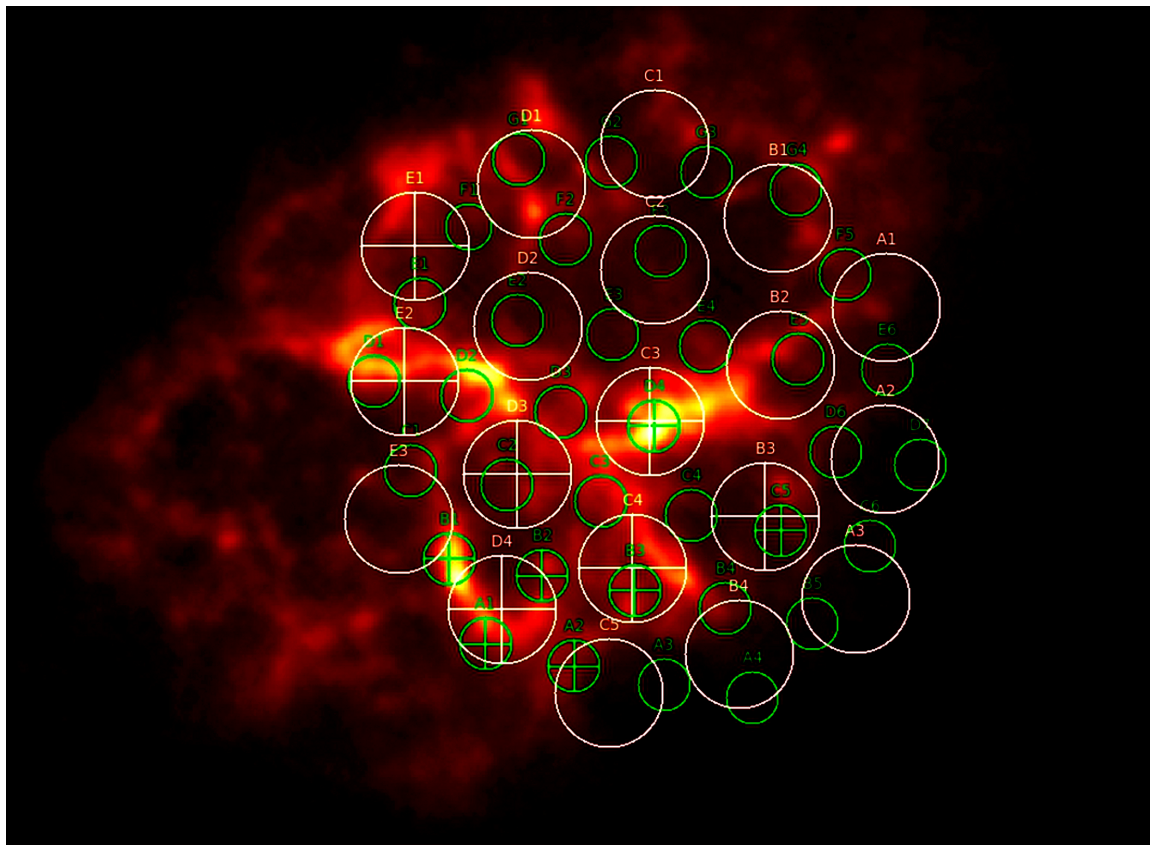
Figure 3.6. A map of the 158 μm $[\text{C II}]$ for each PACS-IFU spaxel, plotted over the PACS 70 μm map plotted as a contour plot. Note the scale is an order of magnitude less than the plots for the $[\text{O I}]$ and $[\text{O III}]$ maps.

Instrument	Date	Time	RA	DEC	TDT/ObsID	Time
SPIRE-FTS	2011-08-22	19:55:15	05h 34m 29.47s	22° 00' 31.48"	1342204022	3476s

Table 3.3. Details of the *Herschel* SPIRE-FTS observation of the Crab Nebula.

3.2 The Crab Nebula with SPIRE-FTS

A single observation of the Crab Nebula was made using *Herschel* SPIRE-FTS. Figure 3.7 shows positions of the SPIRE-FTS spectra of the Crab Nebula are taken on a PACS 70 μm image and Table 3.3 gives details of the observations.

**Figure 3.7.** The SPIRE-FTS observations of the Crab Nebula shown on a 70 μm PACS broadband image. Green circles are the SSW detectors, white circles are the SLW detectors. Circles with a cross denote the detectors in which the unidentified line was observed.

3.2.1 Unidentified Lines

The SPIRE-FTS spectra of the Crab Nebula were largely empty. None of the expected Carbon Monoxide lines are present. The only lines observed are a red and blue shifted J=2-1, F=5/2-3/1 OH⁺ line at 971.8038 GHz which is observed in both the SSW and

SLW spectra and two previously unidentified lines one at 618 GHz in the SSW spectra and one at 1235 GHz in the SLW spectra. Unusually for an unidentified line, it is the strongest line in the spectra in which it is detected, examples of which is shown in Figures 3.8 (SLW) and 3.9 (SSW). Figure 3.7 shows positions of the SPIRE-FTS spectra of the Crab Nebula are taken on a PACS 70 μm image. The SSW detectors are shown in white while the SLW detectors are shown in green. The positions with crosses in are those in which the unidentified line has been detected. The bright knots in the 70 μm image is the dust emission, showing that these unidentified lines are mostly coincident with the dust.

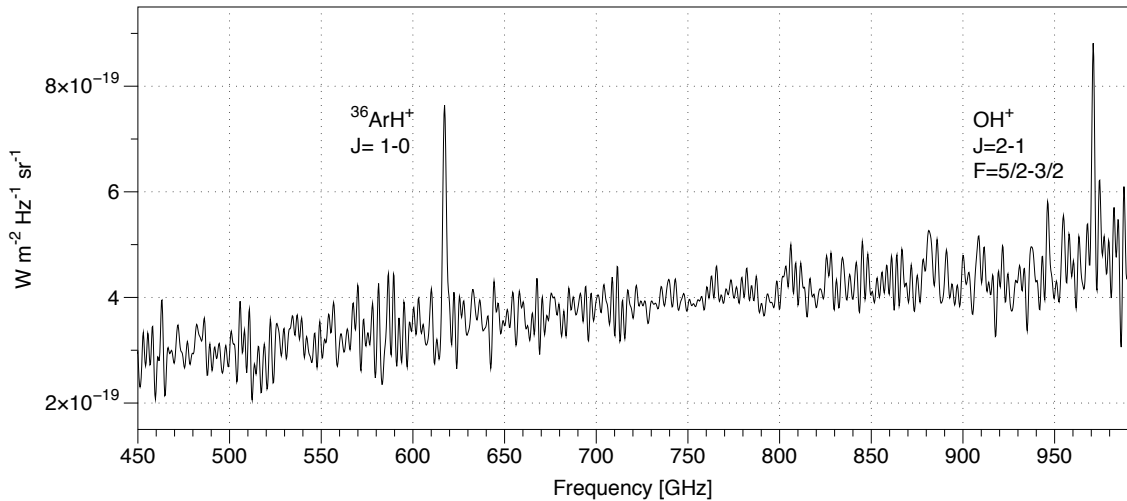


Figure 3.8. SLW D4 spectrum showing the one of the unidentified line at 618 GHz.

3.2.2 Identifying the Line

The knots and filaments in the Crab Nebula exhibit a wide range of expansion velocities (Hester 2008). To determine a rest frequency for the unidentified line emission, the velocity components of the OH⁺ line were taken for each of the spectra. These ranged between -603 and 1037 km s⁻¹ which is consistent with the wide range of velocities exhibited by the knots in the Crab. In the four SLW spectra in which the 618 GHz and OH⁺ lines are present a rest frequency of 617.554 ± 0.209 GHz for the unidentified line. In the five SSW spectra in which the 1235 GHz line and the OH⁺ line are present a mean rest frequency of 1234.768 ± 0.643 GHz.

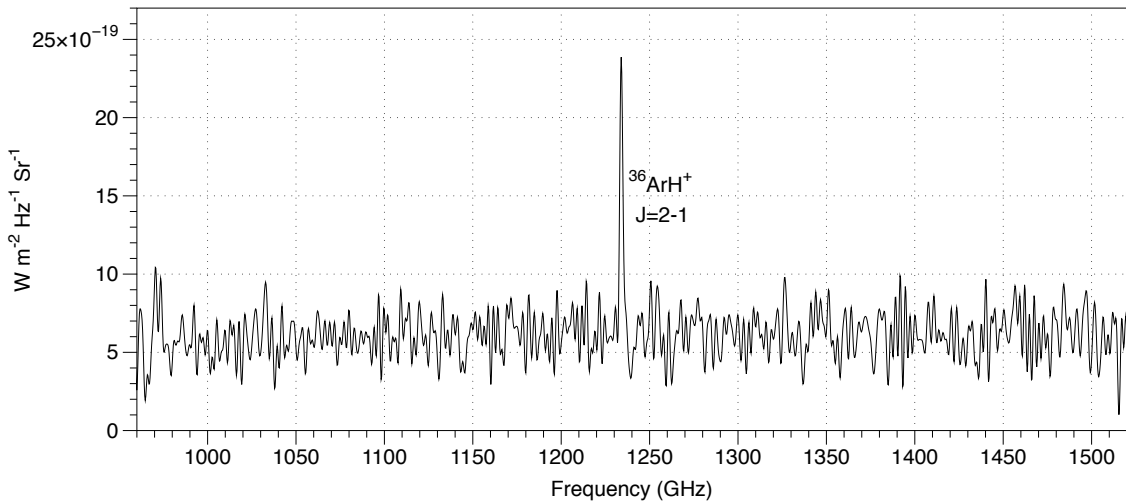


Figure 3.9. SSW B1 spectrum showing the one of the unidentified line at 1235 GHz.

Dividing these two frequencies gives a value of 1.9995 ± 0.0012 a 2:1 ratio implies the $J=1-0$ and $J=2-1$ transitions of a molecule containing two atoms. After an extensive search of the Cologne Molecular Database for Spectroscopy (Mller et al. 2005), the only candidate was discovered to be 36-Argon Hydride cat-ion, $^{36}\text{ArH}^+$ (Barlow et al. 2013). This is the first detection of a molecule containing a noble gas in space. A follow up search in the PACS-IFU spectra failed to find the higher J rotational transitions of ArH^+ , or any other noble gas hydride ions, such as the much searched for HeH^+ .

3.2.3 Line Fluxes

Table 3.4 shows the observed surface brightness and velocities in each of the *Herschel* SPIRE-FTS detectors in which the $J = 1-0$ 617.525 GHz (SLW) and $J = 2-1$ 1234.603 GHz (SSW) $^{36}\text{ArH}^+$ lines are observed. Detectors which are coincident with one another is SLW and SSW are next to each other.

3.2.4 Formation and Destruction Mechanisms for ArH^+

Argon is a noble gas; it has a full outer shell of electrons and in its atomic state is highly unreactive. When ionised it is as reactive as any other species without a full outer shell of electrons. The Crab Nebula is predominantly gas that has been ionised by synchrotron radiation from the pulsar wind Hester (2008). It also contains a large number of clumps of very cold, neutral H_2 clumps Loh et al. (2011) (as shown in Figure 3.10 which show

SLW Detector	Radial Velocity km s ⁻¹	Surface Brightness 10×10 ⁻¹⁰ W m ⁻¹ Sr ⁻¹	SSW Detector	Radial Velocity km s ⁻¹	Surface Brightness 10×10 ⁻¹⁰ W m ⁻¹ Sr ⁻¹
B3	+317 ± 67	2.23 ± 0.41	C5	-1354 ± 26	8.2 ± 1.2
C3	+933 ± 33	4.63 ± 0.40	D4	+743 ± 26	11.7 ± 1.6
C4	-58 ± 50	8.65 ± 0.55	B3	-101 ± 20	17.5 ± 1.4
D3	+826 ± 32	3.13 ± 0.34			
D3	-709 ± 42	2.30 ± 0.34	A1	-51 ± 52	13.9 ± 2.0
D4	+101 ± 27	9.89 ± 0.52	B2	-572 ± 25	10.8 ± 1.7
			B1	+140 ± 34	38.4 ± 1.6
			A2	+61 ± 28	10.1 ± 1.4
E1	+278 ± 46	5.69 ± 0.62			
E2	-594 ± 37	4.25 ± 0.46			

Table 3.4. SPIRE-FTS radial velocity and line surface brightness measurements for the J = 1-0 and 2-1 rotational lines of $^{36}\text{ArH}^+$ from the Crab Nebula

the location of all the Loh et al. (2011) H₂ knots on the *Herschel* PACS 70 μm image). There are transition zones between these two regions where partially ionised argon can

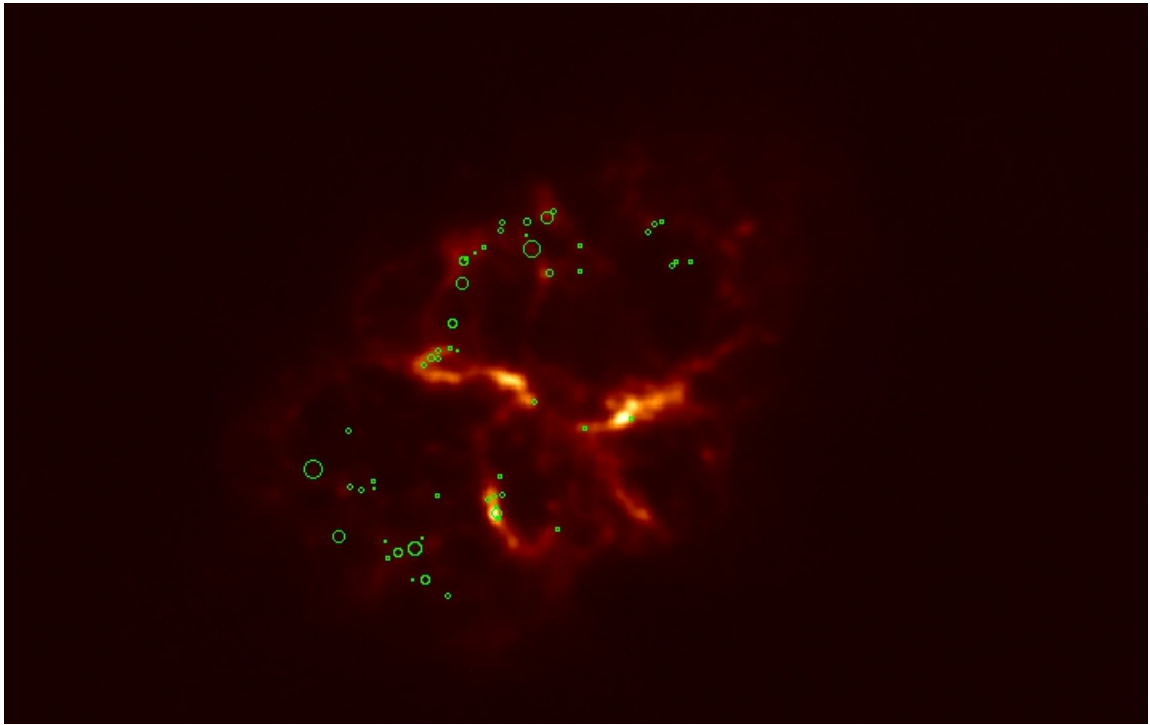


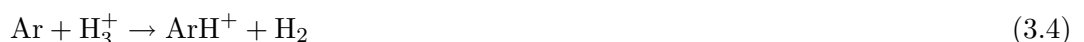
Figure 3.10. A *Herschel* PACS 70 μm image with the size and location of the Loh et al. (2011) H₂ knots shown as green circles.

react with molecular hydrogen to form ArH⁺.



This is an endothermic reaction that releases 1.49 eV of energy. This is because the ionisation potential of atomic argon is less than the ionisation potential of hydrogen and the dissociation energy of H₂. This makes the charge exchange between the two very unlikely meaning that the formation of ArH⁺ is the favoured reaction between the two.

Another formation pathway which can occur in similar regions is the interaction between neutral argon and H₃⁺



ArH⁺ has unusually small photodissociation and dissociative recombination (ArH⁺ +

$e \rightarrow Ar + H$) rates (Roueff et al. 2014). This means it is more stable than most molecules in the ISM and more likely to survive than other noble gas containing molecules such as HeH^+ and NeH^+ , which given the greater abundance of their constituent atoms would be assumed to be far more abundant but are as yet unobserved.

3.2.5 Argon Nucleosynthesis

On earth the most abundant isotope of Argon is ^{40}Ar (99.6%) with only 0.34% of it being the observed isotope ^{36}Ar . The ^{40}Ar is not a product of supernova or stellar nucleosynthesis, but a product of electron capture or positron emission from ^{40}K .



^{40}K also decays to ^{40}Ca via β -decay

^{36}Ar is the product of a chain of α capture in supernovae (Arnett 1996) as well as in the cores of stars. Starting with ^{12}C (which itself is formed in a triple- α process where 3 Helium nuclei fuse forming a resonant state of carbon) multiple fusions between nuclei and α particles fuse to form heavier nuclei.



In the cores of stars this process takes place before the silicon fusing stage and can continue on to ^{56}Ni before core collapse occurs. In core collapse supernovae this process can continue as far as ^{208}Pb . When ^{208}Pb captures another α particle, it becomes ^{212}Po , which has a half life of 299 nanoseconds to α -decay back to ^{208}Pb .

It is not possible to determine isotopes of atomic species via astronomical spectroscopy, so using molecules containing these isotopes is the only way to investigate nucleosynthesis.

3.2.6 ArH⁺ with PACS

The next line in the rotation ladder of $^{36}\text{ArH}^+$ is the J=3-2 line which has a wavelength of $161.98\ \mu\text{m}$. This is in the wavelength range of the PACS-IFU. Figure 3.11 shows the PACS spaxels with the spectral region with the J=3-2 rotational line of $^{36}\text{ArH}^+$.

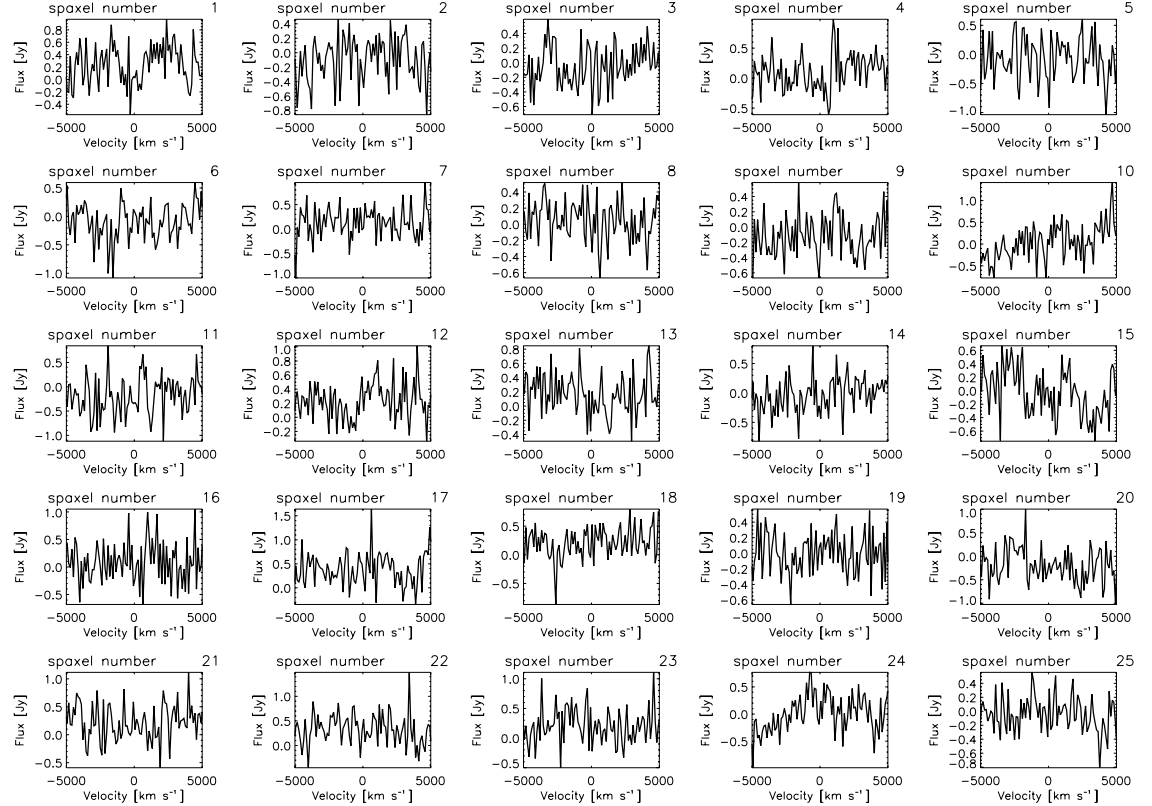


Figure 3.11. PACS-IFU observations of the region of the J=3-2 $161.98\ \mu\text{m}$ $^{36}\text{ArH}^+$ line.

There is no line detection above the noise in the spectra, however we can use these noise levels to set an upper limit on the detection. Taking a standard deviation of the signal per resolution unit and multiplying by the number of bins per resolution unit we find that the upper limit for the detection of the J=3-2 $^{36}\text{ArH}^+$ to be $7.7 \times 10^{-18}\ \text{Wm}^{-2}$.

3.2.7 Temperature

The PACS-IFU observations are coincident with the SPIRE-FTS SLW-C3 and SSW-D4 detectors. This means we have three points and can construct a rotation diagram to estimate the temperature of the molecule as discussed in Section 2.5. Figure 3.12 shows

the rotation diagram for these observations from the slope, the rotation temperature of the $^{36}\text{ArH}^+$ is $T_{rot} = 29 \pm 6$ K. The uncertainty in the temperature is determined from the uncertainty in the slope fitting.

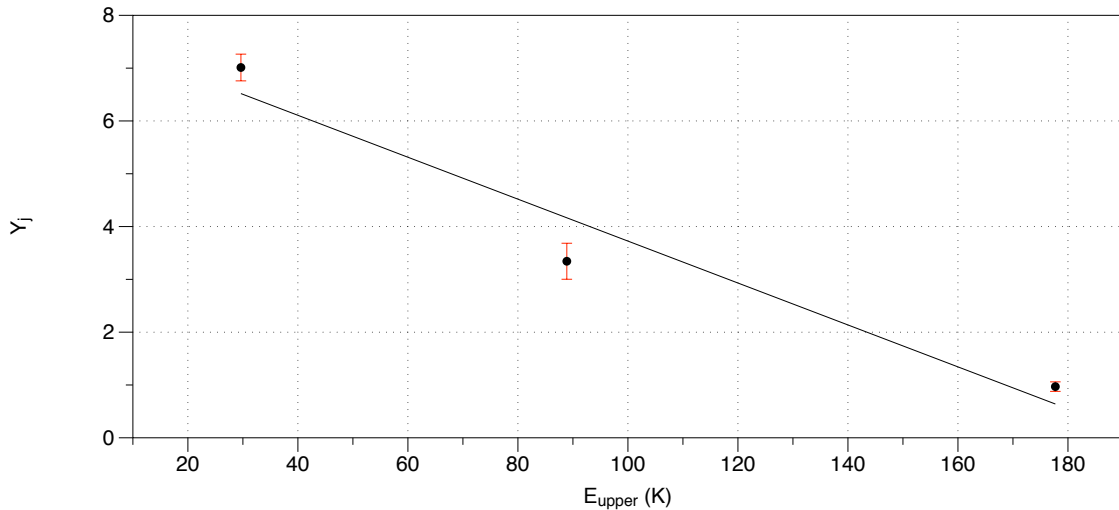


Figure 3.12. The rotation diagram used to determine the temperature of $^{36}\text{ArH}^+$ in the SLW-C3 SSW D4 and PACS-IFU observations

3.3 Follow-up with the VLT

Due to the lack of a far infrared observatory and the over subscription of ALMA; immediate follow up of the detection using these lines is not possible (although an ALMA proposal (PI:Swinyard) has been accepted to investigate the ratio of ^{36}Ar to ^{38}Ar). However there are also several ro-vibrational lines of ArH^+ , as well as several HeH^+ lines in the near infrared.

HeH^+ has been hypothesised to be the first molecule to form in the early universe; however it has never been observed. Given the conditions to form ArH^+ are similar to those required to form HeH^+ and that there is high Helium abundance in the Crab Nebula it is suggested that it might also be present in similar reasons to the ArH^+ .

During certain times of the year, the Crab Nebula is observable from telescopes in the southern hemisphere. The European Southern Observatorys (ESO) Very Large Telescope (VLT) CRIRES (CRyogenic InfraRed Echelle Spectrograph) instrument is a very high

resolution spectrograph covering the near infrared wavelengths from 1-5 μm .

3.3.1 Observations

As we assume that the $^{36}\text{ArH}^+$ is coincident with the regions of H_2 we took spectra of the brightest H_2 knot in the nebula, knot 1 of Loh et al. (2011), which is also coincident with the detections of $^{36}\text{ArH}^+$ (shown in Figure 3.13, the magenta circle shows the location of the Loh et al. (2011) knot 1 while the green circles show nearby detections of $^{36}\text{ArH}^+$ with SPIRE SLW and the blue circle the detections with SPIRE SSW).

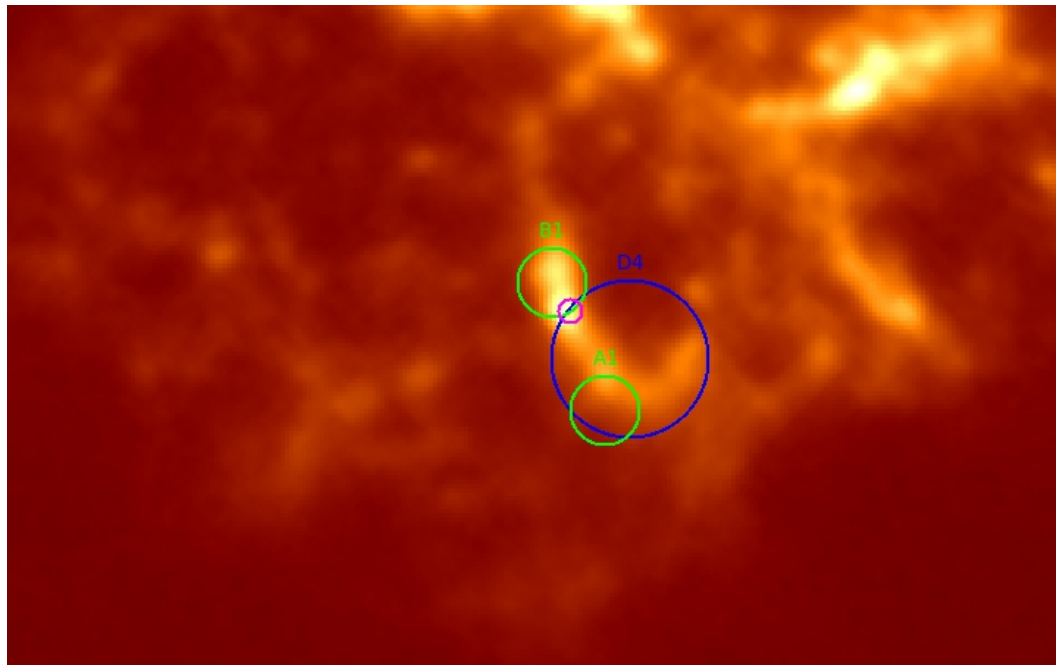


Figure 3.13. The location of the Loh et al. (2011) knot 1 (magenta circle) and nearby *Herschel* SPIRE-FTS detectors that detected $^{36}\text{ArH}^+$ (green circle for SSW, blue circle for SLW).

Figure 3.14 shows the finding chart for the knot. There is some ambiguity in its location with the 2MASS image and the information from Loh et al. (2011) (marked by a green circle) not agreeing. The slit of the spectrograph was positioned so as the knot will be observed whichever of the two is correct.

The two strongest expected vibration-rotation lines of $^{36}\text{ArH}^+$ are at 3827.75 nm ($v=1-0$, $J=1-0$) and at 3799.99 nm ($v=1-0$, $J=2-1$). The measured radial velocity of both knot

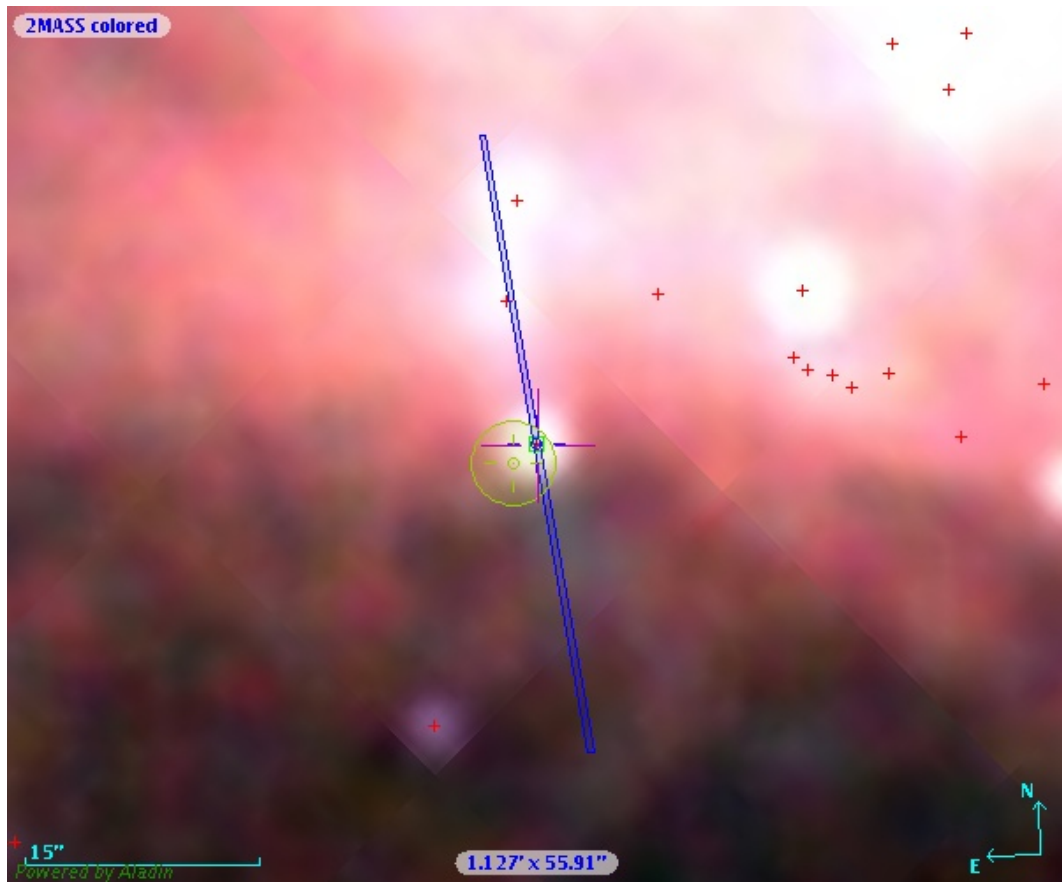


Figure 3.14. Finding chart for the VLT observations showing the slit position of the CRIRES spectrometer in blue on the 2MASS catalogue image of the crab nebula. The Loh et al. (2011) knot 1 position is shown as a green circle.

1 in Loh et al. (2011) and the $^{36}\text{ArH}^+$ observations in this region are $+140 \text{ km s}^{-1}$. This shifts these lines to 3829.40 nm and 3801.63 nm respectively. One observation of an one hour and five minutes was made to observe both these lines, 40 minutes of which was on the source. ι Tau is used as a telluric standard for flux calibration it has effective temperature of 7500 K and a k-band magnitude of +4.25.

In addition to the $^{36}\text{ArH}^+$ lines, we also targeted the R(0) and R(1) lines of HeH^+ . These lines have rest wavelengths of 3364.09 nm and 3302.10 nm respectively which shift to 3365.66 nm and 3303.64 nm. These lines are free from atmospheric line contamination but are far enough apart that they need to be observed separately. Each line was observed for one hour and five minutes including all required overheads. The same telluric standard is used for corrections for these lines as for the $^{36}\text{ArH}^+$ observations.

The observations were made in hour long blocks. The HeH^+ R(1) line observations were taken on the 3rd of February 2014 while the ArH^+ and HeH^+ R(0) line observations were made on the 11th of February. Information on the Science observations can be found in Table 3.5.

Line	OB ID	Date	Exposure Time (s)	Air Mass
HeH^+ R(1)	1047046	2 / 3-Feb-2014	1950.000	1.549
ArH^+	1047031	10 / 11-Feb-2014	2400.000	1.454
HeH^+ R(0)	1047039	10 / 11-Feb-2014	2400.000	1.536

Table 3.5. Information about the VLT-CRIRES observations of the Crab Nebula ArH^+ and HeH^+ .

Figure 3.15 show all of the targeting images of these observations with the slit of the spectrograph over plotted showing that they are all on target.

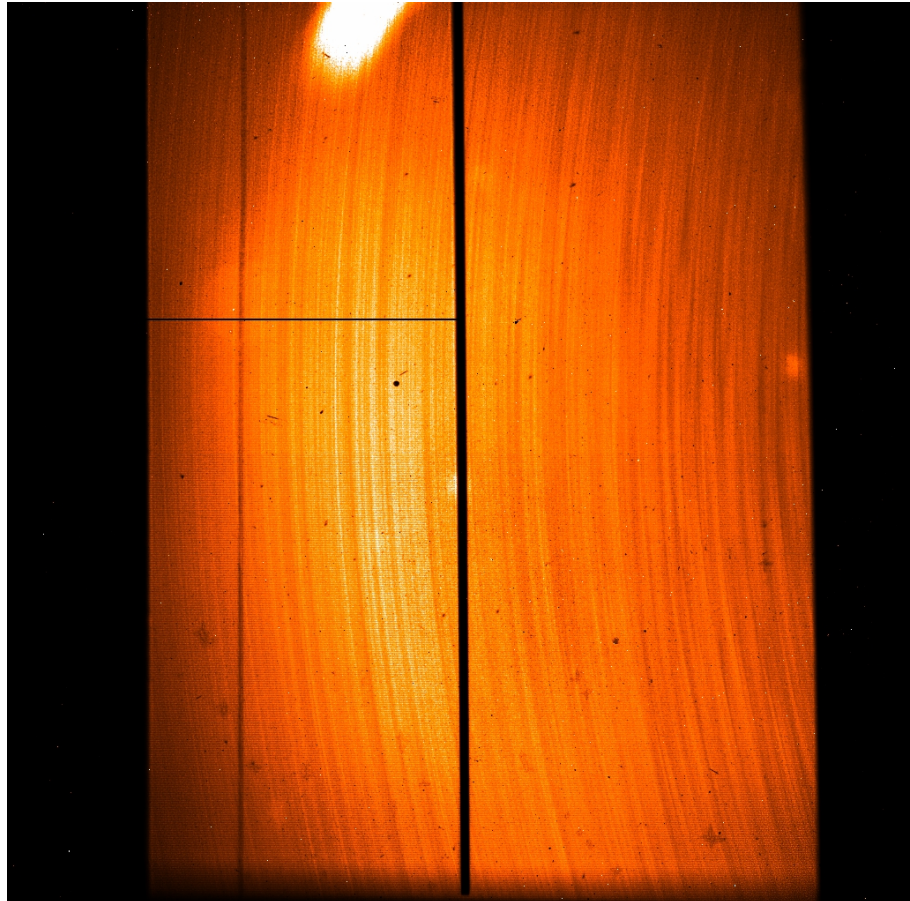


Figure 3.15. The Targeting of the VLT showing the spectrograph slit over the central knots.

3.3.2 Data Reduction

The raw spectra were first cleaned of cosmic rays. This is done using a median filtering technique, a process which involves replacing each pixel in the data file with the median of its neighbouring pixels. The before and after processing image is shown in Figures 3.16 and 3.17. The vastly increased contrast in the image after processing is down to the cosmic ray hits being so much brighter than any of the actual observational data.

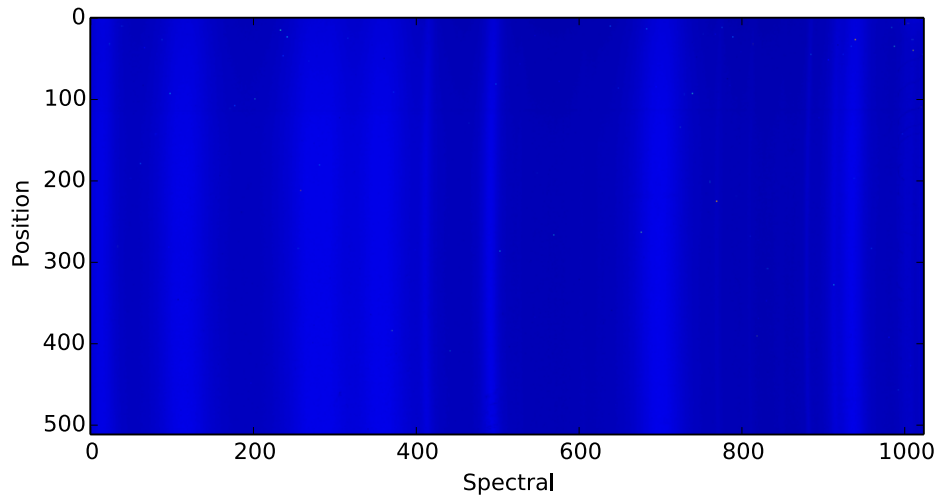


Figure 3.16. The raw spectral data from CRIRES observations of the Crab Nebula before any processing has taken place

The next step in the reduction of the data is to remove the contribute from the earths atmosphere. ESO provides an exposure time calculator tool (ETC) which provides very accurate models of the sky for a given observation angle, air mass and percentage of water vapour for the VLT. These sky lines can be used for both subtraction of the sky and wavelength calibration. As shown in Figure 3.18, which shows the observed spectrum taken from the 8 central spatial pixels of the spectrograph (blue) and the sky model normalised to it (green) that the two do not line up exactly. The difference between them

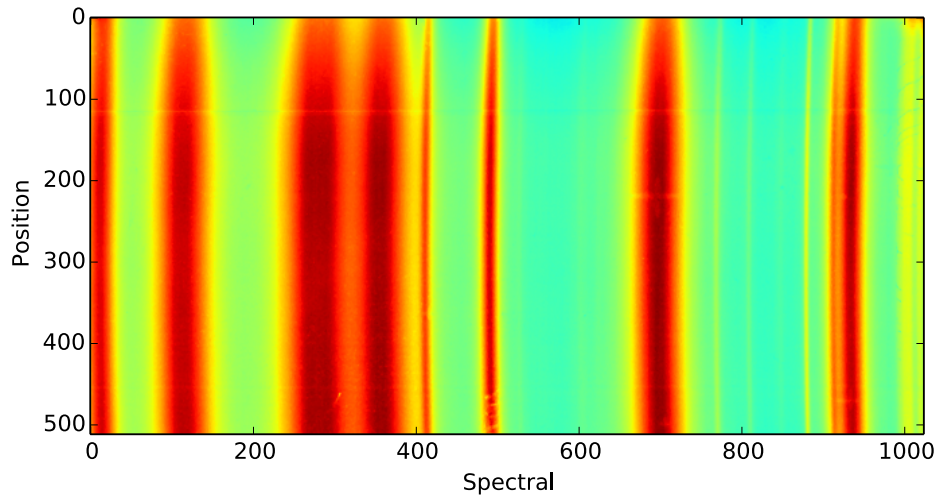


Figure 3.17. The spectral data from CRIRES observations of the Crab Nebula after they have been processed using a median filtering technique to remove cosmic rays from the data.

is also non linear across the detector array so the lines bracketing the region of interest are used to calibrate that region of the spectrum accurately.

The spectra are in units of counts of the analogue to digital converter (ADU) so need to be translated in to a flux unit. After calibrating the wavelength the spectrum needs to be flux calibrated. At the same time as each observation is made and observation is also made of a star of known brightness and temperature which means that its flux is well known and can be used to convert from detector counts to units of flux. In this case the star ι Tau is used. It is a A7V with $T_{eff} = 7500$ K it has an R-band magnitude of 4.48. The R-band wavelength is $0.64 \mu\text{m}$ and the zero point is or $2.26 \times 10^{-8} \text{ W m}^{-2} \mu\text{m}^{-1}$. A blackbody spectrum is generated with this temperature and then normalised to that R-band flux. Figure 3.19 shows this normalised blackbody curve with the normalisation point shown as a green dot, also shown are the regions of interest for our observations.

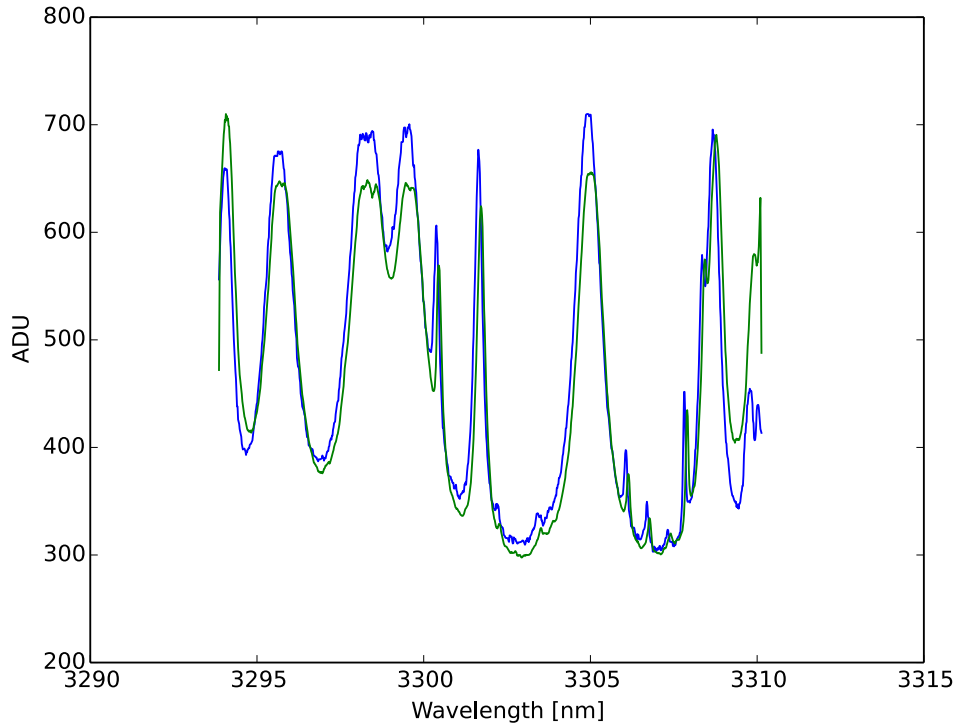


Figure 3.18. The spectrum of the observation of $\text{HeH}^+ \text{ R}(1)$ (blue) and model sky from the ETC (green).

The flux of this blackbody curve is the modelled flux of ι Tau. We then take the observed of ι Tau in ADU, which has been reduced in the same way as the Crab Nebula spectra, and divide it by this modelled flux. This gives the Relative Spectral Response Function (RSRF) in $\text{ADU W}^{-1} \text{ m}^2 \mu\text{m}$. We can now use this to flux calibrate the Crab nebula spectra. This is done by dividing the observed spectrum by the RSRF.

3.3.3 Results

Figures 3.20, 3.21, 3.23 and 3.22 show the region of interest calibrated spectra for the central 8 spaxels of each observation. There is no clear detection of any of the lines we investigated, so we must put upper limits on the potentially observed fluxes based on the noise in the data.

Figures 3.25, 3.24, 3.26 and 3.27 show the region of interest calibrated spectra for the 8 spaxels of each observation for the 8 sets of 8 spaxels down the entire spectrograph. There are no clear detections of any of the lines we investigated. All apparent features are coin-

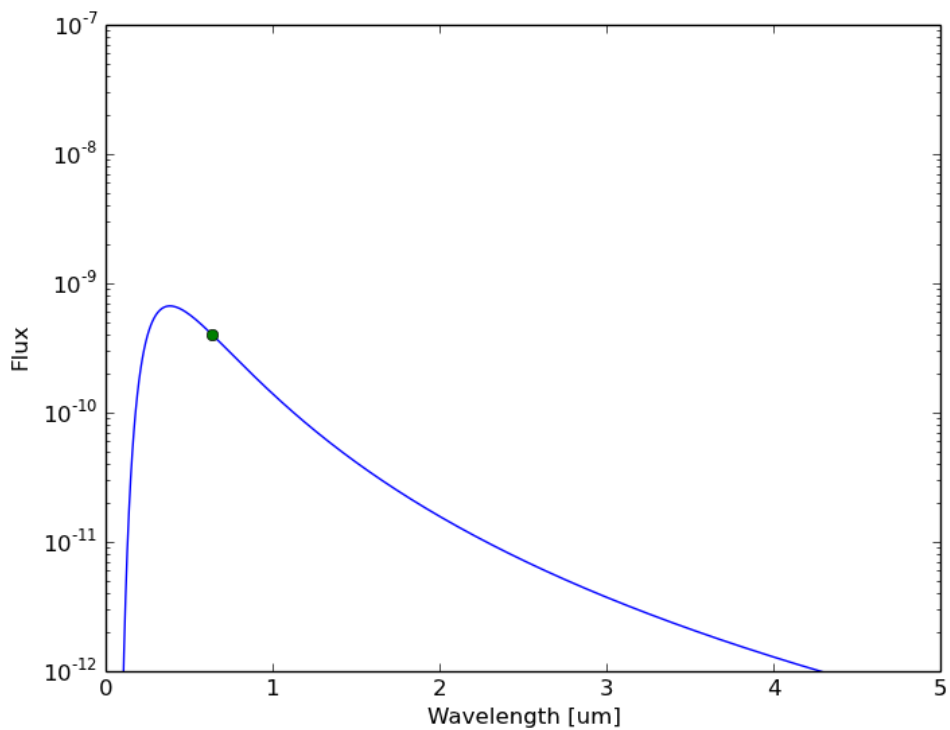


Figure 3.19. The modelled blackbody spectrum of ι Tau used for flux calibration.

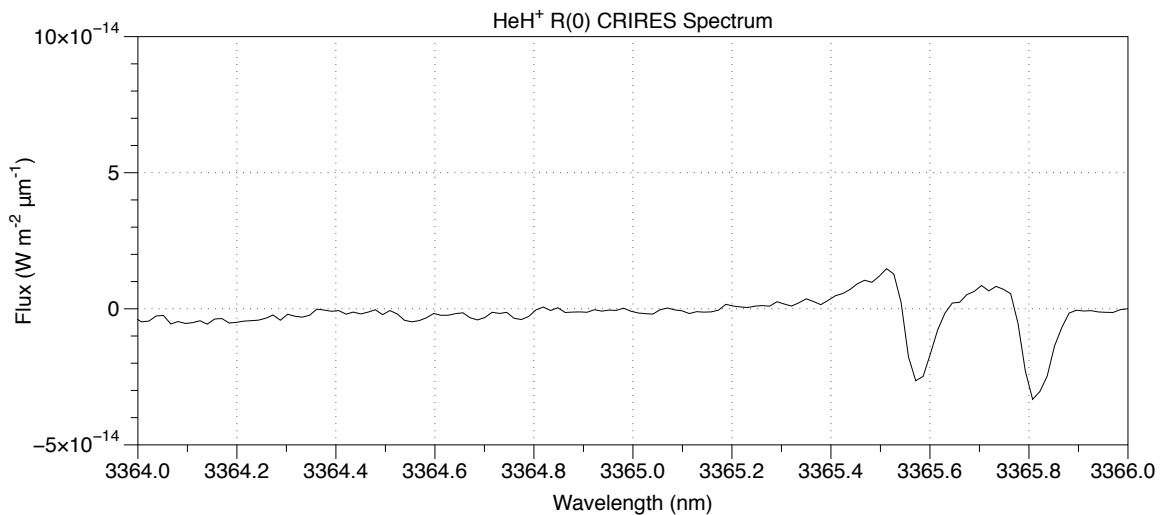


Figure 3.20. The spectrum of the region of the HeH^+ R(0) 3364.09 nm line taken with VLT-CRIRES.

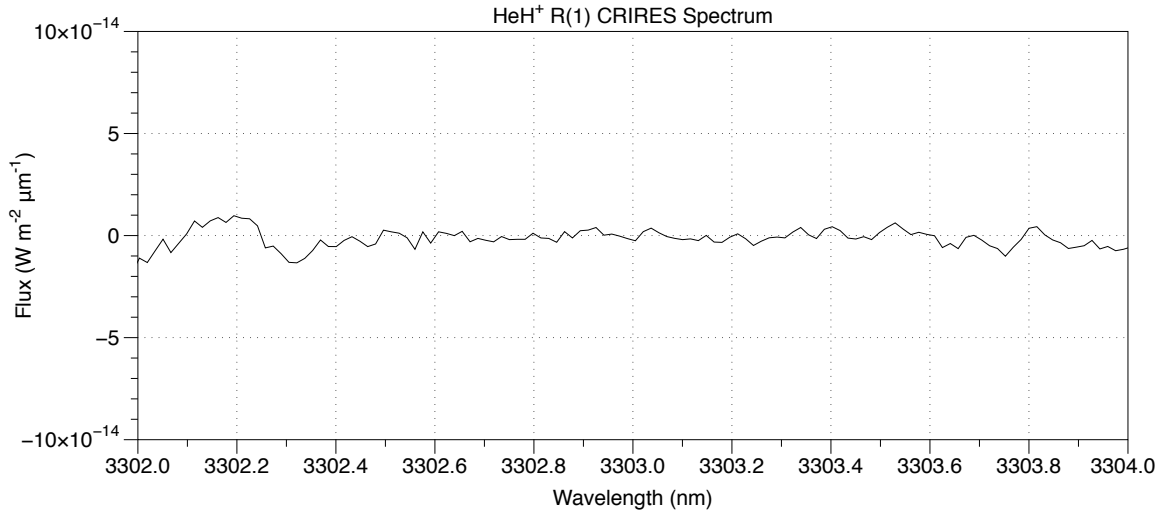


Figure 3.21. The spectrum of the region of the HeH⁺ R(1) 3302.10 nm line taken with VLT-CRIRES.

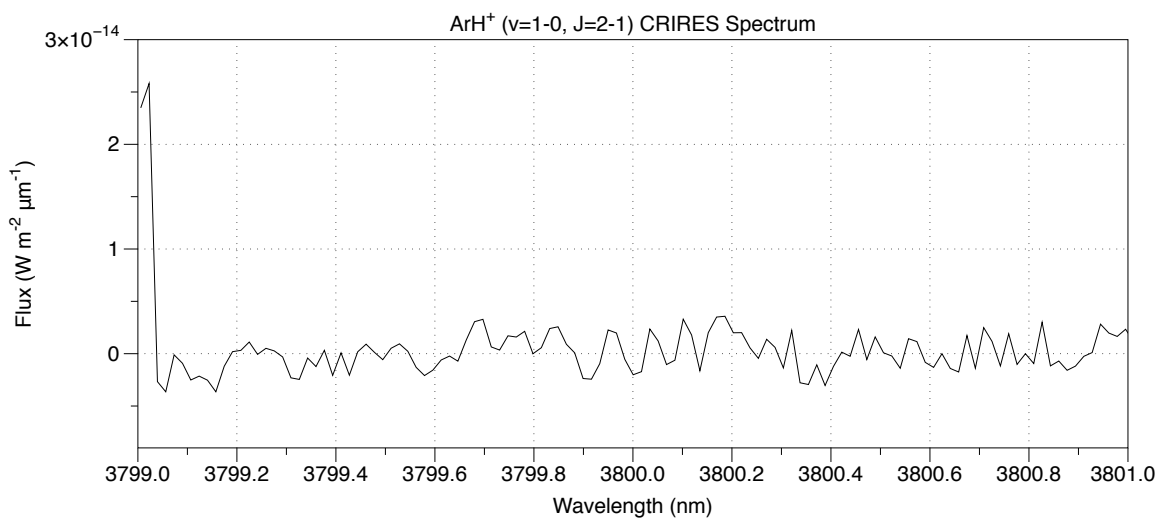


Figure 3.22. The spectrum of the region of the ArH⁺ (v=1-0, J=2-1)) 3799.99 nm line taken with VLT-CRIRES.

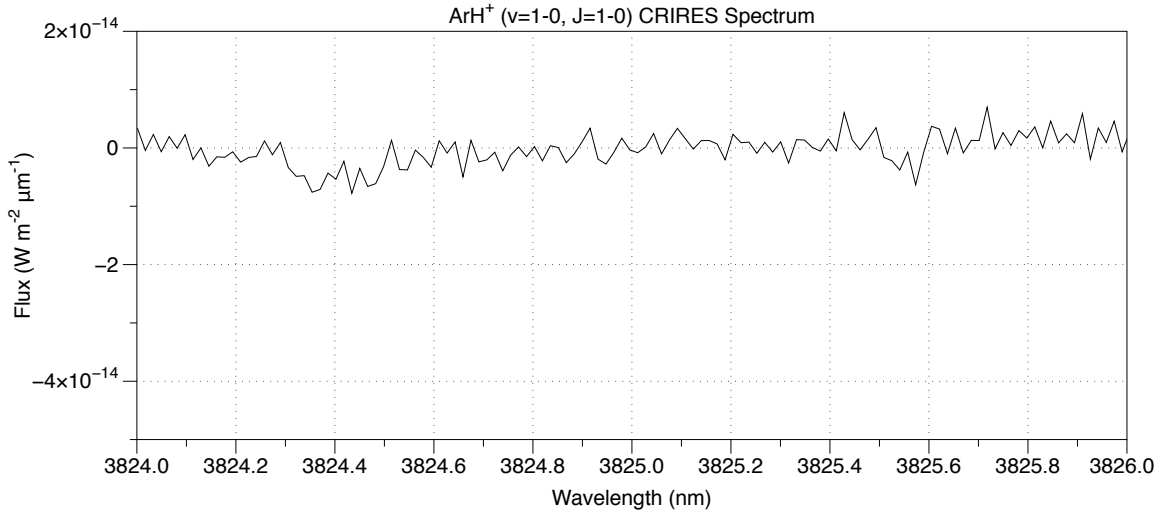


Figure 3.23. The spectrum of the region of the rH⁺ (v=1-0, J=1-0) 3827.75 nm line taken with VLT-CRIRES.

cident with sky features which have either not been fully subtracted or over compensated for.

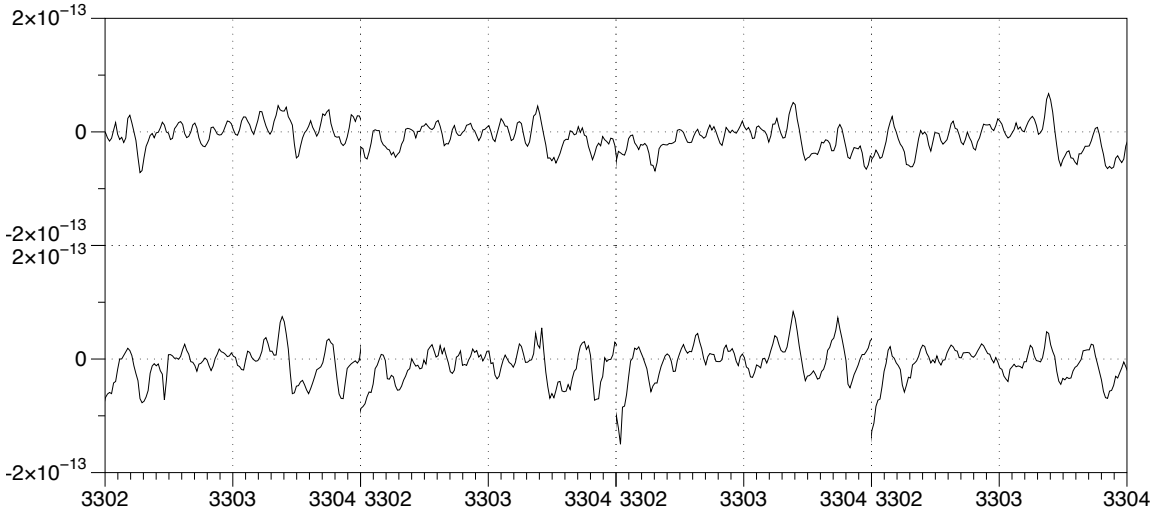


Figure 3.24. The 8 coadded spectra of the whole slit of the spectrograph in the region of the HeH⁺ R(1) 3302.10 nm line taken with VLT-CRIRES.

3.3.4 Upper Limits

The resolving power of CRIRES with the 0.4 arcsec slit is given as 50000 so at 3302 nm the resolution element is 0.066 nm which is 4 spectral samples. We binned the data into 4 sample bins and take the standard deviation in each bin as representative of the noise on

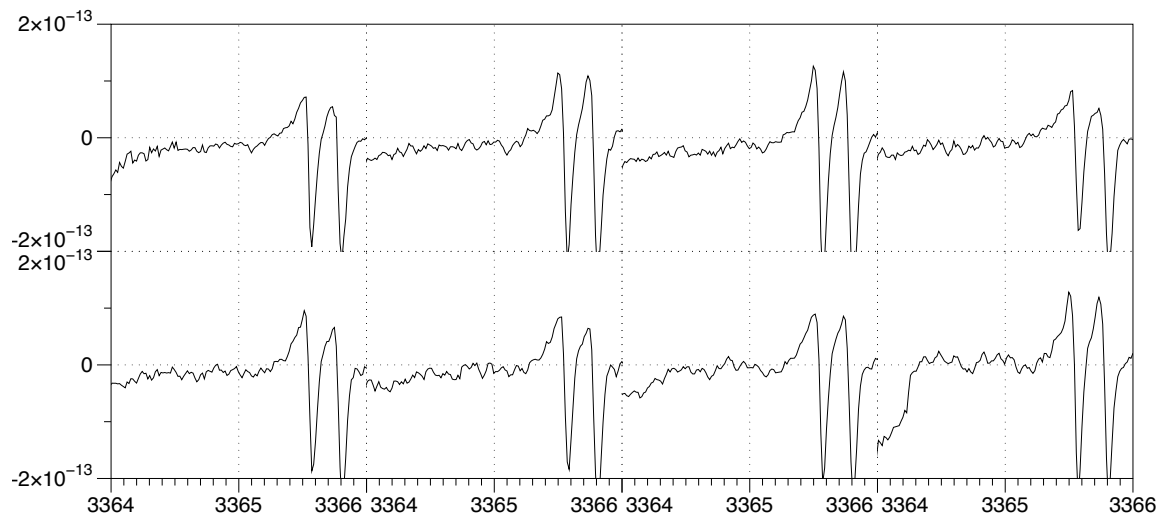


Figure 3.25. The 8 coadded spectra of the whole slit of the spectrograph in the region of the HeH^+ $R(0)$ 3364.09 nm line taken with VLT-CRIRES.

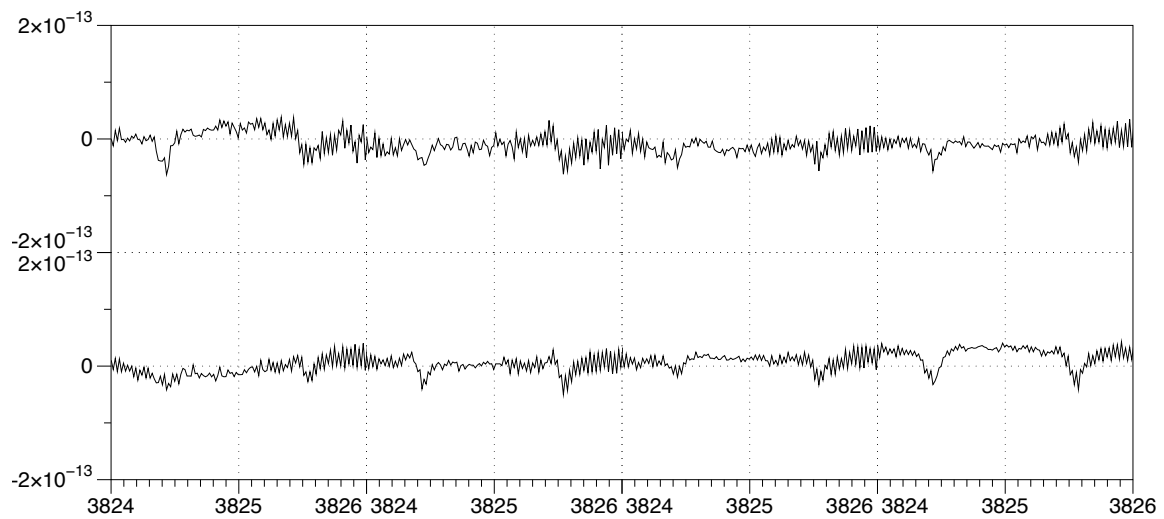


Figure 3.26. The 8 coadded spectra of the whole slit of the spectrograph in the region of the $r\text{H}^+$ ($v=1-0$, $J=1-0$) 3827.75 nm line taken with VLT-CRIRES.

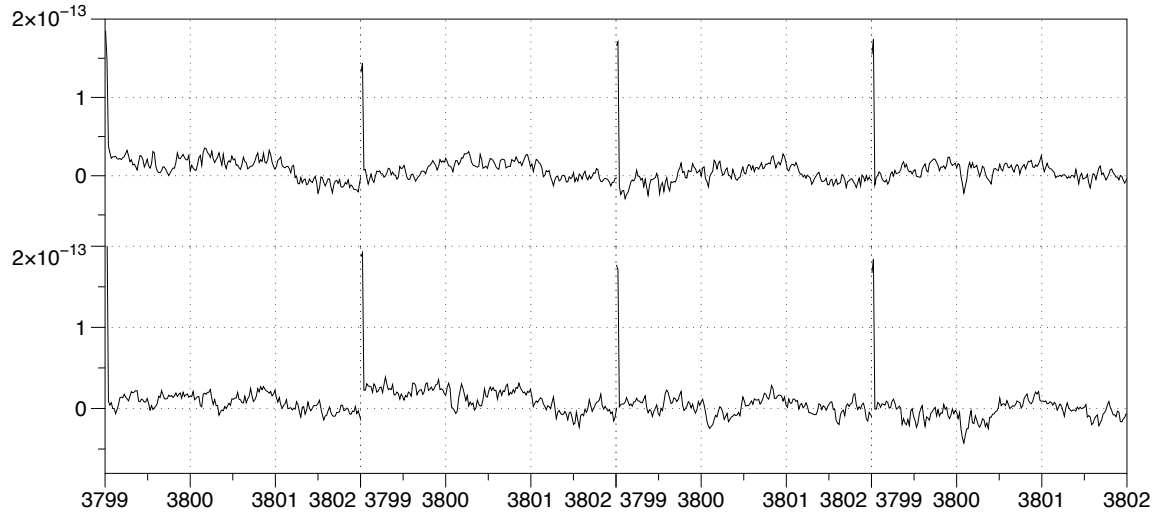


Figure 3.27. The 8 coadded spectra of the whole slit of the spectrograph in the region of the ArH^+ ($v=1-0$, $J=2-1$) 3799.99 nm line taken with VLT-CRIRES.

an integrated line. This noise can then be multiplied by the resolution to give the estimate of a 1-sigma detection limit. The H_2 emission in the region we are observing is known to lie between +90 and +145 km s^{-1} . The spectra are plotted in velocity and corrected for the motion of the earth and an upper limit is then fitted to this region of the spectrum. The spectra plotted in velocity space are shown in Figures 3.29, 3.28, 3.30 and 3.31. The values of the heliocentric correction and size of resolution element are shown in Table 3.6.

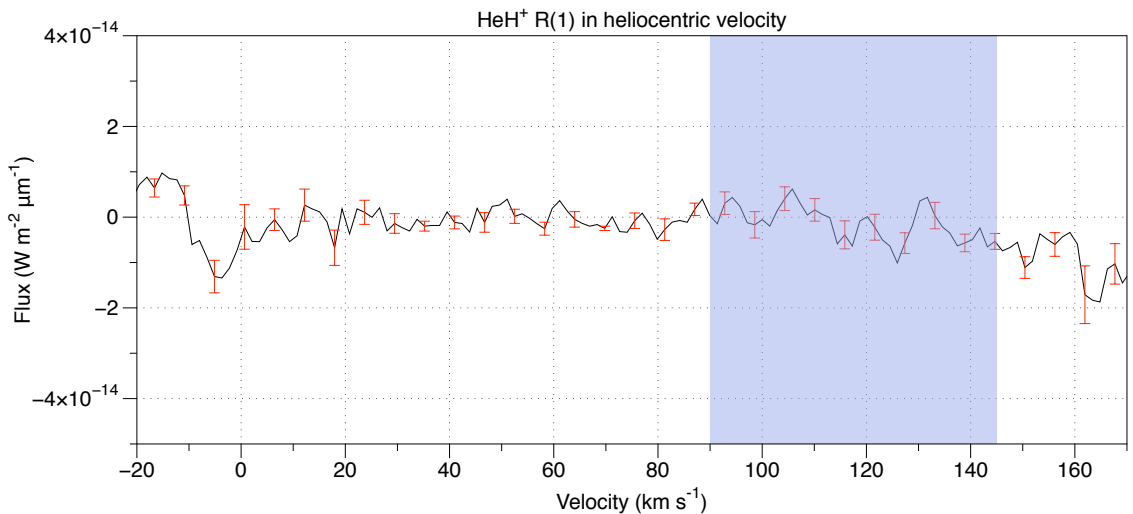


Figure 3.28. The spectrum of the region of the HeH^+ R(1) 3302.10 nm line taken with VLT-CRIRES.

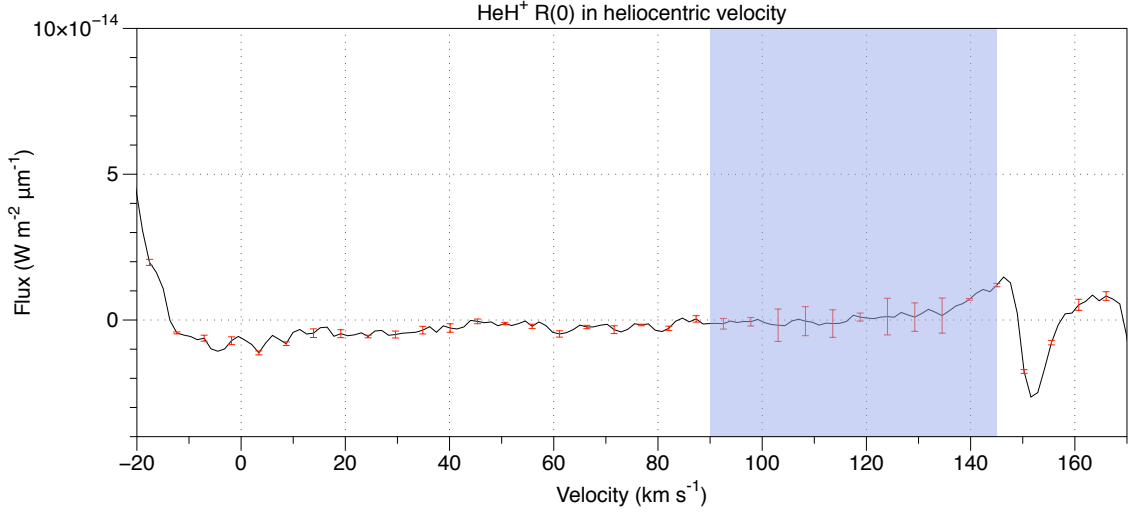


Figure 3.29. The spectrum of the region of the HeH^+ $R(0)$ 3364.09 nm line taken with VLT-CRIRES.

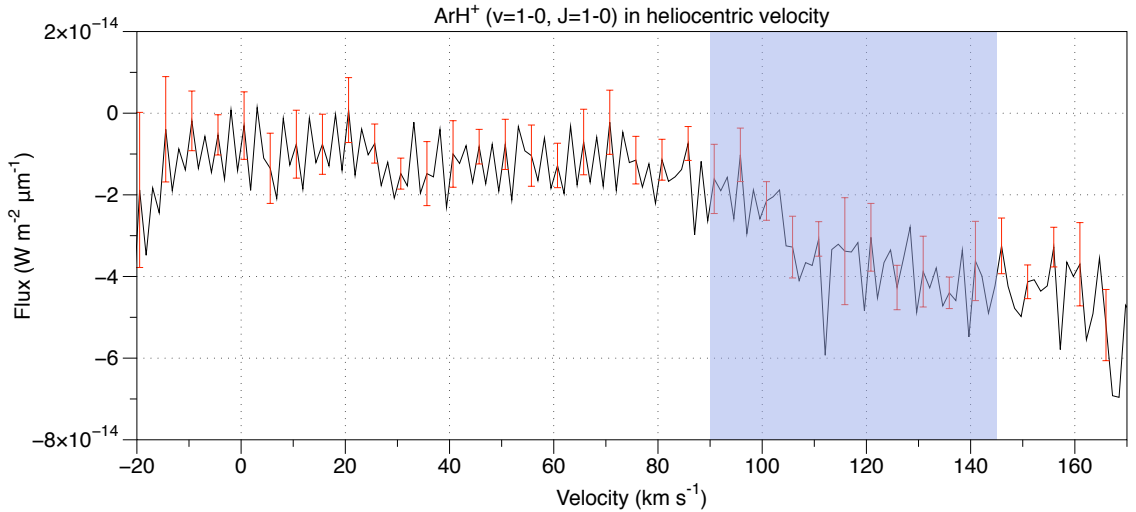


Figure 3.30. The spectrum of the region of the $r\text{H}^+$ ($v=1-0$, $J=1-0$) 3827.75 nm line taken with VLT-CRIRES.

Line	resolution element	Heliocentric Correction
HeH^+ $R(0)$	0.067 nm	-25.98 km s^{-1}
HeH^+ $R(1)$	0.066 nm	-23.69 km s^{-1}
ArH^+ ($v=1-0$, $J=1-0$)	0.076 nm	-26.12 km s^{-1}
ArH^+ ($v=1-0$, $J=2-1$)	0.076 nm	-26.12 km s^{-1}

Table 3.6. The factors used in calculating the upper limits of detection in the CRIRES spectra. Heliocentric correction for motion of the earth taken from ESO Sky Calendar Tool <http://www.eso.org/sci/observing/tools/calendar/airmass.html>.

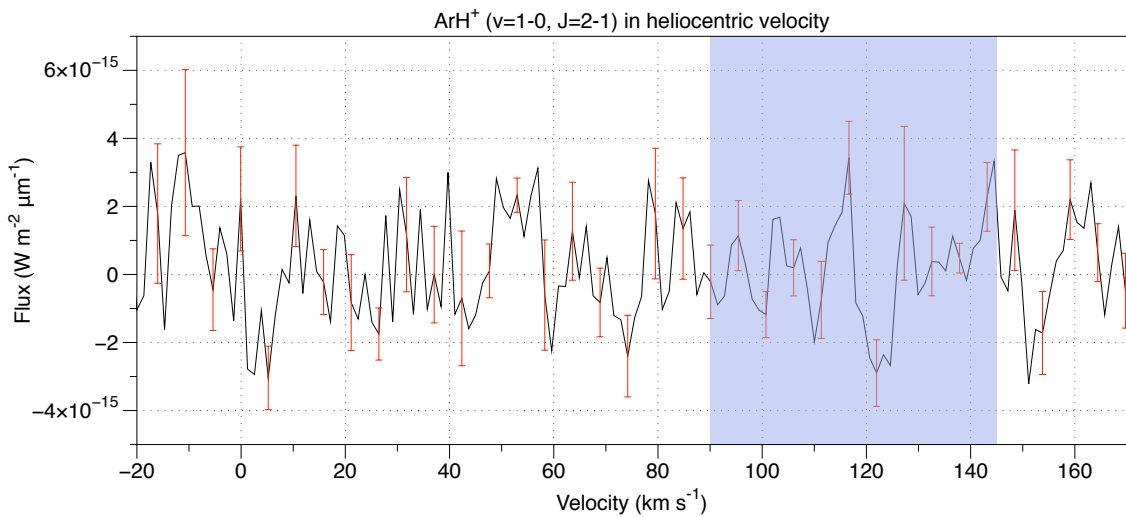


Figure 3.31. The spectrum of the region of the ArH⁺ (v=1-0, J=2-1)) 3799.99 nm line taken with VLT-CRIRES.

The limits are show in Table 3.7.

Line	Wavelength	Detection Limit
HeH ⁺ R(0)	3364.09 nm	3.7×10^{-19} W m ⁻²
HeH ⁺ R(1)	3302.10 nm	1.9×10^{-19} W m ⁻²
ArH ⁺ (v=1-0, J=1-0)	3827.75 nm	6.5×10^{-19} W m ⁻²
ArH ⁺ (v=1-0, J=2-1)	3799.99 nm	1.5×10^{-19} W m ⁻²

Table 3.7. The upper limits of detection of the HeH⁺ R(0), R(1) and ArH⁺ (v=1-0, J=1-0) and (v=1-0, J=2-1) lines with VLT-CRIRES

This lack of a clear detection may mean several things. As the region with the ArH⁺ is very cold, these ro-vibrational states may not be excited. Alternatively it is possible we are investigating the wrong regions and than rather than the bright knots the emission is in fact coming from the more diffuse regions. Further observations and modelling work will be required to determine which of these is the case.

3.4 HeH⁺ with PACS

The J=1-0 and J=2-1 HeH⁺ rotational lines at 149.25 μ m and 74.83 μ m are both within the wavelength range of PACS. Figures 3.33 and 3.33 show the individual PACS-IFU spaxels in velocity space for the two HeH⁺ lines. Putting upper limits on these non detections we find 4.9×10^{-17} W m⁻² for the 1-0 line and 6.3×10^{-17} W m⁻² for the 2-1 line.

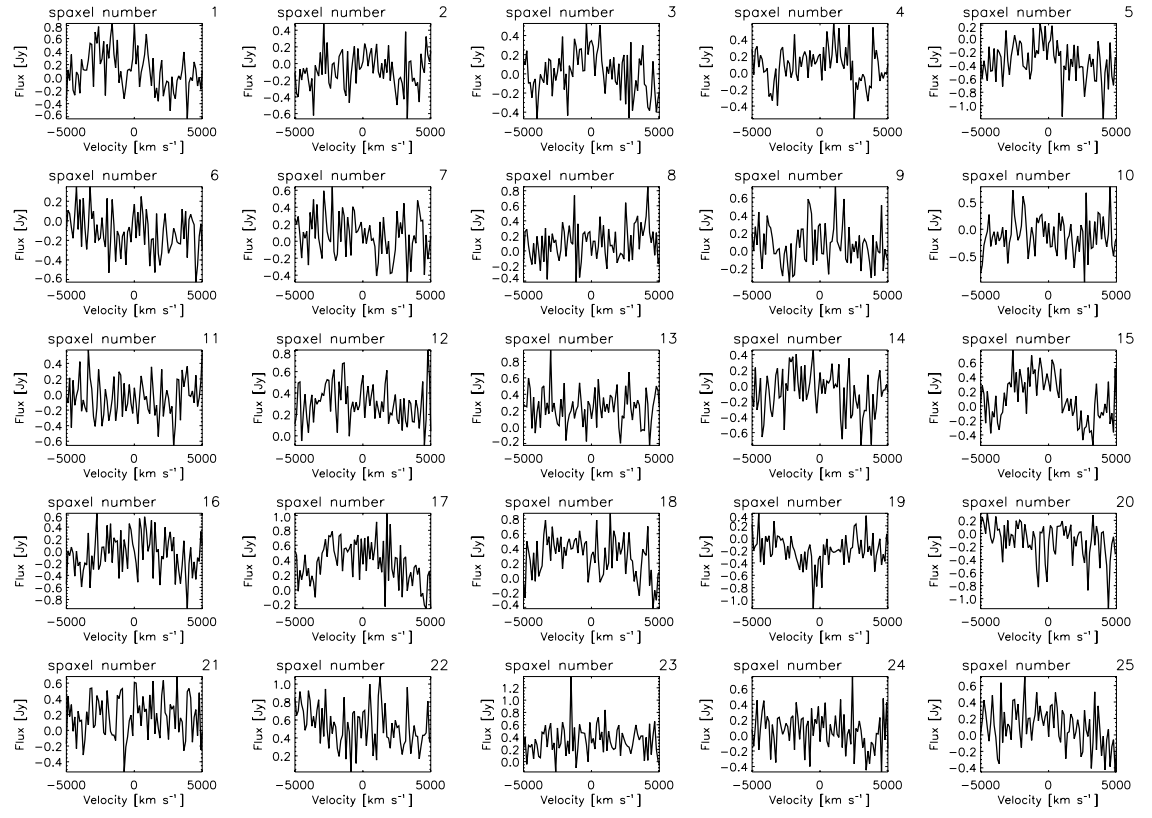


Figure 3.32. PACS-IFU observations of the region of the $J=1-0$ $149.25\text{ }\mu\text{m}$ HeH^+ line.

3.5 Conclusions

Despite its violent nature the Crab Nebula has a diverse structure and chemistry. This exotic chemistry , including the detection of a previously unobserved molecule, is opening new windows in astronomy as it can be used to investigate the abundances of other molecular gasses such as Hydrogen which can not be directly probed. In addition to this it can provide observational constraints on supernova nucleosynthesis models for the first time via the observations of different isotopologues. Future observations with ALMA will probe the ratios of $^{36}\text{Ar}/^{38}\text{Ar}$. As discussed, ^{36}Ar is formed in an explosive α capture process, whereas ^{38}Ar is formed by a slow neutron capture process (the S-process).

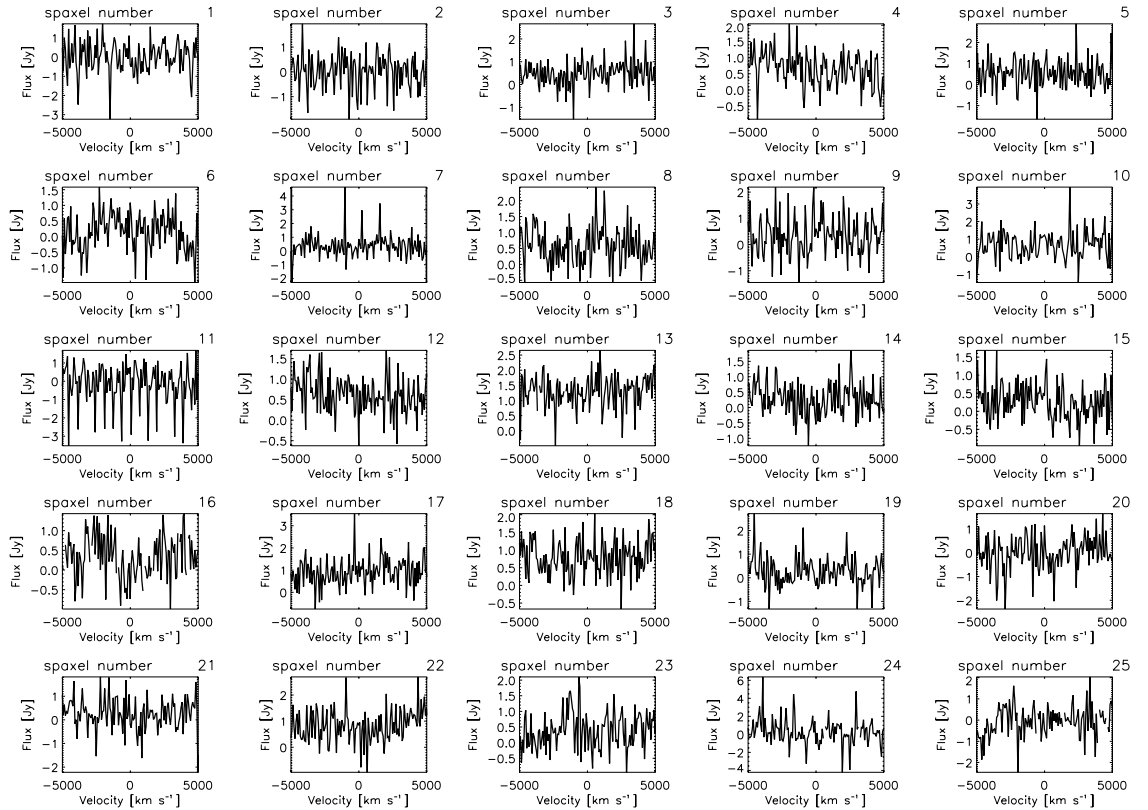


Figure 3.33. PACS-IFU observations of the region of the $J=2-1$ $74.83\text{ }\mu\text{m}$ HeH^+ line.

Chapter 4

Herschel Spectroscopy of Cassiopeia A

Nothing says romance like the gift of a kidnapped, injured woman

Neal Gaiman in Stardust

Cassiopeia A is a young oxygen rich supernova remnant (SNR). It is approximately 3.4 kpc away (Reed et al. 1995) and around 330 years old (Fesen et al. 2006). Cas A is one of the most-studied objects in the sky, having been observed in all wavelengths from radio waves through to γ -rays. Recent observations in the near infrared of light echoes due to absorption, re-emission and scattering by interstellar dust show that it is the remnant of a Type IIb supernova of intial mass of around $15 M_{\odot}$ (Krause et al. 2008).

4.1 Cassiopeia A with PACS

Spectra of Cas A were taken of nine different positions around the Cas A supernova remnant on January 1st 2011 using the PACS-IFU instrument. They focused on the reverse shock and central regions. Their positions are shown in Figure 4.1 plotted on a $70\mu\text{m}$ image of Cas A, along with the off-target positions used by the chopping to remove background. At each position two observations are made, one for the wavelength ranges 51-72

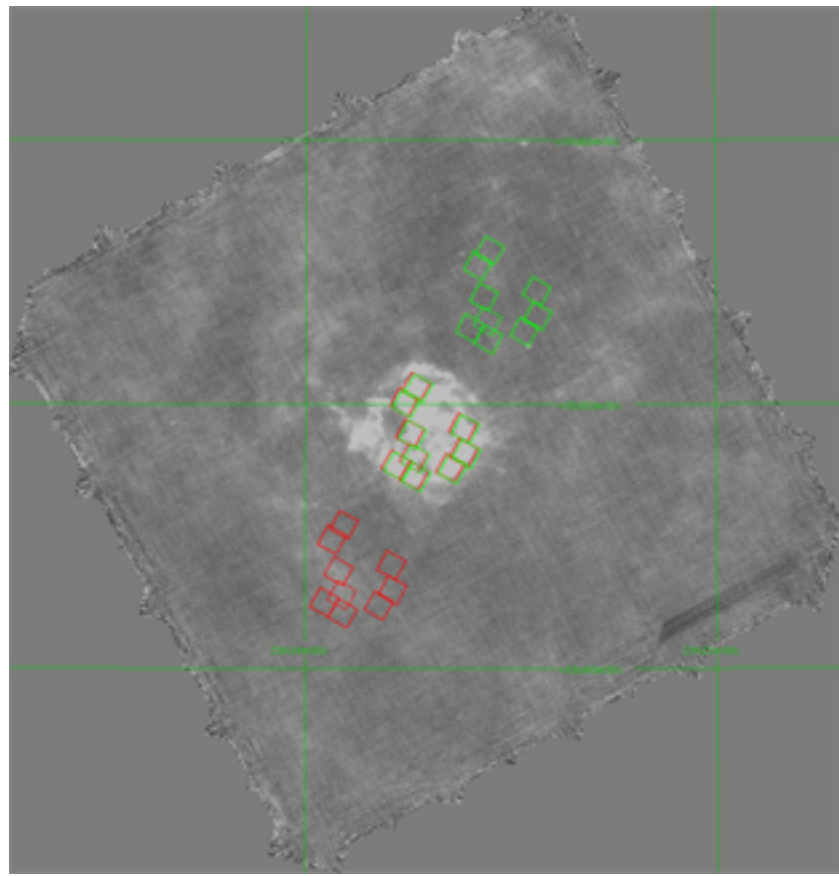


Figure 4.1. The observations of Cas A with *Herschel* PACS-IFU plotted on a PACS 70 μm image.

μm and 102-146 μm (Range Mode SED B2A + Short R1) and one for the 70-105 μm and 140-220 μm (Range Mode SED B2B + Long R1). Data was reduced to level 2 using the standard PACS chopped large range scan and SED pipeline in HIPE 8.0.1 (Ott, 2010) using the PACS_CAL_32_0 calibration file. RA, DEC, the time the observation was made, the observation ID and the time on source are shown in Table ??.

Object	Date	Time	RA	DEC	ObsID	Time on source
Cas A - SP1	2011-01-01	17:46:11	23h 23m 28.61s	58° 48' 59.17"	1342212249	2267
Cas A - SP1	2011-01-01	18:26:10	23h 23m 28.20ss	58° 49' 5.10"	1342212250	1139
Cas A - SP2	2011-01-01	19:48:25	23h 23m 24.94s	58° 51' 26.98"	1342212253	2267
Cas A - SP2	2011-01-01	20:28:24	23h 23m 24.50s	58° 51' 33.31"	1342212254	1139
Cas A - SP3	2011-01-01	21:50:39	23h 23m 12.76s	58° 49' 12.26"	1342212257	2267
Cas A - SP3	2011-01-01	22:30:38	23h 23m 13.19s	58° 49' 18.37"	1342212258	1139
Cas A - SP4	2011-01-01	15:43:57	23h 23m 32.82s	58° 47' 48.39"	1342212245	2267
Cas A - SP4	2011-01-01	16:23:56	23h 23m 32.41s	58° 47' 54.44"	1342212246	1139
Cas A - SP5	2011-01-01	18:47:18	23h 23m 27.40s	58° 47' 23.04"	1342212251	2267
Cas A - SP5	2011-01-01	19:27:17	23h 23m 26.99s	58° 47' 28.89"	1342212252	1139
Cas A - SP6	2011-01-01	14:42:50	23h 23m 40.49s	58° 48' 52.93"	1342212243	2267
Cas A - SP6	2011-01-01	15:22:49	23h 23m 39.61s	58° 49' 05.82"	1342212244	1139
Cas A - SP7	2011-01-01	16:45:04	23h 23m 30.45s	58° 50' 10.21"	1342212247	2267
Cas A - SP7	2011-01-01	17:25:03	23h 23m 30.03s	58° 50' 16.42"	1342212248	1139
Cas A - SP8	2011-01-01	20:49:32	23h 23m 16.84s	58° 47' 41.01"	1342212255	2267
Cas A - SP8	2011-01-01	21:29:31	23h 23m 16.43s	58° 47' 46.89"	1342212256	1139
Cas A - SP9	2011-01-01	22:51:46	23h 23m 12.87s	58° 48' 15.45"	1342212259	2267
Cas A - SP9	2011-01-01	23:31:45	23h 23m 12.46s	58° 48' 21.36"	1342212260	1139

Table 4.1. The positions of the PACS Spectroscopic observations of Cas A

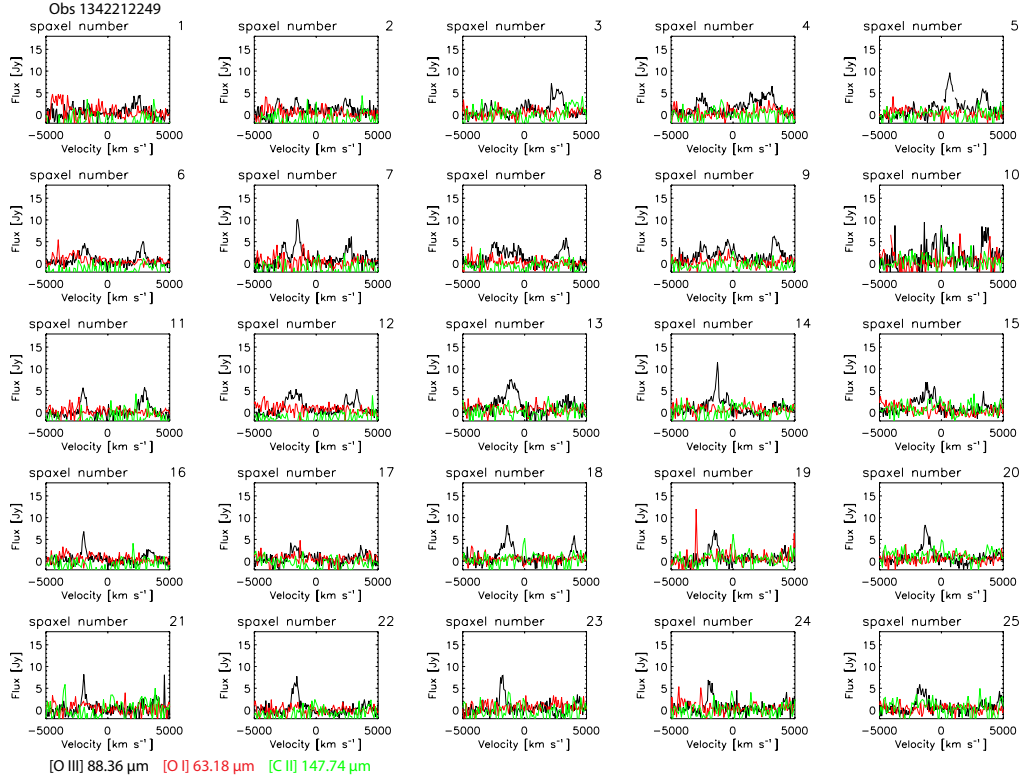


Figure 4.2. The 5x5 PACS-IFU observation SP1 of Cas A in velocity space. The black line shows the 88 μm [O III] line, the red line shows the 63 μm [O I] line and the green shows the 157 μm [C II] line.

4.1.1 Oxygen

Cas A is an oxygen rich supernova remnant. There is a strong [O III] 88 μm coinciding with both the bright 70 μm emission and regions with less emission as shown in Figure 4.11 which is the relative flux of the red shifted lines and 4.12 shows the relative flux of the blue shifted emissions of the [O III] 88 μm detected by PACS-IFU plotted over a contour plot of the PACS 70 μm image.

Whilst some spaxels have a 63 μm [O I] line, shown in Figure 4.13 and 4.14, there is no 145 μm [O I] line observed anywhere in the nebula. Only exciting to the ${}^3\text{P}_1$ level (gives 63 μm) rather than ${}^3\text{P}_0$ which gives both lines (see Figure 4.15). The statistical ratio of these lines for purely thermal excitation is 5:3:1, so we would expect to see at least some emission from the ${}^3\text{P}_0$ to ${}^3\text{P}_1$ transition. Strong [O I] 63 μm is an indicator of shocked material (Tielens 2005), and there are many strong shocks in Cas A (Sutherland & Dopita

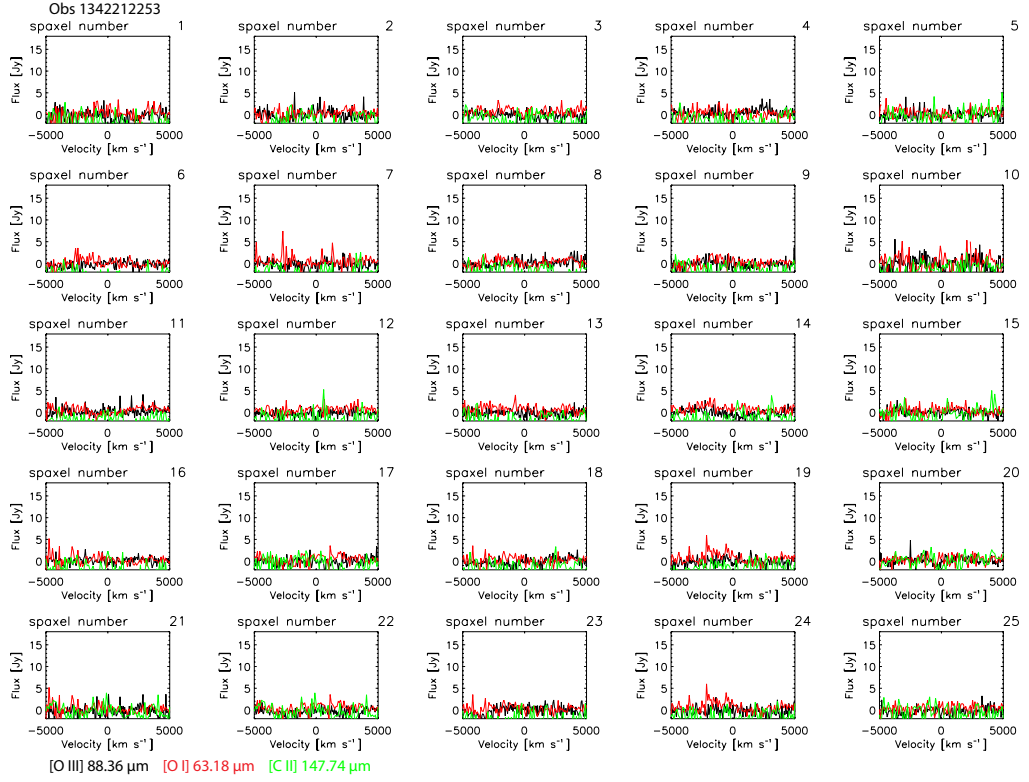


Figure 4.3. The 5x5 PACS-IFU observation SP2 of Cas A in velocity space. The black line shows the 88 μm [O III] line, the red line shows the 63 μm [O I] line and the green shows the 157 μm [C II] line.

1995), which explain the increased emission at 63 μm , but models still predict some [O I] 145 μm (Docenko & Sunyaev 2010). Optical Thickness and self absorption (Liseau et al. 2006) used to explain the other way around. These observations are consistent with the ISO observations of Cas A.

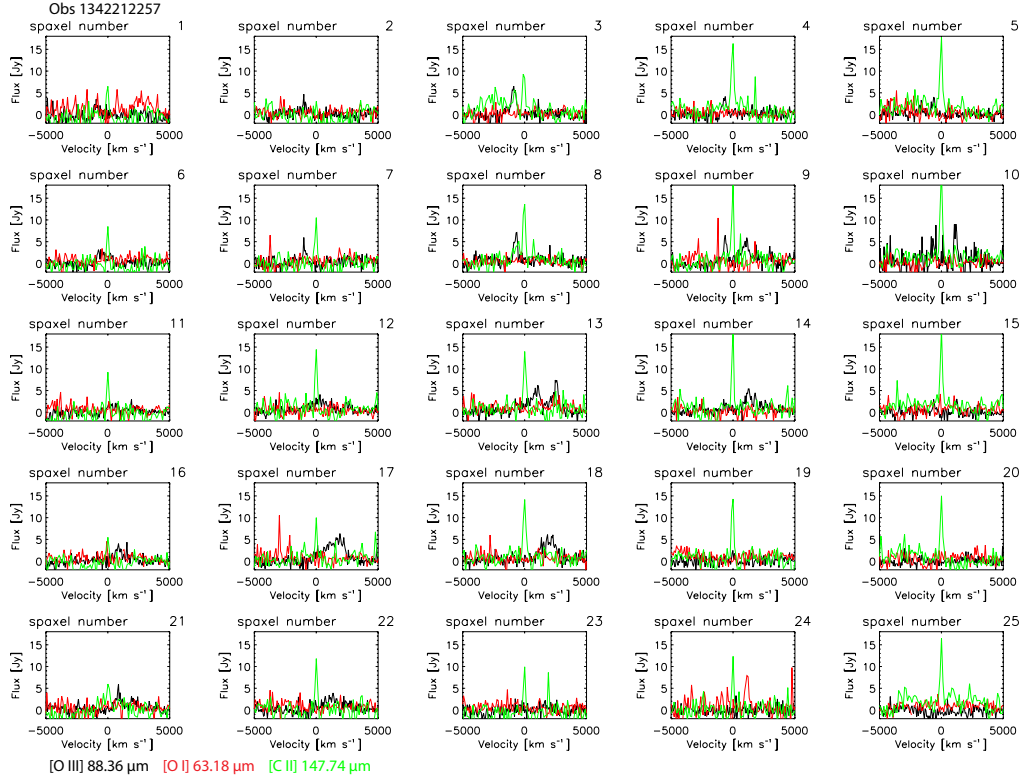


Figure 4.4. The 5x5 PACS-IFU observation SP3 of Cas A in velocity space. The black line shows the 88 μ m [O III] line, the red line shows the 63 μ m [O I] line and the green shows the 157 μ m [C II] line.

4.1.2 Upper Limits on the [O I] 145 μ m line

The [O I] 145 μ m line is not observed in the PACS spectra, so we fitted upper limits on its detection. Assuming that it will be moving at the same velocity and line width as the [O I] 63 μ m in the same spaxels, an upper limit is determined based on the noise in that spaxel to determine the strongest emission that would be present if the line is there. The results for these upper limits as shown in Tables 4.2, 4.3, 4.4, 4.5, 4.6, 4.7, 4.8, 4.9, 4.10, 4.11 and 4.12.

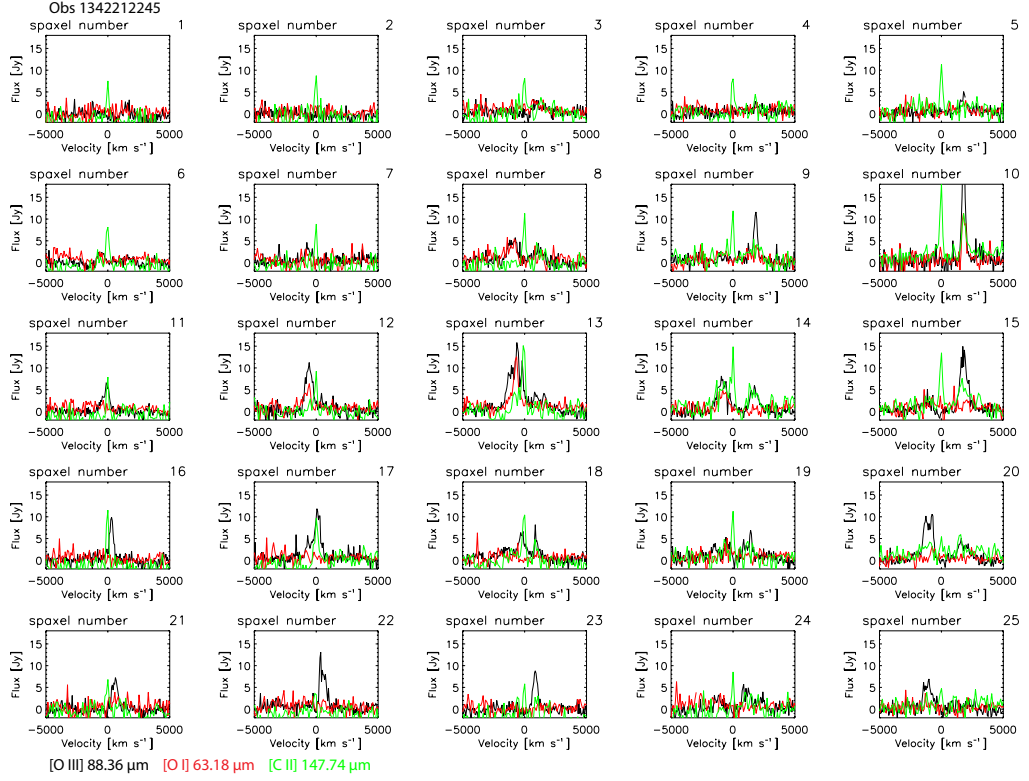


Figure 4.5. The 5x5 PACS-IFU observation SP4 of Cas A in velocity space. The black line shows the 88 μm [O III] line, the red line shows the 63 μm [O I] line and the green shows the 157 μm [C II] line.

RA	Dec	Flux
350.8830041766	58.8147052523	9.80E-18
350.8811420635	58.8106073526	1.80E-17
350.8714753377	58.8144745884	7.89E-18
350.8624284116	58.8176549156	7.88E-18

Table 4.2. The upper limits on the red shifted component of the [O I] 145 μm emission in the SP1 observations of Cas A measured by PACS-IFU

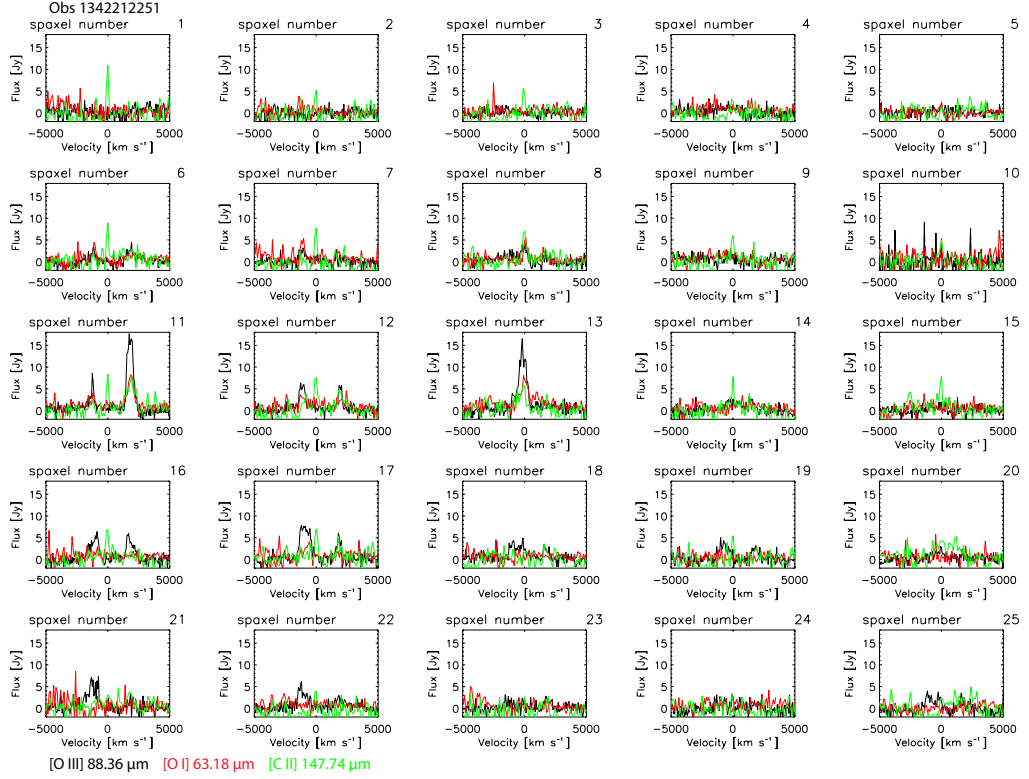


Figure 4.6. The 5x5 PACS-IFU observation SP5 of Cas A in velocity space. The black line shows the 88 μm [O III] line, the red line shows the 63 μm [O I] line and the green shows the 157 μm [C II] line.

RA	Dec	Flux
350.8763587573	58.8210604144	4.89E-18
350.8785458073	58.8191391838	1.97E-17
350.8850600699	58.8127963966	3.46E-18
350.8726196781	58.8190778149	3.73E-18
350.8811420635	58.8106073526	1.04E-18
350.8714753377	58.8144745884	2.38E-17
350.8624284116	58.8176549156	3.33E-17

Table 4.3. The upper limits on the blue shifted component of the [O I] 145 μm emission in the SP1 observations of Cas A measured by PACS-IFU

RA	Dec	Flux
350.8968227127	58.7927970741	3.92E-17
350.8986712345	58.7909393377	2.01E-17

Table 4.4. The upper limits on the red shifted component of the [O I] 145 μm emission in the SP4 observations of Cas A measured by PACS-IFU

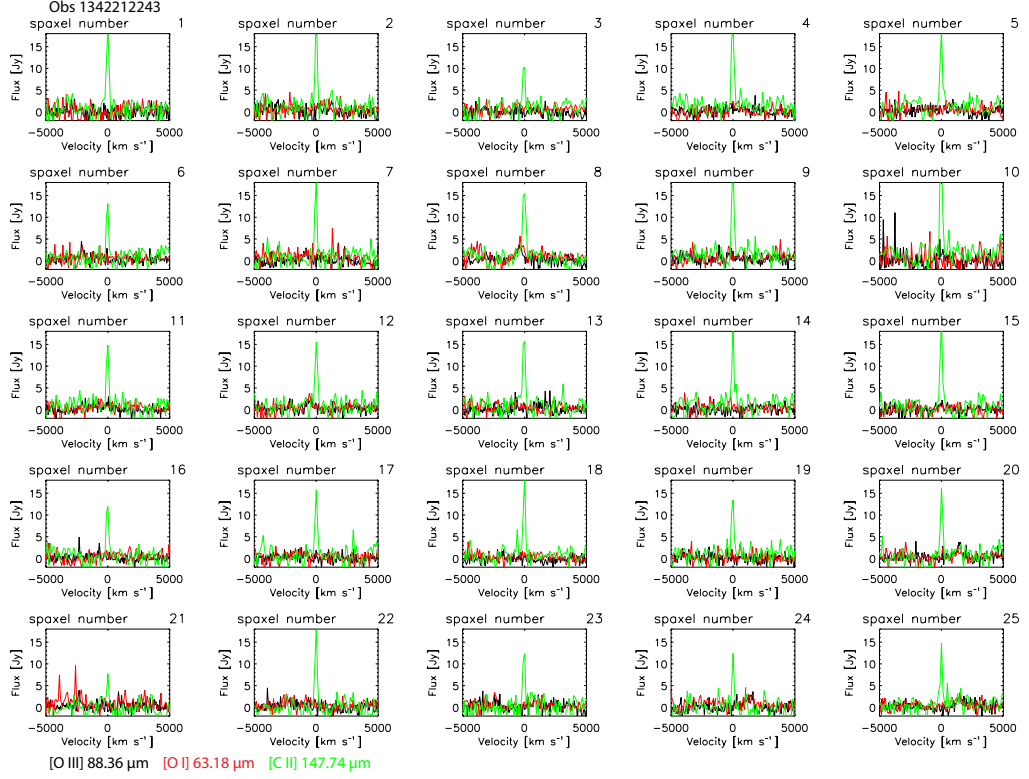


Figure 4.7. The 5x5 PACS-IFU observation SP6 of Cas A in velocity space. The black line shows the 88 μm [O III] line, the red line shows the 63 μm [O I] line and the green shows the 157 μm [C II] line.

RA	Dec	Flux
350.894666527	58.7949748759	6.10E-18
350.8968227127	58.7927970741	1.03E-18
350.8869758637	58.7969446412	4.40E-18
350.8890209363	58.7948138774	1.02E-17
350.8911321659	58.7926585358	3.90E-18

Table 4.5. The upper limits on the blue shifted component of the [O I] 145 μm emission in the SP4 observations of Cas A measured by PACS-IFU

RA	Dec	Flux
350.8644343096	58.7899062966	2.00E-18
350.8664881628	58.7877779052	3.00E-18

Table 4.6. The upper limits on the red shifted component of the [O I] 145 μm emission in the SP5 observations of Cas A measured by PACS-IFU

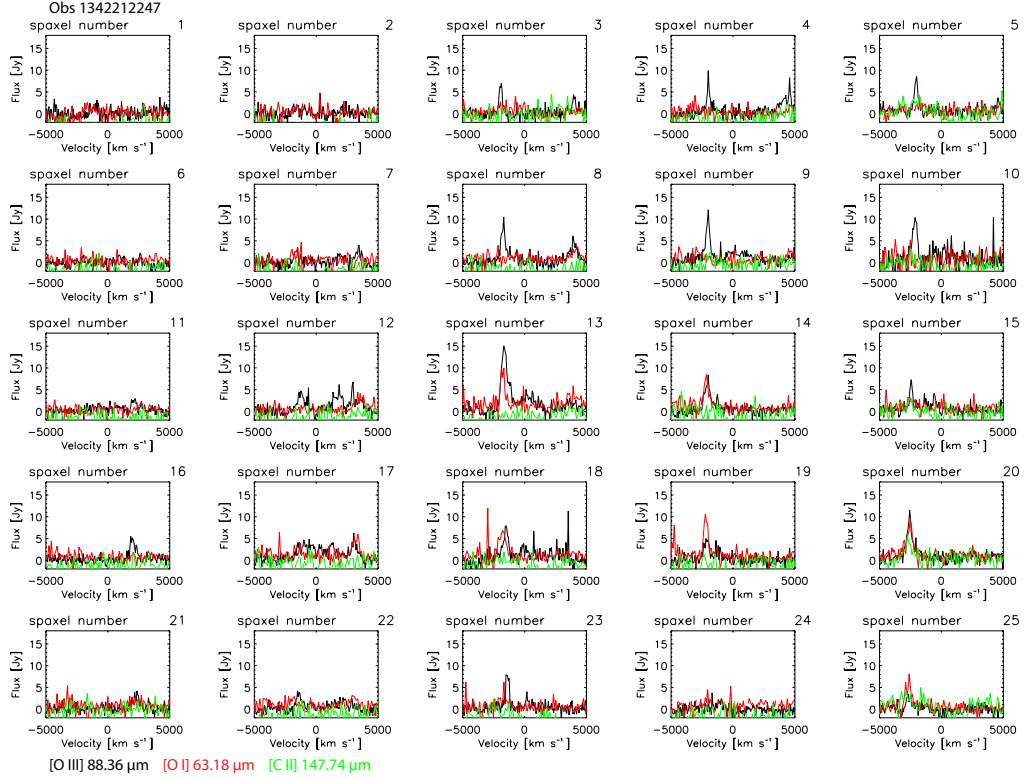


Figure 4.8. The 5x5 PACS-IFU observation SP7 of Cas A in velocity space. The black line shows the $88 \mu\text{m}$ [O III] line, the red line shows the $63 \mu\text{m}$ [O I] line and the green shows the $157 \mu\text{m}$ [C II] line.

RA	Dec	Flux
350.8594759427	58.7890197747	3.90E-18
350.8615779471	58.7868464578	8.11E-18
350.86355583589	58.7847086645	2.03E-17
350.8571245719	58.7856160718	6.07E-18

Table 4.7. The upper limits on the blue shifted component of the [O I] $145 \mu\text{m}$ emission in the SP5 observations of Cas A measured by PACS-IFU

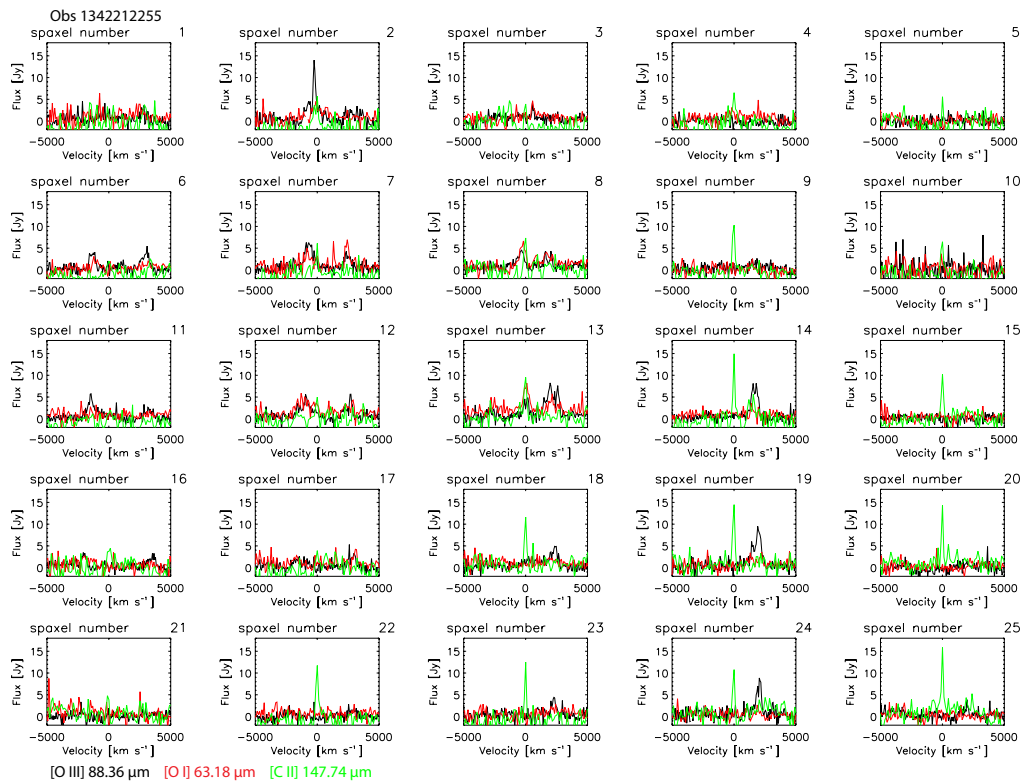


Figure 4.9. The 5x5 PACS-IFU observation SP8 of Cas A in velocity space. The black line shows the $88 \mu\text{m}$ [O III] line, the red line shows the $63 \mu\text{m}$ [O I] line and the green shows the $157 \mu\text{m}$ [C II] line.

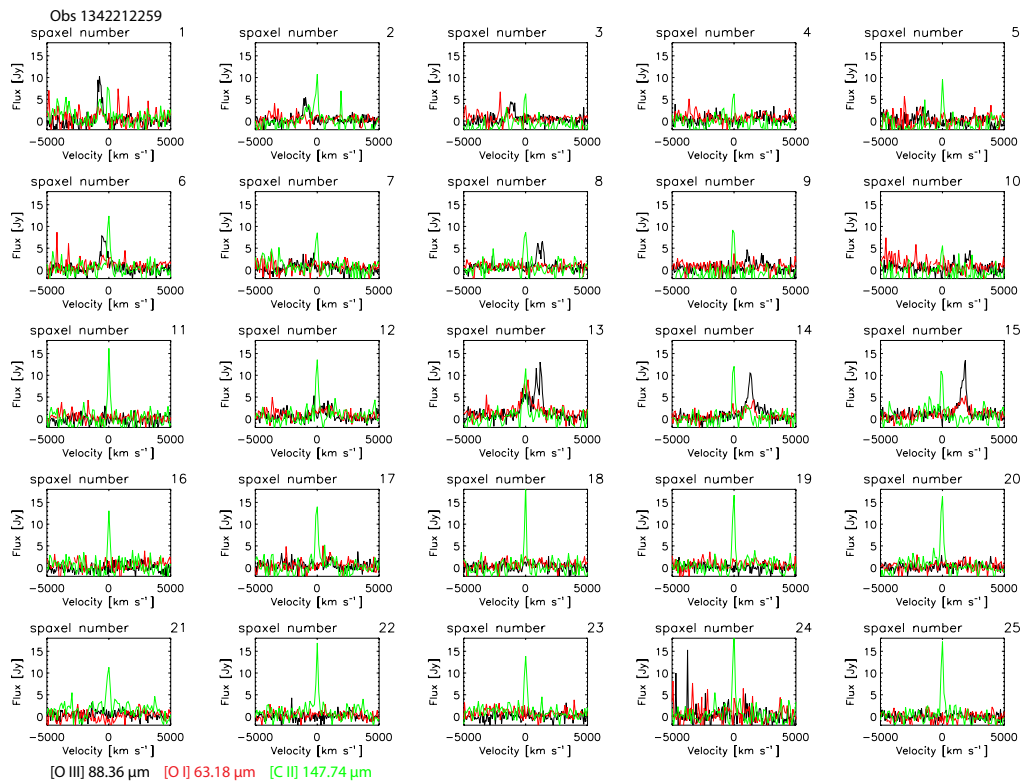


Figure 4.10. The 5x5 PACS-IFU observation SP9 of Cas A in velocity space. The black line shows the $88 \mu\text{m}$ [O III] line, the red line shows the $63 \mu\text{m}$ [O I] line and the green shows the $157 \mu\text{m}$ [C II] line.

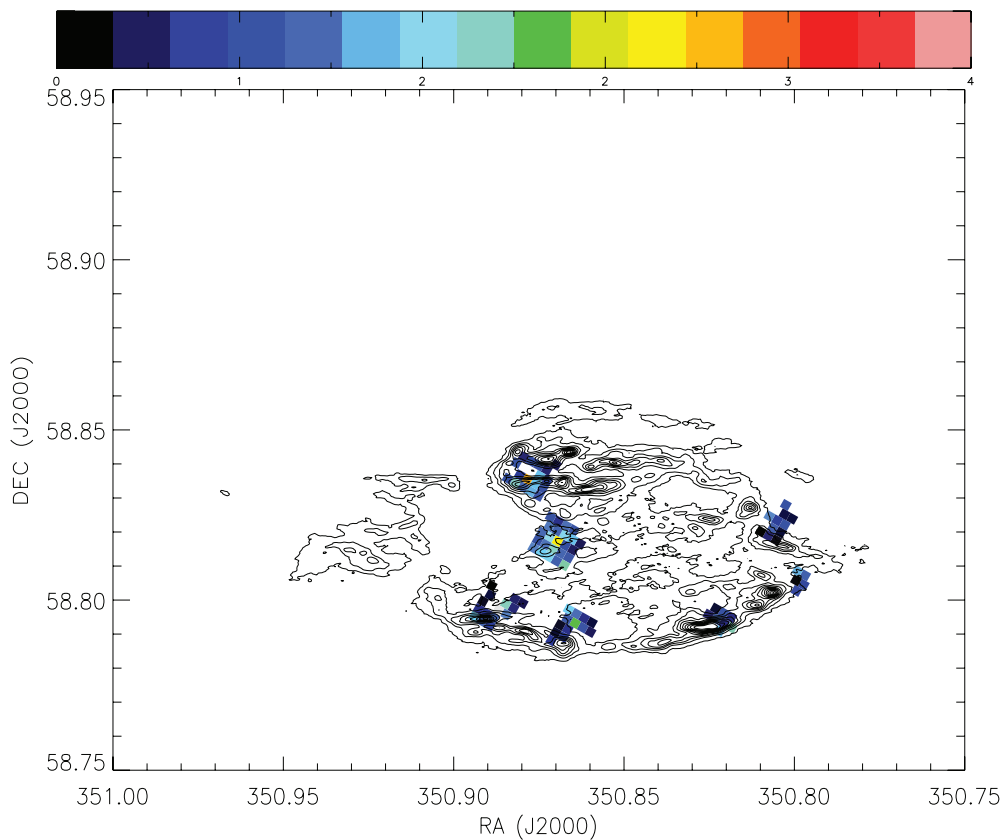


Figure 4.11. The relative flux of the red shifted emission of the [O III] 88 μm in Cas A plotted over a contour map of the PACS 70 μm image.

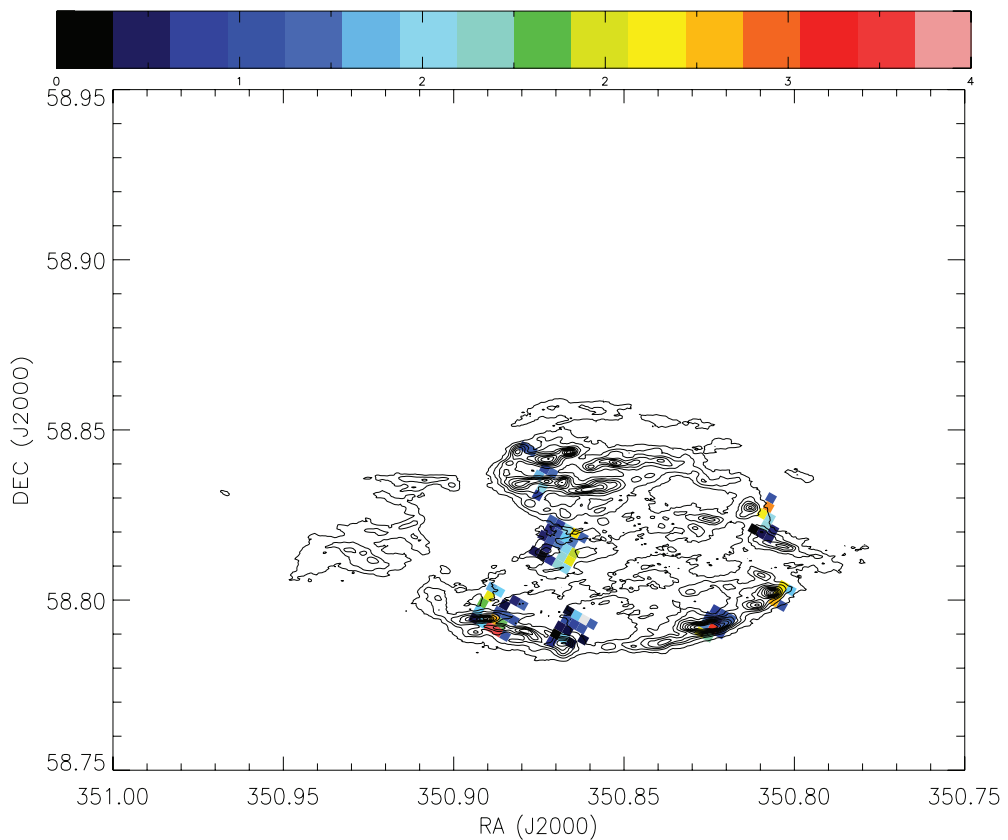


Figure 4.12. The relative flux of the blue shifted emission of the [O III] $88 \mu\text{m}$ in Cas A plotted over a contour map of the PACS $70 \mu\text{m}$ image.

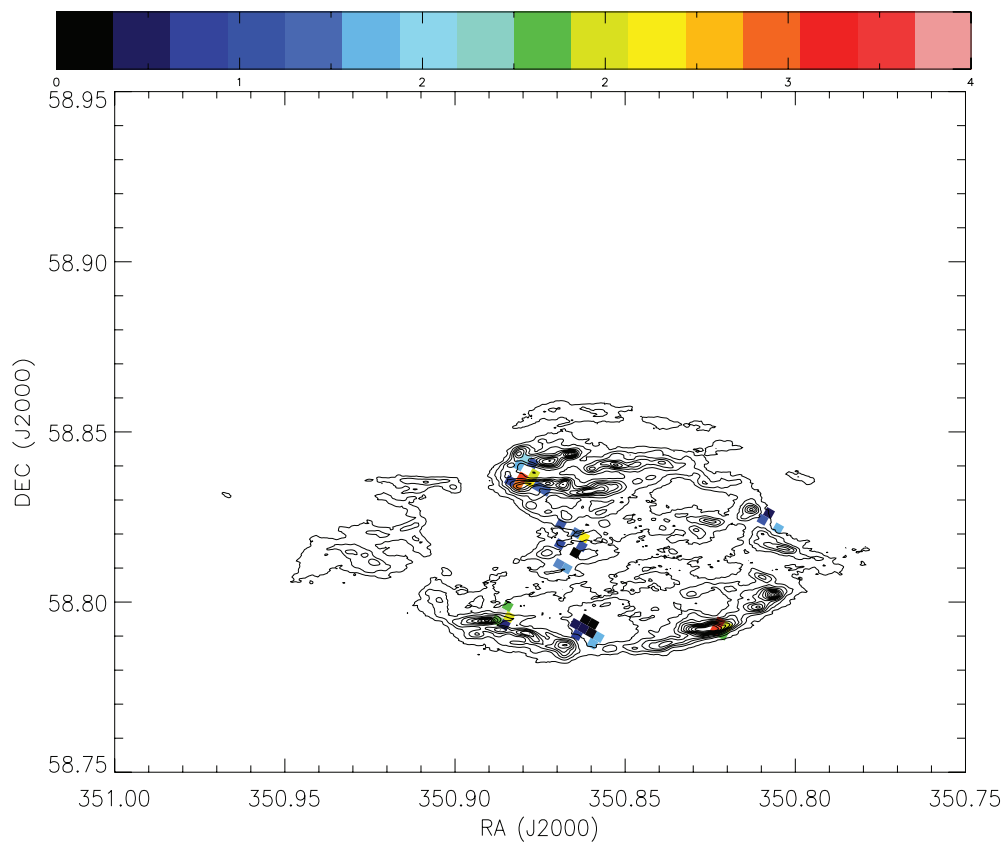


Figure 4.13. The relative flux of the red shifted emission of the [O I] 63 μm in Cas A plotted over a contour map of the PACS 70 μm image.

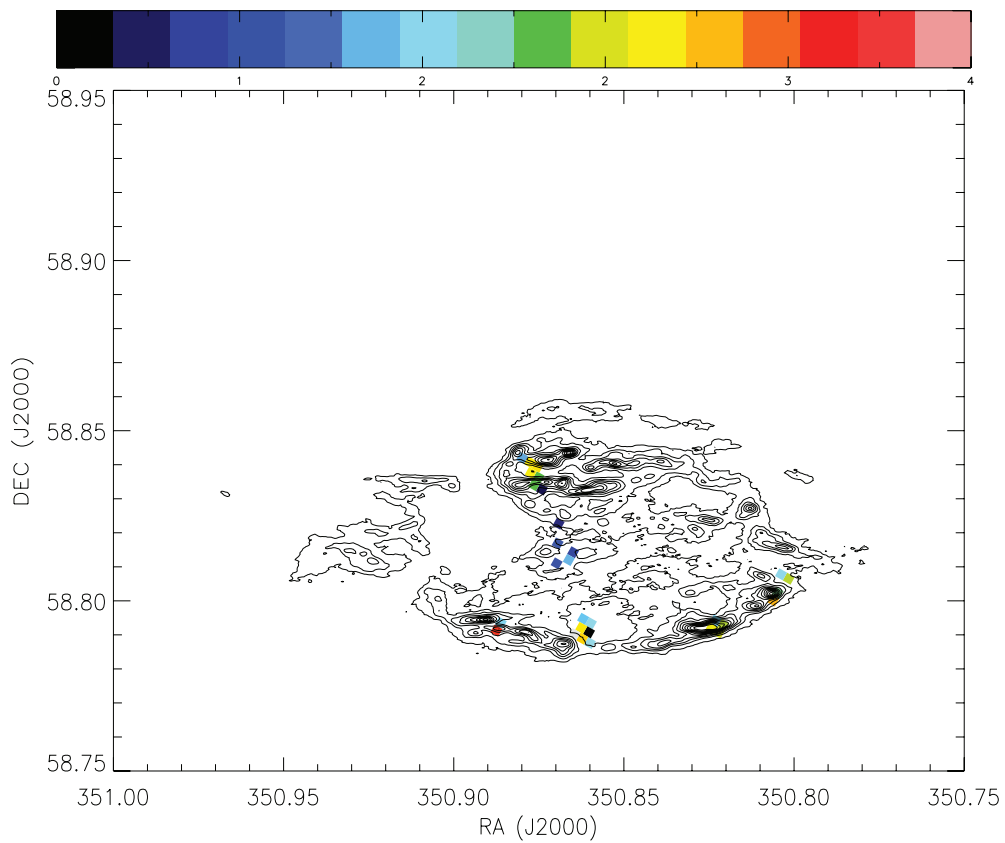


Figure 4.14. The relative flux of the blue shifted emission of the [O I] 63 μm in Cas A plotted over a contour map of the PACS 70 μm image.

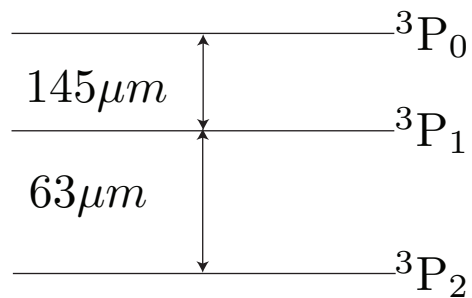


Figure 4.15. [O I] Fine-structure energy levels

RA	Dec	Flux
350.890621377	58.83448768	7.55E-18
350.8678495805	58.83422957	1.98E-18

Table 4.8. The upper limits on the red shifted component of the [O I] 145 μm emission in the SP7 observations of Cas A measured by PACS-IFU

RA	Dec	Flux
350.890621377	58.83448768	2.88E-18
350.8790856104	58.8342617396	2.12E-18
350.8812020454	58.8321071293	3.20E-18
350.8720677503	58.8355092957	8.54E-19
350.8761425978	58.8311948793	4.01E-18
350.8780441564	58.8291442994	4.45E-18
350.8678495805	58.8342295703	1.99E-18
350.8697029339	58.8321075041	2.12E-18
350.8735146164	58.8277734357	2.69E-18

Table 4.9. The upper limits on the blue shifted component of the [O I] 145 μm emission in the SP7 observations of Cas A measured by PACS-IFU

4.1.3 Carbon

Although Cas A is vastly oxygen rich, we have also detected the [C II] 157 μm line. Whilst most the observation of this line towards Cas A is narrow and slow moving and interstellar in origin, we have also detected broad lines moving at similar velocities to the oxygen lines for the first time. Figure 4.16 (red) and 4.17 (blue) show the locations of both red and blue shifted broad [C II] 157 μm line emissions in Cas A.

Small amounts of carbon are predicted to be in the remnant by Docenko & Sunyaev (2010) due to the strong 6300 Å oxygen line, which implies a charge exchange between

RA	Dec	Flux
350.8260403057	58.79509426	2.32E-18
350.8281278818	58.7929659927	2.10E-18
350.820422112	58.7949193869	1.64E-18
350.8224839402	58.7927929771	2.10E-18

Table 4.10. The upper limits on the red shifted component of the [O I] 145 μm emission in the SP8 observations of Cas A measured by PACS-IFU

RA	Dec	Flux
350.8260403057	58.79509426	2.78E-18
350.8281278818	58.7929659927	1.54E-18
350.820422112	58.7949193869	6.11E-18
350.8224839402	58.7927929771	1.32E-18

Table 4.11. The upper limits on the blue shifted component of the [O I] 145 μm emission in the SP8 observations of Cas A measured by PACS-IFU

RA	Dec	Flux
350.8042411615	58.8044410837	5.21E-18
350.8082356366	58.800207324	8.90E-18
350.8102679303	58.7980498646	2.58E-18
350.7991018882	58.8036397956	3.07E-18

Table 4.12. The upper limits on the red shifted component of the [O I] 145 μm emission in the SP9 observations of Cas A measured by PACS-IFU

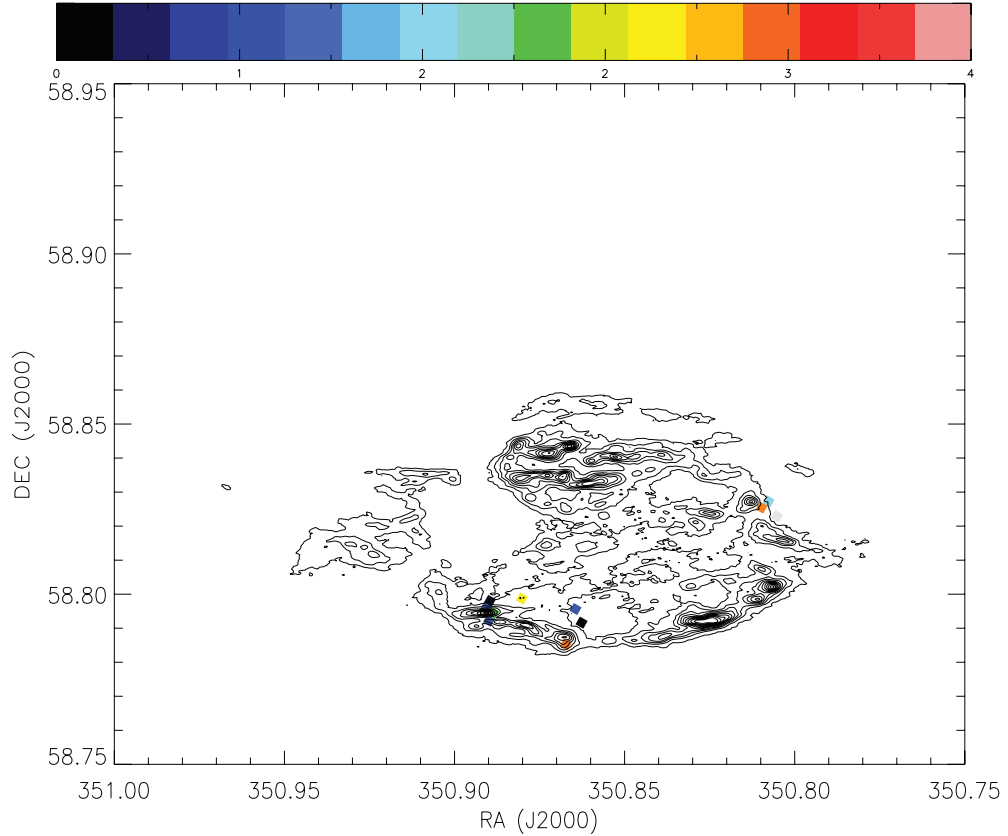


Figure 4.16. The relative flux of the red shifted emission of the [C II] 157 μm in Cas A plotted over a contour map of the PACS 70 μm image.

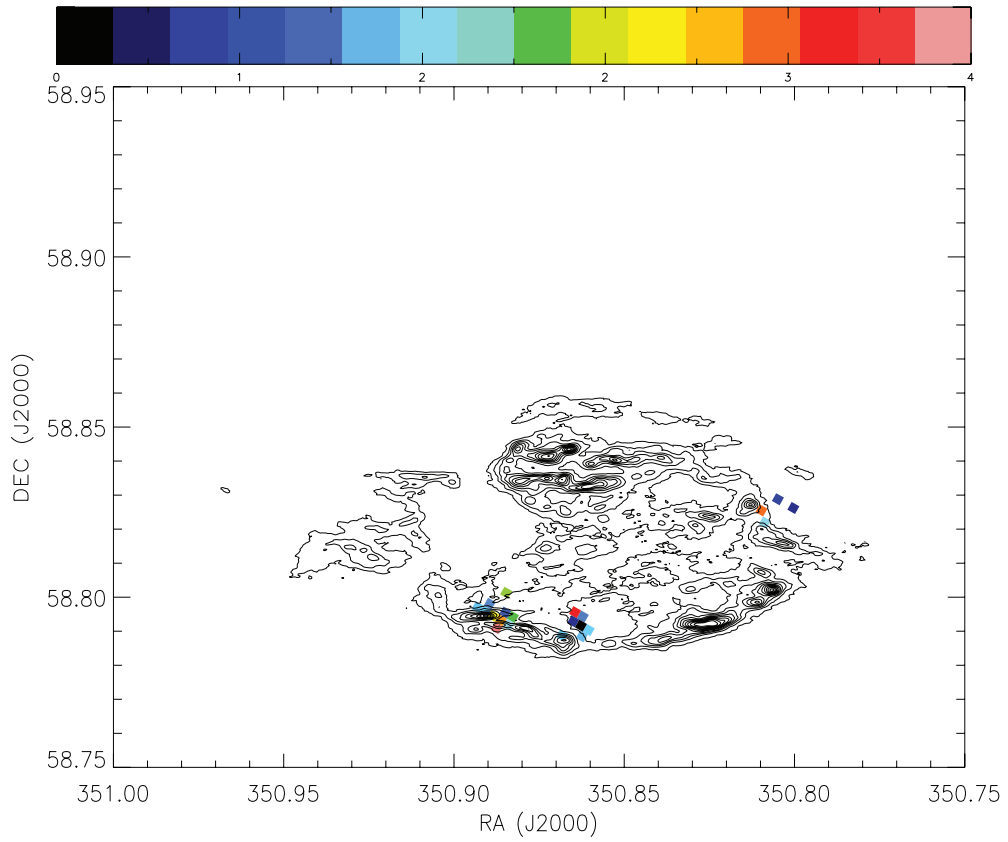


Figure 4.17. The relative flux of the blue shifted emission of the[C II] 157 μm in Cas A plotted over a contour map of the PACS 70 μm image.

carbon and oxygen. Although most of the carbon will be locked up in CO, some of it will be free as CO formation is a two way process particularly in high energy environments such as supernovae (Clayton et al. 1999).

4.2 Cas A with SPIRE

The fundamental vibrational mode of Carbon Monoxide (CO) have been observed in Cas A using *Spitzer* (Rho et al. 2009). Whilst both hot (2000 K) and cold (200 K) populations of highly rotationally excited CO have been observed with *Herschel*-PACS (Wallström et al. 2013).

Herschel SPIRE-FTS was used to observe 3 positions on Cas A on the 23rd of August 2010 using the range mode. The positions of the SSW detectors for each of these obser-

vations are shown in Figure 4.18. Data were processed using HIPE version 11.0.1 (Ott 2010b) using the standard pipeline. A polynomial was fitted to remove the continuum and then lines were fitted with a sinc function. A sinc function is used because this is the Fourier transform of a line, and is thus the instrument profile of a fourier transform spectrometer such as SPIRE-FTS.

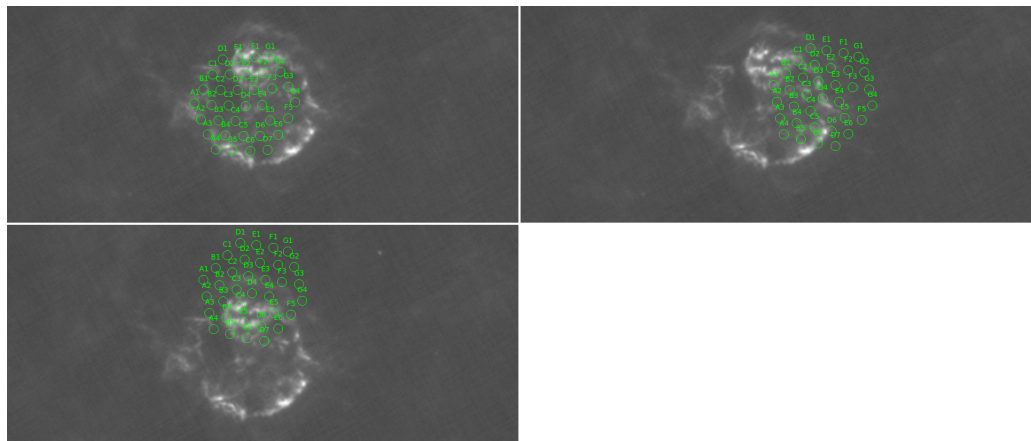


Figure 4.18. Positions of the SSW detectors of the three *Herschel* SPIRE-IFU on Cas A plotted on a 70 μm image. The "Central" observation is shown in top left, top right is the "North West" and bottom left is the "North" observation.

The majority of the SPIRE spectra contain narrow [C I] and J=5-4 and 4-3 CO lines which are interstellar in origin. However, in two detector pointings at the North of the remnant on the bright right we observed several broad, fast moving high-J CO lines. These observed in a structure related to those observed by Wallström et al. (2013) as shown in Figure 4.19 plotted on a 70 μm *Herschel* image tracing the dust. One of the SPIRE positions is coincident with the Wallström et al. (2013) and Rho et al. (2009) observations, whilst the other is in a separate structure to the north of it.

Figure 4.20 is a rotation population diagram of the CO observed with SPIRE-FTS detector SSWC4 using the technique described in section 2.5. The best fit parameters for this give a CO rotation temperature of 305 ± 15 K and assuming a knot size of 0.5" (Rho et al. 2009; Wallström et al. 2013) a column density of $8.7 \pm 0.5 \times 10^{16} \text{ cm}^{-2}$. This is comparable with the values determined for the adjacent region by Wallström et al. (2013), although both temperature and column density are lower.

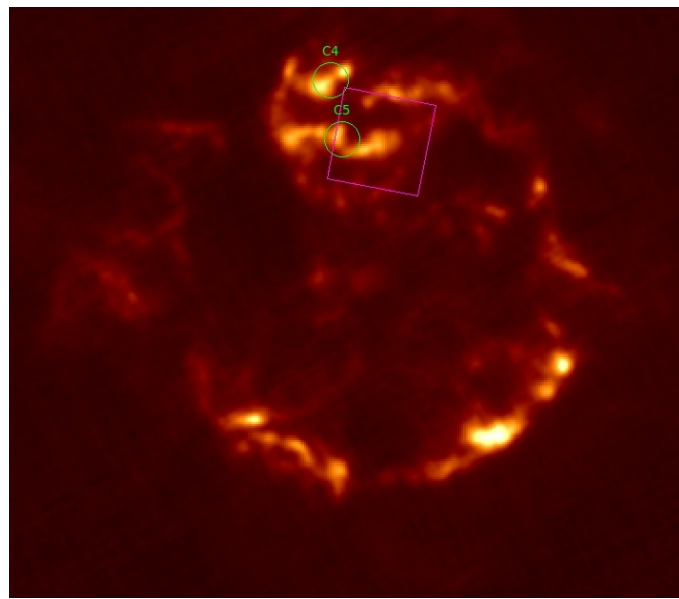


Figure 4.19. Positions on Cas A of the regions where CO is detected by SPIRE. Also included the PACS CO detections of Wallström et al. (2013) plotted on a 70 μm image.

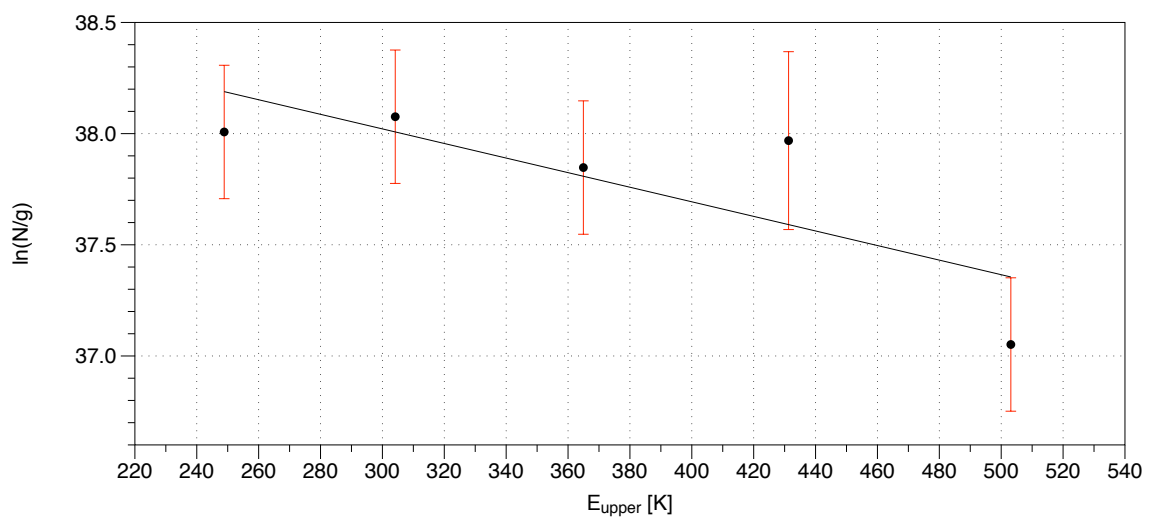


Figure 4.20. A CO population to determine temperature and column density using Herschel SPIRE-FTS observations of Cas A-NW with detector SSW C4.

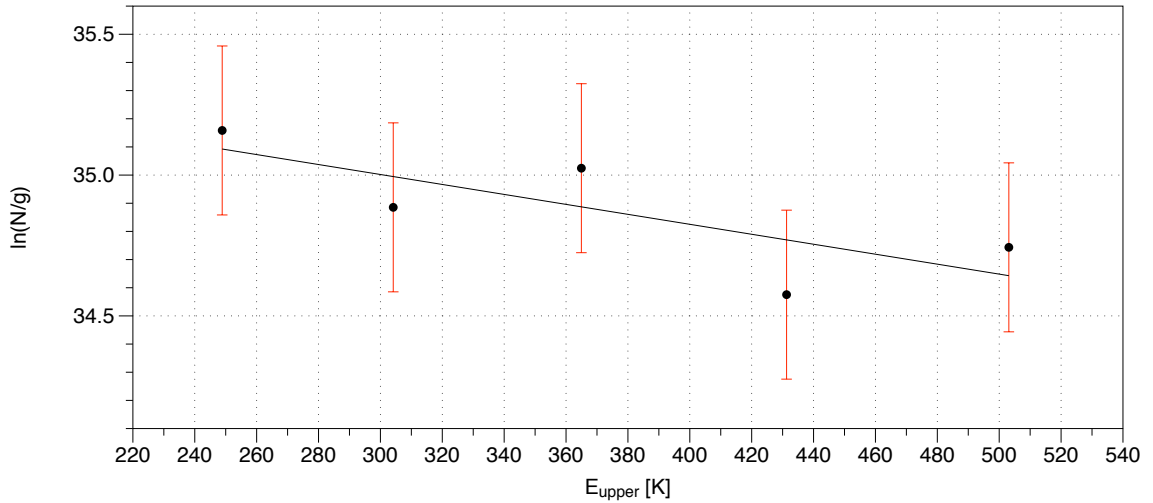


Figure 4.21. A CO population to determine temperature and column density using Herschel SPIRE-FTS observations of Cas A-NW with detector SSW C5.

Figure 4.21 is a rotation population diagram of the CO observed with SPIRE-FTS detector SSWC5. This is the detector that is coincident with the Rho et al. (2008) and Wallström et al. (2013) observations of Cas A. The rotational temperature is determined to be 554 ± 25 K with a column density of $4.0 \pm 0.5 \times 10^{17}$ cm $^{-2}$ which is entirely in agreement with Wallström et al. (2013).

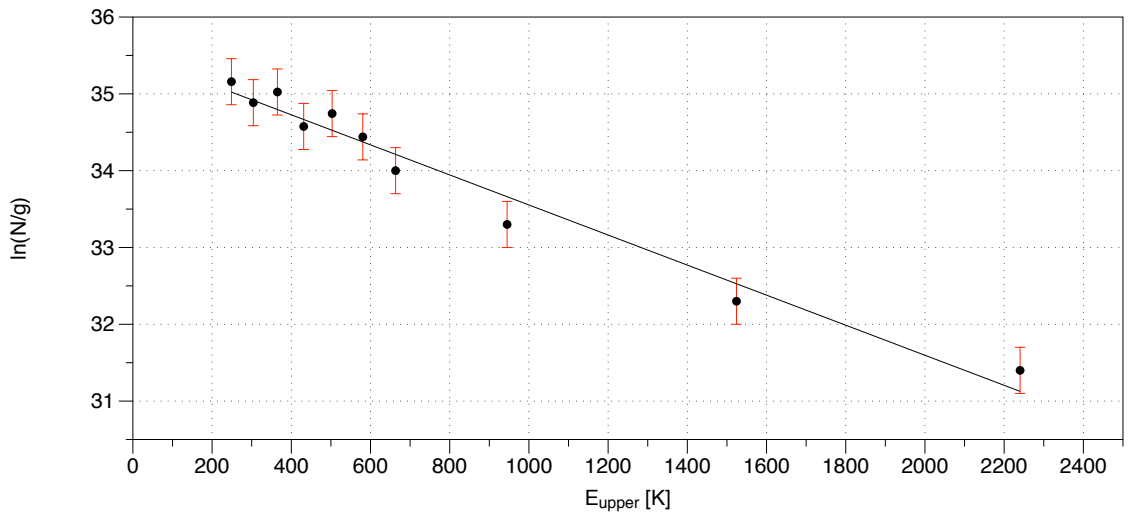


Figure 4.22. A CO population to determine temperature and column density using Herschel SPIRE-FTS observations of Cas A-NW with detector SSW C5 and the *Herschel* PACS observations from Wallström et al. (2013).

Figure 4.22 shows the same observations and also includes the Wallström et al. (2013)

observations. The best fit parameters for the temperature without the Wallström et al. (2013) observations is 540 ± 25 K with a column density of $4.3 \pm 0.5 \times 10^{17}$ cm $^{-2}$.

4.3 CO and Carbon

The regions of the nebula in which the CO is detected and those in which the [C II] lines are observed are completely different as shown in Figure 4.23. The carbon in the region with the CO will be locked up in the CO while CO is yet to form or reform after shock interactions in the regions when the [C II] lines are observed.

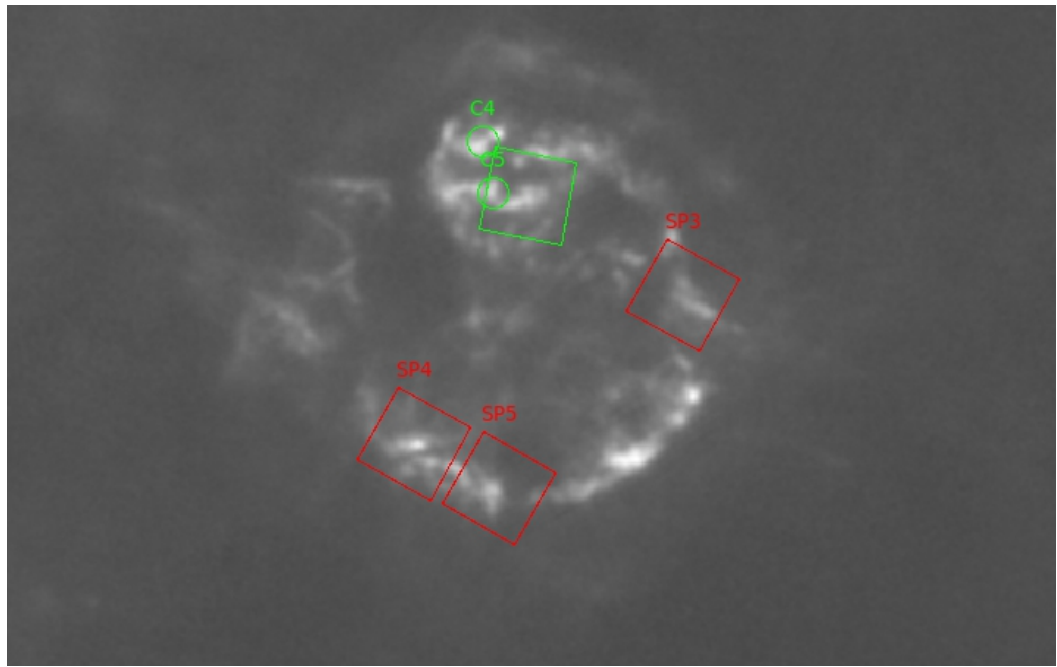


Figure 4.23. *Herschel* PACS 70 μm map of Cas A with the regions with where CO has been detected shown in green and the regions where the [C II] lines have been observed shown in red.

4.4 Dust in Cas A

As discussed in Section 2.3.3, approximately $0.1 M_{\odot}$ of dust has been observed in Cas A with *Herschel* and *Spitzer* (Barlow et al. 2010). Investigating where this dust was formed and how it may be heated is of great interest in understanding the evolution of dust in supernova remnants, and this dust's eventual survival into the interstellar medium.

4.4.1 NuSTAR

NuSTAR (Nuclear Spectroscopic Telescope Array) is a space-based X-ray telescope operating in the range of 5 to 80 keV. 1.2 mega seconds of observations of Cas A have been made using it. which have been used the map the radioactive ^{44}Ti within the remnant shown in Figure 4.24 . These data were originally used to prove that core collapse supernovae are asymmetric and that a large amount of "sloshing" happens during the explosion (Grefenstette et al. 2014).

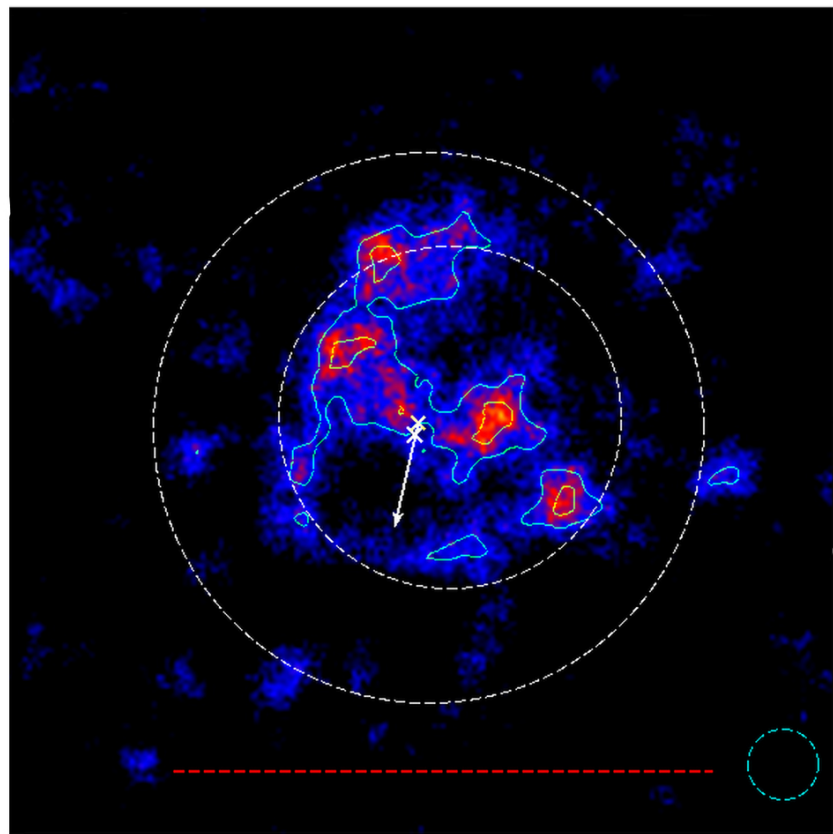


Figure 4.24. ^{44}Ti map of Cas A made with the NuSTAR telescope taken from (Grefenstette et al. 2014).

^{44}Ti decays via electron capture ^{44}Sc with a half life of 60 Years. Electron capture is a process by which a proton rich nucleus can capture one of its own inner electrons to decay. This gap, usually in the K or L shell left by the captured electron often also leads to the emission of an Auger electron with energy 3.45-4.48 keV for K shell and 0.3-0.5 keV for L shell electrons (Bé et al. 2013). ^{44}Sc is also radioactive and decays to ^{44}Ca by emitting a 595.8 keV positron or by electron capture with a branching ratio of 94.27% to 5.73%

(Bé et al. 2013), these process has a half life of 3.97 hours. Its K shell auger electrons have energies from 3.123-3.987 keV. ^{44}Ca is stable. These processes mean that there are highly energetic electrons and positrons as well as lots of γ -rays present in the region with the ^{44}Ti . While this radiation is too high energy to interact with the dust directly, it is highly ionising, which will produce lots of heavy ions and free electrons which are capable of destroying dust.

4.4.2 Comparisons of the NuSTAR and Herschel images of Cas A

Figure 4.25 shows the NuSTAR ^{44}Ti overlaid on the PACS 70 μm map, both as a colour and contour plot as well as the individual maps for comparison. The strongest ^{44}Ti emission is in the regions where there is no dust emission, implying that the strong radiation field from the ^{44}Ti is either destroying, preventing the formation of, or very efficiently heating the dust.

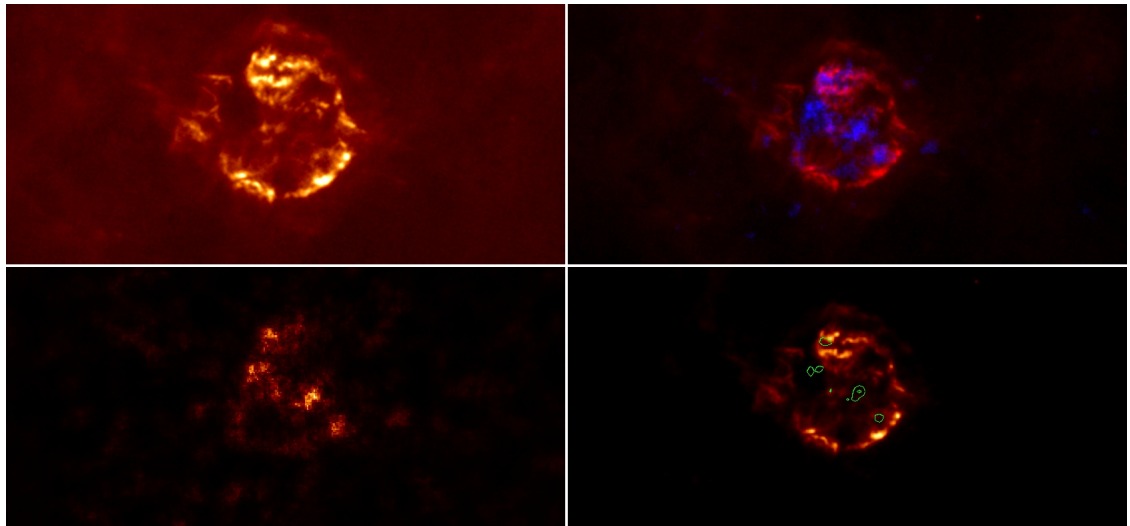


Figure 4.25. The top left is the *Herschel* PACS 70 μm map, the bottom left is ^{44}Ti map of Cas A made with the NuSTAR telescope taken from (Grefenstette et al. 2014). The top right is the ^{44}Ti in blue over the PACS 70 μm dust emission in red and the bottom right is the PACS 70 μm dust emission with the ^{44}Ti shown as contours in green.

4.5 Conclusions

Cassiopeia A was observed with Herschel PACS and SPIRE Spectrometers. Unfortunately the lower end of the PACS-IFU not going short enough to detect the 52 μm [O III] line

means that the electron density can not be estimated using the diagnostics discussed in the previous chapter. The 158 μm [C II] line was observed for the first time in Cas A in the south of the remnant, while Carbon Monoxide has been observed with SPIRE, as well as previous observations (Wallström et al. 2013; Rho et al. 2009) in the north of the remnant showing. The 63 μm [O I] line is also observed, the 145 μm [O I] line is not, so upper limits are determined for its observation based on the velocity, and line width of the 63 μm [O I] line and the noise in the PACS data around 145 μm . The ratio of 63 μm to 145 μm [O I] observed can not be explained using thermal excitation alone as to get the strength of 63 μm observed with the upper detection limit of the 145 μm [O I] line would require temperature of 80 K, this is far too low for even the neutral region of the remnant, so shock processes must be involved.

Analysis of the CO lines observed with SPIRE using rotation diagrams is consistent with previous observations from Wallström et al. (2013) giving a temperature of 460 K and a column density 10^{17} cm^{-2} . We could not perform a more detailed non LTE analysis using a code such as RADEX as they all assume that the collision partner is hydrogen. Cas A is so oxygen rich that it, rather than hydrogen will be the collision partner and data does not exist for collisions between oxygen and CO.

Cas A was also observed with the NuSTAR γ -ray telescope (Grefenstette et al. 2014).

Chapter 5

Dust in the Crab Nebula

You've got to make the dust before you can destroy it

Mike Barlow

Mid infrared estimates of dust mass using *Spitzer* found minimal amounts of dust in the Crab Nebula supernova remnant. Temim et al. (2006) found $0.001\text{--}0.01 M_{\odot}$ of dust, which was later refined to an even lower $2.4 \times 10^{-3} M_{\odot}$ using *Spitzer* MIPS spectroscopy rather than relying purely on photometry (Temim et al. 2012).

These observations did not have either the resolution or the far infrared information needed to accurately measure the dust mass. Gomez et al. (2012) presented far infrared dust emission data from *Herschel* along with observations from the *Planck* point sources in the sub-mm and mm wavelength ranges which were used to more tightly constrain the synchrotron background than any previous measurements of dust mass. Using these data, along with Spitzer and WISE (Wide-field Infrared Survey Explorer), allowing an estimate of the total dust mass in the remnant for the first time. They found between 0.1 and $0.3 M_{\odot}$ of dust, depending on the grain species assumed.

The Crab Nebula is rare among supernova remnants as it is photo-ionized by synchrotron emissions from wind driven by the central pulsar. This means that it can be

successfully modelled using photo-ionization codes which allow this clumpy density distribution and a more accurate temperature profile and grain size distribution to be treated.

Dust absorbs light in the UV and optical regimes. This heats the dust which then causes it to emit light in the far infrared. This infrared emission leads to an excess over the continuum. By observing and fitting to this infrared excess it is possible to quantify the mass of dust in an object. This is normally done by fitting a modified black body curve to the emission and using the equation

$$M_d = \frac{S_\nu D^2}{\kappa_\nu B(\nu, T)} \quad (5.1)$$

where S_ν is the flux density, D is the distance, κ_ν is the dust mass absorption coefficient (which is calculated from the dust emissivity and the density of the dust grains) and $B(\nu, T)$ is the Planck function. Different temperature grains can be considered by using multiple Planck functions. This in turn can be considered analogous to different grain sizes as smaller grains are more easily heated and are thus warmer. Observational fits typically use two temperature components; one for warm dust and one for cold dust. Regardless of how many different temperature components are used, this method does not take in to account how the dust is heated and assumes that each grain of the same size is the same temperature. This method also does not consider the location of the dust, assuming it to be isotropically distributed. If the dust is contained within dense clumps, rather than smoothly distributed though out the nebula then the dust on the outside of the clumps will absorb all the heating photons. This will mean that the dust further in to the clumps is heated less. This means it will emit less which in turn means that a higher mass of dust will be needed to give the observed emitted flux. Figure 5.1 is a composite Hubble Space Telescope and *Herschel* 70 μm image showing the dust emission closely aligned with the optical knots and filaments in thus not homogeneously distributed throughout the nebula.

There are several different species of dust in the interstellar medium. The two main types are amorphous carbon and silicate grains. For each of these species there are several sets of optical constants, available determined using different experimental techniques and theoretical models. Amorphous carbon is an umbrella term used for grains made of car-

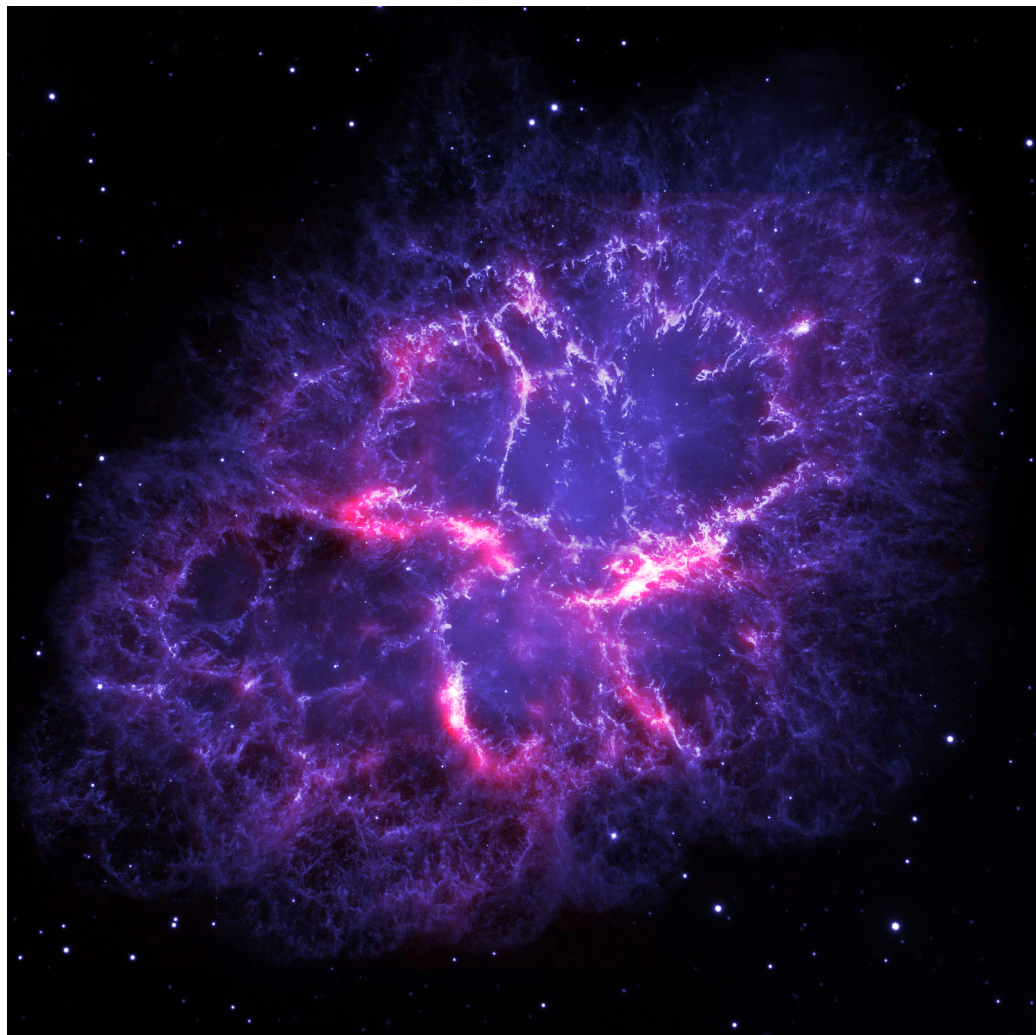


Figure 5.1. A composite HST and *Herschel* 70 μm image showing the dust emission closely tied to the optical knots and filaments.

bon and hydrocarbon chains. Silicate grains are made up of several compounds containing silicon and oxygen. They are more reflective than carbon grains thus absorb less and so emit less. This means that typically more silicate dust is required to fit the Infrared excess emission. Which species of dust dominates depends on the elemental abundances and chemistry in the region.

5.1 The Model

MOCASSIN (Ercolano et al. 2003, 2005, 2008) is a fully validated 3D photo-ionization and dust radiative transfer code. It allows for arbitrary geometries for gas and dust, multiple or diffuse radiation sources with a given input spectrum, multiple dust grain species and a specified grain size distribution. With these parameters it self consistently solves the equations of radiative transfer to calculate the degree of ionisation, electron and dust grain temperatures in each cell as well as an overall spectral energy distribution (SED) of the whole region being modelled. Using MOCASSIN 2.02.70 we have constructed a model of the Crab Nebula to determine the mass of dust formed in its ejecta by fitting to the observed far infrared excess in the SED (Temim et al. 2006; Gomez et al. 2012; Planck Collaboration 2011) and optical line fluxes (Smith 2003).

5.1.1 Geometry and Spectrum

The general geometry of the model is an ellipsoid with a major axis of 4.0 pc and a minor axis of 2.9 pc (Hester 2008). The ionizing input spectrum for the synchrotron emission of the Pulsar Wind Nebula is adapted from a digitized version of the spectrum in Hester (2008). The sub-millimeter part of the spectrum needed to be lowered slightly to be consistent with Planck observations in that wavelength range (Planck Collaboration 2011) as shown in Figure ???. It is a much smoother spectrum than the one many models use which are taken from the Davidson & Fesen (1985) parametrization. This fits three power laws to different parts of the spectrum and misses out the ultraviolet region where a large number of the ionizing photons are emitted. This spectrum is used to provide diffuse heating source with an integrated luminosity of 1.3×10^{38} erg s $^{-1}$ (Hester 2008). This photon source heats the dust radiatively rather than assuming a given temperature for a each grain size or that all grains are the same temperature. Rather than using a point source, the photon packets are emitted from a diffuse source occupying the middle two thirds of the ellipsoid to better simulate the synchrotron emission from the pulsar wind nebula.

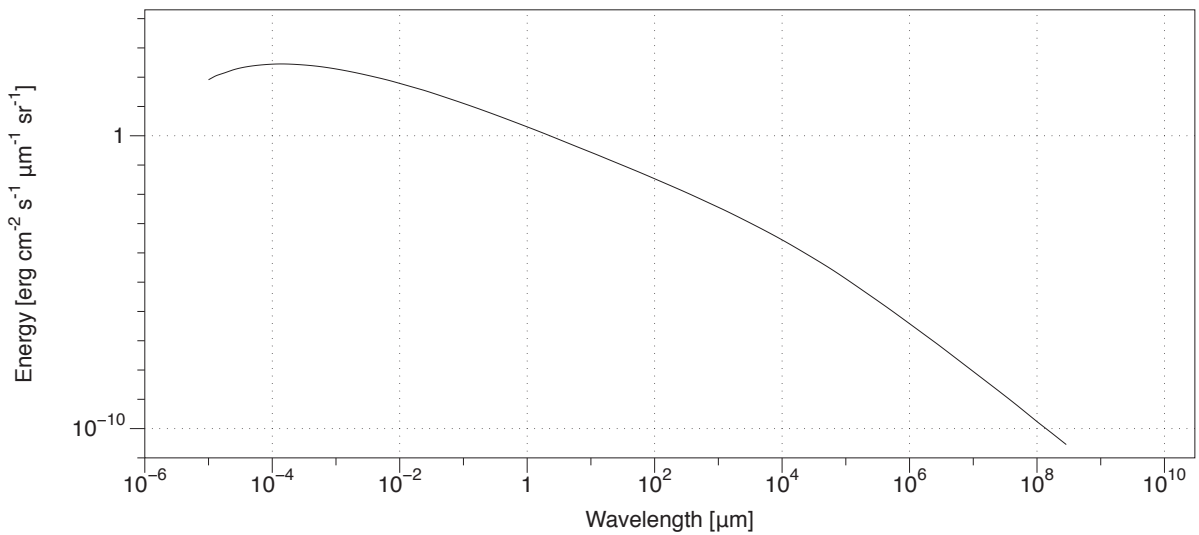


Figure 5.2. The input Spectrum used to heat the dust and ionise the gas, taken from Hester (2008) and adjusted for Planck Collaboration (2011) in the sub-mm.

5.1.2 Spectral Energy Distribution

The model is fitted to the infrared spectral energy distribution with observations made by *Spitzer* from Temim et al. (2006), *Herschel* from Gomez et al. (2012) and *Planck* from Planck Collaboration (2011) observatories. The 24, 70 and 100 μm points have been corrected for line emissions. A list of fluxes can be found in Table 5.1. Fitting is done by assuming that the uncertainty in each observed point is gaussian and sampling randomly within this range to generate 1000 points. These are all then compared to the modelled SED thus taking in to account the uncertainties in each of the observed points. The set of parameters with the lowest mean χ^2 is taken to be the most likely. The dust parameters that are varied to fit the SED are the mass of dust, the maximum and minimum grain size and the slope of the power law that characterises the distribution of grain sizes.

5.1.3 Optical Lines

As well as fitting to the photometric fluxes, de-reddened optical lines from Smith (2003) are used. Matching these lines gives confidence that chemical abundances and densities are correct as well as giving a handle on the filling factor and ratio of material in the clump and inter-clump medium in the clumpy model.

Wavelength (μm)	Flux (Jy)	Uncertainty (Jy)	Instrument
3.6	12.68	0.22	<i>Spitzer</i>
4.5	14.4	0.26	<i>Spitzer</i>
5.8	16.8	0.1	<i>Spitzer</i>
8	18.3	0.13	<i>Spitzer</i>
24	46.4	8.0	<i>Spitzer</i>
70	202.37	20	<i>Herschel</i>
100	196.48	20	<i>Herschel</i>
160	141.8	15	<i>Herschel</i>
250	103.4	7.2	<i>Herschel</i>
350	102.4	7.2	<i>Herschel</i>
350	99.3	2.1	<i>Planck</i>
500	129	9.0	<i>Herschel</i>
550	117.7	2.1	<i>Planck</i>
850	128.6	3.1	<i>Planck</i>
1382	147.2	3.1	<i>Planck</i>

Table 5.1. Integrated Fluxes for the Crab Nebula. *Spitzer* data are taken from Temim et al. (2006), *Herschel* data are taken from Gomez et al. (2012) and *Planck* data are taken from Planck Collaboration (2011).

Starting with the abundances taken from MacAlpine & Satterfield (2008), with a modified helium abundance to take in to account free-free interactions (Gomez et al. 2012), the lines were matched by first matching the H_β flux by varying the electron density. The abundances of metals are then iteratively adjusted to change the amount of cooling in order to match the observed line fluxes.

5.1.4 Grain species and optical properties

The Crab Nebula is a carbon rich nebula and there is no feature in its spectrum at 20 μm which would be caused by the Si-O bond vibrations in silicate grains so we focus on carbonaceous grain species. As well as fitting several sets of amorphous carbon dust optical properties and graphite we do fit one set of silicate optical constants. Silicates tend to require more dust than amorphous carbon grains as they are lighter in colour and thus reflect and scatter more rather than absorbing and heating up to re-emit. Graphite dust being even darker than other carbon species requires less.

As well as investigating different species of dust, each species have multiple sets of optical constants. The optical constants are the real and imaginary parts of the refraction index.

$$\tilde{n}(\lambda) = n(\lambda) - ik(\lambda) \quad (5.2)$$

where n is the refractive index and k is the absorption index. These govern how much light at a given wavelength is absorbed and how much is scattered by a dust particle. There are several different sets of these constants available for difference species of cosmic dust based on sets of laboratory experiments to determine the wavelength dependent extinction coefficients of materials similar to those considered as constituents of dust. Earlier sets of amorphous carbon we based on inconsistent sets of laboratory data (e.g. Rouleau & Martin (1991) using the data sets from Bussoletti et al. (1987)). The more recent sets of optical constants using self consistent data sets (e.g. Zubko et al. (1996) using the data from Colangeli et al. (1995)) are likely to be more reliable. Most sets of optical constants also provide multiple sets of constants for the cosmic dust analogues produced in different ways. Usually two methods are used: one involving electrical discharge through a carbon electrode (AC) and another burning benzine samples (BE). The optical constants determined from these different methods of preparing dust analogues also have very different optical properties. Optical properties used here are the ACAR and BE samples from Zubko et al. (1996) and those from Rouleau & Martin (1991) and Hanner (1988) for amorphous carbon and Draine & Lee (1984) for silicates and graphite.

The dust analogue used for determining these optical properties that is most like the dust thought to be formed in supernovae is the Zubko et al. (1996) BE sample. It is highly graphitic and formed in a more chemically reactive environment, closer to that of a supernova than the ACAR samples (Colangeli et al. 1995).

The Zubko et al. (1996) optical constants have no data points shorter than 500 Å(0.05 μm). As the majority of the energy is emitted in this range, the constants have been extended by using data from Uspenskii et al. (2006) where the data from the Zubko et al. (1996) finishes. Special attention is paid to the data at around 4.4 nm, where the carbon k-edge is. The K-edge is the point at which there is a sudden increase in the attenuation

coefficient of photons occurring at a photon energy just above the binding energy of the K shell electron of the atoms. It is caused by the photoelectric absorption of photons. The optical constants from Rouleau & Martin (1991) do not have any data points longer than $300 \mu\text{m}$. These data are extended by fitting power laws to the n and k data from $10\text{-}300 \mu\text{m}$ as they change smoothly over this range. These extrapolations can be found in Appendix ??.

As well as the models based on single grain species, a model using multiple grain species is run. The ratios of amorphous carbon to silicates used are based on the constraints imposed by the nucleosynthesis models using the Zubko et al. (1996) BE amorphous carbon and Draine & Lee (1984) silicate optical properties.

5.1.5 Density distributions

Four separate dust and gas distributions are considered:

- I. smooth distribution where all gas and dust is isotropically distributed throughout the ellipsoid. The electron density $N_e = 775 \text{ cm}^{-3}$ is selected so the modelled H_β flux matches observed flux shown in Figure 5.3.

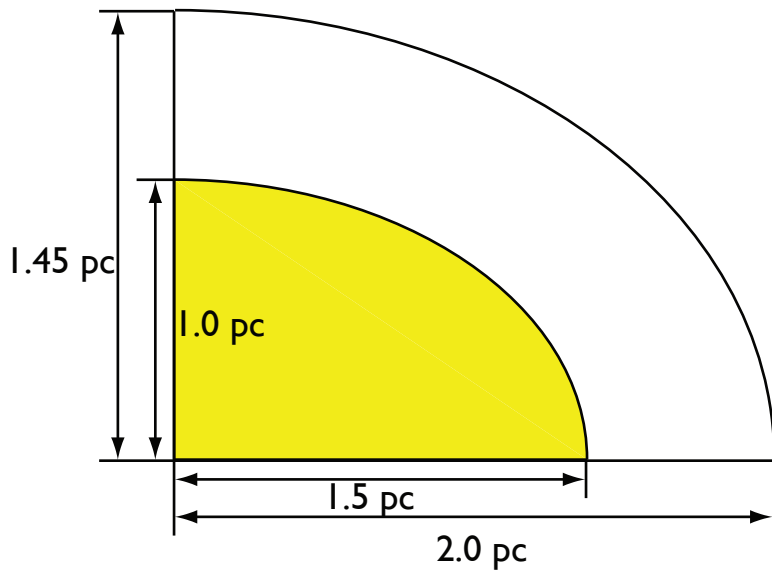


Figure 5.3. A cartoon schematic of the geometry I

- II. a smooth shell distribution where all the gas and dust is isotropically distributed in a shell in the outer third of the ellipsoid. This means that all the gas and dust are outside the ionising source. $N_e = 850 \text{ cm}^{-3}$ is selected so the total modelled H_β flux matches observed flux shown in Figure 5.4.

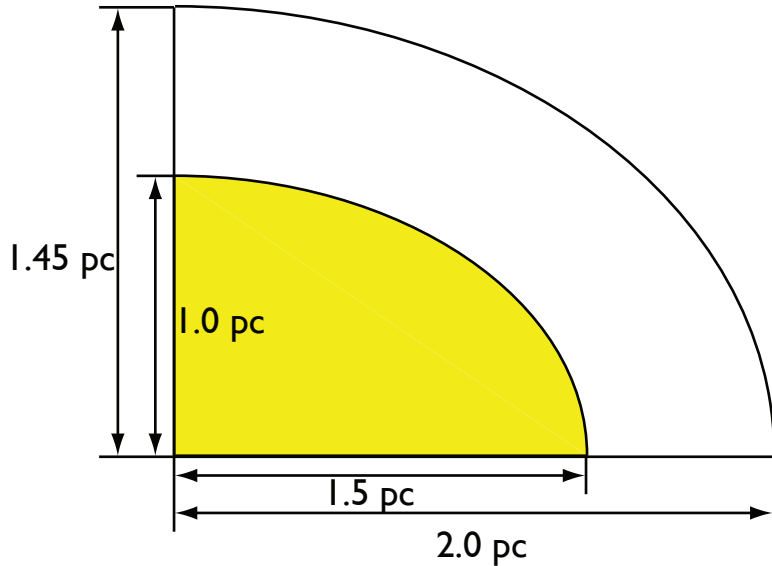


Figure 5.4. A cartoon schematic of the geometry II

- III. a smooth shell distribution where the gas and dust are isotropically distributed in a shell of 0.5 pc thickness at a radius of $1.05 \times 0.7 \text{ pc}$, entirely inside the ionising radiation source in agreement with Davidson & Fesen (1985). A density of 850 cm^{-3} is selected to match total modelled H_β flux matches observed flux
- IV. a smooth shell distribution where the gas and dust are isotropically distributed in all the way to the edge of the nebula starting at a radius of $1.05 \times 0.7 \text{ pc}$, entirely inside the ionising radiation source in agreement with Davidson & Fesen (1985). A density of 550 cm^{-3} is selected to match total modelled H_β flux matches observed flux. A cartoon schematic is shown in 5.6
- V. a smooth shell distribution where the gas and dust are isotropically distributed in all the way to the edge of the nebula starting at a radius of $1.15 \times 0.85 \text{ pc}$, entirely inside the ionising radiation source in agreement with Lawrence et al. (1995). A density of 650 cm^{-3} is selected to match total modelled H_β flux matches observed flux. A

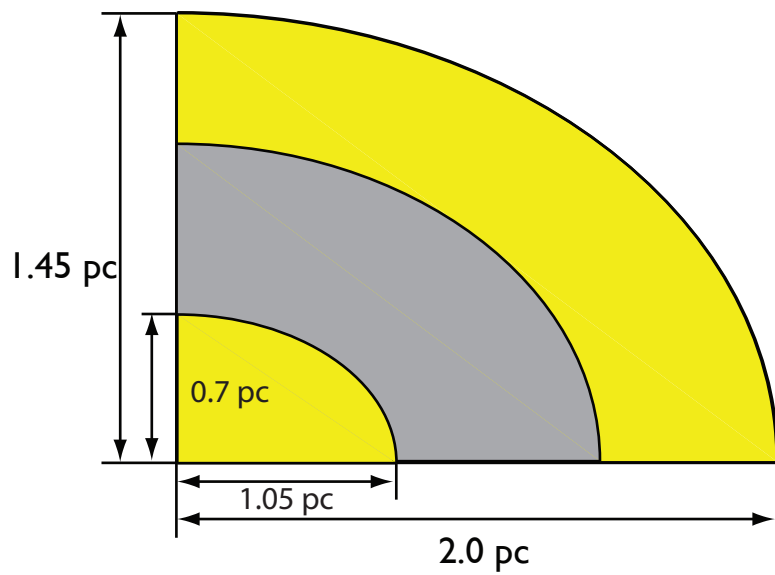


Figure 5.5. A cartoon schematic of the geometry III

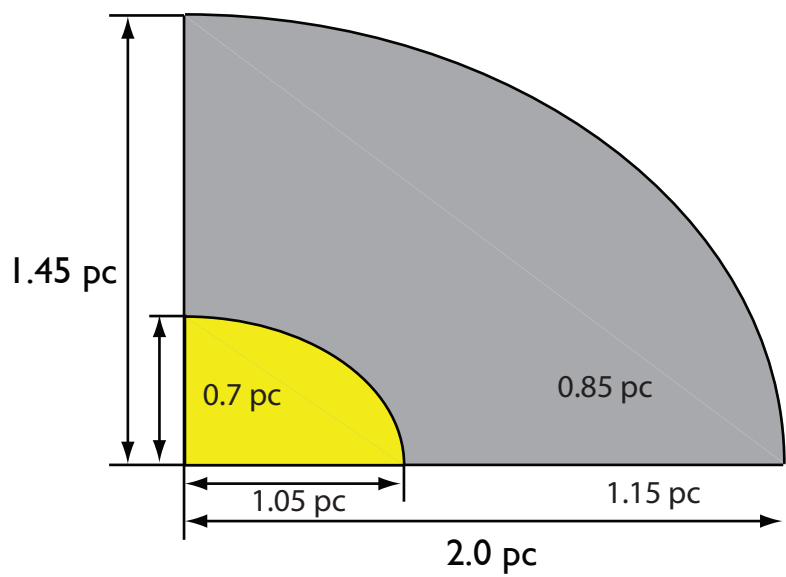


Figure 5.6. A cartoon schematic of the geometry IV

cartoon schematic is shown in 5.7.

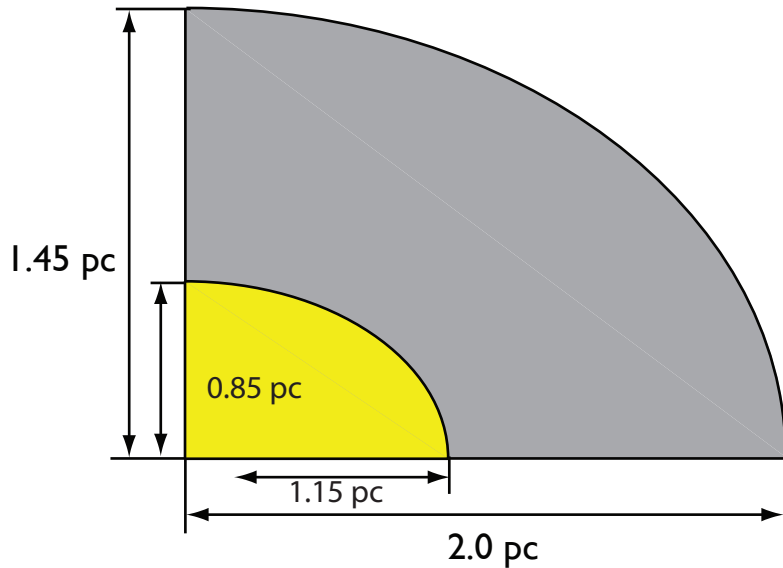


Figure 5.7. A cartoon schematic of the geometry V

VI. a smooth shell distribution with the gas and dust in a shell 0.1 pc thick at a radius of 0.55 pc, entirely inside the ionising radiation field to match models used by Temim & Dwek (2013) and Čadež et al. (2004) observations. A density of 1400 cm^{-3} is selected to match total modelled H_β flux matches observed flux . A cartoon schematic is shown in Figure 5.8.

VII. a clumped distribution with all the material outside the the ionising source. The degree of clumping is determined by fitting to the optical lines. A clump filling factor is found to be 0.1 with a density in the clumps of $N_e = 1400 \text{ cm}^{-3}$. With this clump filling factor and the geometry of the model, the clumps are 0.034 pc in diameter.. The mass of dust and gas decreases linearly with radius. A schematic of this model is shown in Figure 5.9. The clumps are modelled using sub grids for finer variations in the density as in Ercolano et al. (2007).

VIII. a clumped distribution with all the material outside the ionising source. Also determined by matching the optical lines with a filling factor of 0.1 and a of $N_e = 1700 \text{ cm}^{-3}$. The clumps are 0.034 pc in diameter. The mass of dust and gas decreases

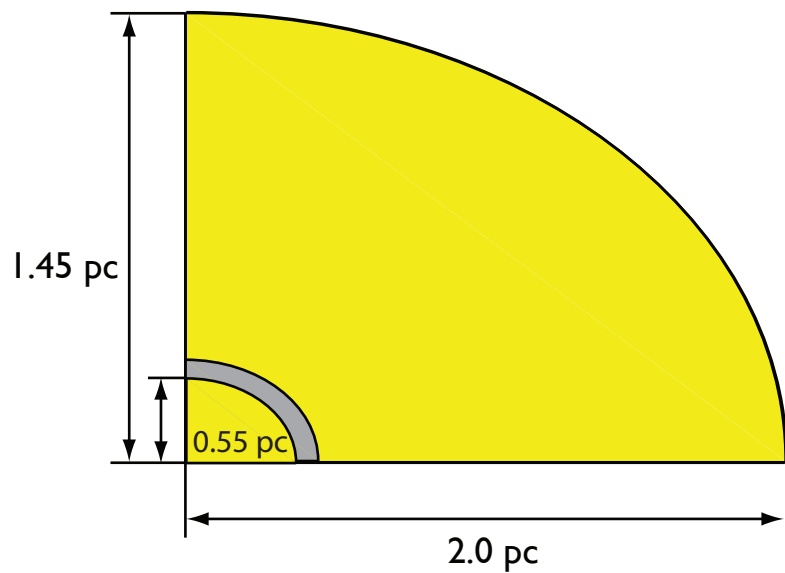


Figure 5.8. A cartoon schematic of the geometry VI

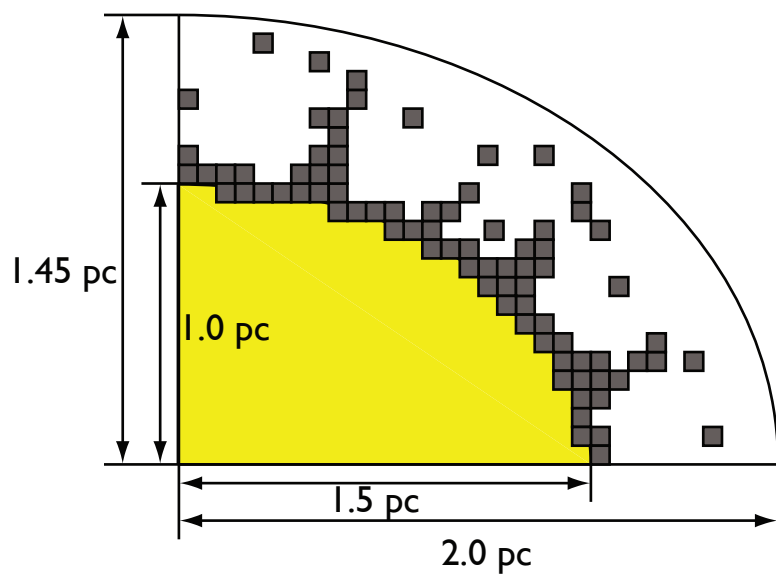


Figure 5.9. A cartoon schematic of the geometry VII

linearly with radius. A schematic of this model is shown in Figure 5.10.

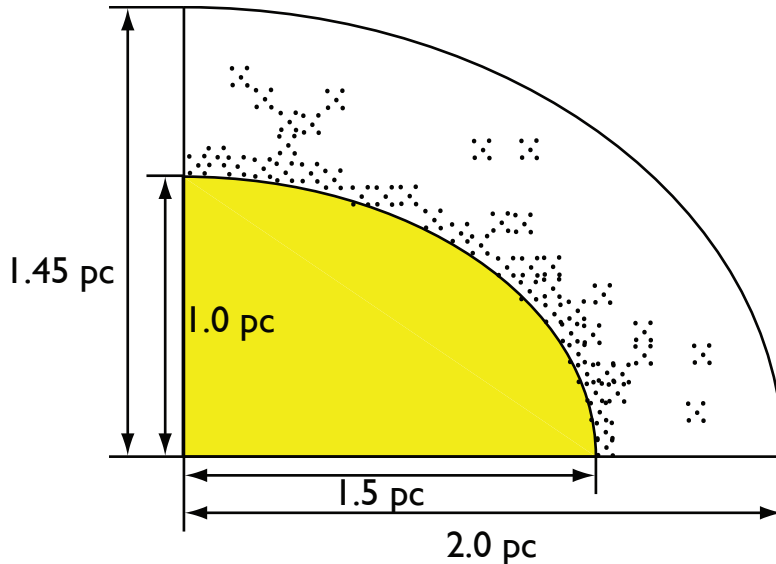


Figure 5.10. A cartoon schematic of the geometry VIII

- IX. a clumped distribution with all of the material inside the ionising source with a filling factor of 0.1 and density of 1900 in the clumps. The inner radius of the material is at 1.05×0.75 pc (Davidson & Fesen 1985) and decreases at r^{-2} . The clumps are 0.034 pc in radius. A cartoon schematic of this model is shown in Figure 5.11.
- X. a clumped distribution with all of the material inside the ionising source with a filling factor of 0.1 and density of 1900 in the clumps. The inner radius of the material is at 1.15×0.85 pc (Lawrence et al. 1995) and decreases at r^{-2} . The clumps are 0.034 pc in radius. A cartoon schematic of this model is shown in Figure 5.15.
- XI. a *smooth* shell distribution, with the gas and dust located at a radius of 0.55 pc in a 0.1 pc thick shell (i.e. both inner axes 1.1 pc in length), **with the PWN diffuse field radiation field emitting uniformly from within the inner nebular radius of 1.1 pc**. This shell geometry was argued for by Čadež et al. (2004) based on their multi-slit spectroscopy and was adopted by Temim & Dwek (2013) for their dust modelling. A shell hydrogen density of 1400 cm^{-3} was found to be needed to match the total (dereddened) H β flux from the nebula.
- XII. a *clumped* shell distribution where the gas and dust clumps start at inner axis diam-

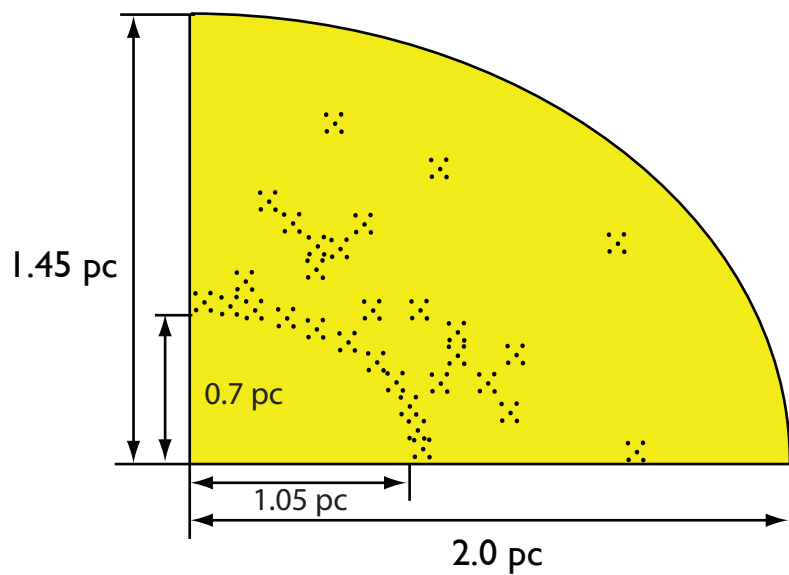


Figure 5.11. A cartoon schematic of the geometry IX

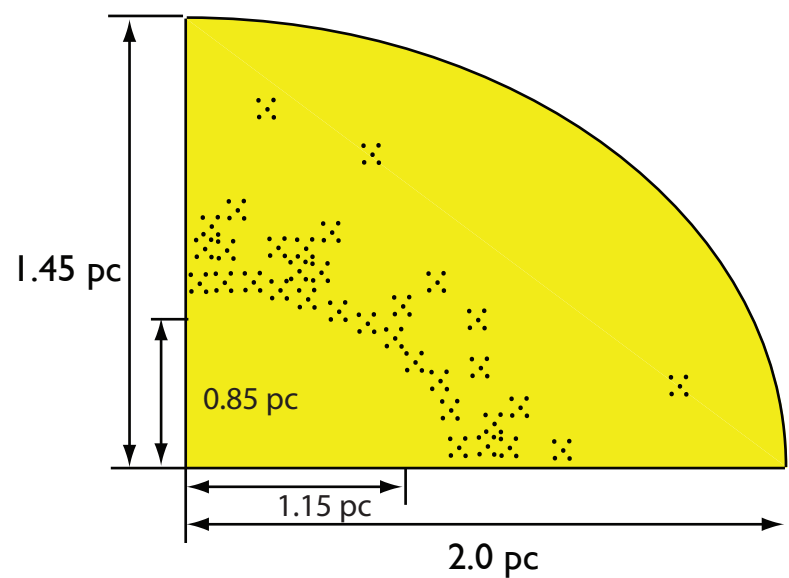


Figure 5.12. A cartoon schematic of the geometry X

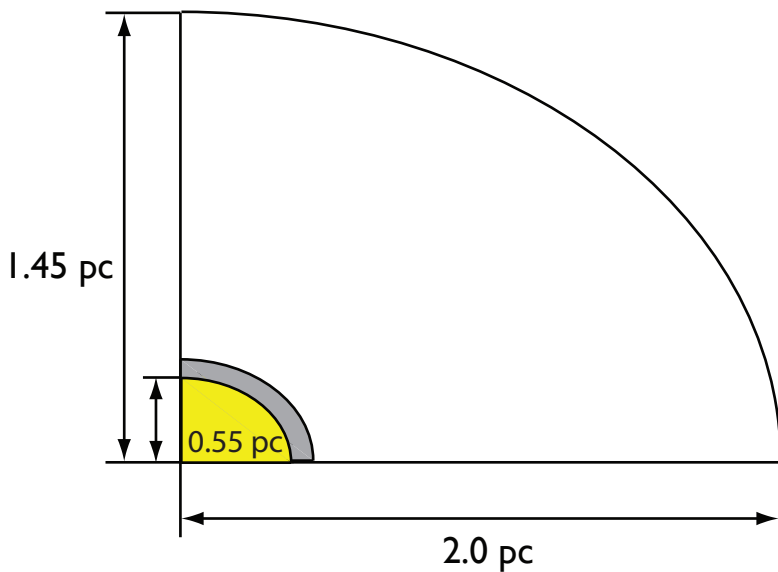


Figure 5.13. A cartoon schematic of the geometry XI

eters of 2.3×1.7 pc (Lawrence et al. 1995), and with an r^{-2} distribution of clumps that extends to the 4.0×2.9 pc outer boundaries of the nebula, with a volume filling factor of 0.10. **The PWN radiation field is a diffuse source emitting uniformly within a 1.1x1.1 pc diameter sphere at the centre of the nebula.** For 0.037-pc radius clumps, a H-density of 1900 cm^{-3} within the clumps was found to match the total H β flux from the nebula.

XIII. a *clumped* shell distribution where the gas and dust clumps start at inner axis diameters of 1.1×1.5 pc (Davidson & Fesen 1985), and with an r^{-2} distribution of clumps that extends to the 4.0×2.9 pc outer boundaries of the nebula, with a volume filling factor of 0.10. **The PWN radiation field is a diffuse source emitting uniformly within a 1.1x1.1 pc diameter sphere at the centre of the nebula.** For 0.037-pc radius clumps, a H-density of 1900 cm^{-3} within the clumps was found to match the total H β flux from the nebula.

5.1.6 Nucleosynthesis

Another constraint on the mass of dust that is able to be formed by a supernova are the abundances of constituent elements of the dust. The supernova nucleosynthesis models of Woosley & Weaver (1995) estimate a carbon mass of $0.11 M_{\odot}$ and $0.27 M_{\odot}$ of oxygen

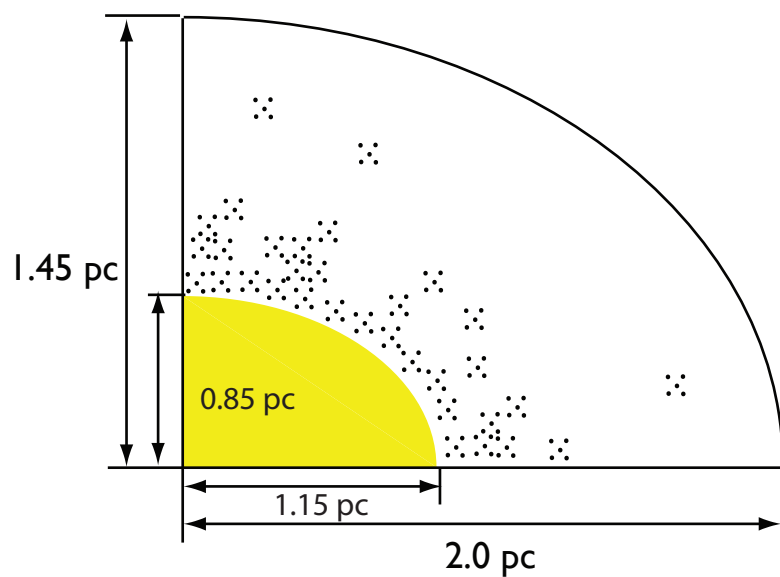


Figure 5.14. A cartoon schematic of the geometry XII

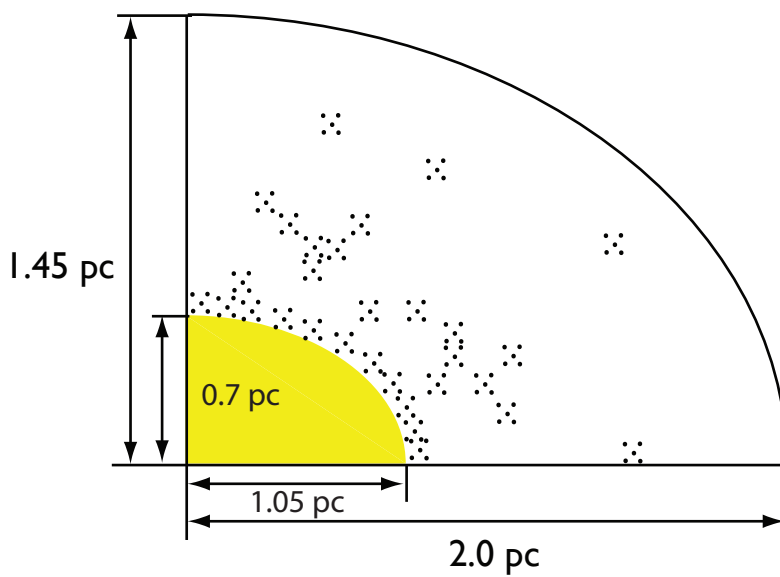


Figure 5.15. A cartoon schematic of the geometry XIII

for a supernova with a progenitor of $12 M_{\odot}$. Previous studies by MacAlpine & Satterfield (2008) have shown that the Crab nebula is carbon rich and oxygen poor, so we take the total abundance of carbon and oxygen combined to be correct, but the ratio of the two to be incorrect. This allows for a carbon mass of up to $0.11 M_{\odot} + (12/16) \times 0.27 M_{\odot} = 0.31 M_{\odot}$.

The abundance of magnesium from the Woosley & Weaver (1995) models is $0.02 M_{\odot}$, $0.06 M_{\odot}$ of Silicon and $0.03 M_{\odot}$ of Iron are predicted. Assuming these go in to $MgSiO_3$ and $FeSiO_3$ we get $0.02 + 0.02 + 3 \times (16/28) \times 0.02 M_{\odot} = 0.074 M_{\odot}$ of $MgSiO_3$ and $0.03 + (28/56) \times 0.03 + 3 \times (16/56) \times 0.03 M_{\odot} = 0.071 M_{\odot}$ of $FeSiO_3$. This gives an upper limit of $0.15 M_{\odot}$ of silicate dust.

5.2 Results

5.2.1 Elemental Abundances

Using the elemental abundances in Table 5.2, the line fluxes from Smith (2003) have been matched with the smooth model with comparison shown in Table 5.10. The smooth models are run are with an electron density of $N_e = 775 \text{ cm}^{-3}$ for the smooth model which is within the range measured from the $3729 \text{ \AA}/3726 \text{ \AA}$ O II ratio (Osterbrock 1957) although above the range determined from the $52 \mu\text{m}/88 \mu\text{m}$ [O III] (Gomez et al. 2012). The clumped models use an electron density of $N_e = 1400 \text{ cm}^{-3}$ which is also within the range of values given in Osterbrock (1957) and a volume filling factor of 0.1 is used. The initial models were far to ionized. To increase cooling both neon, sulphur and argon abundance were raised to obtain the correct balance of [O II] and [O III] whilst maintaining the correct flux for the neon, sulphur and argon.

5.2.2 Dust Masses

I. Smooth Model

The best fits to the observed SED of the Crab Nebula are shown in Figure 5.16 with parameters used to achieve these fits are shown in Table 5.11. The results using the Zubko AC optical constants, as used in Gomez et al. (2012) are in good agreement with the empirically determined dust mass. While the mass determined for the

	Model I	Model II	Model III	Model IV	Model V	Model VI
Hydrogen	1.00	1.00	1.00	1.00	1.00	1.00
Helium	1.90	1.90	1.90	1.85	1.90	1.83
Carbon	9.3×10^{-3}	9.3×10^{-3}	9.3×10^{-3}	1.02×10^{-2}	9.3×10^{-3}	9.7×10^{-3}
Nitrogen	1.5×10^{-4}	1.5×10^{-4}	1.5×10^{-4}	2.5×10^{-4}	1.5×10^{-4}	2.5×10^{-4}
Oxygen	8.0×10^{-3}	8.0×10^{-3}	8.0×10^{-3}	6.2×10^{-3}	7.0×10^{-3}	7.2×10^{-3}
Neon	4.5×10^{-4}	4.5×10^{-4}	4.5×10^{-4}	4.9×10^{-3}	4.5×10^{-4}	2.0×10^{-3}
Sulphur	5.0×10^{-5}	5.0×10^{-5}	5.0×10^{-5}	4.0×10^{-5}	5.0×10^{-5}	4.0×10^{-4}
Argon	6.0×10^{-6}	6.0×10^{-6}	6.0×10^{-6}	1.0×10^{-5}	5.0×10^{-5}	5.0×10^{-5}

Table 5.2. Elemental abundances of emitting gas in the Crab Nebula relative to hydrogen

	Model VII	Model VIII	Model IX	Model X	Model XI	Model XII	Model XIII
Hydrogen	1.00	1.00	1.00	1.00	1.00	1.00	1.00
Helium	1.83	1.83	1.85	1.85	1.83	1.85	1.85
Carbon	9.7×10^{-3}	9.7×10^{-3}	1.02×10^{-2}	1.02×10^{-2}	9.7×10^{-3}	1.02×10^{-2}	1.02×10^{-2}
Nitrogen	2.5×10^{-4}	2.5×10^{-4}	2.5×10^{-4}	2.5×10^{-4}	2.5×10^{-4}	2.5×10^{-4}	2.5×10^{-4}
Oxygen	7.2×10^{-3}	7.2×10^{-3}	6.2×10^{-3}	6.2×10^{-3}	7.2×10^{-3}	6.2×10^{-3}	6.2×10^{-3}
Neon	2.0×10^{-3}	2.0×10^{-3}	4.9×10^{-3}	4.9×10^{-3}	2.0×10^{-3}	4.9×10^{-3}	4.9×10^{-3}
Sulphur	4.0×10^{-4}	4.0×10^{-4}	4.0×10^{-5}	4.0×10^{-5}	4.0×10^{-4}	4.0×10^{-5}	4.0×10^{-5}
Argon	5.0×10^{-5}	5.0×10^{-5}	1.0×10^{-5}	1.0×10^{-5}	5.0×10^{-5}	1.0×10^{-5}	1.0×10^{-5}

Table 5.3. Elemental abundances of emitting gas in the Crab Nebula relative to hydrogen

Species	Wavelength [Å]	Observed Flux 6.64×10^{-11}	Modelled Flux 6.32×10^{-11}	Obs/Model Model I	Modelled Flux Model II	Obs/Model
H_{β}	4861	6.64×10^{-11}	6.32×10^{-11}	1.05	7.74×10^{-11}	0.86
[O II]	3726+3729	18.11	20.3	0.89	18.16	1.00
[Ne III]	3869	4.65	3.99	1.16	3.91	1.19
[S II]	4069	0.37	0.32	1.16	0.36	1.03
[O III] + H $_{\gamma}$	4363	0.57	0.58	1.01	0.48	1.18
He I	4471	0.37	0.43	0.86	0.36	1.04
He II	4686	0.78	0.79	0.98	0.79	0.98
H $_{\beta}$	4861	1.00	1.00	1.00	1.00	1.00
[O III]	5007	11.92	9.28	1.28	9.58	1.24
[N I]	5198+5200	0.13	0.14	0.93	0.14	0.93
H $_{\alpha}$	6563	2.85	2.92	0.98	2.95	0.97
[N II]	6548 + 6584	6.87	6.38	1.08	5.80	1.18
[S II]	6717 + 6731	4.31	3.98	0.90	4.59	0.94
[C I]	9824+9850	0.36	0.66	0.55	0.28	1.29
[Ar III]	7136	0.34	0.33	1.04	0.41	0.84

Table 5.4. Observed and modelled absolute H_{β} flux. Observed and modelled line strengths relative to H_{β} and their ratio. All observed lines are taken from Smith (2003), except for [C I] 9824+9850 from Rudy et al. (1994), [Ar III] 7136+7751 from Davidson & Fesen (1985) and [Ar III] 89911 from Temim et al. (2012).

Species	Wavelength [Å]	Observed Flux	Modelled Flux Model III	Obs/Model Model III	Modelled Flux Model IV	Obs/Model Model IV
H_{β}	4861	6.64×10^{-11}	6.32×10^{-11}	1.05	7.74×10^{-11}	0.86
[O II]	3726+3729	18.11	20.3	0.89	18.16	1.00
[Ne III]	3869	4.65	3.99	1.16	3.91	1.19
[S II]	4069	0.37	0.32	1.16	0.36	1.03
[O III] + H $_{\gamma}$	4363	0.57	0.58	1.01	0.48	1.18
He I	4471	0.37	0.43	0.86	0.36	1.04
He II	4686	0.78	0.79	0.98	0.79	0.98
H $_{\beta}$	4861	1.00	1.00	1.00	1.00	1.00
[O III]	5007	11.92	9.28	1.28	9.58	1.24
[N I]	5198+5200	0.13	0.14	0.93	0.14	0.93
H $_{\alpha}$	6563	2.85	2.92	0.98	2.95	0.97
[N II]	6548 + 6584	6.87	6.38	1.08	5.80	1.18
[S II]	6717 + 6731	4.31	3.98	0.90	4.59	0.94
[C I]	9824+9850	0.36	0.66	0.55	0.28	1.29
[Ar III]	7136	0.34	0.33	1.04	0.41	0.84

Table 5.5. Observed and modelled absolute H_{β} flux. Observed and modelled line strengths relative to H_{β} and their ratio.
All observed lines are taken from Smith (2003), except for [C I] 9824+9850 from Rudy et al. (1994), [Ar III] 7136+7751 from Davidson & Fesen (1985) and [Ar III] 89911 from Temim et al. (2012).

Species	Wavelength [Å]	Observed Flux	Modelled Flux	Obs/Model	Modelled Flux	Obs/Model
			Model V	Model VI		
H_{β}	4861	6.64×10^{-11}	6.32×10^{-11}	1.05	7.74×10^{-11}	0.86
[O II]	3726+3729	18.11	20.3	0.89	18.16	1.00
[Ne III]	3869	4.65	3.99	1.16	3.91	1.19
[S II]	4069	0.37	0.32	1.16	0.36	1.03
[O III] + H $_{\gamma}$	4363	0.57	0.58	1.01	0.48	1.18
He I	4471	0.37	0.43	0.86	0.36	1.04
He II	4686	0.78	0.79	0.98	0.79	0.98
H $_{\beta}$	4861	1.00	1.00	1.00	1.00	1.00
[O III]	5007	11.92	9.28	1.28	9.58	1.24
[N I]	5198+5200	0.13	0.14	0.93	0.14	0.93
H $_{\alpha}$	6563	2.85	2.92	0.98	2.95	0.97
[N II]	6548 + 6584	6.87	6.38	1.08	5.80	1.18
[S II]	6717 + 6731	4.31	3.98	0.90	4.59	0.94
[C I]	9824+9850	0.36	0.66	0.55	0.28	1.29
[Ar III]	7136	0.34	0.33	1.04	0.41	0.84

Table 5.6. Observed and modelled absolute H_{β} flux. Observed and modelled line strengths relative to H_{β} and their ratio. All observed lines are taken from Smith (2003), except for [C I] 9824+9850 from Rudy et al. (1994), [Ar III] 7136+7751 from Davidson & Fesen (1985) and [Ar III] 89911 from Temim et al. (2012).

Species	Wavelength [Å]	Observed Flux	Modelled Flux Model VII	Obs/Model Model VII	Modelled Flux	Obs/Model
H_{β}	4861	6.64×10^{-11}	6.32×10^{-11}	1.05	7.74×10^{-11}	0.86
[O II]	3726+3729	18.11	20.3	0.89	18.16	1.00
[Ne III]	3869	4.65	3.99	1.16	3.91	1.19
[S II]	4069	0.37	0.32	1.16	0.36	1.03
[O III] + H $_{\gamma}$	4363	0.57	0.58	1.01	0.48	1.18
He I	4471	0.37	0.43	0.86	0.36	1.04
He II	4686	0.78	0.79	0.98	0.79	0.98
H $_{\beta}$	4861	1.00	1.00	1.00	1.00	1.00
[O III]	5007	11.92	9.28	1.28	9.58	1.24
[N I]	5198+5200	0.13	0.14	0.93	0.14	0.93
H $_{\alpha}$	6563	2.85	2.92	0.98	2.95	0.97
[N II]	6548 + 6584	6.87	6.38	1.08	5.80	1.18
[S II]	6717 + 6731	4.31	3.98	0.90	4.59	0.94
[C I]	9824+9850	0.36	0.66	0.55	0.28	1.29
[Ar III]	7136	0.34	0.33	1.04	0.41	0.84

Table 5.7. Observed and modelled absolute H_{β} flux. Observed and modelled line strengths relative to H_{β} and their ratio.
All observed lines are taken from Smith (2003), except for [C I] 9824+9850 from Rudy et al. (1994), [Ar III] 7136+7751 from Davidson & Fesen (1985) and [Ar III] 89911 from Temim et al. (2012).

Species	Wavelength [Å]	Observed Flux	Modelled Flux Model IX	Obs/Model Model X	Modelled Flux	Obs/Model
H_{β}	4861	6.64×10^{-11}	6.32×10^{-11}	1.05	7.74×10^{-11}	0.86
[O II]	3726+3729	18.11	20.3	0.89	18.16	1.00
[Ne III]	3869	4.65	3.99	1.16	3.91	1.19
[S II]	4069	0.37	0.32	1.16	0.36	1.03
[O III] + H $_{\gamma}$	4363	0.57	0.58	1.01	0.48	1.18
He I	4471	0.37	0.43	0.86	0.36	1.04
He II	4686	0.78	0.79	0.98	0.79	0.98
H $_{\beta}$	4861	1.00	1.00	1.00	1.00	1.00
[O III]	5007	11.92	9.28	1.28	9.58	1.24
[N I]	5198+5200	0.13	0.14	0.93	0.14	0.93
H $_{\alpha}$	6563	2.85	2.92	0.98	2.95	0.97
[N II]	6548 + 6584	6.87	6.38	1.08	5.80	1.18
[S II]	6717 + 6731	4.31	3.98	0.90	4.59	0.94
[C I]	9824+9850	0.36	0.66	0.55	0.28	1.29
[Ar III]	7136	0.34	0.33	1.04	0.41	0.84

Table 5.8. Observed and modelled absolute H_{β} flux. Observed and modelled line strengths relative to H_{β} and their ratio.
All observed lines are taken from Smith (2003), except for [C I] 9824+9850 from Rudy et al. (1994), [Ar III] 7136+7751 from Davidson & Fesen (1985) and [Ar III] 89911 from Temim et al. (2012).

Species	Wavelength [Å]	Observed Flux	Modelled Flux	Obs/Model	Modelled Flux	Obs/Model
			Model XI	Model XII		
H_{β}	4861	6.64×10^{-11}	6.32×10^{-11}	1.05	7.74×10^{-11}	0.86
[O II]	3726+3729	18.11	20.3	0.89	18.16	1.00
[Ne III]	3869	4.65	3.99	1.16	3.91	1.19
[S II]	4069	0.37	0.32	1.16	0.36	1.03
[O III] + H $_{\gamma}$	4363	0.57	0.58	1.01	0.48	1.18
He I	4471	0.37	0.43	0.86	0.36	1.04
He II	4686	0.78	0.79	0.98	0.79	0.98
H $_{\beta}$	4861	1.00	1.00	1.00	1.00	1.00
[O III]	5007	11.92	9.28	1.28	9.58	1.24
[N I]	5198+5200	0.13	0.14	0.93	0.14	0.93
H $_{\alpha}$	6563	2.85	2.92	0.98	2.95	0.97
[N II]	6548 + 6584	6.87	6.38	1.08	5.80	1.18
[S II]	6717 + 6731	4.31	3.98	0.90	4.59	0.94
[C I]	9824+9850	0.36	0.66	0.55	0.28	1.29
[Ar III]	7136	0.34	0.33	1.04	0.41	0.84

Table 5.9. Observed and modelled absolute H_{β} flux. Observed and modelled line strengths relative to H_{β} and their ratio. All observed lines are taken from Smith (2003), except for [C I] 9824+9850 from Rudy et al. (1994), [Ar III] 7136+7751 from Davidson & Fesen (1985) and [Ar III] 89911 from Temim et al. (2012).

Species	Wavelength [Å]	Observed Flux	Modelled Flux	Obs/Model
		Model XIII	Model XIII	
H_{β}	4861	6.64×10^{-11}	7.74×10^{-11}	0.86
[O II]	3726+3729	18.11	18.16	1.00
[Ne III]	3869	4.65		
1.19			3.91	
[S II]	4069	0.37	0.36	1.03
[O III] + H $_{\gamma}$	4363	0.57	0.48	1.18
He I	4471	0.37	0.43	0.86
He II	4686	0.78	0.79	0.98
H $_{\beta}$	4861	1.00	1.00	1.00
[O III]	5007	11.92	9.28	1.28
[N I]	5198+5200	0.13	0.14	0.93
H $_{\alpha}$	6563	2.85	2.92	0.98
[N II]	6548 + 6584	6.87	6.38	1.08
[S II]	6717 + 6731	4.31	3.98	0.90
[C I]	9824+9850	0.36	0.66	0.55
[Ar III]	7136	0.34	0.33	1.04

Table 5.10. Observed and modelled absolute H_{β} flux. Observed and modelled line strengths relative to H_{β} and their ratio. All observed lines are taken from Smith (2003), except for [C I] 9824+9850 from Rudy et al. (1994), [Ar III] 7136+7751 from Davidson & Fesen (1985) and [Ar III] 89911 from Temim et al. (2012).

silicates is higher than the mean but still within the measured uncertainty.

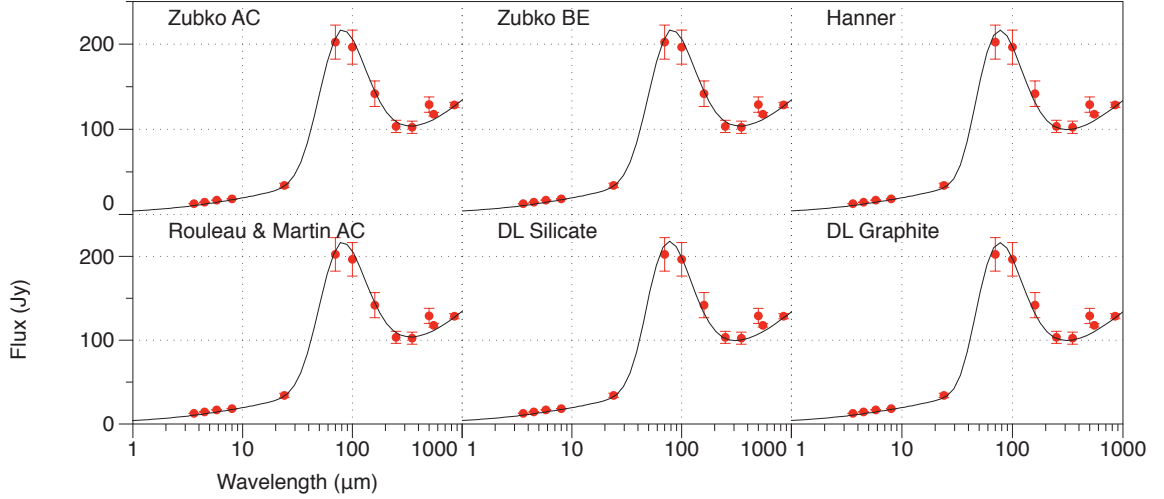


Figure 5.16. Best fit models plotted with observed SEDs for the six different sets of optical constants using a smooth isotropic density distribution with an electron density of 775 cm^{-3} .

Optical Constants	a_{min}	a_{max}	α	M_{dust}	χ^2
Zubko AC	$0.005 \mu\text{m}$	$1.0 \mu\text{m}$	2.9 ± 0.1	$0.30 M_\odot$	3.12
Zubko BE	$0.005 \mu\text{m}$	$0.7 \mu\text{m}$	2.9 ± 0.1	$0.14 M_\odot$	3.97
Hanner	$0.01 \mu\text{m}$	$1.0 \mu\text{m}$	2.9 ± 0.1	$0.30 M_\odot$	4.01
Rouleau & Martin AC	$0.01 \mu\text{m}$	$1.0 \mu\text{m}$	3.0 ± 0.1	$0.08 M_\odot$	10.0
Mixed Model	$0.01 \mu\text{m}$	$0.9 \mu\text{m}$	3.0 ± 0.1	$0.18 M_\odot$ $0.08 M_\odot$ Zubko BE $0.1 M_\odot$ DL silicates	3.33
Draine & Lee Silicate	$0.001 \mu\text{m}$	$1.0 \mu\text{m}$	3.5 ± 0.1	$0.46 M_\odot$	2.99
Draine & Lee Graphite	$0.001 \mu\text{m}$	$0.25 \mu\text{m}$	3.0 ± 0.1	$0.09 M_\odot$	4.01

Table 5.11. The results for model . the smooth isotropic density distribution.

II. Smooth Shell Model

The best fits to the observed SED of the Crab Nebula are shown in Figure 5.17 with parameters used to achieve these fits are shown in Table 5.12. The dust masses determined are slightly less than those measured using a density distribution with material throughout the nebula. As with model i, the masses obtained using the optical constants used in Gomez et al. (2012) are in agreement with the empirical fit.

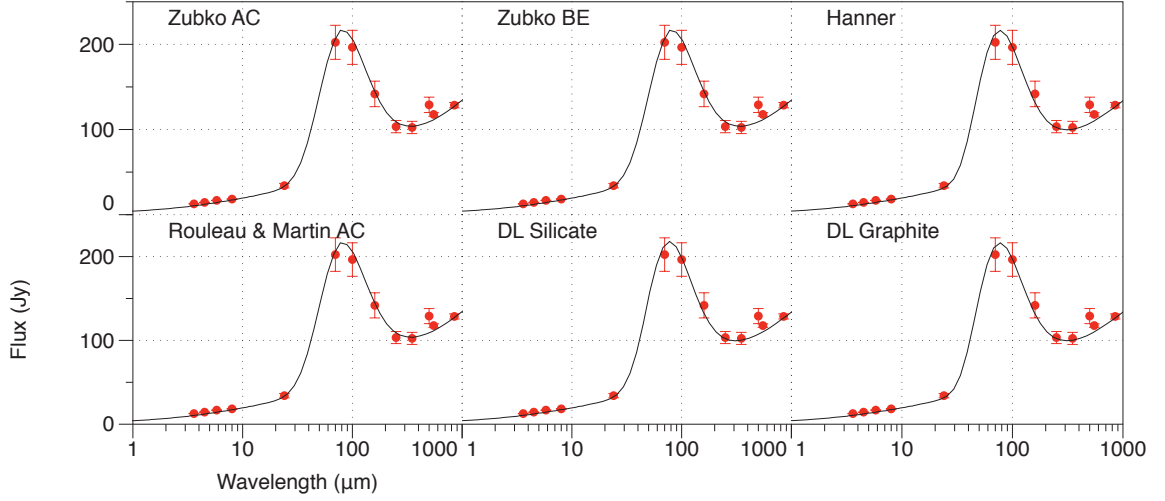


Figure 5.17. Best fit models plotted with observed SEDs for the six different sets of optical constants using a smooth isotropic density distribution in a shell in the outer third of the nebula with a density of 850 cm^{-3} outside the diffuse radiation source

Optical Constants	a_{min}	a_{max}	α	M_{dust}	χ^2
Zubko AC	$0.07 \mu\text{m}$	$1.0 \mu\text{m}$	2.9 ± 0.1	$0.27 M_\odot$	9.9
Zubko BE	$0.07 \mu\text{m}$	$0.2 \mu\text{m}$	2.9 ± 0.1	$0.11 M_\odot$	9.7
Mixed Model	$0.07 \mu\text{m}$	$1.0 \mu\text{m}$	2.9 ± 0.1	$0.27 M_\odot$	10.6
Rouleau & Martin AC	$0.07 \mu\text{m}$	$1.0 \mu\text{m}$	3.0 ± 0.1	$0.08 M_\odot$	12.1
Draine & Lee Silicate	$0.07 \mu\text{m}$	$1.0 \mu\text{m}$	3.5 ± 0.1	$0.40 M_\odot$	11.3
Draine & Lee Graphite	$0.001 \mu\text{m}$	$0.25 \mu\text{m}$	3.0 ± 0.1	$0.08 M_\odot$	11.0

Table 5.12. The results for model II. the smooth isotropic density distribution with outer axes of $4.0 \times 2.9 \text{ pc}$ and inner axes of $3.0 \times 2.0 \text{ pc}$ outside the radiation source.

III. Davidson & Fesen (1985) axes with dust and gas in a shell 0.5 pc thick

Figure 5.18 shows the best fit to observed SEDs for the smooth isotropic density distribution in a shell 0.5 pc thick and a inner axes of $2.1 \times 1.4 \text{ pc}$ entirely inside the diffuse radiation source based Davidson & Fesen (1985). The shell thickness is taken as an intermediate value as the values given in the paper span a range of 0.3-07 pc averaging at 0.5 pc. The dust masses shown in table 5.13, required to fit the SED with this geometry are lower, although still very close to those measured by Gomez et al. (2012).

IV. Davidson & Fesen (1985) axes with dust and gas distributed from the inner radius

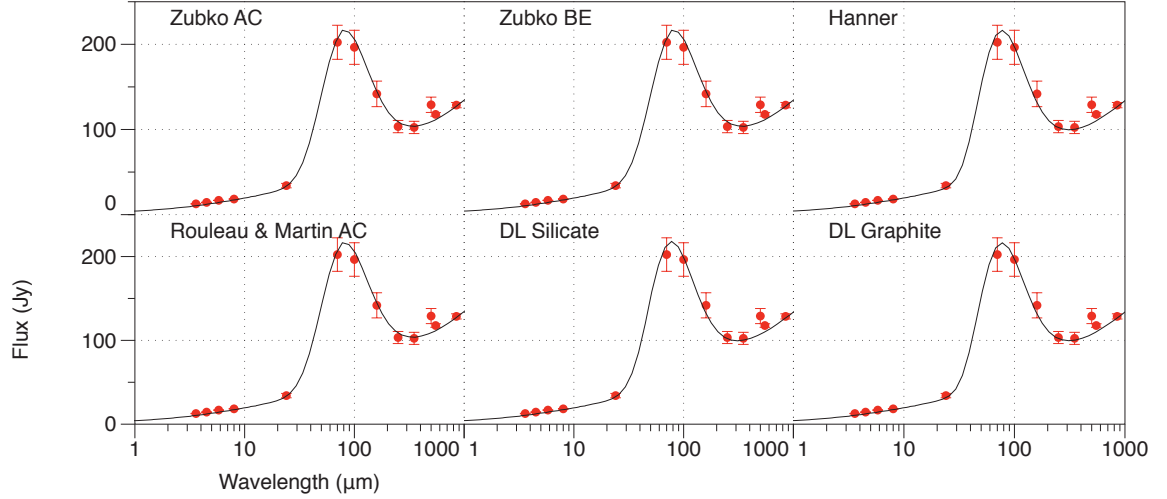


Figure 5.18. Best fit models plotted with observed SEDs for the six different sets of optical constants using a smooth isotropic density distribution in a shell 0.5 pc thick and a inner axes of 2.1×1.4 pc entirely inside the diffuse radiation source.

Optical Constants	a_{min}	a_{max}	α	M_{dust}	χ^2
Zubko et al. ACAR	$0.01 \mu\text{m}$	$0.7 \mu\text{m}$	2.9 ± 0.1	$0.12 \pm 0.03 M_\odot$	5.22
Zubko et al. BE	$0.005 \mu\text{m}$	$0.5 \mu\text{m}$	2.8 ± 0.1	$0.09 \pm 0.02 M_\odot$	5.97
Rouleau & Martin AC1	$0.01 \mu\text{m}$	$0.7 \mu\text{m}$	3.0 ± 0.1	$0.05 \pm 0.01 M_\odot$	4.89
Mixed Model	$0.01 \mu\text{m}$	$0.8 \mu\text{m}$	3.0 ± 0.1	$0.14 \pm 0.02 M_\odot$ $0.05 M_\odot$ Zubko BE $0.09 M_\odot$ DL silicates	6.01
Draine & Lee Silicate	$0.001 \mu\text{m}$	$0.9 \mu\text{m}$	3.5 ± 0.1	$0.32 \pm 0.06 M_\odot$	5.14
Draine & Lee Graphite	$0.001 \mu\text{m}$	$0.25 \mu\text{m}$	2.9 ± 0.1	$0.06 \pm 0.01 M_\odot$	6.66

Table 5.13. The results for model IV. the smooth isotropic density distribution in a shell 0.5 pc thick and a inner axes of 2.1×1.4 pc entirely inside the diffuse radiation source.

to the edge of the nebula

Figure 5.19 shows the best fit to observed SEDs for the smooth isotropic density distribution in a shell with inner axes of 2.1×1.4 pc and outer axes at the edge of the nebula at 4.0×2.9 pc, with the radiation field filling the whole nebula out to the same axes following geometry from Davidson & Fesen (1985). The mass of dust, shown in Table 5.14, required is larger than that needed for the geometry with a thinner shell.

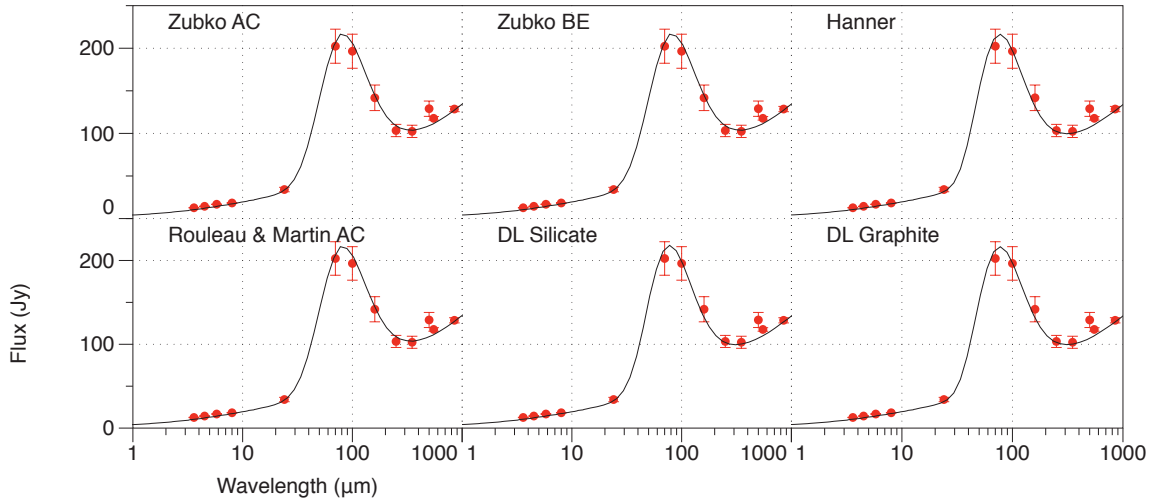


Figure 5.19. Best fit models plotted with observed SEDs for the six different sets of optical constants using a smooth isotropic density distribution in a shell all the way to the edge of the nebula and a inner axes of 2.1×1.4 pc entirely inside the diffuse radiation source.

Optical Constants	a_{min}	a_{max}	α	M_{dust}	χ^2
Zubko et al. ACAR	$0.01 \mu\text{m}$	$1.0 \mu\text{m}$	2.9 ± 0.1	$0.18 M_{\odot}$	9.9
Zubko et al BE	$0.01 \mu\text{m}$	$0.2 \mu\text{m}$	2.9 ± 0.1	$0.14 M_{\odot}$	9.7
Rouleau & Martin AC1	$0.01 \mu\text{m}$	$1.0 \mu\text{m}$	3.0 ± 0.1	$0.08 M_{\odot}$	12.1
Mixed Model	$0.01 \mu\text{m}$	$0.8 \mu\text{m}$	3.0 ± 0.1	$0.21 \pm 0.02 M_{\odot}$ $0.05 M_{\odot}$ Zubko BE $0.09 M_{\odot}$ DL silicates	6.01
Draine & Lee Silicate	$0.01 \mu\text{m}$	$1.0 \mu\text{m}$	3.5 ± 0.1	$0.48 M_{\odot}$	11.3
Draine & Lee Graphite	$0.001 \mu\text{m}$	$0.25 \mu\text{m}$	3.0 ± 0.1	$0.09 M_{\odot}$	11.0

Table 5.14. The results for model IV. the smooth isotropic density distribution with outer axes of 4.0×2.9 pc and inner axes of 2.1×1.4 pc entirely inside the diffuse radiation source.

V. Lawrence et al. (1995) axes with dust and gas distributed from the inner radius to

the edge of the nebula

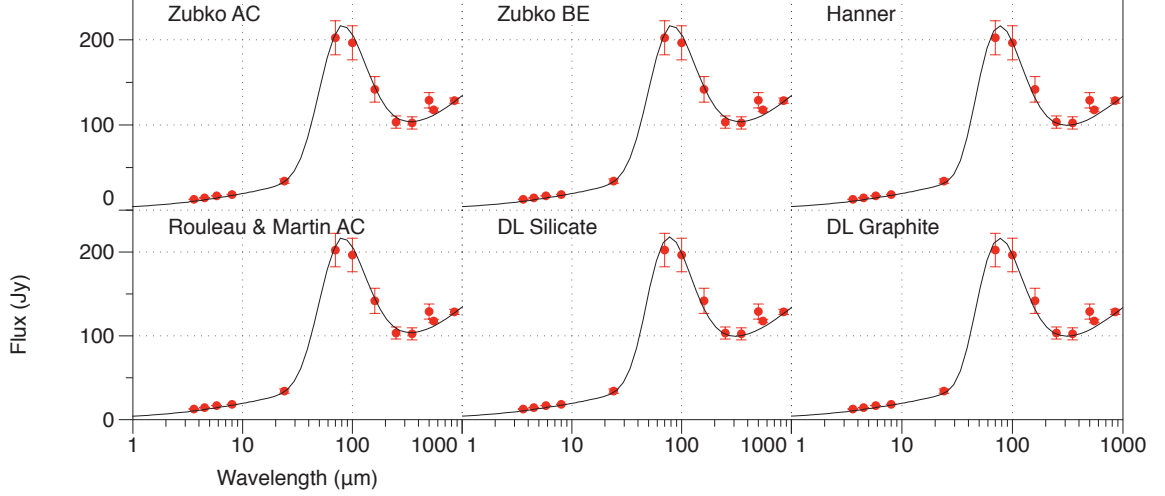


Figure 5.20. Best fit models plotted with observed SEDs for the six different sets of optical constants using a smooth isotropic density distribution in a shell all the way to the edge of the nebula and a inner axes of 2.3×1.7 pc entirely inside the diffuse radiation source.

Optical Constants	a_{min}	a_{max}	α	M_{dust}	χ^2
Zubko et al. ACAR	$0.01 \mu\text{m}$	$0.7 \mu\text{m}$	2.9 ± 0.1	$0.14 \pm 0.04 M_\odot$	5.22
Zubko et al. BE	$0.005 \mu\text{m}$	$0.5 \mu\text{m}$	2.8 ± 0.1	$0.11 \pm 0.02 M_\odot$	5.97
Rouleau & Martin AC1	$0.01 \mu\text{m}$	$0.7 \mu\text{m}$	3.0 ± 0.1	$0.06 \pm 0.01 M_\odot$	4.89
Mixed Model	$0.01 \mu\text{m}$	$0.8 \mu\text{m}$	3.0 ± 0.1	$0.16 \pm 0.02 M_\odot$	6.01
				$0.05 M_\odot$ Zubko BE	
				$0.09 M_\odot$ DL silicates	
Draine & Lee Silicate	$0.001 \mu\text{m}$	$0.9 \mu\text{m}$	3.5 ± 0.1	$0.37 \pm 0.06 M_\odot$	5.14
Draine & Lee Graphite	$0.001 \mu\text{m}$	$0.25 \mu\text{m}$	2.9 ± 0.1	$0.07 \pm 0.01 M_\odot$	6.66

Table 5.15. The results for model v. the smooth isotropic density distribution with outer axes of 4.0×2.9 pc and inner axes of 2.13×1.7 pc entirely inside the diffuse radiation source.

VI. Čadež et al. (2004) axes with dust and gas in a shell 0.1 pc thick

VII. Clumpy Model - Clumps with radius 0.111 pc outside of the radiation field

The best fits to the observed SED for the model with all the material in the clumps with a filling factor of 0.1 and an electron density of density of 1400 cm^{-3} are shown

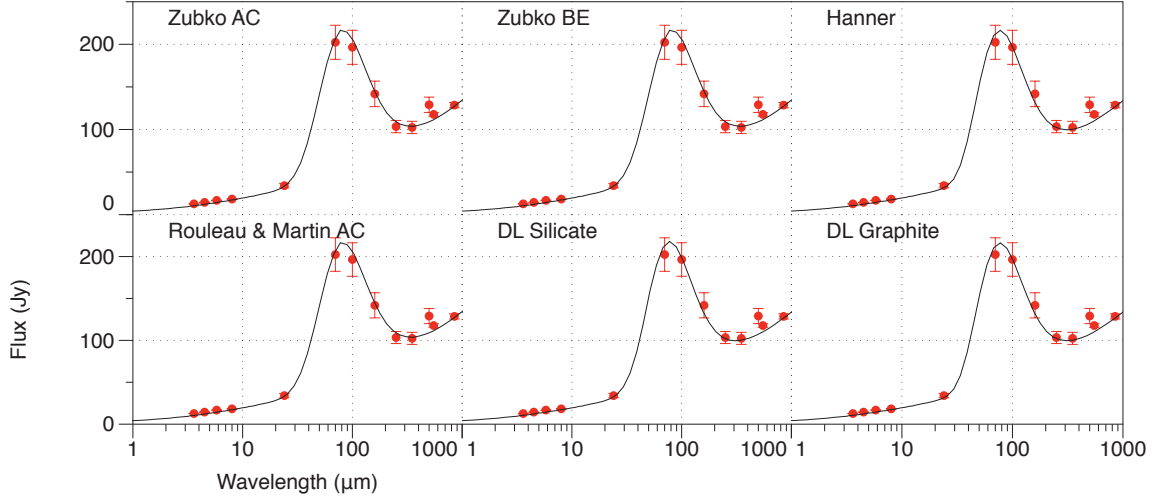


Figure 5.21. Best fit models plotted with observed SEDs for the six different sets of optical constants using a smooth isotropic density distribution in a shell 0.1 pc thick and a inner axes of 1.1×1.1 pc entirely inside the diffuse radiation source.

Optical Constants	a_{min}	a_{max}	α	M_{dust}	χ^2
Zubko et al. ACAR	$0.005 \mu\text{m}$	$0.7 \mu\text{m}$	2.7 ± 0.1	$0.10 \pm 0.02 M_\odot$	6.08
Zubko et al. BE	$0.005 \mu\text{m}$	$0.5 \mu\text{m}$	2.7 ± 0.1	$0.08 \pm 0.01 M_\odot$	5.99
Rouleau & Martin AC1	$0.01 \mu\text{m}$	$0.8 \mu\text{m}$	2.9 ± 0.1	$0.05 \pm 0.01 M_\odot$	4.98
Mixed Model	$0.01 \mu\text{m}$	$1.0 \mu\text{m}$	3.0 ± 0.1	$0.12 \pm 0.02 M_\odot$ $0.04 M_\odot$ Zubko BE $0.08 M_\odot$ DL silicates	5.23
Draine & Lee Silicate	$0.01 \mu\text{m}$	$0.9 \mu\text{m}$	3.5 ± 0.1	$0.26 \pm 0.04 M_\odot$	5.44
Draine & Lee Graphite	$0.001 \mu\text{m}$	$0.25 \mu\text{m}$	2.8 ± 0.1	$0.6 \pm 0.01 M_\odot$	6.03

Table 5.16. The results for model VI. the smooth isotropic density distribution in a shell 0.1 pc thick and a inner axes of 1.1×1.1 pc entirely inside the diffuse radiation source..

in Figure 5.22 with parameters used to achieve these fits are shown in Table ??VII. There is a factor of 2-3 increase in the mass of dust determined using the clumpy models depending on the set of optical constants used. The clumps are outside the radiation field and start at a radius of 3.0×2.0 pc and decrease with an r^{-2} dependence.

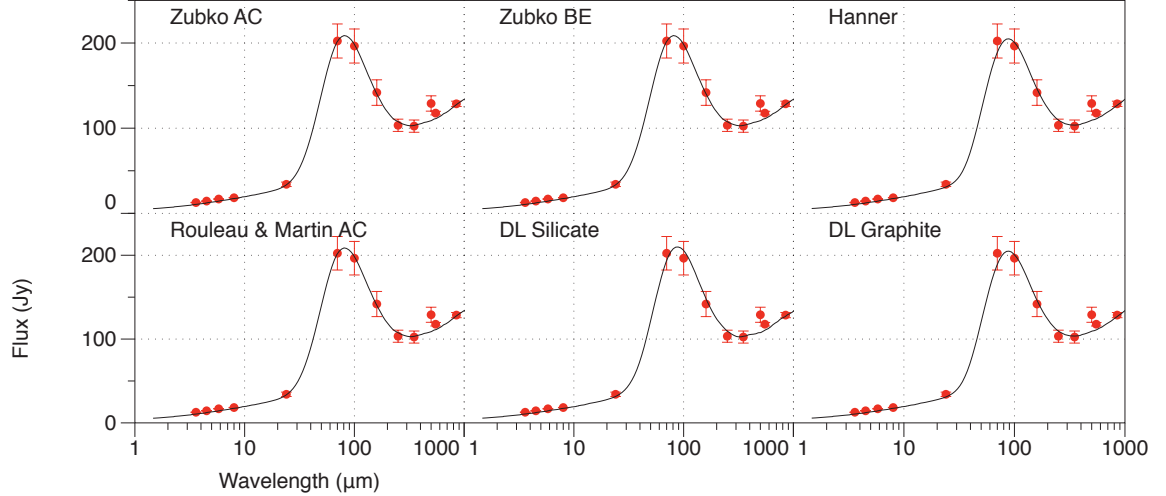


Figure 5.22. Best fit models plotted with observed SEDs for the six different sets of optical constants using a density distribution when all of the matter is in clumps with radius 0.111 pc and a density of 1400 cm^{-3} .

Optical Constants	a_{min}	a_{max}	α	M_{dust}	χ^2
Zubko AC	$0.07 \mu\text{m}$	$1.0 \mu\text{m}$	2.9 ± 0.1	$0.4 M_\odot$	11.3
Zubko BE	$0.07 \mu\text{m}$	$0.2 \mu\text{m}$	2.9 ± 0.1	$0.3 M_\odot$	11.5
Hanner	$0.07 \mu\text{m}$	$1.0 \mu\text{m}$	2.9 ± 0.1	$0.38 M_\odot$	13.1
Rouleau & Martin AC	$0.07 \mu\text{m}$	$1.0 \mu\text{m}$	3.0 ± 0.1	$0.24 M_\odot$	14.3
Mixed Model	$0.07 \mu\text{m}$	$1.0 \mu\text{m}$	3.0 ± 0.1	$0.40 M_\odot$ $0.25 M_\odot$ Zubko BE $0.15 M_\odot$ DL silicates	10.0
Draine & Lee Silicate	$0.07 \mu\text{m}$	$1.0 \mu\text{m}$	3.5 ± 0.1	$1.5 M_\odot$	14.4
Draine & Lee Graphite	$0.001 \mu\text{m}$	$0.25 \mu\text{m}$	3.0 ± 0.1	$0.40 M_\odot$	13.2

Table 5.17. The results for model VII. A clumpy geometry with clumps starting at axes of 3.0×2.0 pc decreasing with r^{-2} entirely outside the radiation source. The clumps have a of radius 0.111 pc with a density of 1400 cm^{-3} .

VIII. Clumpy Model - Clumps with radius 0.037 pc outside of the radiation field

The best fits to the observed SED for the model with all the material in the clumps

with a volume filling factor of 0.1 and a density of $N_e = 1900 \text{ cm}^{-3}$, clump radius of 0.037 pc are shown in Figure 5.23 with parameters used to achieve these fits are shown in Table ??VIII. The clumps are outside the radiation field and start at a axes of $1.5 \times 1.0 \text{ pc}$ and decrease with an r^{-2} dependence.

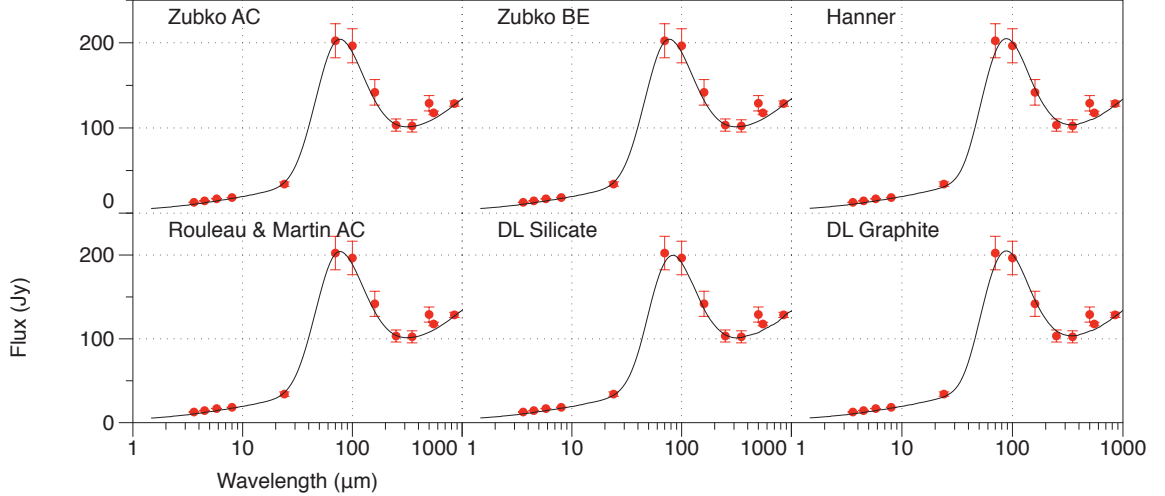


Figure 5.23. Best fit models plotted with observed SEDs for the six different sets of optical constants using a density distribution when all of the matter is in clumps of radius 0.037 pc with a density of 1900 cm^{-3} .

Optical Constants	a_{min}	a_{max}	α	M_{dust}	χ^2
Zubko AC	$0.07 \mu\text{m}$	$1.0 \mu\text{m}$	2.9 ± 0.1	$0.68 M_\odot$	11.2
Zubko BE	$0.07 \mu\text{m}$	$0.2 \mu\text{m}$	2.9 ± 0.1	$0.50 M_\odot$	10.9
Hanner	$0.07 \mu\text{m}$	$1.0 \mu\text{m}$	2.9 ± 0.1	$0.63 M_\odot$	13.9
Rouleau & Martin AC	$0.07 \mu\text{m}$	$1.0 \mu\text{m}$	3.0 ± 0.1	$0.44 M_\odot$	13.7
Draine & Lee Silicate	$0.07 \mu\text{m}$	$1.0 \mu\text{m}$	3.5 ± 0.1	$2.0 M_\odot$	12.1
Draine & Lee Graphite	$0.001 \mu\text{m}$	$0.25 \mu\text{m}$	3.0 ± 0.1	$0.47 M_\odot$	12.2

Table 5.18. The results for model VIII. A clumpy geometry with clumps starting at axes of $3.0 \times 2.0 \text{ pc}$ decreasing with r^{-2} entirely outside the radiation source. The clumps have a of radius 0.037 pc with a density of 1900 cm^{-3} .

IX. Clumpy model with Davidson & Fesen (1985) geometry

The best fits for the clumpy model with the inner axes of $1.05 \times 0.7 \text{ pc}$ decreasing with an r^{-2} dependence with all the clumps inside the radiation field to the observed SED are shown in Figure 5.24 with parameters used to achieve these fits are shown in Table 5.19. The clumps have a density of 1900 cm^{-3} , clump radius of 0.037 pc.

The clump density is decreasing with a r^{-2} dependence.

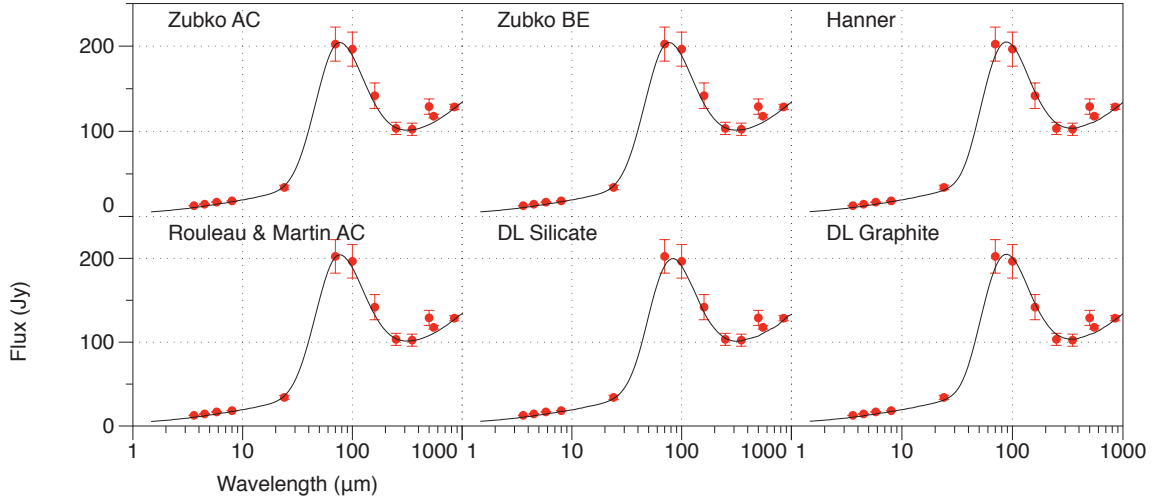


Figure 5.24. Best fit models plotted with observed SEDs for the six different sets of optical constants using a density distribution when all of the matter is in clumps of radius 0.037 pc with a density of 1900 cm^{-3} .

The dust mass determined with the Zubko et al. (1996) BE grain optical properties used in Gomez et al. (2012) give a dust mass almost twice that of the mass determined empirically. The mass determined using Draine & Lee (1984) silicate optical properties give a mass three times higher than the empirically determined value.

Optical Constants	a_{min}	a_{max}	α	M_{dust}	χ^2
Zubko et al. ACAR	$0.005 \mu\text{m}$	$0.7 \mu\text{m}$	2.7 ± 0.1	$0.25 \pm 0.04 M_\odot$	6.08
Zubko et al. BE	$0.005 \mu\text{m}$	$0.5 \mu\text{m}$	2.7 ± 0.1	$0.18 \pm 0.03 M_\odot$	5.99
Rouleau & Martin AC1	$0.01 \mu\text{m}$	$0.8 \mu\text{m}$	2.9 ± 0.1	$0.15 \pm 0.03 M_\odot$	4.98
Mixed Model	$0.01 \mu\text{m}$	$1.0 \mu\text{m}$	3.0 ± 0.1	$0.25 \pm 0.05 M_\odot$	5.23
				$0.13 M_\odot$ Zubko BE	
				$0.12 M_\odot$ DL silicates	
Draine & Lee Silicate	$0.01 \mu\text{m}$	$0.9 \mu\text{m}$	3.5 ± 0.1	$0.98 \pm 0.19 M_\odot$	5.44
Draine & Lee Graphite	$0.001 \mu\text{m}$	$0.25 \mu\text{m}$	2.8 ± 0.1	$0.17 \pm 0.03 M_\odot$	6.03

Table 5.19. The results for model IX. A clumpy geometry with clumps starting at axes of 2.1×1.4 pc decreasing with r^{-2} entirely inside the radiation source.

X. Clumpy model with Lawrence et al. (1995) geometry

The best fits for the clumpy model with the inner axes of 1.15×0.85 pc decreasing with an r^{-2} dependence with all the clumps inside the radiation field to the observed

SED are shown in Figure 5.25 with parameters used to achieve these fits are shown in Table ??IX. The clumps have a density of 1900 cm^{-3} , clump radius of 0.037 pc. The clump density is decreasing with a r^{-2} dependence.

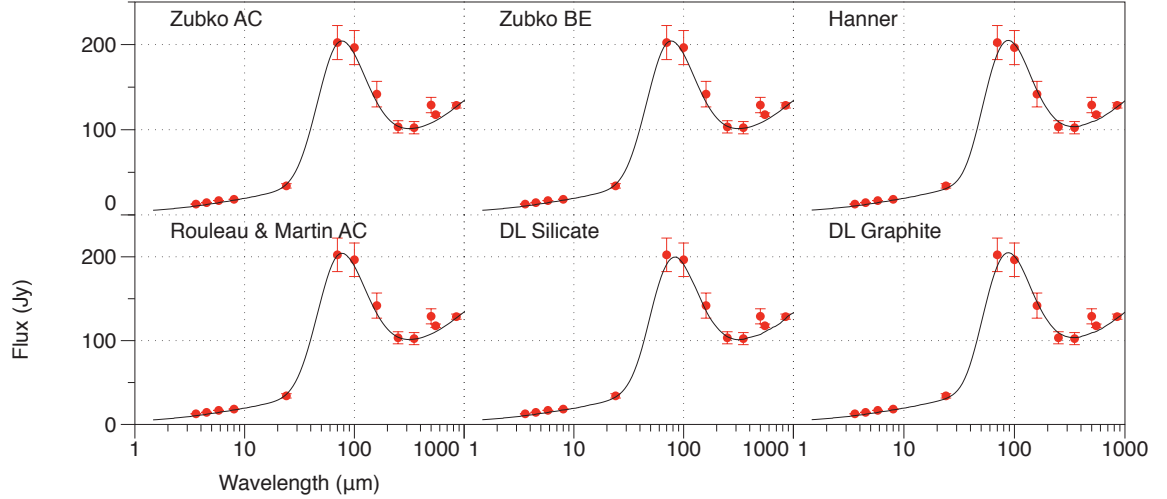


Figure 5.25. Best fit models plotted with observed SEDs for the six different sets of optical constants using a density distribution when all of the matter is in clumps of radius 0.037 pc with a density of 1900 cm^{-3} .

Optical Constants	a_{min}	a_{max}	α	M_{dust}	χ^2
Zubko et al. ACAR	$0.005 \mu\text{m}$	$0.7 \mu\text{m}$	2.7 ± 0.1	$0.25 \pm 0.04 M_{\odot}$	5.12
Zubko et al. BE	$0.005 \mu\text{m}$	$0.5 \mu\text{m}$	2.7 ± 0.1	$0.18 \pm 0.03 M_{\odot}$	6.97
Rouleau & Martin AC1	$0.01 \mu\text{m}$	$0.8 \mu\text{m}$	2.9 ± 0.1	$0.15 \pm 0.03 M_{\odot}$	5.00
Mixed Model	$0.01 \mu\text{m}$	$1.0 \mu\text{m}$	3.0 ± 0.1	$0.25 \pm 0.05 M_{\odot}$	4.98
				$0.13 M_{\odot}$ Zubko BE	
				$0.12 M_{\odot}$ DL silicates	
Draine & Lee Silicate	$0.01 \mu\text{m}$	$0.9 \mu\text{m}$	3.5 ± 0.1	$0.98 \pm 0.19 M_{\odot}$	5.11
Draine & Lee Graphite	$0.001 \mu\text{m}$	$0.25 \mu\text{m}$	2.8 ± 0.1	$0.17 \pm 0.03 M_{\odot}$	6.03

Table 5.20. The results for model x. A clumpy geometry with clumps starting at axes of 2.3×1.7 pc decreasing with r^{-2} entirely inside the radiation source.

The masses for the different clumped geometries are identical. This is unsurprising as they use the same volume filling factor and have the same number of clumps. Each clump is embedded in the heating radiation source so they are heated from all around in the same way, which leads to the identical dust masses.

	Neutral	1^+	2^+	3^+	4^+	5^+
Hydrogen	0.130	0.870				
Helium	0.332	0.630	3.77×10^{-2}			
Carbon	1.01×10^{-2}	0.730	0.248	2.08×10^{-2}	2.01×10^{-6}	1.04×10^{-10}
Nitrogen	1.04×10^{-2}	0.708	0.237	5.39×10^{-3}	1.17×10^{-6}	2.34×10^{-9}
Oxygen	0.144	0.721	0.107	2.75×10^{-3}	1.05×10^{-6}	7.37×10^{-8}
Neon	0.114	0.772	0.113	3.72×10^{-4}	4.10×10^{-6}	9.93×10^{-9}
Sulphur	0.198	0.449	0.299	6.95×10^{-3}	3.34×10^{-5}	5.66×10^{-8}
Argon	2.31×10^{-5}	0.116	0.702	0.178	2.31×10^{-3}	4.25×10^{-5}

Table 5.21. Global ionisation fractions of elements in the clumpy models

5.2.3 Ionisation

Table 5.21 is the global ionisation of the clumped model. Most of the elements were found to have a neutral fraction of 10%. The main exception to this is the neutral fraction of Helium, which is significantly higher at 33%. This high neutral fraction of Helium means that standard abundance analysis using recombination lines with over estimate the He/H ratio and thus mass. Our modelled fraction of Helium (85%) is in agreement with the photoionisation models of MacAlpine & Satterfield (2008) value of 89% of the emitting gas being Helium. The ratio of N^+/N^{2+} is 3.98, which is in good agreement with the values calculated from the *Herschel* and ISO-LWS observations discussed in Chapter 3.

5.3 Discussion

5.3.1 The importance of using both gas and dust

The models need to contain gas to help constrain the dust mass in the models. Figure 5.26 shows the best fitting models' synchrotron subtracted SED and the same dust mass in a dust only model, showing that line heating of the dust by line emission plays an important role in the Crab Nebula. Calculating the integrated flux from the two different models, the dust and gas model gives a dust emission flux of $9.58 \times 10^{-3} \text{ W m}^{-2}$, which the dust only model has a flux of $8.26 \times 10^{-3} \text{ W m}^{-2}$, which is 16% less than the gas and dust model. This difference in heating is also mirrored in the UV SED of the models, shown in Figure 5.27.

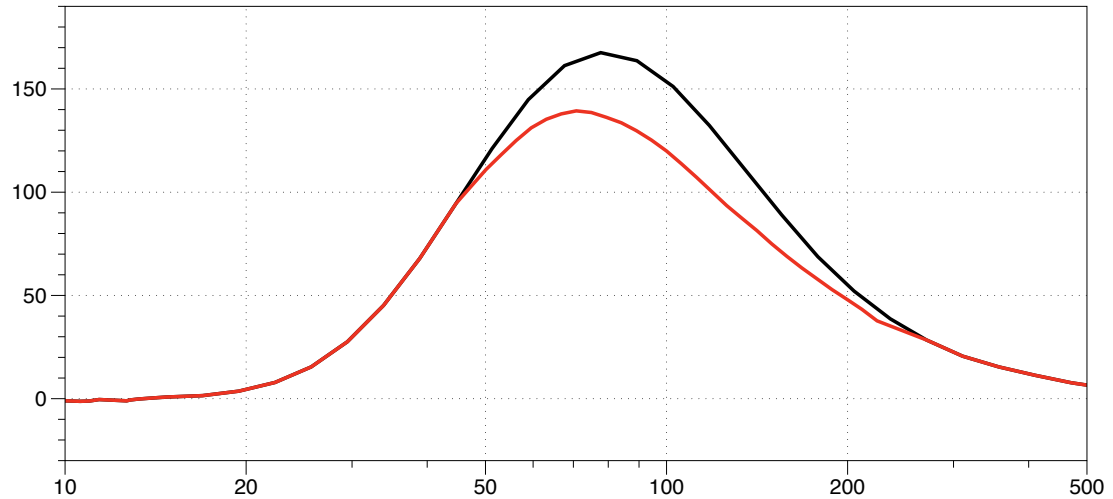


Figure 5.26. Synchrotron subtracted infrared SEDs of the best fit dust mass for the gas and dust model and a model with the same parameters with no gas, just dust.

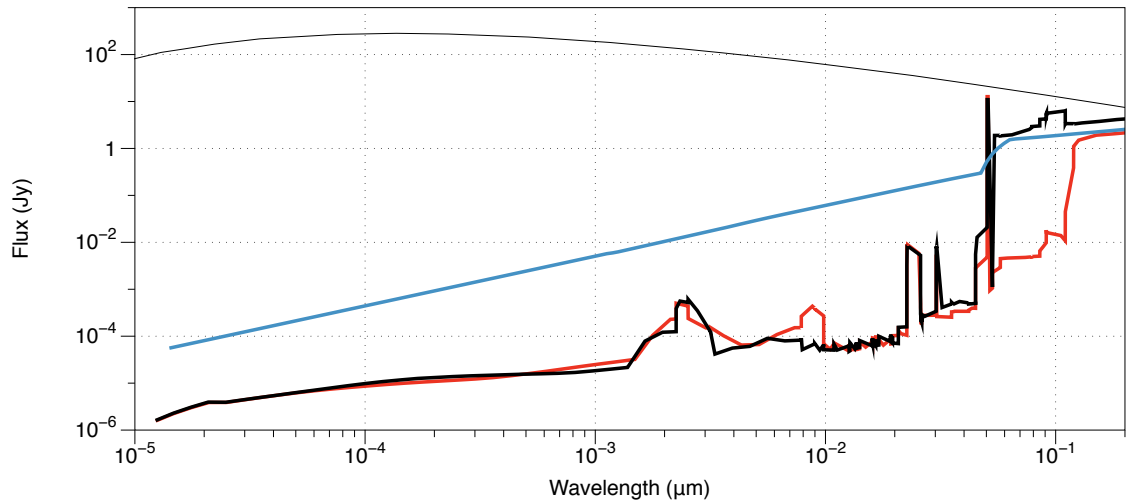


Figure 5.27. The ultraviolet SED for models with gas and dust, gas only and dust only

5.3.2 The importance of using a diffuse heating source

Figure 5.28 shows the Best fit model SED for model x plotted with a black line and a model run with identical geometry, dust mass and elemental abundance but with a central point source as the heating source shown in blue. The central heating source leads to the dust closer to it being heated significantly more than the dust further away. This makes it impossible to fit SED as to fit the mid infrared points (particularly the $24\ \mu\text{m}$ observation) tracing the warm dust, very low dust masses are required, but to fit the far infrared points that trace the colder dust far larger masses of dust are required, it is not possible to fit both at the same time while also matching any observed geometry.

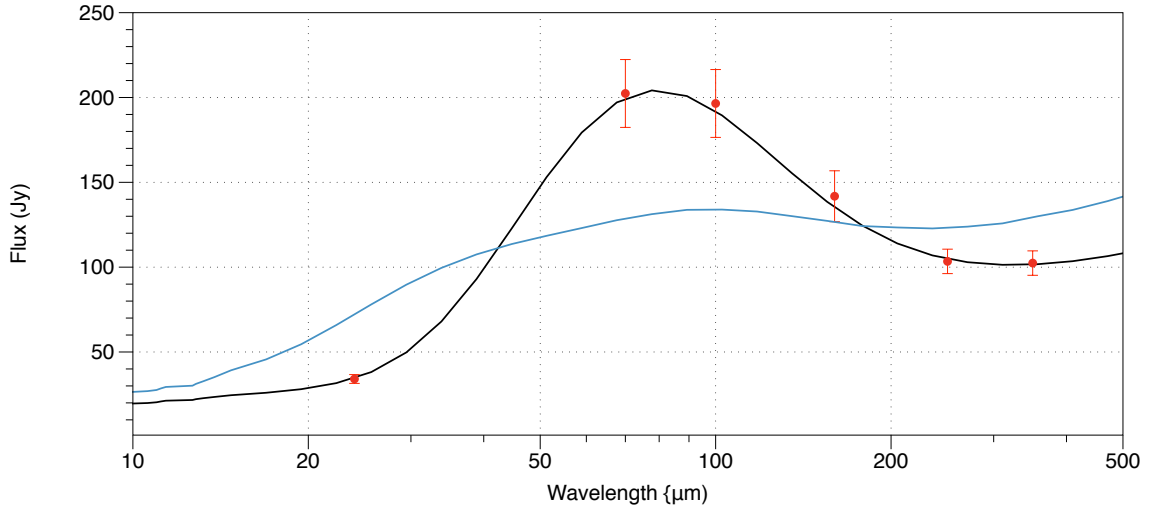


Figure 5.28. Best fit model SED for model x (black line) along with a model run with identical geometry, dust mass and elemental abundance but with a central point source as the heating source (blue line)

5.3.3 Clumping

The models with smooth density distributions (models I and II) both agree within uncertainty to the empirically determined dust mass.

Temim et al. (2012) found the majority of the dust in the crab nebula to be in the clumpy filamentary structures using *Spitzer* spectra. This is also supported by the synchrotron removed maps in Gomez et al. (2012) showing both the warm and cold dust

concentrated in the filaments of the nebula using the *Herschel* PACS 160 μm image. Using a clumped density distribution to simulate the filamentary structure of the Crab Nebula increases the mass of dust observed by a factor of between two and three required to fit the observed SED depending on the optical constants used. This increase is probably down to self shielding and self absorption in the dense regions of the clumps. A diffuse inter-clump medium does cause an increase in the amount of dust needed to fit the observed SED as shown by the differences between models III and IV. The lack of any dust emission from the inter-clump medium leads to favouring model III, with the matter entirely in the clumps. The masses of each clump are shown in Table 5.23 as well as the optical depth of each clump from centre to surface.

5.3.4 Optical Properties

The choice of optical properties has a large effect on the estimate of dust mass. The optical constants of refractive (n) and absorption (k) indices can be used to calculate $Q_{\text{abs}}(\lambda)$, a factor showing how much light is absorbed by a grain of a given wavelength using Mie Scattering (Mie 1908). Figure 5.29 shows $Q_{\text{abs}}(\lambda)$ calculated for each of the amorphous carbon optical constants used for a dust grain size of 0.1 μm to compare the amount of absorption which in turn governs the amount of emission by dust grains.

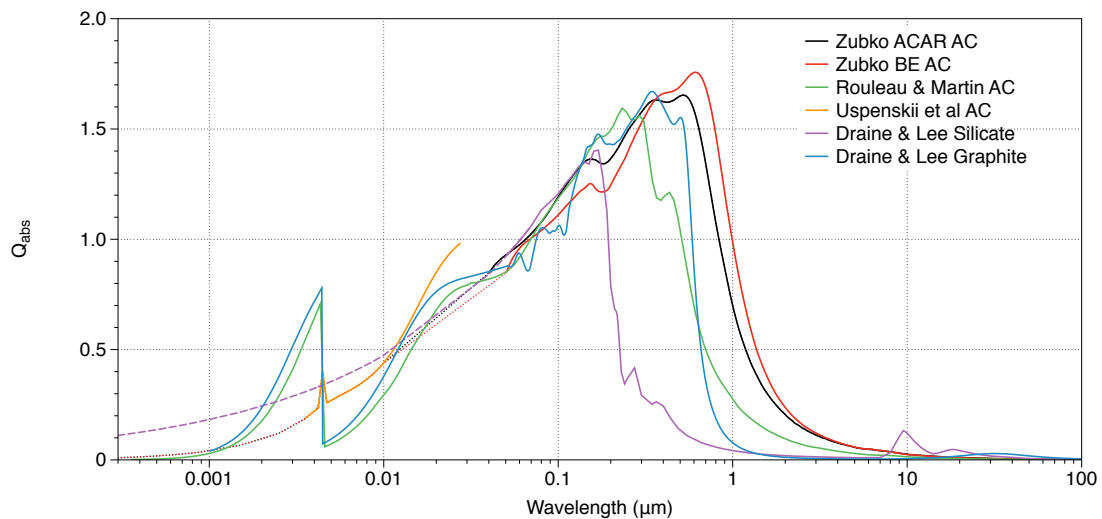


Figure 5.29. $Q_{\text{abs}}(\lambda)$ against Wavelength for amorphous carbon grain optical constants used and a grain size of 0.1 μm .

The absorption factor is much higher for the Rouleau & Martin (1991) and Draine & Lee (1984) graphite, in the region where there is more energy being emitted than the other optical constants which have their peak absorption at longer wavelengths. This is caused by the K-edge of the carbon atoms, it is the point at which the energy photoelectrically excites an electron from its potential well rather than heating the dust grain. This increase in absorption will lead to increased heating which in turn leads to increased emission. This explains why a lower mass of dust is needed to fit the observed SED using these constants as opposed to those from Zubko et al. (1996). There are differences between the different sets of optical constants from Zubko et al. (1996) using the differently prepared samples for similar reasons. It is debatable whether this K-shell absorption will lead to increased heating as the energy goes in to exciting an electron which would mean that less of the energy goes in to heating the dust grains. Running a smooth model with the Rouleau & Martin (1991) optical properties but the with k-shell absorption spike removed sees a factor of 2 increase in the dust mass needed to fit the observed SED.

The silicate K-edge varies depending on the species of silicate, but all are around $6 \times 10^{-4} \mu\text{m}$ (Li et al. 1995), which is shorter than the shortest wavelengths used in these models.

The Zubko et al. (1996) data are calculated using self consistent laboratory data where as those provided by Rouleau & Martin (1991) are not. Both sets of optical constants consider the shapes of the grains as with a continuous discrete ellipsoid approximation, however Rouleau & Martin (1991) give each ellipsoid shape equal weighting while the Zubko et al. (1996) constants weight different grain shapes differently depending on how likely they are to occur. The constants from Hanner (1988) were determined from extinction data from a large polished surface of a glassy carbon rather than grain particles and does not consider grain shape in the constants themselves. The Zubko et al. (1996) optical constants also give a much better fit to the interstellar extinction curves than other optical constants (Zubko et al. 2004). Given the consistency of the laboratory data, considerations of grain shape and the better fit given we favour the results from the Zubko et al. (1996) optical constants. The Zubko et al. (1996) ACAR sample is made by electrical discharge across carbon electrodes in Argon gas, where as the BE sample is made by burning benzene in air. The BE sample is chemically richer and more graphitic and thus considered

to be a better analogue to the dust formed in supernovae.

5.3.5 Grain Size Distribution

With the models run with standard MRN grain size distribution (Mathis, Rumpl, & Nordsieck 1977), the most significant excess is around $24 \mu\text{m}$. This implies that there is too much warm dust in the model. To better fit this, a_{min} , the minimum grain radius, is increased to remove smaller, warmer dust grains. The dust mass must be increased slightly to compensate for this.

The peak of the far infrared dust emission is also at a shorter wavelength than observed. This is addressed by increasing a_{max} , the maximum grain radius. This will make the dust population colder and therefore have its peak at a longer wavelength.

The number of grains of a given radius is proportional to a power law

$$n(a) \propto a^{-\alpha} \quad (5.3)$$

with the mass being proportional to the volume and cross section being proportional to the surface area

$$m(a) \propto a^3 \quad (5.4)$$

$$\sigma(a) \propto a^2 \quad (5.5)$$

if $\alpha = 3.5$ as in the standard MRN the the total distribution of mass of dust grains will be

$$\begin{aligned} \Sigma m(a) &\propto \int_{a_{min}}^{a_{max}} a^3 a^{-\alpha} da \\ &\propto \int_{a_{min}}^{a_{max}} a^3 a^{-3.5} da \propto \int_{a_{min}}^{a_{max}} a^{-0.5} da \propto a^{0.5} \end{aligned} \quad (5.6)$$

for surface area

$$\begin{aligned} \Sigma \sigma(a) &\propto \int_{a_{min}}^{a_{max}} a^2 a^{-\alpha} da \\ &\propto \int_{a_{min}}^{a_{max}} a^2 a^{-3.5} da \propto \int_{a_{min}}^{a_{max}} a^{-1.5} da \propto a^{-0.5} \end{aligned} \quad (5.7)$$

most of the mass is in the smaller grains whilst most of the surface area is in the larger grains. Smaller grains are hotter than larger grains, so fit the data better you vary the maximum and minimum grain sizes. However with $\alpha = 2.9$ as found in these models.

$$\begin{aligned} \Sigma m(a) &\propto \int_{a_{min}}^{a_{max}} a^3 a^{-\alpha} da \\ &\propto \int_{a_{min}}^{a_{max}} a^3 a^{-2.9} da \propto \int_{a_{min}}^{a_{max}} a^{0.1} da \propto a^{1.1} \end{aligned} \quad (5.8)$$

for surface area

$$\begin{aligned} \Sigma \sigma(a) &\propto \int_{a_{min}}^{a_{max}} a^2 a^{-\alpha} da \\ &\propto \int_{a_{min}}^{a_{max}} a^2 a^{-2.9} da \propto \int_{a_{min}}^{a_{max}} a^{-2.1} da \propto a^{-1.1} \end{aligned} \quad (5.9)$$

meaning the mass is distributed with more mass in the larger colder grains but the surface area still being dominated by the smaller grains. This makes sense given the dramatic increase in observed dust mass when the colder dust is observed with *Herschel* as opposed to when just the warmer dust observed with *Spitzer* is taken in to account.

Figure 5.30 shows the effect of varying α on the fitted SED, a higher α of 3.1 (green line) moves the peak of the distribution to shorter wavelengths whilst a lower α of 2.7 moves the peak long ward. This is as mentioned above the lower the value of α the more biased the distribution is towards larger grains, which are colder and thus emit at longer wavelengths. Larger colder grains also require a greater mass than smaller, warmer grains to get the same amount of flux. As a result of this, as α decreases the modelled flux at longer wavelengths also decreases for the same mass of dust.

Figure 5.31 is a plot to show the effect of changing the upper limit of the grain size distribution using model x. The black line shows the best fit parameters, whilst the green line has a maximum grain radius of $1.5 \mu\text{m}$ and the blue line has a maximum grain radius

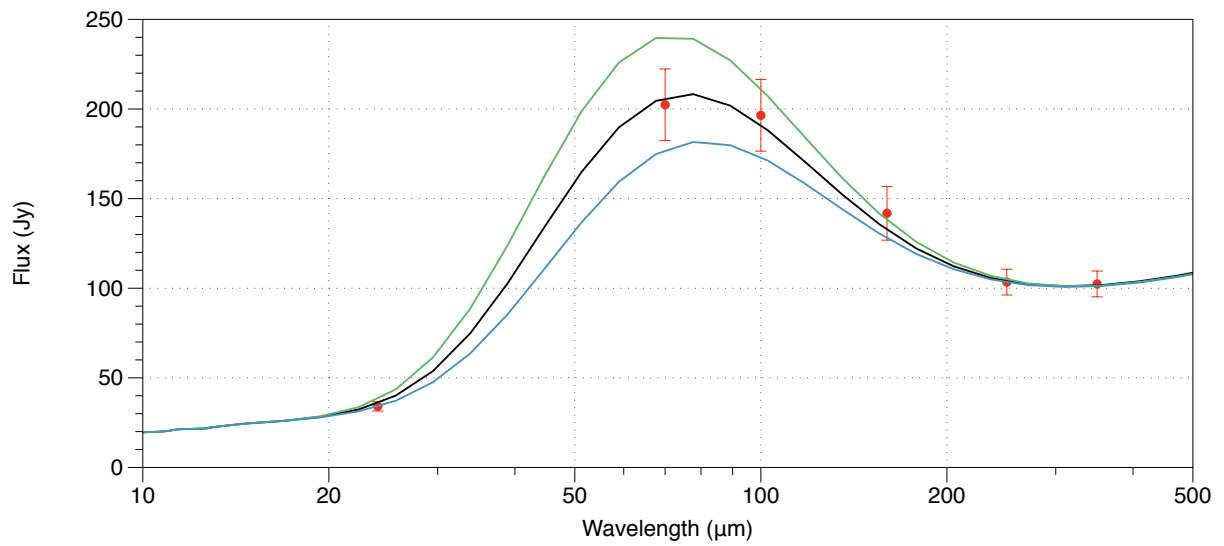


Figure 5.30. the effect of varying the power law slope α on the fitted SED..

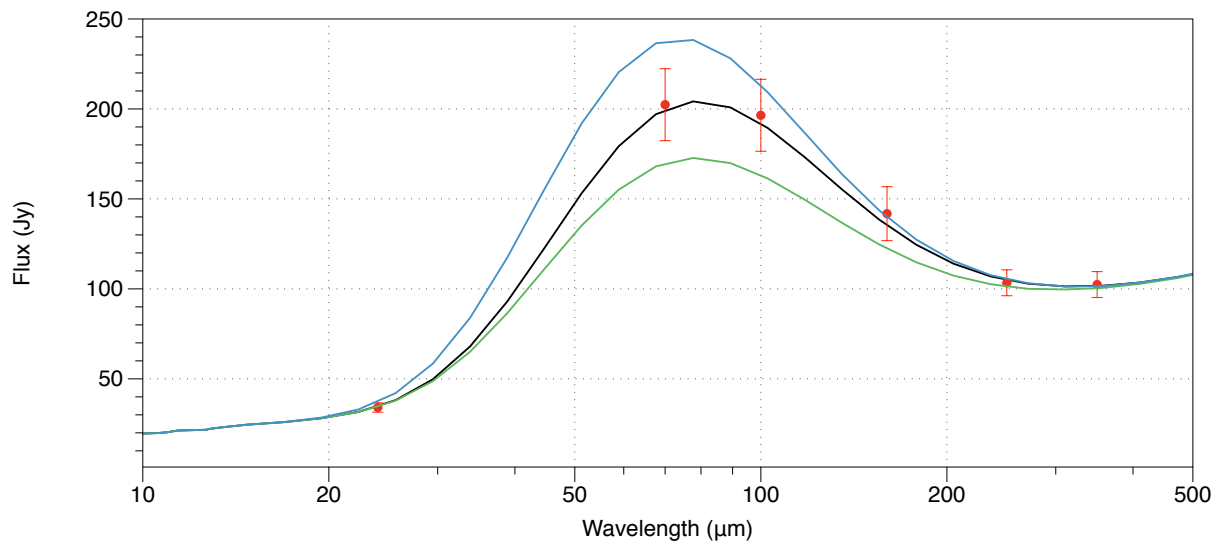


Figure 5.31. the effect of varying the maximum grain size, a_{max} on the fitted SED.

of $0.5 \mu\text{m}$. Whilst the peak flux is in approximately the same place, the flux in the far infrared varies a lot. Larger dust grains are colder and thus require more mass to emit the same flux which is why there is less flux for the larger maximum grain size. Because there is a large mass of cold, large dust grains in the Crab Nebula, the maximum grain size has a big effect on the determination of the overall mass of dust.

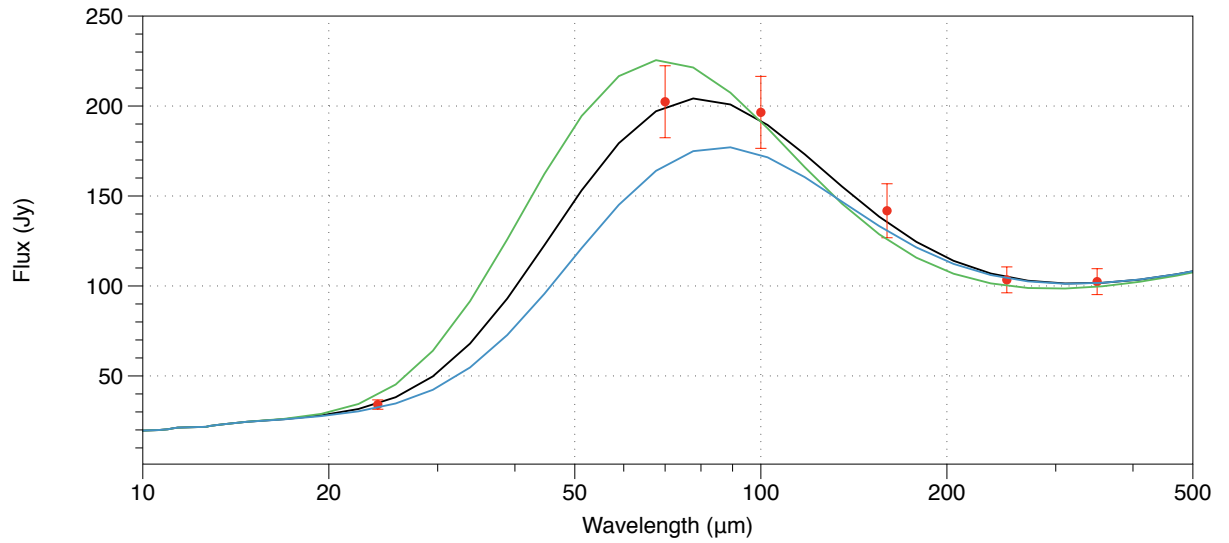


Figure 5.32. the effect of varying the minimum grain size, a_{min} on the fitted SED..

Figure 5.32 is a plot to show the effect of changing the lower limit of the grain size distribution using model x. The black line shows the best fit parameters, the green line shows a model with an a_{min} of $0.0001 \mu\text{m}$ and the blue line shows a model with an a_{min} of $0.01 \mu\text{m}$. As there is very little warm dust in the Crab Nebula, this is a very weak effect and over two orders of magnitude shows only a very little difference in fitting the warm dust component, although it does have an effect on fitting the cooler dust component due to the large skewing effect such a large change in the minimum grain radius has on the power law grain size distribution.

There is a degeneracy between the maximum grain radius and the slope of the power law. It is possible to get similarly good fits to the results presented here using a higher α and a_{max} . However, to do so requires an unphysically large mass of dust to do so. Using model x and the Zubko et al. (1996) BE optical properties, $0.71 M_\odot$ of dust is required to

fit to the observed SED. There is probably a degeneracy with the minimum grain radius as well, but the effect of the minimum grain radius is so small that this becomes negligible.

5.3.6 Continuous Distribution of Ellipsoids

The shape of grains can have an effect on their optical properties. An alternative treatment for the scattering and absorption of light by particles is a continuous distribution of ellipsoids (CDE). Where Mie scattering theory assumes all grains are spherical, CDE takes a distribution of ellipsoids from needles to disks to spheres to attempt to take in to account the non spherical nature of dust grains. This can have a significant effect on the mass of dust, requiring 20% (see Table 5.22 for a set of results using CDE rather than Mie scattering using model x) less dust with carbonaceous species to fit the same observed far infrared flux. Given that this distribution considers everything from needles and discs to spheres, it is arguably less realistic than just assuming that the dust grains are spherical.

Optical Constants	a_{min}	a_{max}	α	M_{dust}	χ^2
Zubko et al. ACAR	$0.005 \mu\text{m}$	$0.7 \mu\text{m}$	2.7 ± 0.1	$0.20 \pm 0.04 M_\odot$	7.52
Zubko et al. BE	$0.005 \mu\text{m}$	$0.5 \mu\text{m}$	2.7 ± 0.1	$0.15 \pm 0.03 M_\odot$	9.69
Rouleau & Martin AC1	$0.01 \mu\text{m}$	$0.8 \mu\text{m}$	2.9 ± 0.1	$0.13 \pm 0.03 M_\odot$	7.50
Mixed Model	$0.01 \mu\text{m}$	$1.0 \mu\text{m}$	3.0 ± 0.1	$0.20 \pm 0.05 M_\odot$	4.89
				$0.13 M_\odot$	Zubko BE
				$0.12 M_\odot$	DL silicates
Draine & Lee Silicate	$0.01 \mu\text{m}$	$0.9 \mu\text{m}$	3.5 ± 0.1	$0.85 \pm 0.19 M_\odot$	8.77
Draine & Lee Graphite	$0.001 \mu\text{m}$	$0.25 \mu\text{m}$	2.8 ± 0.1	$0.14 \pm 0.03 M_\odot$	7.13

Table 5.22. The results for model x. A clumpy geometry with clumps starting at axes of 2.3×1.7 pc decreasing with r^{-2} entirely inside the radiation source using a CDE scattering routine rather than a Mie scattering routine.

5.3.7 Optical Depths of the Clumps

The optical depth is given by

$$\tau(\lambda) = \int \kappa(\lambda) \rho dz \quad (5.10)$$

where κ is the mass absorption coefficient of the dust and ρ is the number density of dust grains. The clump mass or gas and dust and the optical depth of each at τ_v are shown

in Table 5.23 for the larger clumps and 5.24 for the smaller clumps. The smaller clumps shown in 5.24 are in agreement with observed sizes and optical depths of clumps (Sankrit et al. 1998).

Optical Properties	Gas Mass	Dust Mass	τ_v
Zubko ACAR	0.054	0.0029	3.11
Zubko BE	0.054	0.0023	4.29
Rouleau & Martin AC1	0.054	0.0018	3.61
Mixed Model	0.054	0.0031	3.57
Draine & Lee Silicate	0.054	0.012	2.84
Draine & Lee Graphite	0.054		

Table 5.23. The mass of dust, gas and the optical depth of each clump from centre to surface for the model with the clumps outside the radiation field.

Optical Properties	Gas Mass	Dust Mass	τ_v
Zubko ACAR	0.024	8.6×10^{-4}	0.79
Zubko BE	0.024	6.3×10^{-4}	1.05
Rouleau & Martin AC1	0.024	5.2×10^{-4}	0.92
Mixed Model	0.024	8.6×10^{-4}	0.91
Draine & Lee Silicate	0.024	3.4×10^{-3}	0.72
Draine & Lee Graphite	0.024	5.9×10^{-4}	0.95

Table 5.24. The mass of dust, gas and the optical depth of each clump from centre to surface for the model with the clumps embedded in the radiation field.

5.3.8 Total Nebula Mass

Using the electron density and elemental abundances it is possible to determine the mass of gas in the nebula. These masses are shown in table 5.26. The electron density required to match the H_β flux in the smooth models gives a gas mass that is a considerable over estimate. The clumpy models give a mass that is in agreement with masses derived by other radiative transfer models and those determined by other means (MacAlpine & Satterfield 2008; Smith 2013). Other discussions of the mass of the Crab Nebula suggest that a higher progenitor mass is required, and that there is an extra "invisible" (non-emitting) gas component, as the Crab Nebula was bright enough to be visible during the day when it first went supernova (Hester 2008), however Smith (2013) suggest that this observed emitting mass of gas is enough to explain this luminosity with a strong circumstellar

interaction during the initial phase of the supernova. This is also supported by the shell structure of the ejecta.

5.3.9 Predicting Photometric Fluxes

As another way of validating the model, we use the modelled SEDs to predicted the observed broadband photometric flux in each of the *Herschel* bands. This is done using

$$F = \frac{\int_0^\infty F(\lambda)S(\lambda)}{\int_0^\infty S(\lambda)} \quad (5.11)$$

Where $F(\lambda)$ is the flux and $S(\lambda)$ is the filter profile for the wavelength band. This is then colour corrected to account for the difference between actual wavelength that observes that flux and the quoted wavelength. The predicted fluxes are shown, along with observed fluxes and colour corrections for the smooth and clumpy models using the Zubko et al. (1996) BE sample in table 5.27. The predicted fluxes are in good agreement with those observed, with the exception of the $500\ \mu m$ band. This difference is caused by the model also being fitted to the lower flux of the *Planck* $550\ \mu m$ band.

5.4 Alternative Dust Mass Estimates

5.4.1 The Temim and Dwek 2013 Estimate

Temim & Dwek (2013) take a different approach to determining a mass of dust in the Crab Nebula. They do this by balancing an equation for the rate of grain heating with an equation for the radiative cooling of each grain, repeating for a number of different grain sizes they build up a size distribution. This technique assumes that all the dust is in the same location, in this particular case at 0.5 pc from a central point heating source. As a result the dust is heated considerably more than if it were distributed throughout a nebula. This increased heating leads to increased emission and thus a lower estimate of the dust mass. As previously discussed in section 5.3.3, the dust in the Crab Nebula is contained in filamentary structures so will not be uniformly heated. This difference in heating is illustrated in Figure ?? which shows the grain temperature against radius from Temim & Dwek (2013) and the average grain temperature at 0.5 pc from the centre of the nebula taken from the smooth model using the Rouleau & Martin (1991) optical constants as a comparison.

	I Mass (M_{\odot})	II Mass (M_{\odot})	III Mass (M_{\odot})	IV Mass (M_{\odot})	V Mass (M_{\odot})	VI Mass (M_{\odot})
Hydrogen	1.8	5.53	4.47	0.8	0.81	0.81
Helium	13.2	42	33.97	5.86	5.99	5.99
Carbon	0.21	0.62	0.49	9.3×10^{-2}	9.91×10^{-2}	9.91×10^{-2}
Nitrogen	6.3×10^{-3}	1.2×10^{-2}	9.39×10^{-3}	2.8×10^{-3}	2.84×10^{-3}	2.84×10^{-3}
Oxygen	0.2	0.71	0.5	9.2×10^{-2}	7.94×10^{-2}	7.94×10^{-2}
Neon	0.05	5.0×10^{-2}	0.04	3.2×10^{-2}	7.8×10^{-2}	7.8×10^{-2}
Sulphur	0.02	8.8×10^{-3}	7.15×10^{-3}	1.02×10^{-2}	1.04×10^{-3}	1.04×10^{-3}
Argon	3.1×10^{-3}	1.2×10^{-3}	6.48×10^{-3}	1.4×10^{-3}	2.9×10^{-3}	2.9×10^{-3}
Total	15.5	48.9	40.1	6.89	7.02	7.02

Table 5.25. The masses of emitting gas phase elements in the Crab Nebula determined by the MOCASSIN models

	VII Mass (M_{\odot})	VIII Mass (M_{\odot})	IX Mass (M_{\odot})	X Mass (M_{\odot})	XI Mass (M_{\odot})	XII Mass (M_{\odot})	XIII Mass (M_{\odot})
Hydrogen	1.8	5.53	4.47	0.8	0.81	0.81	
Helium	13.2	42	33.97	5.86	5.99	5.99	
Carbon	0.21	0.62	0.49	9.3×10^{-2}	9.91×10^{-2}	9.91×10^{-2}	
Nitrogen	6.3×10^{-3}	1.2×10^{-2}	9.39×10^{-3}	2.8×10^{-3}	2.84×10^{-3}	2.84×10^{-3}	
Oxygen	0.2	0.71	0.5	9.2×10^{-2}	7.94×10^{-2}	7.94×10^{-2}	
Neon	0.05	5.0×10^{-2}	0.04	3.2×10^{-2}	7.8×10^{-2}	7.8×10^{-2}	
Sulphur	0.02	8.8×10^{-3}	7.15×10^{-3}	1.02×10^{-2}	1.04×10^{-3}	1.04×10^{-3}	
Argon	3.1×10^{-3}	1.2^{-3}	6.48×10^{-3}	1.4×10^{-3}	2.9×10^{-3}	2.9×10^{-3}	
Total	15.5	48.9	40.1	6.89	7.02	7.02	

Table 5.26. The masses of emitting gas phase elements in the Crab Nebula determined by the MOCASSIN models

Wavelength (μm)	Observed Flux (Jy)	Uncertainty	Smooth (Jy)	Correction	Clumpy (Jy)	Correction
24	46.4	8.0	40.63	1.026	41.21	1.0114
70	202.37	20	209.33	0.9819	193.27	1.0105
100	196.48	20	196.27	0.9940	200.07	0.9822
160	141.8	15	134.63	1.0245	147.99	1.0197
250	103.4	7.2	102.67	1.0063	113.97	0.9961
350	102.4	7.2	100.53	1.0033	106.3	1.0095
500	129	9.0	107.98	1.0079	110.55	1.0203

Table 5.27. Observed and predicted photometric fluxes for the *Herschel* wave bands and their colour correction factors.

5.4.2 Empirical Dust Masses

As the choice of optical constant seems to play a major role in the estimated dust mass, investigating the effect it has on the more often used empirical estimations of dust mass becomes a useful. Calculating κ , the dust mass absorption coefficient for a single grain size of $0.1 \mu m$ using a Mie scattering routine and using a single temperature planck function fit to the SED of the Crab Nebula, we can use equation 5.1 to investigate the effect that the different sets of optical properties for amorphous carbon species have in this case. The results are shown in table 5.28.

Optical properties	Dust Mass (M_{\odot})
Zubko AC	0.13
Zubko BE	0.09
Hanner	0.12
Rouleau & Martin	0.08

Table 5.28. Dust masses in the crab nebula calculated empirically using equation 5.1.

As the empirical dust determinations only use the optical data in the IR region where they are much more similar, the differences in dust mass calculated using this method are far less pronounced than they are when considering realistic heating and cooling of the dust using the entire wavelength range.

5.5 Conclusions

We have constructed a series of radiative transfer models to investigate and accurately determine the mass of dust formed in the ejecta of the supernova that has formed the Crab Nebula. Determining the mass of dust in the crab nebula using radiative transfer modelling gives higher dust masses than by fitting a simple two component black body to the spectral energy distribution giving a mass of 0.1-0.5 M_{\odot} of dust depending on the species of dust and optical constants used. These values are still in good agreement with those determined by empirical fitting to the SED. The mass only increases slightly when a smooth distribution of matter in the nebula is used. When clumped dust density distributions are used, the dust mass is determined to be 2-3 times higher depending on the optical properties are chosen with 0.3-1.5 M_{\odot} of dust.

How the dust is heated has a bigger impact on the mass of dust than the geometry it is in within the nebula. When the dust is placed within the diffuse radiation field, the models with smooth distributions have dust masses within uncertainty of one another, although systematically increasing with the volume of the nebula filled by gas and dust. When the clumps are embedded in the radiation source, the mass of dust required to fit the SEDs is independent of where the dust is in the geometry and is entirely down to how it is heated. The size of the clumps also plays a role in the mass of dust required to fit observations although these are contained by other observations.

The choice of optical constants used for a grain species to determine the mass of dust formed is very important. Different samples of carbon prepared in different ways have very different extinction curves which in turn means very different masses of dust are required to fit a given SED. There is a factor of 2-3 difference in the mass of dust between models that are otherwise identical using different sets of optical constants for amorphous carbon.

In reality the dust composition in the crab nebula is likely to be a mixture of many different grain types so the true value for the dust mass will lie somewhere within the limits presented here. This is a very large amount of dust leading a dust to gas mass ratio significantly higher than the interstellar medium. This means that dust condensation has been very efficient in the supernova remnant and that core collapse supernovae and their

remnants can provide enough dust to provide the observed dust masses at high redshift and make up the deficit in the dust budgets of local metal poor galaxies.

This page was intentionally left blank

Chapter 6

Conclusions and Future Work

If you can avoid using supernovae in your research, do!

Saul Perlmutter

This thesis presents a collection of work investigating galactic core collapse supernova remnants in the far infrared. The work is based around observations made using the *Herschel* Space Observatory's PACS and SPIRE instruments, supplemented by many other observatories across all wavelengths to investigate the physical conditions in supernovae and their effect on dust and molecule formations and destruction.

6.1 The Crab Nebula

The discovery of $^{36}\text{ArH}^+$ is a significant one that has opened up a new area of study in astrochemistry. It's been suggested as a better tracer of regions of molecular hydrogen than those currently used. This discovery in the Crab Nebula will be followed up with ALMA. This will resolve the lines giving us much more accurate information about the conditions under which it exists and has formed. These observations will also be sensitive enough to see any $^{38}\text{ArH}^+$ present. ^{36}Ar is formed by the s-process of neutron capture whereas ^{36}Ar is formed by explosive α capture. This ratio of $^{36}\text{Ar}/^{38}\text{Ar}$ will be the first observational constraint on the ratio between S-process and α capture process in supernovae.

We have constructed a series of radiative transfer models to determine the mass of dust present in the Crab Nebula supernova remnant. In the preferred models the gas and dust are located in clumps within an ellipsoidal diffuse synchrotron radiation source, powered by the pulsar wind nebula. The models are insensitive to the inner axis diameters from which the clump distributions extend.

Models with a smooth distribution of material require $0.10\text{--}0.18 M_{\odot}$ of Zubko et al. (1996) BE or ACAR amorphous carbon, respectively, or $0.35\text{--}0.48 M_{\odot}$ of Draine & Lee (1984) silicates, to fit the infrared and submillimeter SED defined by the *Herschel* and *Spitzer* observations of the nebula. This compares with the $0.12 \pm 0.02 M_{\odot}$ of Zubko BE amorphous carbon, or the $0.24^{+0.32}_{-0.08} M_{\odot}$ of Weingartner & Draine (2001) silicate dust, derived by Gomez et al. (2012) from two-component blackbody fits modified by the mass absorption coefficients for those materials.

Our smooth distribution models required implausibly large nebular gas masses of $16\text{--}49 M_{\odot}$ to fit the integrated optical line fluxes measured by Smith (2003) for the Crab Nebula, much larger than the $8\text{--}10 M_{\odot}$ initial mass usually estimated for the progenitor star, whereas our clumped models for the gas and dust, more consistent with the filamentary appearance of the nebula, required only $7.0 \pm 0.5 M_{\odot}$ of gas to match the integrated nebular emission line fluxes. The clumped model infrared SED fits, which are therefore preferred over those from the smooth models, required either $0.18 M_{\odot}$ (BE) or $0.25 M_{\odot}$ (ACAR) of Zubko amorphous carbon, $0.98 \pm 0.19 M_{\odot}$ of Draine & Lee silicate, or, for mixed chemistry dust, $0.11\text{--}0.21 \pm 0.04 M_{\odot}$ of Zubko BE amorphous carbon plus $0.4\text{--}0.6 \pm 0.03 M_{\odot}$ of silicates. Since our photoionization modelling yielded an overall gas-phase C/O ratio of 1.65 by number for the Crab Nebula, the clumped model dust masses obtained using just amorphous carbon, or amorphous carbon plus silicates, are favoured over silicate-only models. The total nebular mass (gas plus dust) is estimated to be $7.2 \pm 0.5 M_{\odot}$. The Crab Nebula's gas to dust mass ratio of 28–40 (depending on the exact grain type) is about 5–7 times lower than for the general ISM. As discussed in the Introduction, CCSN ejecta dust masses of $0.1 M_{\odot}$ or more, a constraint satisfied by the Crab Nebula, Cas A and SN 1987A, can potentially make a significant contribution to the dust budgets of galaxies.

Our best fit power-law grain size distributions, $n(a) \propto a^{-\alpha}$, had $\alpha \sim 3$, so that the majority of the dust mass resides in the largest particles, with $a_{max} = 0.5\text{-}1.0 \mu\text{m}$. Larger particles better withstand destruction by shock sputtering, for which the rate of reduction of grain radius, da/dt , is independent of the grain radius a , so that the smallest particles disappear first. The preponderance of larger particles in the Crab Nebula's dust, and the fact that they are in clumps, can help their longer-term survival when they eventually encounter the interstellar medium (Nozawa et al. 2007).

A mass of 8-13 M_\odot has previously been estimated for the Crab Nebula progenitor star (Hester 2008; Smith 2013). The fact that earlier nebular mass estimates have fallen well short of this mass range had been used as one of the arguments that faster moving material must exist beyond the main nebular boundaries (see e.g. Hester 2008). Arguments against that conclusion have however been presented by Smith (2013). The total nebular mass of $(7.2 \pm 0.5) M_\odot$ derived here, combined with a pulsar mass of at least $1.4 M_\odot$, implies a total mass of at least $8.6 M_\odot$, removing a nebular mass deficit as an argument for the existence of additional material beyond the visible boundaries of the Crab Nebula.

6.2 Cassiopeia A

Cassiopeia A is predominantly shock ionised rather than photo ionised. This makes modelling far more difficult as both have to be taken in to account. In addition to this Cas A is oxygen rich to the point where there isn't always hydrogen to scale to, meaning that some of the regularly used equations can not be applied. New modelling schemes will be required to create realistic models of Cas A to determine its composition and dust mass.

6.3 Other future work

The modelling of dust in the Crab Nebula along with other work (e.g. Gall et al. (2014); Wesson et al. (2015)) have discovered that much better fits to supernova dust emission data can be made using non standard grain size distributions. Chemical kinetic dust formation models also predict non standard size distributions (Sarangi & Cherchneff 2013). This can be investigated with observations. The red-blue asymmetry displayed in optical emission lines in supernovae can be used to build up a curve of showing how the extinction by dust across the remnant varies with wavelength. This can then be used to determine a grain

size distribution which will help to validate models such as the ones contained in this thesis.

When studying dust evolution in galaxies, most work is carried out starting with a standard size distribution for all dust regardless of how and where it is formed. This size distribution is usually assumed to be that of evolved galaxy dust such as the standard MRN size distribution. Such models can be improved by using supernova determined size distributions as inputs to better understand the evolution of dust in galaxies.

Ultimately a picture is starting to emerge in which supernovae produce large amounts of dust in their remnants. Whether this dust survives in to return to the interstellar medium is a question that remains to be answered.

Appendix A

Appendix A

RA	Dec	Velocity	FWHM	Flux
83.62852218	22.01323803	-923	659	2.50E-16 ± 1.00E-17
83.62866621	22.01101197	-861	532	3.30E-16 ± 7.00E-18
83.62871147	22.00850666	-767	569	5.01E-16 ± 3.00E-17
83.62870622	22.00601326	-792	487	8.30E-16 ± 3.00E-17
83.62879153	22.00382905	-792	460	7.30E-16 ± 2.00E-17
83.62568949	22.01235416	-895	562	5.40E-16 ± 2.00E-17
83.62576296	22.0097284	-760	651	6.10E-16 ± 2.00E-17
83.62574985	22.00734111	-688	489	1.12E-15 ± 3.00E-17
83.6257573	22.0048935	-755	504	5.40E-16 ± 1.00E-17
83.62576837	22.00280341	-796	496	3.40E-16 ± 1.00E-17
83.62282148	22.01320358	-773	762	6.10E-16 ± 2.00E-17
83.62288508	22.01090502	-664	594	1.70E-15 ± 4.00E-17
83.62285993	22.00852548	-598	535	3.20E-15 ± 6.00E-17
83.62285583	22.00610845	-730	503	7.70E-16 ± 2.00E-17
83.62278817	22.00379783	-850	576	5.00E-16 ± 1.00E-17
83.61992343	22.01348996	-684	512	8.20E-16 ± 2.00E-17
83.61998262	22.01128774	-572	530	2.27E-15 ± 3.00E-17
83.6199592	22.00885683	-626	647	1.75E-15 ± 6.00E-17
83.61989292	22.00648624	-813	744	6.50E-16 ± 3.00E-17
83.619833	22.00421238	-876	608	2.30E-16 ± 2.00E-17
83.61733989	22.01346304	-678	666	1.23E-15 ± 6.00E-17
83.61725791	22.01114049	-561	694	2.52E-15 ± 1.00E-16
83.61713863	22.00881434	-757	802	1.20E-15 ± 7.00E-17
83.61709364	22.00654089	-841	666	4.70E-16 ± 2.00E-17
83.61690854	22.00405717	-893	614	3.40E-16 ± 1.00E-17

Table A.1. The red shifted component of the [O I] 63 μm emission in the Crab Nebula measured by PACS-IFU

RA	Dec	Velocity	FWHM	Flux
83.62852218	22.01323803	-955	456	6.90E-16 ± 9.00E-17
83.62866621	22.01101197	-881	532	1.60E-16 ± 1.00E-17
83.62871147	22.00850666	-562	735	4.50E-16 ± 1.00E-17
83.62870622	22.00601326	-790	1300	4.70E-16 ± 2.00E-17
83.62568949	22.01235416	-769	657	1.70E-16 ± 1.00E-17
83.62576296	22.0097284	-684	999	4.60E-16 ± 2.00E-17
83.62574985	22.00734111	-662	684	3.50E-16 ± 2.00E-17
83.6257573	22.0048935	-755	504	2.50E-16 ± 2.00E-17
83.62576837	22.00280341	-851	609	7.67E-16 ± 3.00E-17
83.62282148	22.01320358	-756	614	4.60E-16 ± 3.00E-17
83.62288508	22.01090502	-496	1024	6.55E-15 ± 1.00E-17
83.62285993	22.00852548	-522	638	4.10E-16 ± 4.00E-17
83.62285583	22.00610845	-463	641	2.52E-16 ± 2.00E-17
83.62278817	22.00379783	-578	588	2.80E-16 ± 2.00E-17
83.61992343	22.01348996	-722	704	4.10E-17 ± 2.00E-17
83.61998262	22.01128774	-572	530	4.30E-16 ± 2.00E-17
83.61989292	22.00648624	-813	744	1.00E-16 ± 3.00E-01
83.61733989	22.01346304	-599	874	4.70E-16 ± 3.00E-17
83.61725791	22.01114049	-445	920	4.00E-16 ± 2.00E-17
83.61713863	22.00881434	-599	778	5.00E-16 ± 3.00E-17

Table A.2. The blue shifted component of the [O I] 63 μm emission in the Crab Nebula measured by PACS-IFU

RA	Dec	Velocity	FWHM	Flux
83.62852218	22.01323803	1057	457	4.30E-16 ± 1.00E-17
83.62866621	22.01101197	1095	500	5.40E-16 ± 2.00E-17
83.62871147	22.00850666	1103	661	7.14E-16 ± 3.00E-17
83.62870622	22.00601326	1094	654	5.80E-16 ± 2.60E-17
83.62879153	22.00382905	1058	566	3.50E-16 ± 3.00E-17
83.62568949	22.01235416	1091	494	4.50E-16 ± 2.00E-17
83.62576296	22.0097284	1059	665	6.80E-16 ± 3.00E-17
83.62574985	22.00734111	1076	678	7.70E-16 ± 3.00E-17
83.6257573	22.0048935	1013	661	5.40E-16 ± 1.00E-17
83.62576837	22.00280341	911	512	6.40E-16 ± 1.00E-17
83.62282148	22.01320358	967	557	9.10E-16 ± 2.00E-17
83.62288508	22.01090502	965	735	7.80E-16 ± 2.00E-17
83.62285993	22.00852548	1020	1147	8.30E-16 ± 6.00E-17
83.62285583	22.00610845	1099	680	3.90E-16 ± 1.00E-17
83.62278817	22.00379783	950	518	4.30E-16 ± 1.00E-17
83.61992343	22.01348996	732	446	6.60E-16 ± 5.00E-17
83.61998262	22.01128774	780	486	4.60E-16 ± 2.00E-17
83.6199592	22.00885683	740	619	7.60E-16 ± 5.00E-17
83.61989292	22.00648624	916	746	4.60E-16 ± 2.00E-17
83.619833	22.00421238	1035	669	3.60E-16 ± 1.00E-17
83.61733989	22.01346304	674	470	3.70E-16 ± 2.00E-17
83.61725791	22.01114049	693	416	6.00E-16 ± 4.00E-17
83.61713863	22.00881434	717	475	7.00E-16 ± 2.00E-17
83.61709364	22.00654089	1069	912	5.60E-16 ± 5.00E-17
83.61690854	22.00405717	1082	501	9.30E-17 ± 1.00E-17

Table A.3. The red shifted component of the [O III] 88 μm emission in the Crab Nebula measured by PACS-IFU

RA	Dec	Velocity	FWHM	Flux
83.62852218	22.01323803	-923	659	2.50E-16 ± 1.00E-17
83.62866621	22.01101197	-861	532	3.30E-16 ± 7.00E-18
83.62871147	22.00850666	-767	569	5.01E-16 ± 3.00E-17
83.62870622	22.00601326	-792	487	8.30E-16 ± 3.00E-17
83.62879153	22.00382905	-792	460	7.30E-16 ± 2.00E-17
83.62568949	22.01235416	-895	562	5.40E-16 ± 2.00E-17
83.62576296	22.0097284	-760	651	6.10E-16 ± 2.00E-17
83.62574985	22.00734111	-688	489	1.12E-15 ± 3.00E-17
83.6257573	22.0048935	-755	504	5.40E-16 ± 1.00E-17
83.62576837	22.00280341	-796	496	3.40E-16 ± 1.00E-17
83.62282148	22.01320358	-773	762	6.10E-16 ± 2.00E-17
83.62288508	22.01090502	-664	594	1.70E-15 ± 4.00E-17
83.62285993	22.00852548	-598	535	3.20E-15 ± 6.00E-17
83.62285583	22.00610845	-730	503	7.70E-16 ± 2.00E-17
83.62278817	22.00379783	-850	576	5.00E-16 ± 1.00E-17
83.61992343	22.01348996	-684	512	8.20E-16 ± 2.00E-17
83.61998262	22.01128774	-572	530	2.27E-15 ± 3.00E-17
83.6199592	22.00885683	-626	647	1.75E-15 ± 6.00E-17
83.61989292	22.00648624	-813	744	6.50E-16 ± 3.00E-17
83.619833	22.00421238	-876	608	2.30E-16 ± 2.00E-17
83.61733989	22.01346304	-678	666	1.23E-15 ± 6.00E-17
83.61725791	22.01114049	-561	694	2.52E-15 ± 1.00E-16
83.61713863	22.00881434	-757	802	1.20E-15 ± 7.00E-17
83.61709364	22.00654089	-841	666	4.70E-16 ± 2.00E-17
83.61690854	22.00405717	-893	614	3.40E-16 ± 1.00E-17

Table A.4. The blue shifted component of the [O III] 88 μm emission in the Crab Nebula measured by PACS-IFU

RA	Dec	Velocity	FWHM	Flux
83.62574985	22.00734111	997	810	4.70E-17 ± 6.00E-18
83.62288508	22.01090502	1004	11187	8.90E-17 ± 4.00E-18
83.62285993	22.00852548	964	1112	5.80E-17 ± 3.00E-18
83.61998262	22.01128774	864	1130	8.50E-17 ± 4.00E-17
83.6199592	22.00885683	764	996	8.50E-17 ± 6.00E-18
83.61733989	22.01346304	702	1326	8.20E-17 ± 4.00E-18
83.61725791	22.01114049	764	1284	1.00E-16 ± 6.00E-18
83.61713863	22.00881434	769	927	8.90E-17 ± 5.00E-18

Table A.5. The red shifted component of the [C II] 158 μm emission in the Crab Nebula measured by PACS-IFU

RA	Dec	Velocity	FWHM	Flux
83.62574985	22.00734111	-663	911	6.63E-17 ± 3.00E-18
83.62288508	22.01090502	-602	911	1.39E-16 ± 3.00E-18
83.62285993	22.00852548	-548	823	2.22E-16 ± 8.00E-18
83.61998262	22.01128774	-566	881	1.97E-16 ± 5.00E-18
83.6199592	22.00885683	-575	950	1.78E-16 ± 4.00E-18
83.61733989	22.01346304	-614	869	9.20E-17 ± 5.00E-18
83.61725791	22.01114049	-528	861	1.70E-16 ± 4.00E-18
83.61713863	22.00881434	-683	1016	9.50E-17 ± 6.00E-18

Table A.6. The red shifted component of the [C II] 158 μm emission in the Crab Nebula measured by PACS-IFU

Appendix B

Appendix B

B.1 SP1

RA	Dec	Velocity	FWHM	Flux
350.8763587573	58.8210604144	-3988	1388	6.30E-16 ± 5.00E-17
350.8785458073	58.8191391838	-3624	1280	2.80E-16 ± 5.00E-17
350.8850600699	58.8127963966	-3188	2201	3.7E-16 ± 2.00E-17
350.8726196781	58.8190778149	-2646	1543	4.20E-16 ± 2.00E-17
350.8811420635	58.8106073526	-4370	969	4.60E-16 ± 1.00E-17
350.8714753377	58.8144745884	-2036	703	3.70E-16 ± 6.00E-17
350.8624284116	58.8176549156	-1187	1813	2.40E-16 ± 1.00E-17

Table B.1. The blue shifted component of the [O I] 63 μm emission in the SP1 observations of Cas A measured by PACS-IFU

RA	Dec	Velocity	FWHM	Flux
350.8830041766	58.8147052523	2848	2024	2.50E-16 ± 4.00E-017
350.8811420635	58.8106073526	1657	1375	2.10E-16 ± 1.00E-17
350.8714753377	58.8144745884	1074	1413	2.40E-16 ± 2.00E-17
350.8624284116	58.8176549156	1812	1244	1.90E-16 ± 2.00E-17

Table B.2. The red shifted component of the [O I] 63 μm emission in the SP1 observations of Cas A measured by PACS-IFU

RA	Dec	Velocity	FWHM	Flux
350.8763587573	58.8210604144	-2971	646	3.20E-016 ± 1.00E-017
350.8785458073	58.8191391838	-2728	1290	1.50E-016 ± 1.00E-017
350.8830041766	58.8147052523	-2355	644	3.50E-016 ± 1.00E-017
350.8726196781	58.8190778149	-2629	670	3.30E-016 ± 1.00E-017
350.8750456714	58.8167709739	-2318	1109	5.30E-016 ± 2.00E-017
350.8771236703	58.8146398673	-2529	1351	9.00E-016 ± 1.00E-016
350.8792872363	58.812463694	-2554	839	5.50E-016 ± 3.00E-017
350.8811420635	58.8106073526	-1977	703	9.00E-017 ± 8.00E-017
350.8673003148	58.8186234215	-1782	1384	2.20E-016 ± 1.00E-017
350.8694230882	58.8166038052	-1187	1579	6.10E-006 ± 4.00E-017
350.8714753377	58.8144745884	-1282	1619	1.04E-015 ± 6.00E-017
350.8735938572	58.8123208429	-1479	2089	7.60E-016 ± 6.00E-017
350.8755172641	58.8102349872	-1879	889	8.70E-016 ± 5.00E-017
350.8624284116	58.8176549156	-1808	870	2.20E-016 ± 1.00E-017
350.8644595806	58.8157192724	-1404	1138	2.90E-016 ± 3.00E-017
350.8665599515	58.8135451114	-1507	949	6.20E-016 ± 2.00E-017
350.8685386921	58.8114065225	-1248	1126	4.50E-016 ± 1.00E-017
350.8704423008	58.8093567199	-1895	748	5.70E-017 ± 1.00E-017
350.8583337102	58.8165401478	-1652	859	2.50E-016 ± 3.00E-017
350.8602457757	58.8144378199	-1771	797	3.90E-016 ± 2.00E-017
350.8621013114	58.8123165127	-1839	785	3.70E-016 ± 2.00E-017
350.8640287235	58.8102734529	-1583	955	3.60E-016 ± 1.00E-017
350.865917443	58.8079840044	-2512	1177	3.90E-016 ± 3.00E-017

Table B.3. The blue shifted component of the [O III] 88 μm emission in the SP1 observations of Cas A measured by PACS-IFU

B.2 SP3

RA	Dec	Velocity	FWHM	Flux
350.8785458073	58.8191391838	2620	1254	2.40E-016 ± 1.00E-017
350.8808206346	58.8169275996	2900	1271	7.00E-016 ± 3.00E-017
350.8830041766	58.8147052523	3335	1306	1.00E-015 ± 1.00E-016
350.8850600699	58.8127963966	2738	897	4.80E-016 ± 2.00E-017
350.8726196781	58.8190778149	2645	1224	3.00E-016 ± 1.00E-017
350.8750456714	58.8167709739	3127	948	3.60E-016 ± 1.20E-017
350.8771236703	58.8146398673	3485	1221	4.20E-016 ± 3.00E-017
350.8792872363	58.812463694	3611	968	5.20E-016 ± 2.00E-017
350.8811420635	58.8106073526	2948	914	5.40E-016 ± 3.00E-017
350.8673003148	58.8186234215	2947	1449	3.70E-016 ± 1.00E-017
350.8694230882	58.8166038052	3435	1625	5.20E-016 ± 8.00E-017
350.8714753377	58.8144745884	3719	1500	4.10E-016 ± 2.00E-017
350.8624284116	58.8176549156	3596	1068	2.00E-016 ± 2.00E-017
350.8644595806	58.8157192724	4020	3207	1.50E-016 ± 3.00E-017
350.8665599515	58.8135451114	4107	1103	2.80E-016 ± 1.00E-017
350.8685386921	58.8114065225	4499	666	1.90E-016 ± 2.00E-017
350.8583337102	58.8165401478	4008	786	2.40E-016 ± 2.00E-017
350.8602457757	58.8144378199	4382	993	1.00E-016 ± 1.00E-017

Table B.4. The red shifted component of the [O III] 88 μm emission in the SP1 observations of Cas A measured by PACS-IFU

RA	Dec	Velocity	FWHM	Flux
350.814987606	58.8162021106	995	950	6.50E-016 ± 3.00E-017
350.8168549018	58.8143490926	1169	452	4.00E-016 ± 1.00E-017
350.8071616039	58.8181990968	942	1095	6.10E-016 ± 4.00E-017
350.8092946018	58.8160491418	1159	500	7.40E-016 ± 5.00E-017
350.8112320019	58.8139667308	1129	374	1.79E-016 ± 5.00E-018
350.8001368762	58.8194313019	1495	1912	1.50E-015 ± 7.00E-017
350.8022518745	58.8172608934	1369	810	1.12E-015 ± 4.00E-017
350.7940049212	58.8202412936	842	626	4.34E-016 ± 2.00E-017

Table B.5. The red shifted component of the [O III] 88 μm emission in the SP3 observations of Cas A measured by PACS-IFU

RA	Dec	Velocity	FWHM	Flux
350.8120065904	58.8248046807	-985	500	1.60E-016 ± 3.00E-017
350.8142021845	58.8228883179	-904	592	3.90E-016 ± 3.00E-117
350.8164955674	58.8206775782	-684	460	4.90E-016 ± 4.00E-017
350.818694051	58.8184591207	-641	453	2.51E-016 ± 5.00E-018
350.8207741793	58.8165502378	-594	702	2.30E-016 ± 1.00E-017
350.8082755355	58.8228043033	-948	511	5.10E-016 ± 4.00E-017
350.8107170766	58.8205017979	-709	564	2.80E-016 ± 1.00E-017
350.8128094107	58.8183744099	-621	557	4.30E-016 ± 3.00E-017
350.814987606	58.8162021106	-600	566	4.00E-016 ± 3.00E-017
350.8168549018	58.8143490926	-428	1045	3.60E-016 ± 2.00E-017

Table B.6. The blue shifted component of the [O III] 88 μm emission in the SP3 observations of Cas A measured by PACS-IFU

RA	Dec	Velocity	FWHM	Flux
350.8128094107	58.8183744099	914	935	1.63E-016 ± 6.46E-001
350.8022518745	58.8172608934	1878	1421	1.00E-016 ± 2.50E-018
350.7940049212	58.8202412936	1186	716	1.53E-016 ± 1.00E-017
350.8016460967	58.8116986855	901	808	1.85E-016 ± 1.25E-017

Table B.7. The red shifted component of the [C II] 157 μm emission in the SP3 observations of Cas A measured by PACS-IFU

RA	Dec	Velocity	FWHM	Flux
350.8128094107	58.8183744099	-609	1016	1.30E-016 ± 6.00E-018
350.8001368762	58.8194313019	-922	956	1.63E-016 ± 4.08E-018
350.8022518745	58.8172608934	-1167	873	8.37E-017 ± 5.49E-018

Table B.8. The blue shifted component of the [C II] 157 μm emission in the SP3 observations of Cas A measured by PACS-IFU

B.3 SP4

RA	Dec	Velocity	FWHM	Flux
350.8939201758	58.8013959773	1587	1016	3.80E-016 ± 2.00E-017
350.8983678486	58.7972597937	1252	1642	2.60E-016 ± 3.00E-017
350.9025932041	58.7931253998	1836	1203	2.90E-016 ± 1.00E-017
350.8901776232	58.7994162188	1382	1064	1.10E-016 ± 1.00E-017
350.894666527	58.7949748759	1139	1266	3.30E-016 ± 2.00E-017
350.8968227127	58.7927970741	1775	1251	5.60E-016 ± 4.00E-017
350.8986712345	58.7909393377	2083	779	1.01E-015 ± 2.00E-017
350.8848599927	58.7989658594	887	1280	3.90E-016 ± 2.00E-017
350.8911321659	58.7926585358	1380	1514	4.30E-016 ± 1.00E-017
350.8930485793	58.7905712324	1754	1285	1.05E-015 ± 2.00E-017
350.8799881142	58.7980010509	1836	1288	4.20E-016 ± 1.00E-017
350.8820126715	58.7960638733	226	1359	1.00E-015 ± 1.00E-016
350.8841057123	58.7938881269	1290	1455	3.30E-016 ± 2.00E-017
350.8860772854	58.7917480454	1780	1399	4.40E-016 ± 3.00E-017
350.8879740138	58.7896968079	624	1132	4.50E-016 ± 2.00E-017
350.8758925836	58.7968893928	517	1351	4.10E-016 ± 2.00E-017
350.8777976336	58.7947856183	941	1094	6.60E-016 ± 3.00E-017
350.8796461261	58.7926629079	1393	1765	4.10E-016 ± 2.00E-017
350.8815666694	58.7906183913	1740	1572	3.80E-016 ± 3.00E-017

Table B.9. The red shifted component of the [O III] 88 μm emission in the SP4 observations of Cas A measured by PACS-IFU

B.4 SP5

RA	Dec	Velocity	FWHM	Flux
350.8939201758	58.8013959773	-1586	2176	3.50E-016 ± 3.00E-017
350.8901776232	58.7994162188	-360	1005	1.50E-016 ± 1.00E-017
350.8925957275	58.7971075478	-712	1488	2.10E-016 ± 6.00E-018
350.894666527	58.7949748759	-959	1645	5.30E-016 ± 2.00E-017
350.8869758637	58.7969446412	-530	1271	8.10E-016 ± 2.00E-017
350.8890209363	58.7948138774	-717	1679	1.77E-015 ± 5.00E-017
350.8911321659	58.7926585358	-859	1393	7.50E-016 ± 2.00E-017
350.8841057123	58.7938881269	-1405	1368	5.30E-016 ± 2.00E-017
350.8860772854	58.7917480454	-1670	1657	2.70E-016 ± 1.00E-017
350.8879740138	58.7896968079	-1115	1315	9.80E-016 ± 5.00E-017
350.8815666694	58.7906183913	-1210	1149	2.50E-016 ± 1.00E-017
350.8834478383	58.7883275168	-1109	1318	4.90E-016 ± 1.00E-017

Table B.10. The blue shifted component of the [O III] 88 μm emission in the SP4 observations of Cas A measured by PACS-IFU

RA	Dec	Velocity	FWHM	Flux
350.8968227127	58.7927970741	1602	1751	1.20E-15 ± 3.00E-17
350.8986712345	58.7909393377	1574	800	4.1E-16 ± 3.00E-16

Table B.11. The blue shifted component of the [O I] 63 μm emission in the SP4 observations of Cas A measured by PACS-IFU

RA	Dec	Velocity	FWHM	Flux
350.894666527	58.7949748759	-1026	1202	6.10E-16 ± 3.00E-17
350.8968227127	58.7927970741	-898	1403	1.03E-15 ± 3.00E-17
350.8869758637	58.7969446412	-741	1246	5.40E-16 ± 2.00E-17
350.8890209363	58.7948138774	-659	1624	1.11E-15 ± 3.00E-17
350.8911321659	58.7926585358	-791	1374	4.80E-16 ± 1.00E-17

Table B.12. The blue shifted component of the [O I] 63 μm emission in the SP4 observations of Cas A measured by PACS-IFU

RA	Dec	Velocity	FWHM	Flux
350.9005438729	58.7950358024	1377	737	5.42E-017 ± 1.11E-018
350.9025932041	58.7931253998	1850	1020	4.52E-017 ± 9.21E-019
350.8968227127	58.7927970741	1296	723	2.67E-017 ± 5.45E-019
350.8986712345	58.7909393377	1756	1234	7.43E-017 ± 1.52E-018
350.8848599927	58.7989658594	1863	777	9.42E-017 ± 1.92E-018
350.8869758637	58.7969446412	2019	873	5.69E-017 ± 1.16E-018
350.8930485793	58.7905712324	1692	1137	6.39E-017 ± 1.30E-018
350.8799881142	58.7980010509	1751	1177	1.01E-016 ± 2.06E-018
350.8860772854	58.7917480454	949	524	3.32E-017 ± 6.77E-019
350.8879740138	58.7896968079	1433	757	3.87E-017 ± 7.90E-019
350.8834478383	58.783275168	1120	766	3.74E-017 ± 7.62E-019

Table B.13. The red shifted component of the [C II] 157 μm emission in the SP4 observations of Cas A measured by PACS-IFU

RA	Dec	Velocity	FWHM	Flux
350.8939201758	58.8013959773	-1078	576	5.52E-017 ± 1.13E-018
350.8911321659	58.7926585358	-940	1368	4.61E-017 ± 9.40E-019
350.8930485793	58.7905712324	-1086	567	2.52E+014 ± 5.14E+012
350.8841057123	58.7938881269	-1123	512	3.72E-018 ± 7.59E-020
350.8860772854	58.7917480454	-849	612	1.61E-017 ± 3.28E-019

Table B.14. The blue shifted component of the [C II] 157 μm emission in the SP4 observations of Cas A measured by PACS-IFU

RA	Dec	Velocity	FWHM	Flux
350.8676247405	58.7923815851	1807	675	3.40E-016 ± 3.00E-017
350.8623101489	58.7919250597	1810	631	1.19E-015 ± 2.00E-017
350.8644343096	58.7899062966	1907	571	2.80E-016 ± 2.00E-017
350.8574434412	58.7909546022	1780	711	3.90E-016 ± 2.00E-017
350.8594759427	58.7890197747	1784	501	2.40E-016 ± 1.00E-017
350.8615779471	58.7868464578	1709	547	1.62E-016 ± 6.00E-018
350.8552672942	58.7877366342	1924	1069	2.90E-016 ± 2.00E-017

Table B.15. The red shifted component of the [O III] 88 μm emission in the SP5 observations of Cas A measured by PACS-IFU

RA	Dec	Velocity	FWHM	Flux
350.8676247405	58.7923815851	-1176	598	3.00E-016 ± 3.00E-017
350.8700523166	58.7900757196	-1059	716	3.10E-016 ± 2.00E-017
350.8623101489	58.7919250597	-1284	768	3.10E-016 ± 2.00E-017
350.8644343096	58.7899062966	-1114	786	4.03E-014 ± 8.00E-018
350.8574434412	58.7909546022	-1096	892	5.00E-016 ± 3.00E-017
350.8594759427	58.7890197747	-894	974	8.70E-016 ± 3.00E-017
350.853353556	58.7898381949	-1231	1110	6.70E-016 ± 3.00E-017
350.8552672942	58.7877366342	-1111	1025	4.50E-016 ± 2.00E-017
350.8571245719	58.7856160718	-1325	748	1.23E-015 ± 4.00E-017

Table B.16. The blue shifted component of the [O III] 88 μm emission in the SP5 observations of Cas A measured by PACS-IFU

RA	Dec	Velocity	FWHM	Flux
350.8644343096	58.7899062966	2243		3.50E-16 ± 2.00E-17
350.8664881628	58.7877779052	838	1870	8.40E-16 ± 2.00E-17

Table B.17. The blue shifted component of the [O I] 63 μm emission in the SP5 observations of Cas A measured by PACS-IFU

B.5 SP7

RA	Dec	Velocity	FWHM	Flux
350.8594759427	58.7890197747	-1281	751	5.90E-16 ± 3.00E-17
350.8615779471	58.7868464578	-1077	511	3.10E-16 ± 2.00E-17
350.8635583589	58.7847086645	-2715	1774	2.80E-16 ± 2.00E-17
350.8571245719	58.7856160718	-716	968	2.50E-16 ± 3.00E-17

Table B.18. The blue shifted component of the [O I] 63 μm emission in the SP5 observations of Cas A measured by PACS-IFU

RA	Dec	Velocity	FWHM	Flux
350.8700523166	58.7900757196	1977	1112	2.10E-016 ± 1.68E-017
350.8721319017	58.7879454493	1880	1156	1.90E-016 ± 1.52E-017
350.8623101489	58.7919250597	1848	973	1.80E-016 ± 1.44E-017
350.8644343096	58.7899062966	1999	1064	3.60E-017 ± 2.88E-018
350.8574434412	58.7909546022	1831	1050	4.69E-016 ± 3.75E-017
350.8594759427	58.7890197747	1872	909	9.10E-017 ± 7.28E-018
350.8635583589	58.7847086645	1888	777	2.10E-016 ± 1.68E-017
350.8654704362	58.7826877874	1157	1103	2.90E-016 ± 2.32E-017

Table B.19. The red shifted component of the [C II] 157 μm emission in the SP5 observations of Cas A measured by PACS-IFU

RA	Dec	Velocity	FWHM	Flux
350.8644343096	58.7899062966	-937	405	9.10E-017 ± 8.03E-018
350.8705401838	58.7835680921	-1559	1221	3.40E-016 ± 3.00E-017
350.8574434412	58.7909546022	-1017	717	9.80E-017 ± 8.65E-018

Table B.20. The blue shifted component of the [C II] 157 μm emission in the SP5 observations of Cas A measured by PACS-IFU

RA	Dec	Velocity	FWHM	Flux
350.8884399872	58.8367109184	4029	838	1.60E-016 ± 1.00E-017
350.890621377	58.83448768	4331	1286	4.30E-016 ± 3.00E-017
350.8926755235	58.8325779855	4559	711	3.00E-016 ± 2.00E-017
350.8826614911	58.8365566596	3380	595	9.00E-017 ± 1.00E-017
350.8847374178	58.8344247047	3938	860	2.30E-016 ± 2.00E-017
350.8700383774	58.8374457693	2029	681	2.50E-016 ± 1.00E-017
350.8659396337	58.8363326806	2282	755	2.30E-016 ± 2.00E-017

Table B.21. The red shifted component of the [O III] 88 μm emission in the SP7 observations of Cas A measured by PACS-IFU

RA	Dec	Velocity	FWHM	Flux
350.8884399872	58.8367109184	-1932	451	2.70E-016 ± 1.00E-017
350.890621377	58.83448768	-1964	653	3.50E-016 ± 2.00E-017
350.8926755235	58.8325779855	-2024	547	3.20E-016 ± 1.00E-017
350.8826614911	58.8365566596	-1552	550	8.00E-017 ± 1.00E-017
350.8847374178	58.8344247047	-1696	714	4.40E-016 ± 3.00E-017
350.8868988897	58.8322476487	-2037	658	4.90E-017 ± 2.00E-017
350.8887519343	58.8303905509	-2167	5113	5.10E-016 ± 3.00E-017
350.8770354436	58.8363917944	-1169	916	3.49E-016 ± 2.00E-017
350.8790856104	58.8342617396	-1620	9332	1.06E-015 ± 5.00E-017
350.8812020454	58.8321071293	-2086	580	4.20E-016 ± 4.00E-017
350.883123358	58.8300204889	-2434	569	2.20E-016 ± 2.00E-017
350.8720677503	58.8355092957	-1546	653	5.70E-016 ± 4.00E-017
350.8761425978	58.8311948793	-2156	575	2.85E-016 ± 7.00E-018
350.8780441564	58.8291442994	-2541	848	7.00E-016 ± 4.00E-017
350.8678495805	58.8342295703	-1350	657	4.00E-016 ± 2.00E-017
350.8697029339	58.8321075041	-1400	504	3.20E-016 ± 1.00E-017
350.8735146164	58.8277734357	-2557	632	1.60E-016 ± 2.00E-017

Table B.22. The blue shifted component of the [O III] 88 μm emission in the SP7 observations of Cas A measured by PACS-IFU

B.6 SP8

RA	Dec	Velocity	FWHM	Flux
350.890621377	58.83448768	4763	919	7.90E-16 ± 7.00E-17
350.8678495805	58.8342295703	3047	1320	2.30E-16 ± 1.00E-17

Table B.23. The red shifted component of the [O I] 63 μm emission in the SP7 observations of Cas A measured by PACS-IFU

RA	Dec	Velocity	FWHM	Flux
350.890621377	58.83448768	-3056	744	1.90E-16 ± 3.00E-17
350.8790856104	58.8342617396	-1755	632	5.20E-16 ± 2.00E-17
350.8812020454	58.8321071293	-2131	1195	6.34E-16 ± 3.00E-17
350.8720677503	58.8355092957	-1422	511	5.29E-17 ± 1.00E-17
350.8761425978	58.8311948793	-2158	918	7.20E-16 ± 4.00E-17
350.8780441564	58.8291442994	-2627	1134	6.00E-16 ± 4.00E-17
350.8678495805	58.8342295703	-1916	1089	3.25E-16 ± 2.00E-17
350.8697029339	58.8321075041	-1697	1220	3.00E-16 ± 2.00E-17
350.8735146164	58.8277734357	-2624	839	5.90E-16 ± 2.00E-17

Table B.24. The blue shifted component of the [O I] 63 μm emission in the SP7 observations of Cas A measured by PACS-IFU

RA	Dec	Velocity	FWHM	Flux
350.8236040659	58.7973977824	2943	797	2.40E-016 ± 2.00E-017
350.8260403057	58.79509426	2444	832	1.82E-016 ± 7.00E-018
350.8281278818	58.7929659927	1763	764	2.20E-016 ± 1.00E-017
350.818290374	58.796936098	3216	831	1.00E-016 ± 2.00E-017
350.820422112	58.7949193869	2680	433	2.30E-016 ± 2.00E-017
350.8224839402	58.7927929771	1986	943	8.20E-016 ± 3.00E-017
350.8246121337	58.7906421276	1657	728	4.90E-016 ± 1.00E-017
350.8134264889	58.795960913	3484	863	1.20E-016 ± 1.00E-017
350.8154662478	58.7940280537	2806	622	1.50E-016 ± 1.00E-017
350.8175763939	58.79185677	2265	763	2.90E-016 ± 2.00E-017
350.8195648182	58.7897208897	1863	940	6.30E-016 ± 3.00E-017

Table B.25. The red shifted component of the [O III] 88 μm emission in the SP8 observations of Cas A measured by PACS-IFU

RA	Dec	Velocity	FWHM	Flux
350.829526158	58.7974672769	-895	391	6.40E-016 ± 5.00E-017
350.8236040659	58.7973977824	-1320	613	2.04E-016 ± 8.00E-018
350.8260403057	58.79509426	-657	1008	5.30E-016 ± 1.00E-017
350.8281278818	58.7929659927	-413	702	3.10E-016 ± 2.00E-017
350.818290374	58.796936098	-1465	602	3.40E-016 ± 2.00E-017
350.820422112	58.7949193869	-878	626	4.60E-016 ± 2.00E-017
350.8134264889	58.795960913	-2013	576	1.20E-016 ± 1.00E-017
350.8154662478	58.7940280537	-1613	660	1.20E-016 ± 1.00E-017

Table B.26. The blue shifted component of the [O III] 88 μm emission in the SP8 observations of Cas A measured by PACS-IFU

B.7 SP9

RA	Dec	Velocity	FWHM	Flux
350.8260403057	58.79509426	2508	1132	3.50E-16 ± 2.00E-17
350.8281278818	58.7929659927	1786	963	3.70E-16 ± 2.00E-17
350.820422112	58.7949193869	2493	944	2.30E-16 ± 1.00E-17
350.8224839402	58.7927929771	2148	807	2.00E-16 ± 2.00E-17

Table B.27. The red shifted component of the [O I] 63 μm emission in the SP8 observations of Cas A measured by PACS-IFU

RA	Dec	Velocity	FWHM	Flux
350.8260403057	58.79509426	-686	1764	3.70E-16 ± 3.00E-17
350.8281278818	58.7929659927	-258	702	4.60E-16 ± 1.00E-17
350.820422112	58.7949193869	-967	1612	6.60E-16 ± 6.00E-17
350.8224839402	58.7927929771	-2464	810	5.00E-16 ± 1.00E-17

Table B.28. The blue shifted component of the [O I] 63 μm emission in the SP8 observations of Cas A measured by PACS-IFU

RA	Dec	Velocity	FWHM	Flux
350.8119013036	58.8023898812	1175	683	4.30E-016 ± 1.00E-017
350.8158887667	58.7982225351	2129	615	1.40E-016 ± 1.00E-017
350.8062201934	58.8023395694	1068	756	9.20E-016 ± 5.00E-017
350.8082356366	58.800207324	1353	1032	8.20E-016 ± 6.00E-017
350.8102679303	58.7980498646	1708	609	7.60E-016 ± 4.00E-017

Table B.29. The red shifted component of the [O III] 88 μm emission in the SP9 observations of Cas A measured by PACS-IFU

RA	Dec	Velocity	FWHM	Flux
350.811210103	58.8088119511	-720	512	4.55E-016 ± 9.00E-018
350.8134594132	58.8066811511	-929	670	3.10E-016 ± 1.00E-017
350.8157584073	58.8045989801	-1150	745	3.30E-016 ± 1.00E-017
350.8076881567	58.8066675773	-386	760	5.60E-016 ± 3.00E-017

Table B.30. The blue shifted component of the [O III] 88 μm emission in the SP9 observations of Cas A measured by PACS-IFU

RA	Dec	Velocity	FWHM	Flux
350.8042411615	58.8044410837	674	1565	3.40E-16 ± 5.00E-17
350.8082356366	58.800207324	1361	890	7.20E-16 ± 8.90E-17
350.8102679303	58.7980498646	1569	990	4.90E-16 ± 2.00E-16
350.7991018882	58.8036397956	897	1120	2.90E-16 ± 3.00E-17

Table B.31. The red shifted component of the [O I] 63 μm emission in the SP9 observations of Cas A measured by PACS-IFU

Appendix C

Appendix C

Table A1 lists the values of n and k measured by Uspenskii et al. (2006) between 2.8 nm and 30 nm for an amorphous carbon sample. It also lists extrapolated n and k values for the Zubko et al. (1996) ACAR and BE amorphous carbon samples, obtained by fitting power-laws to the short wavelength ends of their n and k distributions and then extrapolating these from their shortest wavelength points, at 40 nm and 54 nm, respectively, to shorter wavelengths until they intersected the n and k data of Uspenskii et al. (2006), which were then used from the intersection wavelength down to 2.8 nm. Power-law extrapolations of the Uspenskii et al. (2006) n and k data were then used from 2.8 nm down to 0.35 nm.

Wavelength (nm)	n Uspenskii	k Uspenskii	n Zubko ACAR	k Zubko ACAR	n Zubko BE	k Zubko BE
0.3			9.970E-01	1.72E-06	9.970E-01	1.72E-06
0.4			9.970E-01	3.26E-06	9.970E-01	3.26E-06
0.5			9.970E-01	5.36E-06	9.970E-01	5.36E-06
0.6			9.970E-01	8.04E-06	9.970E-01	8.04E-06
0.7			9.970E-01	1.13E-05	9.970E-01	1.13E-05
0.8			9.970E-01	1.52E-05	9.970E-01	1.52E-05
0.9			9.970E-01	1.98E-05	9.970E-01	1.98E-05
1.5			9.970E-01	6.16E-05	9.970E-01	6.16E-05
3.55	9.970E-01	4.477E-04	9.970E-01	4.477E-04	9.970E-01	4.477E-04
3.76	9.970E-01	5.226E-04	9.970E-01	5.226E-04	9.970E-01	5.226E-04
3.98	9.971E-01	6.004E-04	9.971E-01	6.004E-04	9.971E-01	6.004E-04
4.13	9.980E-01	2.000E-03	9.980E-01	2.000E-03	9.980E-01	2.000E-03
4.21	9.980E-01	1.700E-03	9.971E-01	1.700E-03	9.971E-01	1.700E-03
4.27	9.980E-01	1.000E-03	9.980E+00	1.000E-03	9.980E+00	1.000E-03
4.35	1.000E+00	3.000E-03	1.000E+00	3.000E-03	1.000E+00	3.000E-03
4.42	9.980E-01	1.000E-04	9.980E-01	1.000E-04	9.980E-01	1.000E-04
4.59	9.970E-01	1.000E-04	9.970E-01	1.000E-04	9.970E-01	1.000E-04
4.72	9.971E-01	1.062E-03	9.971E-01	1.062E-03	9.971E-01	1.062E-03
5.00	9.970E-01	1.062E-03	9.970E-01	1.062E-03	9.970E-01	1.062E-03
5.29	9.969E-01	1.062E-03	9.969E-01	1.062E-03	9.969E-01	1.062E-03
5.60	9.967E-01	1.174E-03	9.967E-01	1.174E-03	9.967E-01	1.174E-03
5.93	9.964E-01	1.297E-03	9.964E-01	1.297E-03	9.964E-01	1.297E-03
6.27	9.960E-01	1.433E-03	9.960E-01	1.433E-03	9.960E-01	1.433E-03
6.64	9.956E-01	1.586E-03	9.956E-01	1.586E-03	9.956E-01	1.586E-03
7.03	9.950E-01	1.755E-03	9.950E-01	1.755E-03	9.950E-01	1.755E-03
7.44	9.943E-01	1.949E-03	9.943E-01	1.949E-03	9.943E-01	1.949E-03
7.88	9.935E-01	2.174E-03	9.935E-01	2.174E-03	9.935E-01	2.174E-03
8.34	9.925E-01	2.431E-03	9.925E-01	2.431E-03	9.925E-01	2.431E-03
8.82	9.913E-01	2.731E-03	9.913E-01	2.731E-03	9.913E-01	2.731E-03
9.34	9.899E-01	3.087E-03	9.899E-01	3.087E-03	9.899E-01	3.087E-03
9.89	9.882E-01	3.511E-03	9.882E-01	3.511E-03	9.882E-01	3.511E-03
10.46	9.863E-01	4.009E-03	9.863E-01	4.009E-03	9.863E-01	4.009E-03
11.08	9.841E-01	4.612E-03	9.841E-01	4.612E-03	9.841E-01	4.612E-03
11.73	9.814E-01	5.333E-03	9.814E-01	5.333E-03	9.814E-01	5.333E-03
12.42	9.784E-01	6.209E-03	9.784E-01	6.209E-03	9.784E-01	6.209E-03
13.14	9.749E-01	7.251E-03	9.749E-01	7.251E-03	9.749E-01	7.251E-03
13.91	9.709E-01	8.519E-03	9.709E-01	8.519E-03	9.709E-01	8.519E-03
14.72	9.663E-01	1.005E-02	9.663E-01	1.005E-02	9.663E-01	1.005E-02
15.58	9.610E-01	1.192E-02	9.610E-01	1.192E-02	9.610E-01	1.192E-02
16.50	9.549E-01	1.417E-02	9.549E-01	1.417E-02	9.549E-01	1.417E-02
17.46	9.480E-01	1.691E-02	9.480E-01	1.691E-02	9.480E-01	1.691E-02
18.49	9.400E-01	2.022E-02	9.400E-01	2.022E-02	9.400E-01	2.022E-02
19.56	9.310E-01	2.422E-02	9.310E-01	2.422E-02	9.310E-01	2.422E-02
20.71	9.207E-01	2.909E-02	9.207E-01	2.909E-02	9.207E-01	2.909E-02
21.92	9.091E-01	3.496E-02	9.091E-01	3.496E-02	9.091E-01	3.496E-02
23.21	8.958E-01	4.206E-02	8.958E-01	4.206E-02	8.958E-01	4.206E-02
24.56	8.807E-01	5.064E-02	8.807E-01	5.064E-02	8.807E-01	5.064E-02
26.00	8.637E-01	6.101E-02	8.637E-01	6.101E-02	8.637E-01	6.101E-02
27.52	8.443E-01	7.350E-02	8.443E-01	7.350E-02	8.443E-01	7.350E-02
29.13	8.224E-01	8.860E-02	8.224E-01	8.860E-02	8.224E-01	8.860E-02
40.00			8.63800E-01	1.93800E-01	9.410E-01	9.780E-02
50.00			8.60100E-01	2.35100E-01	9.18300E-01	1.26400E-01

Table C.1. Values of n and k measured by Uspenskii et al. (2006) between 2.8 nm and 30 nm for an amorphous carbon sample and extrapolated n and k for Zubko et al. (1996) ACAR and BE amorphous carbon samples

Bibliography

- Arnett, D. 1996, Supernovae and Nucleosynthesis
- Barlow, M. J., Krause, O., Swinyard, B. M., et al. 2010, A&A, 518, L138
- Barlow, M. J., Swinyard, B. M., Owen, P. J., et al. 2013, Science, 342, 1343
- Bé, M.-M., Chisté, V., Dulieu, C., et al. 2013, Monographie BIPM-5, Vol. 7, Table of Radionuclides (Pavillon de Breteuil, F-92310 Sèvres, France: Bureau International des Poids et Mesures)
- Bertoldi, F., Carilli, C. L., Cox, P., et al. 2003, A&A, 406, L55
- Bertoldi, F., & Cox, P. 2002, A&A, 384, L11
- Bianchi, S., & Schneider, R. 2007, MNRAS, 378, 973
- Boehler, Y., Dutrey, A., Guilloteau, S., & Piétu, V. 2013, MNRAS, 431, 1573
- Bouwens, R. J., Illingworth, G. D., Labbe, I., et al. 2011, Nature, 469, 504
- Bussoletti, E., Colangeli, L., Borghesi, A., & Orofino, V. 1987, A&AS, 70, 257
- Carilli, C. L., Bertoldi, F., Rupen, M. P., et al. 2001, ApJ, 555, 625
- Cherchneff, I., & Dwek, E. 2009, ApJ, 703, 642
- . 2010, ApJ, 713, 1
- Clayton, D. D., Liu, W., & Dalgarno, A. 1999, Science, 283, 1290
- Colangeli, L., Mennella, V., Palumbo, P., Rotundi, A., & Bussoletti, E. 1995, A&AS, 113, 561
- Davidson, K., & Fesen, R. A. 1985, Ann. Rev. Astr. Astrophys., 23, 119

- Docenko, D., & Sunyaev, R. A. 2010, *A&A*, 509, A59
- Draine, B. T., & Lee, H. M. 1984, *ApJ*, 285, 89
- Dunne, L., Eales, S., Ivison, R., Morgan, H., & Edmunds, M. 2003, *Nature*, 424, 285
- Dwek, E., Galliano, F., & Jones, A. P. 2007, *ApJ*, 662, 927
- Ercolano, B., Barlow, M. J., & Storey, P. J. 2005, *MNRAS*, 362, 1038
- Ercolano, B., Barlow, M. J., Storey, P. J., & Liu, X.-W. 2003, *MNRAS*, 340, 1136
- Ercolano, B., Barlow, M. J., & Sugerman, B. E. K. 2007, *MNRAS*, 375, 753
- Ercolano, B., Young, P. R., Drake, J. J., & Raymond, J. C. 2008, *ApJSS*, 175, 534
- Fesen, R. A., Hammell, M. C., Morse, J., et al. 2006, *ApJ*, 645, 283
- Gall, C., Hjorth, J., Watson, D., et al. 2014, *Nature*, 511, 326
- Gomez, H., Krause, O., Barlow, M., et al. 2012, *ApJ*, 760, 96
- Gomez, H. L., Vlahakis, C., Stretch, C. M., et al. 2010, *MNRAS*, 401, L48
- Gomez, H. L., Clark, C. J. R., Nozawa, T., et al. 2012, *MNRAS*, 420, 3557
- Grefenstette, B. W., Harrison, F. A., Boggs, S. E., et al. 2014, *Nature*, 506, 339
- Greif, T. H., & Bromm, V. 2006, *MNRAS*, 373, 128
- Griffin, M. J., Abergel, A., Abreu, A., et al. 2010, *A&A*, 518, L3
- Hanner, M. 1988, Grain optical properties, Tech. rep.
- Hester, J. J. 2008, *Ann. Rev. Astr. Astrophys.*, 46, 127
- Hirashita, H., & Ferrara, A. 2002, *MNRAS*, 337, 921
- Indebetouw, R., Matsuura, M., Dwek, E., et al. 2014, *ApJL*, 782, L2
- Kamenetzky, J., McCray, R., Indebetouw, R., & Barlow, M. J. e. a. 2013, *ApJL*, 773, L34
- Kotak, R., Meikle, W. P. S., Farrah, D., et al. 2009, *ApJ*, 704, 306
- Krause, O., Birkmann, S. M., Rieke, G. H., et al. 2004, *Nature*, 432, 596

- Krause, O., Birkmann, S. M., Usuda, T., et al. 2008, *Science*, 320, 1195
- Lawrence, S. S., MacAlpine, G. M., Uomoto, A., et al. 1995, *AJ*, 109, 2635
- Li, A., & Draine, B. T. 2002, *ApJ*, 564, 803
- Li, D., Bancroft, G. M., Fleet, M., & Feng, X. H. 1995, *Physics and Chemistry of Minerals*, 22, 115
- Liseau, R., Justtanont, K., & Tielens, A. G. G. M. 2006, *A&A*, 446, 561
- Loh, E. D., Baldwin, J. A., Curtis, Z. K., et al. 2011, *ApJSS*, 194, 30
- MacAlpine, G. M., Lawrence, S. S., Sears, R. L., Sosin, M. S., & Henry, R. B. C. 1996, *ApJ*, 463, 650
- MacAlpine, G. M., & Satterfield, T. J. 2008, *AJ*, 136, 2152
- Mathis, J. S., Rumpl, W., & Nordsieck, K. H. 1977, *ApJ*, 217, 425
- Matsuura, M., Woods, P. M., & Owen, P. J. 2013, *MNRAS*, 429, 2527
- Matsuura, M., Barlow, M. J., Zijlstra, A. A., et al. 2009, *MNRAS*, 396, 918
- Matsuura, M., Dwek, E., Meixner, M., et al. 2011, *Science*, 333, 1258
- Meixner, M., Panuzzo, P., Roman-Duval, J., et al. 2013, *AJ*, 146, 62
- Mie, G. 1908, *Annalen der Physik*, 330, 377
- Morgan, H. L., & Edmunds, M. G. 2003, *MNRAS*, 343, 427
- Mller, H. S., Schlder, F., Stutzki, J., & Winnewisser, G. 2005, *Journal of Molecular Structure*, 742, 215 , {MOLECULAR} {SPECTROSCOPY} {AND} {STRUCTURE} A Collection of Invited Papers in Honor of Dr. Walter J. Lafferty
- Nozawa, T., Kozasa, T., Habe, A., et al. 2007, *ApJ*, 666, 955
- Omont, A., Cox, P., Bertoldi, F., et al. 2001, *A&A*, 374, 371
- Osterbrock, D. E. 1957, *PASP*, 69, 227
- Ott, S. 2010a, in *Astronomical Society of the Pacific Conference Series*, Vol. 434, *Astro-nomical Data Analysis Software and Systems XIX*, ed. Y. Mizumoto, K.-I. Morita, & M. Ohishi, 139

- Ott, S. 2010b, in Astronomical Society of the Pacific Conference Series, Vol. 434, Astronomical Data Analysis Software and Systems XIX, ed. Y. Mizumoto, K.-I. Morita, & M. Ohishi, 139
- Pilbratt, G. L., Riedinger, J. R., Passvogel, T., et al. 2010, A&A, 518, L1
- Planck Collaboration. 2011, A&A, 536, A7
- . 2014, ArXiv e-prints, arXiv:1405.0871
- Poglitsch, A., Waelkens, C., Geis, N., et al. 2010, A&A, 518, L2
- Reed, J. E., Hester, J. J., Fabian, A. C., & Winkler, P. F. 1995, ApJ, 440, 706
- Rho, J., Jarrett, T. H., Reach, W. T., Gomez, H., & Andersen, M. 2009, ApJL, 693, L39
- Rho, J., Kozasa, T., Reach, W. T., et al. 2008, ApJ, 673, 271
- Roueff, E., Alekseyev, A. B., & Le Bourlot, J. 2014, A&A, 566, A30
- Rouleau, F., & Martin, P. G. 1991, ApJ, 377, 526
- Rudy, R. J., Rossano, G. S., & Puetter, R. C. 1994, ApJ, 426, 646
- Sankrit, R., Hester, J. J., Scowen, P. A., et al. 1998, ApJ, 504, 344
- Sarangi, A., & Cherchneff, I. 2013, ApJ, 776, 107
- Schneider, R., Ferrara, A., & Salvaterra, R. 2004, MNRAS, 351, 1379
- Smith, N. 2003, MNRAS, 346, 885
- . 2013, ArXiv e-prints, arXiv:1304.0689
- Sugerman, B. E. K., Ercolano, B., Barlow, M. J., et al. 2006, Science, 313, 196
- Sutherland, R. S., & Dopita, M. A. 1995, ApJ, 439, 381
- Temim, T., & Dwek, E. 2013, ArXiv e-prints, arXiv:1302.5452
- Temim, T., Sonneborn, G., Dwek, E., et al. 2012, ApJ, 753, 72
- Temim, T., Gehrz, R. D., Woodward, C. E., et al. 2006, AJ, 132, 1610
- Tielens, A. G. G. M. 2005, The Physics and Chemistry of the Interstellar Medium

- Todini, P., & Ferrara, A. 2001, MNRAS, 325, 726
- Trimble, V. 1968, AJ, 73, 535
- Uspenskii, Y. A., Seely, J. F., Kjornrattanawanich, B., et al. 2006, in Society of Photo-Optical Instrumentation Engineers (SPIE) Conference Series, Vol. 6317, Society of Photo-Optical Instrumentation Engineers (SPIE) Conference Series
- Čadež, A., Carramiñana, A., & Vidrih, S. 2004, ApJ, 609, 797
- Wallström, S. H. J., Biscaro, C., Salgado, F., et al. 2013, A&A, 558, L2
- Wesson, R., Barlow, M. J., Matsuura, M., & Ercolano, B. 2015, MNRAS, 446, 2089
- Wood-Vasey, W. M., Miknaitis, G., Stubbs, C. W., et al. 2007, ApJ, 666, 694
- Wooden, D. H., Rank, D. M., Bregman, J. D., et al. 1993, ApJSS, 88, 477
- Woosley, S. E., & Weaver, T. A. 1995, ApJSS, 101, 181
- Zubko, V., Dwek, E., & Arendt, R. G. 2004, ApJSS, 152, 211
- Zubko, V. G., Mennella, V., Colangeli, L., & Bussoletti, E. 1996, MNRAS, 282, 1321

French 75

30 ml Gin

20 ml Lemon Juice

10 ml Simple Syrup

95 ml Champagne

Shake the gin, lemon juice and simple sugar syrup over ice, double strain in to a champagne flute and then top up with champagne.